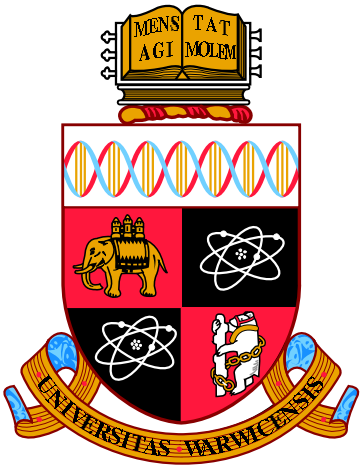

The Development of Methods to Study Structure and Dynamics in Biological Systems using Solid-State NMR

by

Benjamin Paul Tatman

Thesis

Submitted to the University of Warwick

for the degree of

Doctor of Philosophy

Department of Chemistry

July 2023

Contents

List of Tables

List of Figures

Acknowledgments

I would like to thank my supervisors, Józef and Steven, for their continued support and guidance throughout my PhD, and for giving me the opportunity to attend so many interesting conferences and have access to the amazing equipment here at Warwick. Thank you also to Angelo, Rosalie, and Trent for their guidance, support, and feedback. Special thank you to my Advisory Committee, Dominik Kubicki, Jon Duffy, and Matt Broome for their help and support.

A great deal of thanks goes to Anjali, Anton, Jacky, Jairah, Mo, Sarah, Svetlana, and Zainab for their unceasing attempts to keep me at least slightly sane. Thank you to Alex, Callum, Joe, Leo, Michaela, Rosemary, Sophie, Stephen, and Victoria for their unceasing attempts to do the opposite.

Thank you to Katherine Stott, Morag Hunter, and Rita Monson for their inspiration and teaching. Thanks to Cock van Oosterhout for his guidance, advice, and support. Also thank you to my school teachers — too many to name! — for inspiring me to pursue this.

Finally, thank you to my family for their love and support over the past 25 years.

Declarations

This thesis is submitted to the University of Warwick in support of my application for the degree of Doctor of Philosophy. It has been composed by myself and has not been submitted in any previously application for any degree.

The work presented (including data generated and data analysis) was carried out by the author except in the cases outlined below:

Chapter 5

Several of the relaxation rates used in this chapter have been previously published. These are cited and referred to in text. The protein samples used were those which had been produced for those previous works.

Chapter 6:

The majority of the relaxation rate experiments were performed by previous PhD students and postdocs (Dr Jonathan Lamley, Dr Rebecca Stevens, Dr Trent Franks), using labelled protein expressed and purified by Dr Arun Gupta and Dr Simone Kosol. Fitting the experimental data to obtain relaxation rates was performed by Dr Jacqueline Tognetti.

Parts of this thesis have been published by the author:

Chapter 4

This chapter is derived from work published in

B. P. Tatman, W. T. Franks, S. P. Brown, J. R. Lewandowski, Nuclear spin diffusion under fast magic-angle spinning in solid-state NMR, **J. Chem. Phys.**, 2023, **158**, 184201

Chapter 6

The variable temperature molecular dynamics simulations presented in this chapter have been previously published in a different context in

W. T. Franks, B. P. Tatman, J. Trenouth, J. R. Lewandowski, Dipolar Order Parameters in Large Systems with Fast Spinning, **Front. Mol. Biosci.**, 2021, **8**, 1151

During my PhD I was also co-author on the following publications, the results of which are not presented in this thesis.

B. P. Tatman, H. Modha, S. P. Brown, Comparison of methods for ^{14}N-^{1}H recoupling in ^{14}N-^{1}H HMQC MAS NMR, **J. Magn. Reson.**, 2023, **352**, 107459

P. M. J. Szell, Z. Rehman, B. P. Tatman, L. P. Hughes, H. Blade, S. P. Brown, Exploring the Potential of Multinuclear Solid-state ^{1}H, ^{13}C, and ^{35}Cl Magnetic Resonance to Characterize Static and Dynamic Disorder in Pharmaceutical Hydrochlorides, **ChemPhysChem.**, 2022, **24**, e202200558

G. N. M. Reddy, G. M. Peters, B. P. Tatman, T. S. Rajan, S. M. Kock, J. Zhang, B. G. Frenguelli, J. T. Davis, A. Marsh, S. P. Brown, Magic-angle spinning NMR spectroscopy provides insight into the impact of small molecule uptake by G-quartet hydrogels, **Mater. Adv.**, 2020, **1**, 2236–2247

Abstract

Solid-state Nuclear Magnetic Resonance (NMR) can provide insight into the structure and dynamics of biological systems. Magic-Angle Spinning (MAS) can help to increase the limited resolution and sensitivity of the technique. This thesis aims to both investigate how fast MAS may affect spin diffusion and to develop methodology to enable greater insight into the local molecular motions occurring in protein systems.

Under fast MAS conditions, the coherent diffusion of spin order becomes strongly dependent on resonance offset. In Chapter 4, a new basis set selection method is introduced to enable the application of low-order Liouville space methods to the simulation of spin diffusion under fast MAS conditions. Consideration is given to the effects of spinning frequency, magnetic field, and dynamics. In Section 4.5, two experimental case studies are introduced to explore the experimental impacts of this truncation.

The measurement of relaxation rates to probe local molecular motions may be prohibitively long, especially for sensitivity-limited samples. In Chapter 5, a new method is introduced in which separating the dynamic and paramagnetic contributions to relaxation in paramagnetically doped samples can provide a picture of the molecular motions with significant time savings. This method is applied to a very large protein complex which is practically inaccessible to traditionally dynamical analyses.

The reduction in spin diffusion at fast MAS enables the measurement of site-specific relaxation on $^{13}C'$. In Chapter 6, it is found possible to gain insight into the local anisotropy of motions by comparing the dynamics as observed through $^{13}C'$ and ^{15}N relaxation. Insight is gained into the types of motion affecting different secondary structure elements, and how the motions occurring may be related to intermolecular hydrogen-bonding interfaces, antibody recognition, and docking.

Abbreviations

COMFORD CO-Modelfree Fitting Of Relaxation Data 173

CoMPaDReS Concerted Motion and Paramagnetic Dynamics Relaxation Analysis 12

CryoEM Cryogenic Electron-Microscopy 1

CSA Chemical Shift Anisotropy 10

CW Continuous Wave (e.g., CW-NMR) 65

DQ Double-Quantum 70

DTPA-BMA diethylenetriaminepentaacetic acid bis(methylamide) 138

EMF Extended Model Free 54

FID Free Induction Decay 64

FT Fourier Transform 47

GAF Gaussian Axial Fluctuation 173

GB1 $\beta - 1$ domain of Protein G 12

GB1:IgG GB1:Immunoglobulin G complex 12

IDP Intrinsically Disordered Protein 55

IDR Intrinsically Disordered Region 55

IMPACT Interpretation of Motions by Projection onto an Array of Correlation Times 55

LCL Low-order Correlation in Liouville space 30

LR-LCL Locally Restricted Low-order Correlation in Liouville space 92

MAS Magic-Angle Spinning 7

MD Molecular Dynamics 9

MF Model Free 54

Professor Bloch has told you how one can detect the precession of the magnetic nuclei in a drop of water. Commonplace as such experiments have become in our laboratories, I have not yet lost a feeling of wonder, and of delight, that this delicate motion should reside in all the ordinary things around us, revealing itself only to him who looks for it.

Edward M. Purcell, *Nobel Lecture*

Chapter 1

Introduction

The development of techniques to probe the structure and dynamics of biologically relevant molecules since the early 20th century has led to a revolution in our view of biology. The introduction and maturation of tools such as X-ray crystallography, Nuclear Magnetic Resonance (NMR) spectroscopy, and cryo-electron microscopy (CryoEM) have enabled us to peer ever deeper into the complex chemical and physical underpinnings of life. Relating structure to function has given greater insight into the physical basis of disease, the complex biochemistry of life, and enabled the intelligent design of drugs and pharmaceuticals. Figure 1.1 shows a timeline of significant innovations in the structural and dynamic study of biology.

The invention of X-ray crystallography in the 1910s laid the foundations for the structural view of biochemistry we have today.[1–4] The pioneering work of the Braggs enabled the first crystal structure, that of rock salt (NaCl), to be uncovered in 1913.[5] The interpretation of the complex pattern of spots arising from the diffraction of X-rays by the regular spacings of atoms in a rigid crystalline lattice enabled the determination of structure on a scale never previously possible. Though initially only applied to well-ordered simple salts, in 1922 the technique was first applied to determine the crystal structure of an organic molecule, hexamethylene tetramine.[6] The later development of new detectors to enable the quantitative measurement

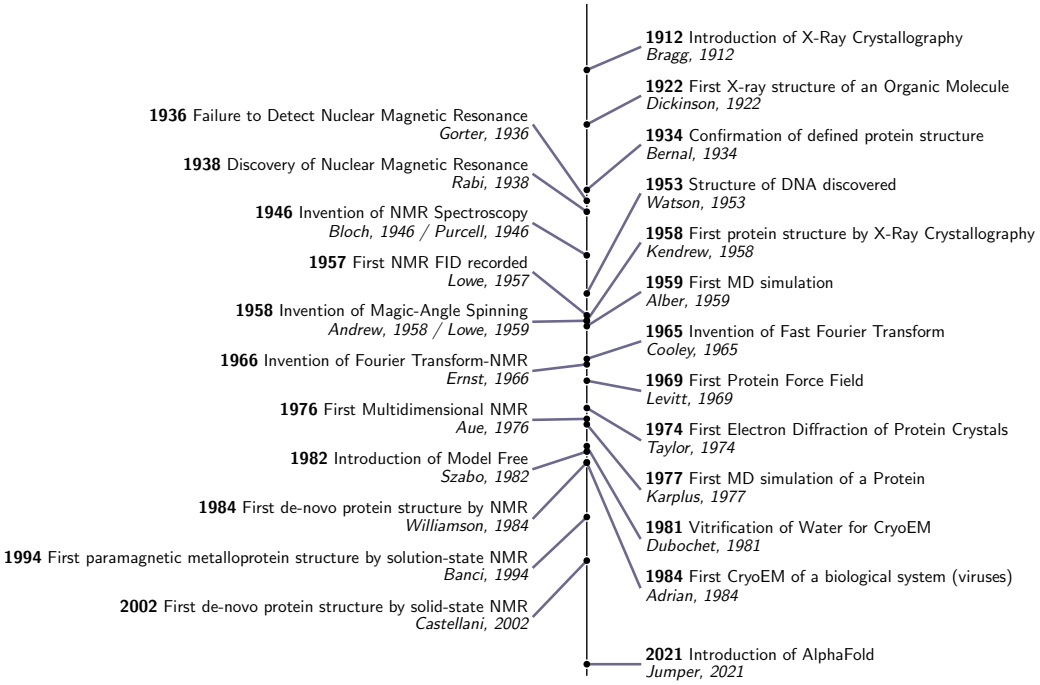

Figure 1.1: Non-exhaustive timeline of important discoveries and events in nuclear magnetic resonance (left) and structural and dynamical biology more generally (right).

of X-ray spot intensity, as well as the Fourier synthesis of X-ray crystallographic analysis only enhanced its utility.[7,8]

Though protein crystals had been known to exist since the early 19th century,[9*] the confirmation that these contained 'an arrangement of atoms inside the protein molecule . . . of a perfectly definite kind' did not come until the first successful X-ray images of hydrated protein crystals by Bernal and Crowfoot in 1934.[11] Despite this, the difficulty in processing and interpreting the X-ray diffraction patterns meant that it was another 24 years before the first protein crystal structure (of myoglobin) could be determined in 1958.[12] In the same decade came the determination of the structure of deoxyribonucleic acid (DNA) by Watson and Crick[13] using data obtained by Franklin and coworkers.[14,15] The structure of DNA gave one of the most beautiful indications of the relation between structure and function, with the structure immediately indicating to Watson and Crick 'a possible copying mechanism for the

*as referenced in ref 10.

genetic material'.[13] The ability of crystallography to provide useful structural insight was also made evident by the determination of Vitamin B_{12} in 1956, which had previously eluded other techniques for determining chemical structure.[16] Several historically relevant structures determined using X-ray techniques are shown in Figure 1.2.

Contemporaneously with these developments in crystallographic techniques was the discovery of 'nuclear magnetic resonance' in 1938 (NMR)[19] and the later development of NMR Spectroscopy in 1946.[20–22] NMR relies on completely different physical underpinnings to X-ray techniques; while X-ray crystallography relies on long-range crystallographic order to diffract systematically incident X-rays, NMR instead probes local magnetic interactions. The variation in electronic environment experienced by distinct spin-active nuclei owing to the local structures around them causes these to resonate at different frequencies in an applied magnetic field. As a result, NMR can provide insight to the local structure and dynamics of samples without long range crystallographic order. This is of relevance to interpreting structure, as the conditions required for X-ray structure determination of proteins and other biological molecules are generally completely different to those that these molecules would exist in naturally; being both cryogenically cooled, and existing in a rigid crystalline lattice. These structures may therefore sometimes be misrepresentative of the true biologically relevant structure.[23,24] Furthermore, while X-ray diffraction is dependent on the density of electrons and is therefore insensitive to lightweight atoms such as protons, NMR is instead sensitive to the nuclear gyromagnetic ratio, which is independent of the atomic weight. NMR can therefore provide a highly complementary view of structure to X-rays, in particular with regard to the structure of non-crystalline samples and the positioning of small atoms such as protons.

The invention of Fourier-Transform NMR,[25] aided by the rapid increases in computational power and development of faster Fourier transform algorithms in the 1960s[26] drastically improved the sensitivity of the technique, and enabled the invention of two-dimensional NMR methods.[27] These developments, among others,[28,29]

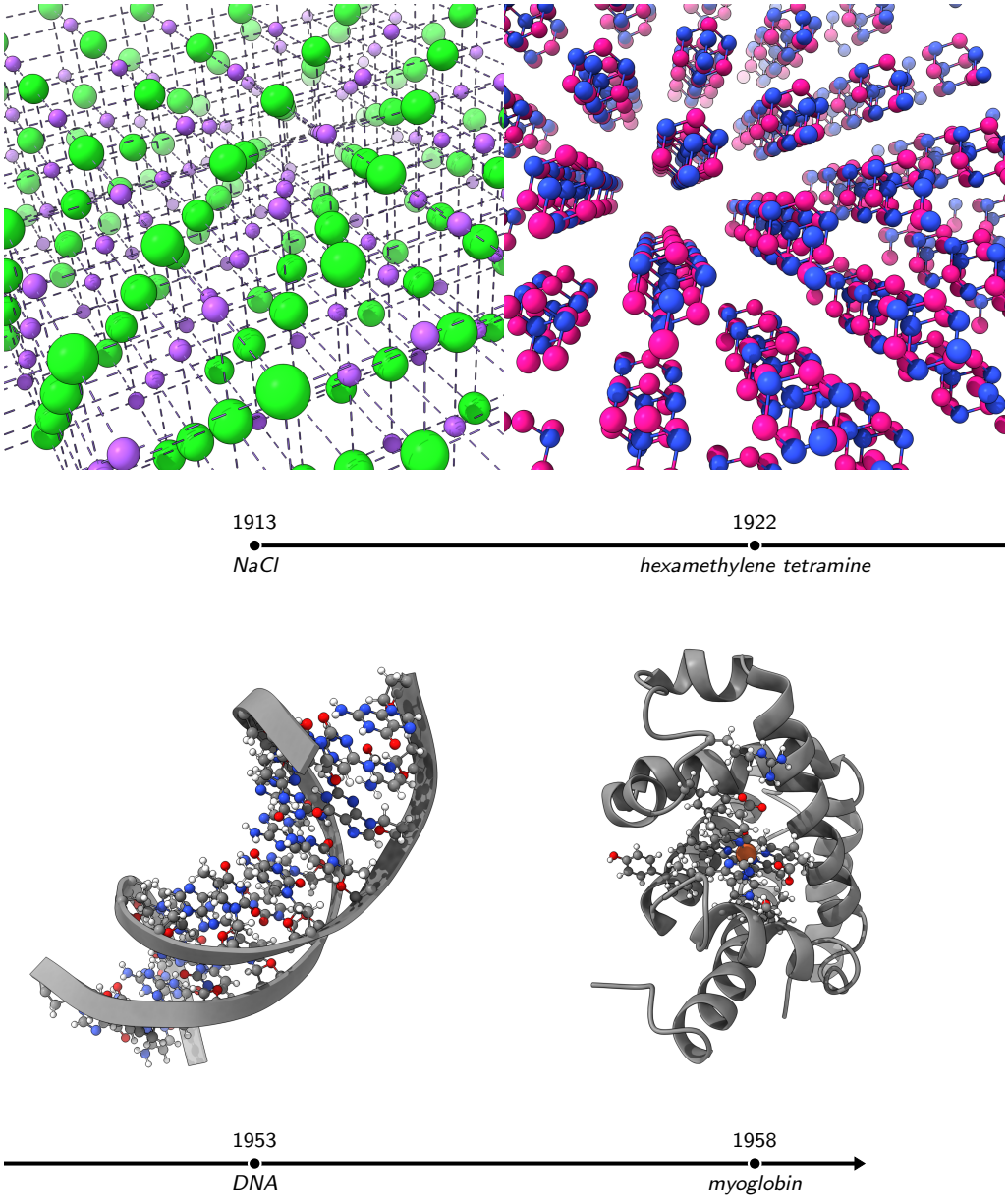

Figure 1.2: Notable structures determined by X-ray crystallographic methods in the 20th Century. Left to right: First X-ray crystal structure, NaCl from 1913.[5] (Inorganic Crystal Structure Database (ICSD): 53815[5]); First X-ray crystal structure of an organic molecule, hexamethylene tetramine from 1922.[6] (Cambridge Crystallographic Data Centre (CCDC): HXMTAM[17]); X-ray determination of the crystal structure of DNA, 1953.[13] (Protein Data Bank (PDB): 2BNA[18]); First X-ray crystal structure of a protein, myoglobin, from 1958.[12] (PDB: 1MBN, note that this is a 1976 structure).

enabled the *de-novo* structural determination of BUSI IIA, a proteinase inhibitor, by solution-state NMR in 1985.[30] Figure 1.3 shows some historically relevant protein

structures determined by NMR.

While the majority of early protein structures solved by X-ray crystallography were metalloproteins, where structure determination is aided by the X-ray scattering of the highly electron dense metal species,[12,31] these can pose particular problems for the structural and dynamical analysis of proteins by NMR. In the case of diamagnetic metals, this difficulty typically arises due to the metal centre representing a discontinuity in the structure[32] as it is not usually feasible to obtain $^{1}\mathrm{H}-\mathrm{M}$ distances owing to these metal centres typically having low gyromagnetic ratios and often large quadrupolar couplings. This problem is particularly exacerbated in the case of paramagnetic metal centres, as the presence of unpaired electrons within these leads to additional paramagnetic effects resulting in a 'blind sphere', within which the paramagnetic relaxation enhancement broadening or paramagnetic contact shift is sufficiently large that these spins often cannot be readily observed.[33] While a further discussion of these paramagnetic effects will be given in Chapter 5, to continue the current discussion it is interesting to note that the first solution-state structure of a paramagnetic metalloprotein (the iron-sulfur protein iso-1 from *Ectothiorhodospira halophila*) was determined in 1994.[34] The investigation of the structure and dynamics of such systems is of interest as many of these play key functional roles owing to the useful properties of transition metal ions with regards to redox chemistry,[35,36] and their importance in cellular respiration may indicate that these were among the first proteins to evolve and therefore may contain clues as to the origin of life itself.[37–40]

Whilst the majority of structural studies of biological systems using NMR have been performed in the solution state, this is not always possible as many systems of interest may be insoluble, too large, or require supporting membranes. Anisotropic interactions, such as dipolar couplings and chemical shift anisotropy may cause significant peak broadening. In the solid state, these interactions make it almost impossible to interpret static solid spectra in unoriented biological systems. A benefit of performing NMR experiments in the solution state is that the overall

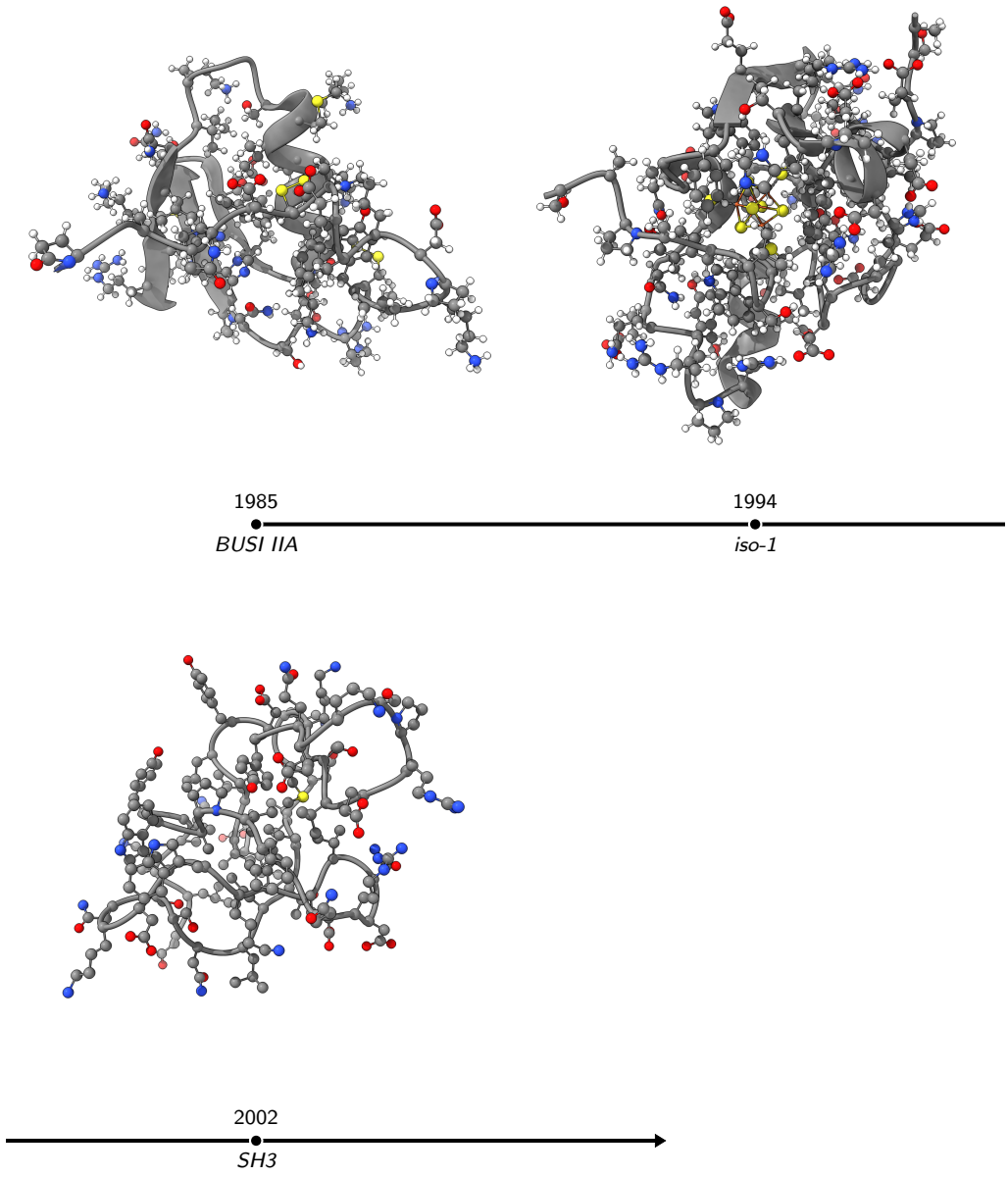

Figure 1.3: Left-to-right: The first protein structure determined using solution-state NMR (Williamson *et al*. (1985)[30]); The first structure of a paramagnetic metalloprotein determined using solution-state NMR (Banci *et al*. (1994)[34]); and the first protein structure determined using solid-state NMR (Castellani *et al*. (2002)[41]). The structures are those from the original papers, being 1BUS, 1PIJ, and 1M8M in the PDB, respectively.

tumbling of the molecules being studied averages out these strong anisotropic interactions. This benefit, however, also gives rise to a key limitation of studies in

the solution state: the larger the size of a biological macromolecule, the slower it tumbles. A result of this slow tumbling is a significant incoherent peak broadening, complicating the analysis of large biological systems by NMR in the solution state. Additionally, very large biological complexes or other systems may be insoluble in solution and therefore precipitate out, precluding their study by solution-state NMR. Consequently, solution NMR faces an upper limit on the size of molecule accessible.

Solid-state NMR, on the other hand, does not face this limitation. As a result, it may be applied to structures which are both impossible to crystallise in their native structures and too large to be studied by solution-state NMR. For example, solid-state NMR has found particular utility in studying membrane proteins[42–48] and precipitated complexes.[49–51] To allow for structural or dynamical information to be extracted in a local manner, however, site-specific resonance assignments must be made. The significant peak broadening arising from the unaveraged anisotropic interactions typically makes this infeasible in unoriented static spectra. 'Magic-angle spinning' (MAS), invented simultaneously by Andrew *et al*.[52] and Lowe[53] in the late 1950s, relies on the mechanical rotation of the sample about the magic angle of 54.7° to introduce a time dependence to the Hamiltonian and systematically average out the anisotropic interactions. While a more in-depth discussion of how MAS works will be given in Chapter 2, for now it is enough to know that greater MAS frequencies typically lead to greater averaging of anisotropic interactions and thus enable an increase in resolution. The development of probes able to access faster MAS frequencies, combined with developments in methodology such as site-specific labelling techniques, enabled the first *de-novo* solid-state structural determination of a protein, SH3, in 2002.[41]

In recent years, several significant developments have taken place in structural biology. The 'resolution revolution' of CryoEM has enabled the determination of high-resolution biological structures without the requirement of large crystals, as needed for X-ray crystallography.[54–59] New machine learning methods such as

AlphaFold[60] and RoseTTAFold[61] have led to an exponential increase in the availability of structural information, with the creation of databases containing millions of predicted protein structures[62,63] and the wide availability of software to predict the full 3D structure of a protein from its amino acid sequence. These computational tools may complement NMR, by allowing NMR to act as a structural validation method to verify experimentally machine learning predictions without necessarily requiring a full set of structural calculation experiments to be performed.[64]

The presence of strong anisotropic interactions which are not completely averaged by MAS leads to significant line broadening in the solid state, making it very difficult in many cases to isolate resonances. In recent years, developments in magnetic field technology[65,66] and MAS[67–70] have enabled access to even greater resolution NMR spectra. Figure 1.4 shows how the maximum attainable MAS frequency has changed since the original introduction of the technique. However, with the increase in resolution obtained using these tools comes a few complications. Many structure determination methods applied in solid-state NMR rely on the coherent diffusion of spin order, 'spin diffusion', to transfer magnetisation through space between nuclear spins.[41,71–74] While at low MAS frequencies such techniques are readily applied, spin diffusion is known to be highly sensitive to resonance offset.[75,76] Understanding how spin diffusion is affected by fast MAS, however, is difficult. Spin diffusion is inherently a many-body effect, and therefore requires simulations of large numbers of spins.[77–80] However, the exponential scaling of traditional Hilbert-space density matrix simulations of NMR makes such simulations computationally infeasible;[77–79,81,82] such simulations are generally limited to $\leq$12 spins.[83] It has been found that by systematically reducing the space of interactions considered it is possible to simulate significantly larger spin systems.[77–79,84,85] Chapter 4 builds upon these previous reduced space models to allow for simulations of spin diffusion under fast MAS conditions, by introducing a new basis set selection methodology. This is then used to simulate the effects of increasing MAS frequency and magnetic field on spin diffusion, and how this is related to the spatial and spectral arrange-

ment of spins. This discussion will then be extended in Chapter 5, which focuses on how these effects impact NMR experiments.

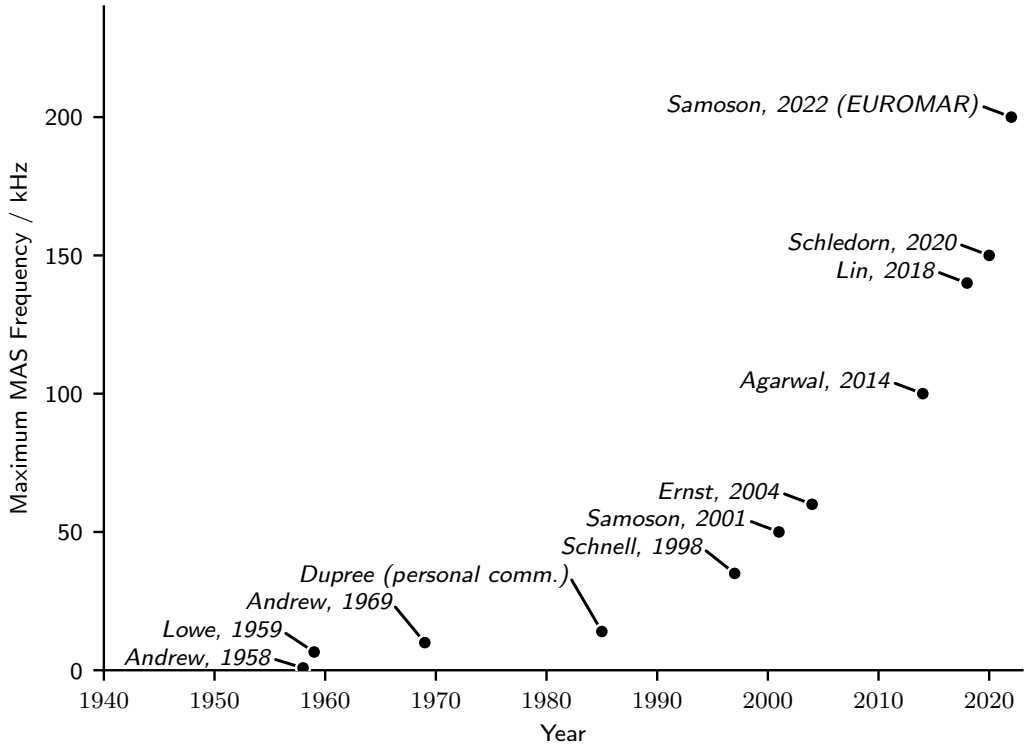

Figure 1.4: Maximum achieved MAS frequency over time.[52,53,67,68,86–90]

While structure can give insight into function, biology is rarely at rest. Function arises from the dynamical motions present within a system, and quantifying and understanding these motions is also important for understanding how biological systems function.[91,92] This was apparent even for the first protein to have a crystal structure determined, myoglobin in 1958,[12] for which the haem pocket is blocked by a histidine sidechain. The transport of oxygen by both this protein and other globin proteins relies on the mobility of this sidechain to control access to this pocket.[36,93] Several techniques can provide insight into these local dynamics.[94–96] Perhaps the most useful are molecular dynamics (MD) and NMR, as these can provide insight into both the timescales and amplitudes of motions on a site-specific local basis in a complementary manner.

MD relies on integration of the Newtonian equations of motion to propagate forward

the atomic positions within a protein structure according to a given forcefield. These empirical forcefields were originally introduced to study atomic interactions[97–99] and to minimize X-ray crystal structures.[100,101] In 1959, Alder *et al*. ran the first MD simulation of 'several hundred interacting classical particles'.[102] Later, in 1977, McCammon *et al*. ran the first MD simulation of a full protein (bovine pancreatic trypsin inhibitor, BPTI) for 8.8 picoseconds.[103] Since then, developments in computational power have enabled significantly longer, and significantly larger, MD simulations to be performed.[104–111] Of particular note is Anton, a custom-built MD simulation supercomputer capable of running millisecond-scale MD simulations.[112]

NMR can similarly provide insight into local dynamics. The modulation of anisotropic interactions such as dipolar couplings and chemical shift anisotropy (CSA) by local dynamics gives rise to a stochastic time-dependent Hamiltonian. The evolution of the spin system under this Hamiltonian provides a pathway by which the system may relax back to thermal equilibrium.[113] By quantifying the rate at which a given spin returns to thermal equilibrium it is therefore possible to quantify the motions which gave rise to that relaxation.[114–116] Such analysis is possible both in the solution state and solid state. In the solution state it is not possible to use relaxation rate analysis to probe motions occurring on timescales slower than the overall tumbling ($\approx$ nanoseconds), and analysis on such motions must be performed using other methods, such as residual dipolar couplings.[96,117,118] In contrast, the lack of overall tumbling on the solid state means that slower (ns-μs) motions may be observed in the same manner as faster motions.

Both NMR and MD have their advantages and disadvantages for the study of local dynamics. As has been alluded to previously, MD simulations face a computational barrier both in terms of the timescales which may be accessed, and the size of the systems accessible.[109,110] As such, typical MD simulations (such as those presented in this thesis) are usually limited to lengths of at most several microseconds. As these present only a single trajectory of the motions occurring, they therefore only

sufficiently sample motions occurring on the nanosecond timescale. To obtain simulations on larger systems over longer timescales, techniques such as accelerated MD[107–111] or coarse graining[119,120] may be utilised, however these come with their own respective challenges. In contrast, NMR relaxation is indicative of an ensemble average of motions from many individual proteins. Relaxation rates may additionally be sensitive to motions occurring on slower timescales; for instance, spin-lattice relaxation in the rotating frame ($R_{1\rho}$) is sensitive to motions occurring on timescales as slow as milliseconds, which would be inaccessible to current MD methodologies.[121–123]

A limitation of NMR is the spatial resolution of motions attainable. Only the dynamics at spin-active nuclei may be observed, and at MAS frequencies currently available spin diffusion causes many of these to be partially or wholly averaged across the system. For example, it is not possible to obtain site-specific sidechain ^{13}C relaxation rates at the most commonly used MAS frequencies ($\leq$ 111 kHz) without expensive site-specific isotopic labelling schemes or the use of insensitive unlabelled samples.[124,125] Furthermore, the requirement to record individual experiments for each different isotope of interest (typically ^{15}N and ^{13}C′) adds additional complexity, and as a result most studies of dynamics in NMR, especially in the solid-state, have relied only on ^{15}N relaxation. The relaxation measured on ^{15}N amide sites is dominated by the anisotropic motions of the ^{15}N – ^{1}H dipolar vector,[126] which may cause them to not fully sample the range of motions occurring within the protein.[127] On the other hand, an MD trajectory provides exact coordinates for every atom within the system.

Being a computational technique, MD requires experimental validation to ensure that it is representative of the system of interest. In this manner, NMR and MD have been found to be highly complementary; by using NMR to validate the MD trajectory, and then using the MD to look at the specifics of the motions occurring.[128–130] A related issue pertains to the use of MD to look at systems for which there is no complete structure available as MD simulation requires the creation of a suitable

model for the system being studied. In the case of a crystalline protein or an isolated protein in solution with a known structure this is reasonably straight forward. However, for studying interfaces without atomic scale structural information this can lead to systematic deficiencies in the resulting trajectory.

A key issue of NMR dynamics analysis is the experimental time required. This is particularly acute in the case of protein complexes made up of multiple components. The effective dilution of the labelled protein of interest in this case may mean that experimental times are substantially increased to the extent that it is no longer feasible to record sufficient data to quantify the local motions. Chapter 5 introduces a new method, Concerted Motion and Paramagnetic Dynamics Relaxation analysis (CoMPaDReS), which is then applied to a paramagnetically doped complex of GB1 with human Immunoglobulin G (GB1:IgG). It is found to be possible to make use of data doped with paramagnetic agents to quantify local dynamics. The paramagnetic relaxation enhancement resulting from the doping makes it feasible to record sufficient relaxation rates to investigate the local dynamics, while additionally providing insight into the paramagnetic interaction and consequences this has in terms of the solvent accessibility.

In Chapter 6, a large dataset of $^{13}C'$ and ^{15}N R_1 and $R_{1\rho}$ relaxation rates are combined to investigate the local motions occurring within the microcrystalline $\beta - 1$ domain of Protein G, GB1. A combined analysis based on two nuclei provides a greater resolution as to the dynamics occurring. The use of variable temperature relaxation rates to increase the effective range of timescales observable is demonstrated. The resulting dynamics are then compared to MD, where good agreement is found to a 2.28 microsecond trajectory of a model of the microcrystalline protein. Finally, differences between $^{13}C'$ and ^{15}N motions are interpreted in terms of their possible relation to anisotropic motions occurring within the protein.

Chapter 2

Theory

2.0 Quantum Mechanics

This section aims to outline the basic quantum mechanics required for the later discussion of NMR. In this thesis, the following notation style is used:

- *matrices are typeset in bold with underlining, $\underline{\boldsymbol{A}}$, which if using Latin script will be capitalised.*
- *vectors are typeset in bold and will generally be lower case, $\boldsymbol{a}$.*
- *vector expansions in text will be given using commas if row vectors ($[1, 0]$), and with semi-colons if column vectors ($[1; 0]$).*
- *operators will be denoted using a hat, $\hat{A}$, and capitalised if Latin.*
- *symbols which are a mixture of the above will have their notation combined; e.g., a matrix operator, $\hat{\underline{\boldsymbol{A}}}$, will be bold, underlined, capitalized, and denoted using a hat.*

A fundamental postulate of quantum mechanics (QM) is that any closed system possesses a wavefunction which completely describes the quantum state of that system. In Dirac notation, a wavefunction is given as a ket, $|\psi\rangle$, with its complex conjugate being given as a bra, $\langle\psi|$. A wavefunction ket may be composed as a linear superposition of (typically orthonormal) basis set vectors describing the

system,

$$|\psi\rangle = \sum_{i}^{N} \lambda_i \, |\psi_i\rangle \, , \tag{2.1}$$

where the sum is over all N components of the basis set, $|\psi_i\rangle$. The combination of a 'bra' and 'ket' gives a 'braket', the scalar product

$$\langle \phi | \psi \rangle \equiv \int \phi^*(\boldsymbol{x}) \psi(\boldsymbol{x}) d\boldsymbol{x}, \tag{2.2}$$

integrating over all space, where the asterisk denotes complex conjugate. Supposing that the basis set vectors, $|\psi_i\rangle$, have been chosen to be orthonormal, the following relation holds

$$\langle \psi_i | \psi_j \rangle = \begin{cases} 1 & \text{for } i = j \\ 0 & \text{otherwise} \end{cases} . \tag{2.3}$$

We may then introduce the concept of an 'operator', which may be considered as a function which maps one wavefunction onto another. An operator acting on an eigenfunction of itself will give the product of the eigenvalue with the eigenfunction:

$$\hat{A} \, |\psi\rangle = a \, |\psi\rangle \, , \tag{2.4}$$

where $|\psi\rangle$ is an eigenfunction of the operator $\hat{A}$ with eigenvalue a. Any physical observable may be represented by an operator, which must necessarily be Hermitian (self-adjoint) to ensure that the eigenvalues are real. The expectation value of an operator can be defined as

$$\langle \hat{A} \rangle = \langle \psi | \hat{A} | \psi \rangle \, . \tag{2.5}$$

Possibly the most important operator is the Hamiltonian, $\hat{H}$, for which the eigenvalue represents the total energy for a given eigenfunction. The time-dependent Schrödinger equation,

$$i\hbar\frac{d}{dt}\left|\psi(t)\right\rangle = \hat{H}\left|\psi(t)\right\rangle \tag{2.6}$$

describes how a given state evolves with time.

A convenient notation for describing these operators and wavefunctions, which is particularly applicable to NMR, is to denote operators as matrices, $\hat{\underline{\boldsymbol{A}}}$, and wavefunctions as vectors, $|\boldsymbol{\psi}\rangle$. For instance, we may have a wavefunction composed as a linear combination of basis set vectors

$$|\boldsymbol{\psi}\rangle = c_\alpha \begin{bmatrix} 1 \\ 0 \end{bmatrix} + c_\beta \begin{bmatrix} 0 \\ 1 \end{bmatrix} = \begin{bmatrix} c_\alpha \\ c_\beta \end{bmatrix} \tag{2.7}$$

$$\langle\boldsymbol{\psi}| = c_\alpha^* \begin{bmatrix} 1 & 0 \end{bmatrix} + c_\beta^* \begin{bmatrix} 0 & 1 \end{bmatrix} = \begin{bmatrix} c_\alpha^* & c_\beta^* \end{bmatrix} \tag{2.8}$$

and an operator

$$\hat{\underline{\boldsymbol{A}}} = \begin{bmatrix} A_{\alpha\alpha} & A_{\alpha\beta} \\ A_{\beta\alpha} & A_{\beta\beta} \end{bmatrix}, \tag{2.9}$$

with corresponding expectation value

$$\langle \hat{\underline{\boldsymbol{A}}} \rangle = \langle \boldsymbol{\psi} | \hat{\underline{\boldsymbol{A}}} | \boldsymbol{\psi} \rangle \tag{2.10}$$

$$= \begin{bmatrix} c_\alpha^* & c_\beta^* \end{bmatrix} \begin{bmatrix} A_{\alpha\alpha} & A_{\alpha\beta} \\ A_{\beta\alpha} & A_{\beta\beta} \end{bmatrix} \begin{bmatrix} c_\alpha \\ c_\beta \end{bmatrix} \tag{2.11}$$

$$= A_{\alpha\alpha} c_\alpha^* c_\alpha + A_{\alpha\beta} c_\alpha^* c_\beta + A_{\beta\alpha} c_\beta^* c_\alpha + A_{\beta\beta} c_\beta^* c_\beta. \tag{2.12}$$

One operator which is of particular utility in NMR is the density matrix operator. This operator is given as

$$\hat{\underline{\boldsymbol{\sigma}}} = |\boldsymbol{\phi}\rangle \langle \boldsymbol{\phi}| , \tag{2.13}$$

where $|\boldsymbol{\phi}\rangle$ and $\langle \boldsymbol{\phi}|$ are implicitly linear combinations of the basis set vectors. In the case of $|\boldsymbol{\psi}\rangle$ and $\langle \boldsymbol{\psi}|$ as given in equations 2.7 and 2.8, this gives:

$$\hat{\underline{\boldsymbol{\sigma}}} = |\boldsymbol{\psi}\rangle \langle \boldsymbol{\psi}| \tag{2.14}$$

$$= \begin{bmatrix} c_\alpha \\ c_\beta \end{bmatrix} \begin{bmatrix} c_\alpha^* & c_\beta^* \end{bmatrix} \tag{2.15}$$

$$= \begin{bmatrix} c_\alpha^* c_\alpha & c_\beta^* c_\alpha \\ c_\alpha^* c_\beta & c_\beta^* c_\beta \end{bmatrix}. \tag{2.16}$$

The diagonal elements relate to states composed of a single eigenstate, 'populations', while the off-diagonal elements relate to mixed state 'coherences'. The expectation value of an operator may be calculated by taking the trace of the product of the operator with this density matrix:

$$\langle \hat{\underline{\boldsymbol{A}}} \rangle = \mathrm{Tr}(\hat{\underline{\boldsymbol{A}}}\hat{\underline{\boldsymbol{\sigma}}}) \tag{2.17}$$

$$= \mathrm{Tr} \begin{bmatrix} A_{\alpha\alpha}c_\alpha^* c_\alpha + A_{\alpha\beta}c_\alpha^* c_\beta & A_{\alpha\alpha}c_\beta^* c_\alpha + A_{\alpha\beta}c_\beta^* c_\beta \\ A_{\beta\alpha}c_\alpha^* c_\alpha + A_{\beta\beta}c_\alpha^* c_\beta & A_{\beta\alpha}c_\beta^* c_\alpha + A_{\beta\beta}c_\beta^* c_\beta \end{bmatrix} \tag{2.18}$$

$$= A_{\alpha\alpha}c_\alpha^* c_\alpha + A_{\alpha\beta}c_\alpha^* c_\beta + A_{\beta\alpha}c_\beta^* c_\alpha + A_{\beta\beta}c_\beta^* c_\beta. \tag{2.19}$$

In the following section, these fundamental concepts of quantum mechanics will be applied more specifically to the phenomenon of Nuclear Magnetic Resonance.

2.1 NMR Theory

This section will introduce the underlying theory of the NMR experiment. The first section of this is based primarily on reading 'Understanding NMR Spectroscopy' by Keeler (2010),[131] 'Principles of Nuclear Magnetism' by Abragam (1961),[132] 'Spin Dynamics' by Levitt (2008),[133] and 'Lectures on Spin Dynamics: The Theoretical Minimum' by Pileio (2022).[134]

One fundamental property of an atomic nucleus is that of spin. The spin angular momentum of a nucleus is characterised by a spin angular momentum quantum number, I. In the absence of magnetism, the nuclear spins possess $2I + 1$ degenerate nuclear spin states. The magnetic moment of a spin, $\hat{\boldsymbol{\mu}}$, is related to its gyromagnetic ratio, γ and spin angular momentum operator, $\hat{\boldsymbol{I}}$:

$$\hat{\boldsymbol{\mu}} = \gamma \hat{\boldsymbol{I}}, \tag{2.20}$$

where the spin angular momentum operator, $\hat{\boldsymbol{I}}$, may be represented in vector notation as $[\hat{I}_x; \hat{I}_y; \hat{I}_z]$. The gyromagnetic ratios of several nuclei of interest in this thesis are given in Table 2.1. Under the application of a magnetic field, the $2I + 1$ nuclear spin states lose their degeneracy. These non-degenerate spin states are denoted

using the magnetic quantum number, $m = -I, -I+1, \ldots, I-1, I$. The interaction giving rise to this loss of degeneracy is termed the Zeeman Hamiltonian

Table 2.1: Gyromagnetic ratios of several nuclei of interest.[135]

Species	γ / MHz T^{-1}
^{1}H	42.58
^{13}C	10.71
^{15}N	-4.32
^{155}Gd	-1.32
^{157}Gd	-1.73

$$\hat{H}_Z = \hat{\boldsymbol{\mu}} \cdot \boldsymbol{B_0}, \tag{2.21}$$

where $\boldsymbol{B_0}$ represents the applied external magnetic field. By convention, the strong magnetic field applied is defined as being along the z-axis, such that $\boldsymbol{B_0} = [0; 0; B_z]$. In this case, the Zeeman Hamiltonian may then be written as

$$\hat{H}_Z = \hat{\boldsymbol{\mu}} \cdot \boldsymbol{B_0} \tag{2.22}$$

$$= \gamma \begin{bmatrix} \hat{I}_x \\ \hat{I}_y \\ \hat{I}_z \end{bmatrix} \cdot \begin{bmatrix} 0 \\ 0 \\ B_z \end{bmatrix} \tag{2.23}$$

$$= \gamma B_z \hat{I}_z = -\omega_0 \hat{I}_z, \tag{2.24}$$

where ω_0 represents the Larmor frequency,

$$\omega_0 = -\gamma B_z, \tag{2.25}$$

namely the resonant frequency of the nuclei in the applied magnetic field.

The time-independent Schrödinger equation,

$$\hat{H}\,|\psi\rangle = E\,|\psi\rangle\,, \tag{2.26}$$

allows us to determine the energy of a given wavefunction, $|\psi\rangle$. As previously, under the applied magnetic field, our $2I+1$ spin states are no longer degenerate. These m states are the eigenstates of $\hat{I}_z$, with eigenvalues $I_z = m\hbar$

$$\hat{I}_z\,|\psi_m\rangle = I_z\,|\psi_m\rangle \tag{2.27}$$

$$= m\hbar\,|\psi_m\rangle\,. \tag{2.28}$$

We may therefore apply the Schrödinger equation to determine the energy of a given state with magnetic quantum number m, as

$$\underline{\hat{\boldsymbol{H}}}_Z\,|\psi_m\rangle = -\omega_0\hat{I}_z\,|\psi_m\rangle \tag{2.29}$$

$$= -\omega_0 m\hbar\,|\psi_m\rangle\,, \tag{2.30}$$

i.e.,

$$E_m = -m\hbar\omega_0. \tag{2.31}$$

Conventionally in NMR, we express the energies in units of angular frequency (rad s^{-1}) by dividing by the reduced Planck's constant, $\hbar$

$$E_m = -m\omega_0. \tag{2.32}$$

These energy levels are shown for various spin quantum numbers in Figure 2.1. In the case of a spin $I = 1/2$ nucleus (a 'spin-1/2' nucleus), there are then two

nuclear spin states with energies $E_{1/2} = -\frac{1}{2}\omega_0$ and $E_{-1/2} = \frac{1}{2}\omega_0$, with a difference of ω_0.

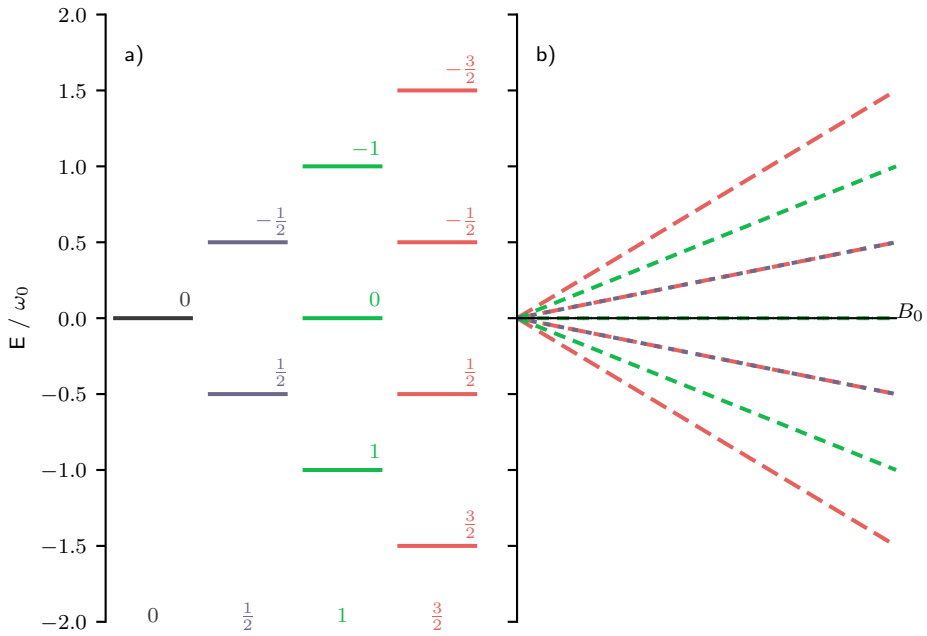

Figure 2.1: (a) Energy level splittings in units of ω_0 for spins with spin angular momentum quantum numbers $I = 0, 1/2, 1, 3/2$. (b) Variation in energy level splitting with increasing magnetic field, B_0.

For simplicity, the remainder of this theory section will focus on the case of a spin-1/2 nucleus. The treatment may be expanded to nuclei with different spin angular momentum quantum numbers. For spin-1/2 nuclei, the two eigenstates may be expressed in vector notation as:

$$|-\frac{1}{2}\rangle = \begin{bmatrix} 0 \\ 1 \end{bmatrix} \tag{2.33}$$

$$|\frac{1}{2}\rangle = \begin{bmatrix} 1 \\ 0 \end{bmatrix}. \tag{2.34}$$

It therefore follows from equation 2.27 that the matrix form of $\hat{\underline{\boldsymbol{I}}}_z$ can therefore be given as:

$$\underline{\hat{\boldsymbol{I}}}_z = \frac{1}{2}\begin{bmatrix} 1 & 0 \\ 0 & -1 \end{bmatrix}, \tag{2.35}$$

again omitting $\hbar$. The forms of the remaining two angular momentum operators in this Zeeman eigenbasis, $\underline{\hat{\boldsymbol{I}}}_x$ and $\underline{\hat{\boldsymbol{I}}}_y$, are then

$$\underline{\hat{\boldsymbol{I}}}_x = \frac{1}{2}\begin{bmatrix} 0 & 1 \\ 1 & 0 \end{bmatrix} \tag{2.36}$$

$$\underline{\hat{\boldsymbol{I}}}_y = \frac{1}{2i}\begin{bmatrix} 0 & 1 \\ -1 & 0 \end{bmatrix}, \tag{2.37}$$

which may alternatively be expressed as the raising and lowering operators, $\underline{\hat{\boldsymbol{I}}}_+$ and $\underline{\hat{\boldsymbol{I}}}_-$

$$\underline{\hat{\boldsymbol{I}}}_+ = \underline{\hat{\boldsymbol{I}}}_x + i\underline{\hat{\boldsymbol{I}}}_y = \frac{1}{2}\begin{bmatrix} 0 & 1 \\ 0 & 0 \end{bmatrix} \tag{2.38}$$

$$\underline{\hat{\boldsymbol{I}}}_- = \underline{\hat{\boldsymbol{I}}}_x - i\underline{\hat{\boldsymbol{I}}}_y = \frac{1}{2}\begin{bmatrix} 0 & 0 \\ 1 & 0 \end{bmatrix}. \tag{2.39}$$

Additionally, we should include the so-called 'unity' operator, $\underline{\hat{\boldsymbol{E}}}$:

$$\underline{\hat{\boldsymbol{E}}} = \begin{bmatrix} 1 & 0 \\ 0 & 1 \end{bmatrix}. \tag{2.40}$$

In an experiment, we are interacting with a large ensemble of interacting nuclear spins. As a result, we must consider the formation of mixed states. Perhaps the simplest way to model these mixed states for an NMR experiment is to use the

density matrix formalism. The density operator was introduced in Section 2.0. As described in that section, we may express the wavefunction of our closed system as a linear combination of our eigenbasis wavefunctions:

$$|\phi\rangle = c_{1/2}\,|\frac{1}{2}\rangle + c_{-1/2}\,|-\frac{1}{2}\rangle \tag{2.41}$$

$$= c_{1/2}\begin{bmatrix}1\\0\end{bmatrix} + c_{-1/2}\begin{bmatrix}0\\1\end{bmatrix} \tag{2.42}$$

$$= \begin{bmatrix}c_{1/2}\\c_{-1/2}\end{bmatrix}. \tag{2.43}$$

The corresponding density matrix (equation 2.14) is therefore:

$$\underline{\hat{\boldsymbol{\sigma}}} = |\phi\rangle\,\langle\phi| \tag{2.44}$$

$$= \begin{bmatrix}c_{1/2}c^*_{1/2} & c_{1/2}c^*_{-1/2}\\ c_{-1/2}c^*_{1/2} & c_{-1/2}c^*_{-1/2}\end{bmatrix}. \tag{2.45}$$

Given that the coefficients, $c_{1/2}$ and $c_{-1/2}$, are complex numbers, it follows that this can alternatively be expressed in polar notation with $c_{\pm 1/2} = r_{\pm 1/2}e^{i\theta_{\pm 1/2}}$ (and equivalently, $c^*_{\pm 1/2} = r_{\pm 1/2}e^{-i\theta_{\pm 1/2}}$) such that

$$\underline{\hat{\boldsymbol{\sigma}}} = \begin{bmatrix}r_{1/2}r_{1/2} & r_{1/2}r_{-1/2}e^{i(\theta_{1/2}-\theta_{-1/2})}\\ r_{1/2}r_{-1/2}e^{i(\theta_{-1/2}-\theta_{1/2})} & r_{-1/2}r_{-1/2}\end{bmatrix}. \tag{2.46}$$

The diagonal elements, $r^2_{1/2}$ and $r^2_{-1/2}$, are referred to as 'populations' and describe the proportion of spins in an ensemble existing in the respective states. The off-diagonal elements are termed 'coherences', and are non-zero only if there exists

phase coherence; otherwise, the random distribution of phase leads to these terms cancelling.

At thermal equilibrium, we may calculate this density matrix assuming the Boltzmann distribution. Given that the total number of spins, $N = n_{1/2,eq} + n_{-1/2,eq}$, we can calculate the equilibrium populations as:

$$r^2_{\pm 1/2,eq} = n_{\pm 1/2,eq}/N \tag{2.47}$$

$$= \frac{1}{2} e^{\pm \frac{\frac{1}{2}\hbar\gamma B_z}{k_B T}}. \tag{2.48}$$

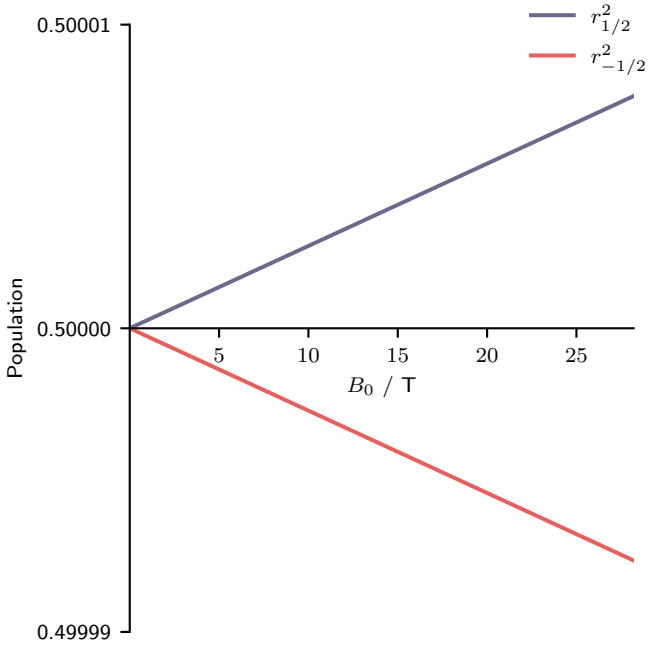

Figure 2.2: Population of the spin-up and spin-down states as a function of magnetic field. Calculated assuming the gyromagnetic ratio of ^{1}H (42.58 MHz/T^{-1}) and a temperature of 300 K.

Figure 2.1 illustrates how these populations vary as a function of magnetic field. This demonstrates one limitation of NMR: as the difference in energy between the spin-up and spin-down states is small ($\frac{1}{2}\hbar\gamma B_z \ll k_B T$), there is very little polarisation at magnetic fields available today (maximum commercially available

as of writing is 28.8 T[65]). We may decompose the resulting density matrix into a basis set of our angular momentum operators by approximating the exponential as a Taylor series:

$$\underline{\hat{\boldsymbol{\sigma}}} = \frac{1}{N}\begin{bmatrix} \frac{1}{2}Ne^{\frac{\frac{1}{2}\hbar\gamma B_z}{k_BT}} & 0 \\ 0 & \frac{1}{2}Ne^{-\frac{\frac{1}{2}\hbar\gamma B_z}{k_BT}} \end{bmatrix} \tag{2.49}$$

$$\approx \frac{1}{2}\begin{bmatrix} 1 & 0 \\ 0 & 1 \end{bmatrix} + \frac{\gamma\hbar B_z}{4k_BT}\begin{bmatrix} 1 & 0 \\ 0 & -1 \end{bmatrix} \tag{2.50}$$

$$\approx \frac{1}{2}\underline{\hat{\boldsymbol{E}}} + \frac{\gamma\hbar B_z}{4k_BT}\underline{\hat{\boldsymbol{I}}}_z, \tag{2.51}$$

where it has been assumed that $\frac{1}{2}\hbar\gamma B_z \ll k_BT$ such that the expansion of the exponential about 0 may be truncated to first order. The unity operator represents spin order which we are unable to interact with. As such, we may ignore it going forward, and will take the equilibrium density operator to be given by $\underline{\hat{\boldsymbol{I}}}_z$:

$$\underline{\hat{\boldsymbol{\sigma}}}_{eq} \propto \underline{\hat{\boldsymbol{I}}}_z. \tag{2.52}$$

For clarity, the proportionality symbol will be dropped in the following. Often in NMR we wish to consider the interactions of multiple spins making up a spin system. These interactions are expressed using product operators, such as the double-quantum $\underline{\hat{\boldsymbol{I}}}_+\underline{\hat{\boldsymbol{S}}}_+$ operator representing in-phase coherence on both spins I and S. In density matrix notation, these product operators are calculated as the Kronecker products of constituent operators,

$$\underline{\hat{\boldsymbol{I}}}_+\underline{\hat{\boldsymbol{S}}}_+ = \underline{\hat{\boldsymbol{I}}}_+ \otimes \underline{\hat{\boldsymbol{S}}}_+, \tag{2.53}$$

where $\otimes$ represents the Kronecker product. Note that single-spin operators in a many-spin eigenbasis must be calculated using the identity operator to ensure that

the matrix dimensionality is maintained. As a result of the Kronecker product, density matrices representing systems of many coupled spins can rapidly scale dramatically. For instance, ten interacting spin-$1/2$ nuclei, each with single-spin operators of dimension 2×2, will give rise to product operator states of dimension $2^{10} \times 2^{10}$. Methods to reduce this computational complexity by way of approximations will be discussed in Chapter 4.

2.1.1 Time Evolution of the Density Matrix

In performing NMR experiments, we are interested in how the spin system evolves with time. The spin system will evolve with time owing to internal interactions within the sample itself, such as dipolar couplings and J-couplings, and external interactions applied by the experimentalist, namely the Zeeman interaction with an applied magnetic field, RF pulses, and MAS. These different interactions will be discussed in Section 2.1.2.

The density matrix analogue of the time-dependent Schrödinger equation (equation 2.6) is the Liouville-von-Neumann equation,

$$\frac{d\hat{\underline{\boldsymbol{\sigma}}}}{dt} = -i\left[\hat{\underline{\boldsymbol{H}}}, \hat{\underline{\boldsymbol{\sigma}}}\right], \tag{2.54}$$

for which the general solution is given as:

$$\hat{\underline{\boldsymbol{\sigma}}}(t) = e^{-i\hat{\underline{\boldsymbol{H}}}t}\hat{\underline{\boldsymbol{\sigma}}}(0)e^{i\hat{\underline{\boldsymbol{H}}}t}. \tag{2.55}$$

We are therefore able to model the evolution of any given initial density matrix, $\hat{\underline{\boldsymbol{\sigma}}}(0)$, under the influence of any given Hamiltonian, $\hat{\underline{\boldsymbol{H}}}$. Time-dependent Hamiltonians may additionally be considered using Average Hamiltonian Theory[136] or Floquet Theory,[137,138] however these will not be discussed further here.

Hamiltonians of importance for NMR may in general be expressed by a Cartesian tensor of varying rank. For instance, a dipolar coupling is represented by a 2$^{\text{nd}}$ rank

tensor, $\underline{\tilde{\boldsymbol{A}}}$, such that

$$\underline{\hat{\boldsymbol{H}}}_D = \boldsymbol{I}\underline{\tilde{\boldsymbol{A}}}\boldsymbol{S} = \begin{bmatrix} \underline{\hat{\boldsymbol{I}}}_x & \underline{\hat{\boldsymbol{I}}}_y & \underline{\hat{\boldsymbol{I}}}_z \end{bmatrix} \begin{bmatrix} A_{xx} & A_{xy} & A_{xz} \\ A_{yx} & A_{yy} & A_{yz} \\ A_{zx} & A_{zy} & A_{zz} \end{bmatrix} \begin{bmatrix} \underline{\hat{\boldsymbol{S}}}_x \\ \underline{\hat{\boldsymbol{S}}}_y \\ \underline{\hat{\boldsymbol{S}}}_z \end{bmatrix} \tag{2.56}$$

for a dipolar interaction between spins I and S. For any interaction, a 'Principal Axes System' (PAS) may be defined such that the interaction tensor is diagonal:

$$\underline{\tilde{\boldsymbol{A}}}^{\text{PAS}} = \begin{bmatrix} A_{xx} & 0 & 0 \\ 0 & A_{yy} & 0 \\ 0 & 0 & A_{zz} \end{bmatrix}. \tag{2.57}$$

Such a Hamiltonian may alternatively be expressed in spherical tensor notation as a sum of products of spin ($\underline{\hat{\boldsymbol{T}}}_{jm}$) and spatial ($A_{jm}$) terms:

$$\underline{\hat{\boldsymbol{H}}} = \sum_{j=0}^{2} \sum_{m=-j}^{+j} (-1)^m A_{jm} \underline{\hat{\boldsymbol{T}}}_{j-m}. \tag{2.58}$$

The subscripts, j and m, are integers which relate to the rank of the tensor and the order of the tensor component ($j \geq m \geq -j$), respectively. Table 2.2 gives the relation between these spherical tensors and the Cartesian tensors. Noting that, in the PAS, all non-diagonal Cartesian tensor components are zero, it follows that the Hamiltonian may be written

$$\underline{\hat{\boldsymbol{H}}}^{\text{PAS}} = A_{00}^{\text{PAS}} \underline{\hat{\boldsymbol{T}}}_{00} + A_{20}^{\text{PAS}} \underline{\hat{\boldsymbol{T}}}_{20} + A_{22}^{\text{PAS}} \underline{\hat{\boldsymbol{T}}}_{2-2} + A_{2-2}^{\text{PAS}} \underline{\hat{\boldsymbol{T}}}_{22} \tag{2.59}$$

since all other A_{jm}^{PAS} terms are equal to 0. This expression may be further simplified for some interactions, as not all interactions possess all spatial components. Table 2.3 states the different spatial tensor components present for the different NMR interactions in their respective PAS, and Section 2.1.2 will provide additional commentary

on these interactions.

The Secular Approximation may be made to simplify the total Hamiltonian. In this approximation, it is assumed that the Zeeman Hamiltonian (that of the interaction between the nuclear spins and the bulk applied magnetic field) is sufficiently large that all other Hamiltonians may be treated as first-order perturbations:

$$\underline{\hat{\boldsymbol{H}}}_{\text{total}} = \underline{\hat{\boldsymbol{H}}}_Z + \underline{\hat{\boldsymbol{H}}}_1, \tag{2.60}$$

where $\underline{\hat{\boldsymbol{H}}}_1$ is composed of all other NMR interaction Hamiltonians. Only terms of $\underline{\hat{\boldsymbol{H}}}_1$ which commute with the Zeeman interaction will contribute to first order:

$$\left[\underline{\hat{\boldsymbol{H}}}_Z, \underline{\hat{\boldsymbol{T}}}_{jm}\right] \propto \left[\underline{\hat{\boldsymbol{I}}}_z, \underline{\hat{\boldsymbol{T}}}_{jm}\right] \propto m\underline{\hat{\boldsymbol{T}}}_{jm}. \tag{2.61}$$

This only holds for terms with tensor order $m = 0$. Therefore, terms with $m \neq 0$ may be omitted to first order, assuming that the Zeeman Hamiltonian is sufficiently dominant, *i.e.*,

$$\underline{\hat{\boldsymbol{H}}}^{\text{PAS}} = A_{00}^{\text{PAS}}\underline{\hat{\boldsymbol{T}}}_{00} + A_{20}^{\text{PAS}}\underline{\hat{\boldsymbol{T}}}_{20}. \tag{2.62}$$

Table 2.2: Correspondence between spherical and Cartesian tensors.

Spherical	Cartesian
A_{00}	$-\frac{1}{\sqrt{3}}(A_{xx} + A_{yy} + A_{zz})$
A_{10}	$-\frac{i}{\sqrt{2}}(A_{xy} - A_{yx})$
$A_{1\pm1}$	$-\frac{1}{2}(A_{zx} - A_{xz} \pm i(A_{zy} - A_{yz}))$
A_{20}	$\frac{1}{\sqrt{6}}(3A_{zz} - (A_{xx} + A_{yy} + A_{zz}))$
$A_{2\pm1}$	$\mp\frac{1}{2}(A_{xz} + A_{zx} \pm i(A_{zy} + A_{yz}))$
$A_{2\pm2}$	$\frac{1}{2}(A_{xx} - A_{yy} \pm i(A_{xy} + A_{yx}))$

A benefit of expressing Hamiltonians as spherical harmonics is that these are rank invariant under rotation. As a result, they can easily be converted between different

*To first order.

Table 2.3: Spatial components present in the PAS for different NMR interactions.

Interaction	Components
Chemical shift	A_{00}^{PAS}, A_{20}^{PAS}, $A_{2\pm2}^{\mathrm{PAS}}$
J coupling	A_{00}^{PAS}
Dipolar coupling	A_{20}^{PAS}
Quadrupolar coupling	A_{20}^{PAS}, $A_{2\pm2}^{\mathrm{PAS}*}$

frames of reference. This is necessary because the PAS of different interactions which must be considered in an NMR experiment are rarely coincident. Spherical harmonics may be rotated between different frames given knowledge of the Euler angles (α, β, and γ) connecting the different frames. These rotations are typically performed in the ZYZ convention with right-handedness: the first rotation is anticlockwise α about z, the second is anticlockwise β about y', and the final rotation is anticlockwise γ about z'', where the primes indicate that these axes are also rotated (*e.g.*, an active rotation). Such a rotation may be applied to a given spherical harmonic A_{jm} using a Wigner *D*-matrix, as:

$$A_{jm'} = \sum_{m=-j}^{+j} D^{j}_{mm'}(\alpha, \beta, \gamma) A_{jm}, \tag{2.63}$$

where the Wigner *D*-matrix element $D^{j}_{mm'}$ is given as:

$$D^{j}_{mm'}(\alpha, \beta, \gamma) = e^{-im\alpha} d^{j}_{mm'}(\beta) e^{-im'\gamma}, \tag{2.64}$$

with the small *d*-matrices $d^{j}_{mm'}$ being well-defined trigonometric functions. In this thesis, the following frames will be referred to:

PAS : Principal axes system, the frame of an interaction (*e.g.*, aligned along the internuclear axis for a dipolar coupling);

MOL : Molecular axes system, the frame of an individual molecule (*e.g.*, a well defined axis system with respect to a single molecule);

ROTOR : Rotor axes system, the frame of the rotor;

LAB : Laboratory axes system, the frame of the applied external magnetic field, B_0.

The set of angles (α, β, γ) denoting a transformation between any of these frames will be given as Ω_{XY}, where X and Y are the first letter of the respective frame. These rotations are composed of the following angles:

$$\Omega_{PM} : \theta, \phi, \omega, \tag{2.65}$$

$$\Omega_{MR} : \alpha, \beta, \gamma, \tag{2.66}$$

$$\Omega_{RL} : -\omega_r t, \beta_{MAS}, 0. \tag{2.67}$$

2.1.1.1 Relation to Liouville Space Approaches

The density operator theory has been introduced here using the 'Hilbert space' formalism. In this, both Hamiltonians and density matrices are represented as $n \times n$ matrices, where n is the product of the spin-state degeneracies for the interacting spins ($n = \prod_i (2I_i + 1)$). However, this is not the only manner in which these equations may be cast. By casting the density operator formalism into the adjoint representation, we obtain an alternative representation, referred to as 'Liouville space'.[139,140] To convert to this formalism, the bra-flipper operator $\hat{\Upsilon}$ may be used to obtain the Liouville-space density matrix, $\hat{\boldsymbol{\sigma}}$[141]

$$\hat{\boldsymbol{\sigma}} = \hat{\Upsilon}(\underline{\hat{\boldsymbol{\sigma}}}) \tag{2.68}$$

$$= \hat{\Upsilon}(|\phi\rangle \langle\phi|) \tag{2.69}$$

$$= |\phi\rangle \otimes |\phi^*\rangle . \tag{2.70}$$

As a result, the Liouville space density matrix has dimensions $n^2 \times 1$; to distinguish this from the Hilbert-space density matrix, here, the Liouville-space density matrix will be denoted as a vector, $\hat{\boldsymbol{\sigma}}$, while the Hilbert-space density matrix will be given

as a matrix, $\underline{\hat{\boldsymbol{\sigma}}}$. Applying this bra-flipper operator to the Liouville-von-Neumann equation, we obtain

$$\hat{\Upsilon}\left(\frac{d\underline{\hat{\boldsymbol{\sigma}}}}{dt} = -i\left[\underline{\hat{\boldsymbol{H}}}, \underline{\hat{\boldsymbol{\sigma}}}\right]\right) \tag{2.71}$$

$$\frac{d\hat{\boldsymbol{\sigma}}}{dt} = -i\hat{\underline{\hat{\boldsymbol{L}}}}\hat{\boldsymbol{\sigma}}, \tag{2.72}$$

where $\hat{\underline{\hat{\boldsymbol{L}}}}$ is termed a 'Liouvillian' or a 'super-operator', and may be calculated as $\hat{\underline{\hat{\boldsymbol{L}}}} = \underline{\hat{\boldsymbol{H}}} \otimes \underline{\hat{\boldsymbol{E}}} - \underline{\hat{\boldsymbol{E}}} \otimes \underline{\hat{\boldsymbol{H}}}^T$, with dimension $n^2 \times n^2$. The solution to this equation in the case of a time-independent Liouvillian is then

$$\hat{\boldsymbol{\sigma}}(t) = e^{-i\hat{\underline{\hat{\boldsymbol{L}}}}t}\hat{\boldsymbol{\sigma}}(0), \tag{2.73}$$

with the implication that each term in $\hat{\underline{\hat{\boldsymbol{L}}}}$ represents the rate of exchange between two coherences or population states within the density operator, $\hat{\boldsymbol{\sigma}}$. While, for normal density matrix calculations, the two formalisms are equivalent, representing the density operator theory in this manner has a number of benefits: for example, relaxation and chemical exchange may be more readily represented in the Liouville space formalism through the introduction of relaxation and chemical exchange super-operators.[140] Additionally, this representation aids the implementation of reduce-space methods. In Chapter 4, a reduced-state-space method, Low-order Correlations in Liouville space (LCL),[77,78,85] will be applied to the study of spin diffusion in large spin systems under fast MAS conditions.

2.1.2 Spin Interactions

2.1.2.1 Zeeman Interaction

Generally, in high-field NMR, the dominant interaction experienced is the Zeeman interaction between the nuclear spin and the applied external magnetic field, B_0. This has the Hamiltonian

$$\underline{\hat{\boldsymbol{H}}}_Z = -\omega_0 \underline{\hat{\boldsymbol{I}}}_z, \tag{2.74}$$

where ω_0 is the nuclear Larmor frequency as defined in equation 2.25. As this interaction is typically orders of magnitude greater than other interactions (*vide infra*), often it is found to be useful to transform the density matrix and other Hamiltonians into the frame of the Zeeman interaction such that it no longer needs to be explicitly accounted for. This is performed by considering a 'rotating-frame' density matrix, $\underline{\tilde{\hat{\boldsymbol{\sigma}}}}$, such that

$$\underline{\tilde{\hat{\boldsymbol{\sigma}}}} = e^{i\underline{\hat{\boldsymbol{H}}}_Z t} \underline{\hat{\boldsymbol{\sigma}}} e^{-i\underline{\hat{\boldsymbol{H}}}_Z t}. \tag{2.75}$$

In the case of a single spin interacting with a bulk magnetic field, this has the effect of cancelling out the Zeeman interaction. Substituting $\underline{\hat{\boldsymbol{\sigma}}}$ for $\underline{\tilde{\hat{\boldsymbol{\sigma}}}}$ in equation 2.55, and assuming that the Zeeman interaction is the only interaction present, we have:

$$\underline{\tilde{\hat{\boldsymbol{\sigma}}}}(t) = e^{-i\underline{\hat{\boldsymbol{H}}}_Z t} \underline{\tilde{\hat{\boldsymbol{\sigma}}}}(0) e^{i\underline{\hat{\boldsymbol{H}}}_Z t} \tag{2.76}$$

$$\underline{\tilde{\hat{\boldsymbol{\sigma}}}}(t) = e^{-i\underline{\hat{\boldsymbol{H}}}_Z t} e^{i\underline{\hat{\boldsymbol{H}}}_Z t} \underline{\hat{\boldsymbol{\sigma}}}(0) e^{-i\underline{\hat{\boldsymbol{H}}}_Z t} e^{i\underline{\hat{\boldsymbol{H}}}_Z t} \tag{2.77}$$

$$\underline{\tilde{\hat{\boldsymbol{\sigma}}}}(t) = \underline{\hat{\boldsymbol{\sigma}}}(0). \tag{2.78}$$

While this is not very useful for a purely Zeeman interaction, the utility of this approach will hopefully become more clear as we consider both chemical shielding and radiofrequency (RF) pulses.

2.1.2.2 RF Pulses

The application of RF pulses is key to the utility of NMR. Nuclear Larmor frequencies at currently available magnetic fields exist typically within the range of tens to thousands of MHz, corresponding to the radio-frequency region of the electro-

magnetic spectrum. Applying RF pulses therefore allows us to excite and convert nuclear spin order. Thanks to the long coherence lifetimes of nuclear spins, it is possible to apply sequences of RF pulses thereby allowing for a substantial array of experiments to be performed, in order to probe different material and spectral properties.

The Hamiltonian for a RF pulse may be written as:

$$\underline{\hat{\boldsymbol{H}}}_{RF}(t) = \omega_1(\cos(-\omega_{rf}t + \phi)\underline{\hat{\boldsymbol{I}}}_x + \sin(-\omega_{rf}t + \phi)\underline{\hat{\boldsymbol{I}}}_y), \tag{2.79}$$

where

$$\omega_1 = -\gamma B_1 \tag{2.80}$$

is the 'nutation frequency', ϕ is the pulse phase ($\phi = 0^\circ$ corresponding to a pulse along $\underline{\hat{\boldsymbol{I}}}_x$, $\phi = 90^\circ$ being a pulse about $\underline{\hat{\boldsymbol{I}}}_y$), and ω_{rf} is the frequency of the pulse applied. This may alternatively be written as

$$\underline{\hat{\boldsymbol{H}}}_{RF}(t) = \omega_1(e^{i(-\omega_{rf}t+\phi)\underline{\hat{\boldsymbol{I}}}_z}\underline{\hat{\boldsymbol{I}}}_x e^{-i(-\omega_{rf}t+\phi)\underline{\hat{\boldsymbol{I}}}_z}). \tag{2.81}$$

The effect of this pulse is easier to interpret if we convert this into the rotating frame of the Zeeman Hamiltonian. As in equation 2.75, we have

$$\underline{\tilde{\hat{\boldsymbol{H}}}}_{RF}(t) = e^{i\underline{\hat{\boldsymbol{H}}}_Z t}\underline{\hat{\boldsymbol{H}}}_{RF}e^{-i\underline{\hat{\boldsymbol{H}}}_Z t} \tag{2.82}$$

$$\underline{\tilde{\hat{\boldsymbol{H}}}}_{RF}(t) = e^{i\underline{\hat{\boldsymbol{H}}}_Z t}\omega_1(e^{i(-\omega_{rf}t+\phi)\underline{\hat{\boldsymbol{I}}}_z}\underline{\hat{\boldsymbol{I}}}_x e^{-i(-\omega_{rf}t+\phi)\underline{\hat{\boldsymbol{I}}}_z})e^{-i\underline{\hat{\boldsymbol{H}}}_Z t} \tag{2.83}$$

$$\underline{\tilde{\hat{\boldsymbol{H}}}}_{RF}(t) = \omega_1 e^{i\omega_0\underline{\hat{\boldsymbol{I}}}_z t}(e^{i(-\omega_{rf}t+\phi)\underline{\hat{\boldsymbol{I}}}_z}\underline{\hat{\boldsymbol{I}}}_x e^{-i(-\omega_{rf}t+\phi)\underline{\hat{\boldsymbol{I}}}_z})e^{-i\omega_0\underline{\hat{\boldsymbol{I}}}_z t} \tag{2.84}$$

$$\underline{\tilde{\hat{\boldsymbol{H}}}}_{RF}(t) = \omega_1 e^{i(\omega_0 t-\omega_{rf}t+\phi)\underline{\hat{\boldsymbol{I}}}_z}\underline{\hat{\boldsymbol{I}}}_x e^{-i(\omega_0 t-\omega_{rf}t+\phi)\underline{\hat{\boldsymbol{I}}}_z} \tag{2.85}$$

$$\underline{\tilde{\hat{\boldsymbol{H}}}}_{RF}(t) = \omega_1 e^{i(\Omega t+\phi)\underline{\hat{\boldsymbol{I}}}_z}\underline{\hat{\boldsymbol{I}}}_x e^{-i(\Omega t+\phi)\underline{\hat{\boldsymbol{I}}}_z}, \tag{2.86}$$

where

$$\Omega = \omega_0 - \omega_{rf} \tag{2.87}$$

and is therefore the resonance offset between the applied pulse and the Larmor frequency. Therefore, if a pulse is applied perfectly on resonance ($\omega_{rf} = \omega_0$, $\Omega = 0$) with a phase $\phi = 0°$, this simply becomes

$$\underline{\underline{\hat{\boldsymbol{H}}}}_{RF} = \omega_1 \hat{\underline{\boldsymbol{I}}}_x. \tag{2.88}$$

That is to say, this represents a nutation of the magnetisation about the x-axis with frequency ω_1. This can be used to convert between different coherences. For example, applying this RF Hamiltonian to equilibrium magnetisation (defined in equation 2.52) gives:

$$\tilde{\underline{\underline{\boldsymbol{\sigma}}}}(t) = e^{-i\underline{\underline{\hat{\boldsymbol{H}}}}_{RF}t} \tilde{\underline{\underline{\boldsymbol{\sigma}}}}_{eq} e^{i\underline{\underline{\hat{\boldsymbol{H}}}}_{RF}t} \tag{2.89}$$

$$= e^{-i\omega_1 t \hat{\underline{\boldsymbol{I}}}_x} \hat{\underline{\boldsymbol{I}}}_z e^{i\omega_1 t \hat{\underline{\boldsymbol{I}}}_x} \tag{2.90}$$

$$= \cos(\omega_1 t)\hat{\underline{\boldsymbol{I}}}_z - \sin(\omega_1 t)\hat{\underline{\boldsymbol{I}}}_y. \tag{2.91}$$

Applying a pulse such that $\omega_1 t = \pi/2$ will therefore have the effect of nutating the magnetisation from along $\hat{\underline{\boldsymbol{I}}}_z$ to $-\hat{\underline{\boldsymbol{I}}}_y$. In this manner, RF pulses can be used to interact with the nuclear spin state populations; this will be discussed further in Chapter 3.

2.1.2.3 Chemical Shift

Electrons within an applied magnetic field will generate an opposing local magnetic field which effectively shields the nuclear spins from the external field. This induced local magnetic field is both significantly smaller in magnitude than the applied

field (typically on the order of $\times 10^{-6}$ smaller), and highly dependent on local chemical environment. The Hamiltonian for chemical shielding is written (in the PAS, assuming the secular approximation — see pg. 27):

$$\underline{\hat{\boldsymbol{H}}}_{CS}^{PAS} = \gamma \left[-\frac{1}{\sqrt{3}}(\sigma_{xx}B_x + \sigma_{yy}B_y + \sigma_{zz}B_z)\hat{T}_{00} + \frac{1}{\sqrt{6}}(2\sigma_{zz}B_z - \sigma_{xx}B_x - \sigma_{yy}B_y)\hat{T}_{20} \right], \tag{2.92}$$

where B_x, B_y, B_z are the components of the external magnetic field in the PAS of the chemical shielding tensor, $\underline{\tilde{\boldsymbol{\sigma}}}$. A neater way to express this is to perform a rotation from the PAS to the laboratory (LAB) frame, characterised by the Euler angles $\Omega_{PL} = (\alpha_{PL}, \beta_{PL}, \gamma_{PL})$:

$$\underline{\hat{\boldsymbol{H}}}_{CS}^{LAB} = -\omega_0 \left[\sigma_{iso} + \frac{\sigma_{aniso}}{2}(3\cos^2(\beta_{PL}) - 1 + \eta \sin^2(\beta_{PL})\cos(2\alpha_{PL})) \right] \underline{\hat{\boldsymbol{I}}}_z, \tag{2.93}$$

where σ_{iso}, σ_{aniso}, and η are the isotropic chemical shielding, anisotropic chemical shielding, and asymmetry parameter defined as:

$$\sigma_{iso} = \frac{1}{3}(\sigma_{xx}^{PAS} + \sigma_{yy}^{PAS} + \sigma_{zz}^{PAS}) \tag{2.94}$$

$$\sigma_{aniso} = \sigma_{zz}^{PAS} - \sigma_{iso} \tag{2.95}$$

$$\eta = \frac{\sigma_{yy} - \sigma_{xx}}{\sigma_{aniso}}. \tag{2.96}$$

Typically, the 'chemical shift' is reported instead of the values of the chemical shielding tensor. This is measured using the frequency shift of the sample (ν_{sample}) relative to a reference compound at frequency ν_{ref} as:

$$\delta_{iso} = \frac{\nu_{sample} - \nu_{ref}}{\nu_{ref}} \times 10^6. \tag{2.97}$$

2.1.2.4 Dipolar & Hyperfine Coupling

As discussed previously, spin-active nuclei possess a magnetic moment (see equation 2.20). They therefore generate a local magnetic dipole, which may interact with the magnetic dipoles arising from other neighbouring nuclear spins. Unpaired electrons, for example those within a paramagnetic species, also generate a local magnetic dipole and may therefore additionally interact. In the case of a nuclear-nuclear dipole-dipole interaction, this is termed a 'dipolar coupling', while for a nuclear-electron dipole-dipole interaction, this is the dipole-dipole component of the 'hyperfine coupling'.

These magnetic dipolar interactions are mediated through space, and the interaction strength decreases proportionally with the volume of a sphere, as r^{-3}. As was noted in Table 2.3, the dipolar coupling in the principal axes system of the interaction (aligned along the internuclear vector) is an axially symmetric anisotropic tensor. The dipolar Hamiltonian is therefore given as

$$\underline{\hat{\boldsymbol{H}}}_D^{PAS} = A_{20}^{PAS}\underline{\hat{\boldsymbol{T}}}_{20}, \tag{2.98}$$

where the spatial component, A_{20}^{PAS}, is

$$A_{20}^{PAS} = \sqrt{6}R_{DD,I,S}, \tag{2.99}$$

with $R_{DD,I,S}$ being the dipolar coupling, given by

$$R_{DD,I,S} = -\left(\frac{\mu_0}{4\pi}\right)\left(\frac{\gamma_I\gamma_S h}{2\pi}\right)\langle r_{IS}^{-3}\rangle \tag{2.100}$$

in units of rad s^{-1}, where the point dipole assumption has been made implicitly[†]. The spin component, $\underline{\hat{\boldsymbol{T}}}_{20}$, is

[†]The point dipole assumption is valid in the case where the size of the dipole is small compared to the distance between them.

$$\hat{\underline{\boldsymbol{T}}}_{20} = \frac{1}{\sqrt{6}}\left[2\hat{\underline{\boldsymbol{I}}}_z\hat{\underline{\boldsymbol{S}}}_z - \hat{\underline{\boldsymbol{I}}}_x\hat{\underline{\boldsymbol{S}}}_x - \hat{\underline{\boldsymbol{I}}}_y\hat{\underline{\boldsymbol{S}}}_y\right]. \tag{2.101}$$

It should be noted that the effective form of this Hamiltonian differs in the case of heteronuclear and homonuclear interactions. This arises due to the conversion of the $\hat{\underline{\boldsymbol{T}}}_{20}$ tensor into the rotating frame of the Zeeman interaction:

$$\tilde{\hat{\underline{\boldsymbol{T}}}}_{20} = e^{i\hat{\underline{\boldsymbol{H}}}_Z t}\hat{\underline{\boldsymbol{T}}}_{20}e^{-i\hat{\underline{\boldsymbol{H}}}_Z t} \tag{2.102}$$

$$= e^{i(\omega_I\hat{\underline{\boldsymbol{I}}}_z+\omega_S\hat{\underline{\boldsymbol{S}}}_z)t}\hat{\underline{\boldsymbol{T}}}_{20}e^{-i(\omega_I\hat{\underline{\boldsymbol{I}}}_z+\omega_S\hat{\underline{\boldsymbol{S}}}_z)t} \tag{2.103}$$

$$= \frac{1}{\sqrt{6}}\left[2\hat{\underline{\boldsymbol{I}}}_z\hat{\underline{\boldsymbol{S}}}_z - e^{i(\omega_I\hat{\underline{\boldsymbol{I}}}_z+\omega_S\hat{\underline{\boldsymbol{S}}}_z)t}(\hat{\underline{\boldsymbol{I}}}_x\hat{\underline{\boldsymbol{S}}}_x + \hat{\underline{\boldsymbol{I}}}_y\hat{\underline{\boldsymbol{S}}}_y)e^{-i(\omega_I\hat{\underline{\boldsymbol{I}}}_z+\omega_S\hat{\underline{\boldsymbol{S}}}_z)t}\right]. \tag{2.104}$$

In the homonuclear case, $\omega_I \approx \omega_S$, and therefore both components transform similarly (*e.g.*, at all times the spin space components are aligned) such that:

$$\tilde{\hat{\underline{\boldsymbol{T}}}}_{20} = \frac{1}{\sqrt{6}}\left[2\hat{\underline{\boldsymbol{I}}}_z\hat{\underline{\boldsymbol{S}}}_z - e^{i\omega_I(\hat{\underline{\boldsymbol{I}}}_z+\hat{\underline{\boldsymbol{S}}}_z)t}(\hat{\underline{\boldsymbol{I}}}_x\hat{\underline{\boldsymbol{S}}}_x + \hat{\underline{\boldsymbol{I}}}_y\hat{\underline{\boldsymbol{S}}}_y)e^{-i\omega_I(\hat{\underline{\boldsymbol{I}}}_z+\hat{\underline{\boldsymbol{S}}}_z)t}\right]. \tag{2.105}$$

On the other hand, in the heteronuclear case, $\omega_I \neq \omega_S$, and the $\hat{\underline{\boldsymbol{I}}}_{x/y}$ and $\hat{\underline{\boldsymbol{S}}}_{x/y}$ operators will rotate separately and, therefore, will effectively dephase and average to zero,

$$\begin{aligned}\tilde{\hat{\underline{\boldsymbol{T}}}}_{20} = \frac{1}{\sqrt{6}}\Big[&2\hat{\underline{\boldsymbol{I}}}_z\hat{\underline{\boldsymbol{S}}}_z - (e^{i\omega_I\hat{\underline{\boldsymbol{I}}}_z t}\hat{\underline{\boldsymbol{I}}}_x e^{-i\omega_I\hat{\underline{\boldsymbol{I}}}_z t}e^{i\omega_S\hat{\underline{\boldsymbol{S}}}_z t}\hat{\underline{\boldsymbol{S}}}_x e^{-i\omega_S\hat{\underline{\boldsymbol{S}}}_z t} \\ &+ e^{i\omega_I\hat{\underline{\boldsymbol{I}}}_z t}\hat{\underline{\boldsymbol{I}}}_y e^{-i\omega_I\hat{\underline{\boldsymbol{I}}}_z t}e^{i\omega_S\hat{\underline{\boldsymbol{S}}}_z t}\hat{\underline{\boldsymbol{S}}}_y e^{-i\omega_S\hat{\underline{\boldsymbol{S}}}_z t})\Big].\end{aligned} \tag{2.106}$$

As a result, the homonuclear and heteronuclear Hamiltonians have different forms:

$$\hat{\underline{\boldsymbol{H}}}^{PAS}_{D,homo} = R_{DD,I,S}\left[2\hat{\underline{\boldsymbol{I}}}_z\hat{\underline{\boldsymbol{S}}}_z - \hat{\underline{\boldsymbol{I}}}_x\hat{\underline{\boldsymbol{S}}}_x - \hat{\underline{\boldsymbol{I}}}_y\hat{\underline{\boldsymbol{S}}}_y\right] \tag{2.107}$$

$$\hat{\underline{\boldsymbol{H}}}^{PAS}_{D,hetero} = R_{DD,I,S}\left[2\hat{\underline{\boldsymbol{I}}}_z\hat{\underline{\boldsymbol{S}}}_z\right]. \tag{2.108}$$

More detail on dipolar couplings, and their evolution over time, will be given in Chapter 4.

2.1.3 Magic-Angle Spinning

In the solid state, the presence of strong unaveraged interactions such as dipolar couplings and chemical shift anisotropy gives rise to substantial line broadening. Reducing this coherent broadening is typically necessary in order to obtain site-specific information about the environments within a sample. A common way to perform this averaging is to spin the sample at high frequency about the so-called 'magic angle'.

We may express the conversion of a given component of any given Hamiltonian from the rotor frame to the lab frame as

$$A^{LAB}_{j0} = \sum_{m=-j}^{j} D^{j}_{m0}(\Omega_{RL})A^{ROTOR}_{jm} \tag{2.109}$$

$$A^{LAB}_{j0} = \sum_{m=-j}^{j} D^{j}_{m0}(-\omega_r t, \beta_{MAS}, 0)A^{ROTOR}_{jm} \tag{2.110}$$

$$A^{LAB}_{j0} = \sum_{m=-j}^{j} e^{-im\omega_r t} d^{j}_{m0}(\beta_{MAS})A^{ROTOR}_{jm}, \tag{2.111}$$

noting that we consider only A^{LAB}_{j0} as other terms will not commute with the Zeeman Hamiltonian and so have been omitted under the secular approximation. For terms in the ROTOR frame with $m \neq 0$, there is a time dependence in the resulting terms in the LAB frame. From average Hamiltonian theory, a time dependent

Hamiltonian may be approximated as:[142]

$$\underline{\hat{\boldsymbol{H}}}(t) \approx \underline{\hat{\boldsymbol{H}}}^{(1)} + \underline{\hat{\boldsymbol{H}}}^{(2)} + \ldots. \tag{2.112}$$

Truncating this to first order, we have

$$\underline{\hat{\boldsymbol{H}}}(t) \approx \underline{\hat{\boldsymbol{H}}}^{(1)} \tag{2.113}$$

$$\approx \frac{1}{t_b - t_a} \int_{t_a}^{t_b} \underline{\hat{\boldsymbol{H}}}(t) dt. \tag{2.114}$$

Under MAS rotation, the time-dependent component of the Hamiltonian will be $e^{-im\omega_r t}$. Over a rotor period (length τ_r), ROTOR frame terms with $m \neq 0$ will therefore average out to 0:

$$\underline{\hat{\boldsymbol{H}}}(t) \propto\!\!\!\approx \frac{1}{\tau_r} \int_0^{\tau_r} e^{-im\omega_r t} dt = 0, m = \pm 1, \pm 2. \tag{2.115}$$

On the hand, for terms in the ROTOR frame with m equal to 0, they will not average out. For tensors with rank j equal to 0 it is not possible to average out these interactions; they are isotropic, and so no rotation will remove them. For tensors of rank 2, however, the component A_{20}^{ROTOR} may be set to zero by selecting the axis of rotation carefully. The small Wigner *d*-matrix, d_{00}^2 is:

$$d_{00}^2(\beta_{MAS}) = \frac{1}{2}(3\cos^2(\beta_{MAS}) - 1). \tag{2.116}$$

Therefore, if β_{MAS} is selected such that $d_{00}^2(\beta_{MAS}) = 0$, these terms will be equal to 0. This gives the magic-angle,

$$\beta_{MAS} = \cos^{-1}\left(\frac{1}{\sqrt{3}}\right) = 54.74°. \tag{2.117}$$

The effect of magic-angle spinning on the line broadening differs depending on whether the interactions giving rise to the broadening are 'homogeneous' or 'inhomogeneous'.[143] This arises due to the second- and higher-order terms of the expansion of the time dependent Hamiltonian in equation 2.112. For example, the second-order term in the expansion is:

$$\underline{\hat{\boldsymbol{H}}}^{(2)} \propto \int_0^{\tau_r} \int_0^{t'} \left[\underline{\hat{\boldsymbol{H}}}(t''), \underline{\hat{\boldsymbol{H}}}(t')\right] dt'' dt', \tag{2.118}$$

where linear prefactor terms have been omitted. While an individual operator will commute with itself, the Hamiltonian $\underline{\hat{\boldsymbol{H}}}(t)$ is a sum of multiple different interactions each with different operator compositions, which will vary with time. In the so-called 'inhomogeneous' case, where these interactions commute, *i.e.*, $\left[\underline{\hat{\boldsymbol{H}}}(t''), \underline{\hat{\boldsymbol{H}}}(t')\right] = 0$, the truncation of the expansion of the Hamiltonian to first order is valid and, therefore, the broadening is completely removed by magic-angle spinning and the spectrum appears isotropic in nature (noting that spinning sidebands will still result). This is the case for chemical shift anisotropy or heteronuclear interactions. This is why very narrow line widths are possible in natural abundance ^{13}C spectra at slow MAS frequencies (≤ 12.5 kHz) with the application of RF-based ^{1}H homonuclear decoupling (see Figure 2.3b)

On the other hand, interactions for which pairs do not commute are termed 'homogeneous'. In this case, the commutator in equation 2.118 does not equal zero and therefore these higher-order terms are not completely averaged by MAS and so can still contribute to the line broadening. This is the case for homonuclear dipolar couplings:

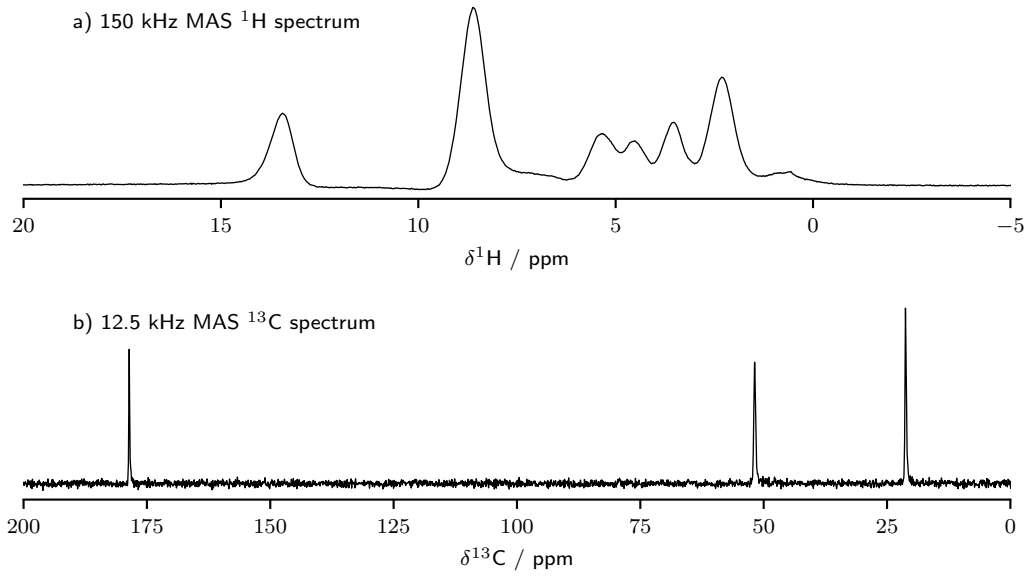

Figure 2.3: (a) A ^{1}H 1D spectrum of [^{13}C,^{15}N]-L-histidine HCl H_2O recorded at a MAS frequency of 150 kHz and a ^{1}H Larmor frequency of 1 GHz using a 0.51 mm HCN probe. (b) A ^{13}C 1D cross-polarisation (CP) MAS spectrum of natural abundance L-alanine recorded at a MAS frequency of 12.5 kHz and a ^{1}H Larmor frequency of 500 MHz using a 4 mm HXY probe, with ^{1}H heteronuclear decoupling. Note that in both cases the spectral width is 25 kHz.

$$\left[\hat{I}_x\hat{S}_x, \hat{S}_y\hat{R}_y\right] = \hat{I}_x\hat{S}_x \times \hat{S}_y\hat{R}_y - \hat{S}_y\hat{R}_y \times \hat{I}_x\hat{S}_x \tag{2.119}$$

$$\neq 0. \tag{2.120}$$

As a result there is residual homonuclear dipolar line broadening in a ^{1}H spectrum even at the fastest possible MAS frequencies where the MAS frequency is well in excess of any single ^{1}H – ^{1}H dipolar coupling in the system (see Figure 2.3a).[144]

2.2 Relaxation Theory

2.2.1 Semi-Classical Relaxation Theory

This section will introduce a semi-classical approach for the treatment of NMR relaxation. The first section of this is based predominantly on reading 'Protein NMR relaxation: theory,

applications and outlook' by Fischer et al. (1998),[145] *'Principles of Nuclear Magnetism' by Abragam (1961),*[132] *and 'Theory of Relaxation Processes' by Redfield (1957).*[113]

Relaxation is the incoherent process by which a spin ensemble returns to its equilibrium magnetisation. In this thesis, we are primarily interested in three types of relaxation: spin-lattice relaxation, R_1, by which a nuclear spin returns to equilibrium z magnetisation; spin-spin relaxation, R_2, by which the spin coherence in the rotating frame decays; and spin-lattice relaxation in the rotating frame, $R_{1\rho}$, whereby the magnetisation decays during a spin-lock pulse. R_1 and R_2 relaxation are shown in Figure 2.4.

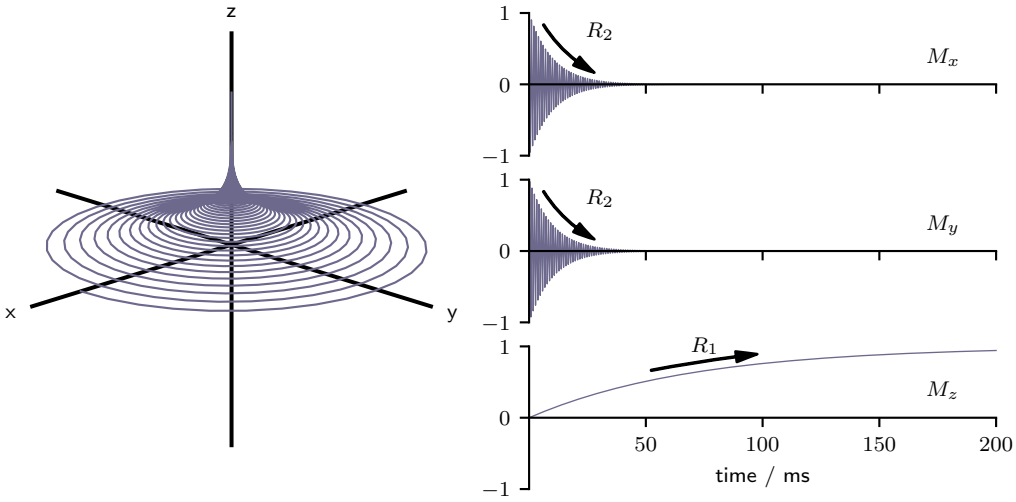

Figure 2.4: Model of how the magnetisation decays after excitation. Left: 3D plot showing the magnetisation decaying back to the z axis after excitation along x. Right: The components of the magnetisation along each of the cartesian axes. In this model, R_1 = 14.3 s^{-1} and R_2 = 100 s^{-1}.

Owing to coherent processes (such as coherent spin diffusion via unaveraged dipolar couplings), R_2 is typically practically inaccessible in the solid state. This is depicted in Figure 2.5, where additional coherent interactions are introduced to a spin when moving from top to bottom in the figure. Note that the underlying R_2 in this model is unchanged; the rapid decay of the nuclear spin coherence in this model, and the resulting increase in line broadening, occur due to the introduction of coherent processes. Additionally, magnetic field inhomogeneities, where the ex-

ternal magnetic field varies slightly across the sample, may lead to line broadening. In the solid state, therefore, the spin-lattice in the rotating frame ($R_{1\rho}$) relaxation rates are more frequently used. In these, the magnetisation is spinlocked along one axis, and decays under the action of this spin lock. How these relaxation rates are experimentally measured will be discussed in more detail in Section 3.3; this section will deal with the theory underpinning our interpretation of this relaxation.

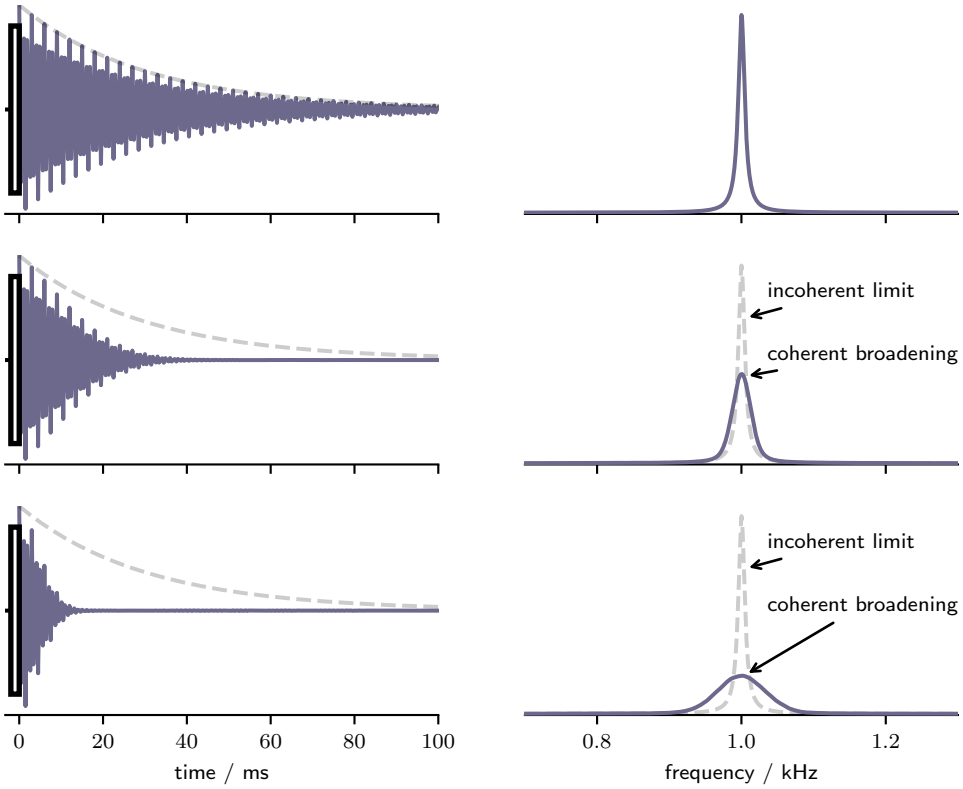

Figure 2.5: Linewidths in the solid state depend not only on the incoherent relaxation processes (*e.g.*, the lifetime of magnetisation in the transverse plane), but also on coherent interactions such as dipolar couplings. Here, the effect of coherent averaging on the observed linewidth is shown. The amount of incoherent broadening is increased from top to bottom, with the incoherent limit (*i.e.*, the limit of no coherent broadening) shown as a grey dashed line.

In Section 2.1.1, the time evolution of the density matrix under the action of a coherent Hamiltonian was presented. The presence of molecular motions, and chemical exchange can give rise to a stochastic, incoherent time-dependent Hamiltonian. This Hamiltonian is responsible for the nuclear spin relaxation. We begin by treating our

incoherent, stochastic Hamiltonian as a time-dependent first-order perturbation to the Hamiltonian, $\hat{\underline{\boldsymbol{H}}}$:

$$\hat{\underline{\boldsymbol{H}}} = \hat{\underline{\boldsymbol{H}}}_0 + \hat{\underline{\boldsymbol{H}}}_1(t). \tag{2.121}$$

It should be noted that a time-dependent Hamiltonian is not necessarily incoherent; under MAS, the sample rotation gives rise to a time-dependent coherent modulation of the Hamiltonian, as discussed in Section 2.1.3. Previously in equation 2.58, the decomposition of a Hamiltonian into spherical harmonics was shown. We may apply the same technique here to our incoherent Hamiltonian:

$$\hat{\underline{\boldsymbol{H}}}_1(t) = \sum_{m'=-2}^{+2} \sum_{m=-2}^{+2} (-1)^m D^2_{mm'}(\Omega(t)) A_{2m} \hat{\underline{\boldsymbol{T}}}_{2-m}, \tag{2.122}$$

where $\Omega(t)$ represents the stochastic reorientation of a given interaction. Under the secular approximation, we only retain terms with $m' = 0$:

$$\hat{\underline{\boldsymbol{H}}}_1(t) = \sum_{m=-2}^{+2} (-1)^m D^2_{m0}(\Omega(t)) A_{2m} \hat{\underline{\boldsymbol{T}}}_{2-m}. \tag{2.123}$$

The benefit of using spherical harmonics in this case is that their rank is invariant under rotation and, therefore, motion. For ease of notation, we factorize this into 'time-dependent' ($F_j(t)$) and 'time-independent' parts ($\hat{\underline{\boldsymbol{V}}}_j$):

$$\hat{\underline{\boldsymbol{H}}}_1(t) = \sum_{m=-2}^{2} F_m(t) \hat{\underline{\boldsymbol{V}}}_m, \tag{2.124}$$

with

$$F_m(t) = D^2_{m0}(\Omega(t)) \tag{2.125}$$

$$\hat{\underline{\boldsymbol{V}}}_m = (-1)^m A_{2m} \hat{\underline{\boldsymbol{T}}}_{2-m}. \tag{2.126}$$

As stated in equation 2.54, the Liouville-von-Neumann equation describes the time-evolution of the density matrix under the action of a Hamiltonian:

$$\frac{d\hat{\underline{\boldsymbol{\sigma}}}(t)}{dt} = -i \left[\hat{\underline{\boldsymbol{H}}}_0 + \hat{\underline{\boldsymbol{H}}}_1(t), \hat{\underline{\boldsymbol{\sigma}}}(t) \right]. \tag{2.127}$$

To aid our analysis, it is best to perform a transformation into the interaction frame of the unperturbed Hamiltonian, $\hat{\underline{\boldsymbol{H}}}_0$:

$$\tilde{\hat{\underline{\boldsymbol{Q}}}} = e^{i\hat{\underline{\boldsymbol{H}}}_0 t} \hat{\underline{\boldsymbol{Q}}} e^{-i\hat{\underline{\boldsymbol{H}}}_0 t}. \tag{2.128}$$

In this interaction frame, $\hat{\underline{\boldsymbol{\sigma}}}(t) \rightarrow \tilde{\underline{\boldsymbol{\sigma}}}(t)$, $\hat{\underline{\boldsymbol{H}}}_1(t) \rightarrow \tilde{\hat{\underline{\boldsymbol{H}}}}_1(t) - \hat{\underline{\boldsymbol{H}}}_0$:

$$\frac{d\tilde{\underline{\boldsymbol{\sigma}}}(t)}{dt} = -i \left[\tilde{\hat{\underline{\boldsymbol{H}}}}_1(t), \tilde{\underline{\boldsymbol{\sigma}}}(t) \right]. \tag{2.129}$$

Integrating this differential equation gives:

$$\tilde{\underline{\boldsymbol{\sigma}}}(t) = \tilde{\underline{\boldsymbol{\sigma}}}(0) - i \int_0^t \langle \left[\tilde{\hat{\underline{\boldsymbol{H}}}}_1(t), \tilde{\underline{\boldsymbol{\sigma}}}(t) \right] \rangle dt, \tag{2.130}$$

which is not generally analytically solvable. One approach is to apply perturbation theory, giving:

$$\tilde{\underline{\underline{\boldsymbol{\sigma}}}}(t) \approx \underbrace{\tilde{\underline{\underline{\boldsymbol{\sigma}}}}(0)}_{\text{zero-order}} \underbrace{- i \int_0^t \langle \left[\tilde{\underline{\underline{\boldsymbol{H}}}}_1(t'), \tilde{\underline{\underline{\boldsymbol{\sigma}}}}(0) \right] \rangle dt'}_{\text{first-order}} - \underbrace{\int_0^t \int_0^{t'} \langle \left[\tilde{\underline{\underline{\boldsymbol{H}}}}_1(t'), \left[\tilde{\underline{\underline{\boldsymbol{H}}}}_1(t''), \tilde{\underline{\underline{\boldsymbol{\sigma}}}}(0) \right] \right] \rangle dt'' dt'}_{\text{second-order}} + \ldots, \tag{2.131}$$

which, assuming that the incoherent perturbing Hamiltonian is small compared to the coherent Hamiltonian, may be truncated to second order. As the perturbing Hamiltonian is incoherent and stationary, it is taken to have an average value of zero (any non-zero average could be incorporated into the non-time-dependent part) and, therefore, the first order correction disappears.

$$i \int_0^t \langle \left[\tilde{\underline{\underline{\boldsymbol{H}}}}_1(t), \tilde{\underline{\underline{\boldsymbol{\sigma}}}}(0) \right] \rangle dt = 0 \tag{2.132}$$

$$\tilde{\underline{\underline{\boldsymbol{\sigma}}}}(t) \approx \tilde{\underline{\underline{\boldsymbol{\sigma}}}}(0) - \int_0^t \int_0^{t'} \langle \left[\tilde{\underline{\underline{\boldsymbol{H}}}}_1(t'), \left[\tilde{\underline{\underline{\boldsymbol{H}}}}_1(t''), \tilde{\underline{\underline{\boldsymbol{\sigma}}}}(0) \right] \right] \rangle dt'' dt'. \tag{2.133}$$

This expression, however, assumes that there is no bulk polarisation (*i.e.*, this is the infinite temperature limit). To correct for finite temperature, assuming we are in the high temperature limit (that is, all energy level separations $\ll k_B T$), it can be shown that a correction factor may be applied:

$$\tilde{\underline{\underline{\boldsymbol{\sigma}}}}(t) \approx \tilde{\underline{\underline{\boldsymbol{\sigma}}}}(0) - \int_0^t \int_0^{t'} \langle \left[\tilde{\underline{\underline{\boldsymbol{H}}}}_1(t'), \left[\tilde{\underline{\underline{\boldsymbol{H}}}}_1(t''), \tilde{\underline{\underline{\boldsymbol{\sigma}}}}(0) - \tilde{\underline{\underline{\boldsymbol{\sigma}}}}_{eq} \right] \right] \rangle dt'' dt', \tag{2.134}$$

where the equilibrium density matrix $\tilde{\underline{\underline{\boldsymbol{\sigma}}}}_{eq}$ has been derived previously in equation 2.52. Then, we can substitute in equation 2.124, noting that the conversion of the operator $\hat{\underline{\underline{\boldsymbol{V}}}}_\alpha$ into the interaction frame gives rise to a modulation with a frequency ω_α, such that $\tilde{\underline{\underline{\boldsymbol{V}}}}_\alpha = e^{i\omega_\alpha t} \hat{\underline{\underline{\boldsymbol{V}}}}_\alpha$, where ω_α depends on the specific operator composition of $\tilde{\underline{\underline{\boldsymbol{V}}}}_\alpha$:

$$\underline{\tilde{\hat{\boldsymbol{\sigma}}}}(t) - \underline{\tilde{\hat{\boldsymbol{\sigma}}}}(0) \approx -\int_0^t \int_0^{t'} \langle \left[\sum_\alpha F_\alpha(t') \underline{\tilde{\hat{\boldsymbol{V}}}}_\alpha, \right. \\ \left. \times \left[\sum_\beta F_\beta(t'') \underline{\tilde{\hat{\boldsymbol{V}}}}_\beta, \underline{\tilde{\hat{\boldsymbol{\sigma}}}}(0) - \underline{\tilde{\hat{\boldsymbol{\sigma}}}}_{eq} \right] \right] \rangle dt'' dt' \tag{2.135}$$

$$\underline{\tilde{\hat{\boldsymbol{\sigma}}}}(t) - \underline{\tilde{\hat{\boldsymbol{\sigma}}}}(0) \approx -\int_0^t \int_0^{t'} \langle \left[\sum_\alpha F_\alpha(t') e^{i\omega_\alpha t'} \underline{\hat{\boldsymbol{V}}}_\alpha, \right. \\ \left. \times \left[\sum_\beta F_\beta(t'') e^{i\omega_\beta t''} \underline{\hat{\boldsymbol{V}}}_\beta, \underline{\tilde{\hat{\boldsymbol{\sigma}}}}(0) - \underline{\tilde{\hat{\boldsymbol{\sigma}}}}_{eq} \right] \right] \rangle dt'' dt'. \tag{2.136}$$

This may be rearranged to give:

$$\underline{\tilde{\hat{\boldsymbol{\sigma}}}}(t) - \underline{\tilde{\hat{\boldsymbol{\sigma}}}}(0) \approx -\sum_{\alpha\beta} \left[\underline{\hat{\boldsymbol{V}}}_\alpha, \left[\underline{\hat{\boldsymbol{V}}}^*_\beta, \underline{\tilde{\hat{\boldsymbol{\sigma}}}}(0) - \underline{\tilde{\hat{\boldsymbol{\sigma}}}}_{eq} \right] \right] \\ \times \int_0^t \int_0^{t'} \langle F_\alpha(t') F^*_\beta(t'') \rangle e^{i(\omega_\alpha t' - \omega_\beta t'')} dt'' dt', \tag{2.137}$$

where the time-dependent and independent parts have been separated. Assuming that the time-dependent functions $F_{\alpha/\beta}(t)$ are stationary and do not themselves vary in time, we may express their product as a correlation function:

$$C_{\alpha\beta}(\tau) = \langle F_\alpha(0) F^*_\beta(\tau) \rangle, \tag{2.138}$$

noting that the time invariance of the function $F_{\alpha/\beta}(t)$ implies that the product is dependent only on the difference in time, τ, and not the absolute time itself. This gives:

$$\underline{\tilde{\hat{\boldsymbol{\sigma}}}}(t) - \underline{\tilde{\hat{\boldsymbol{\sigma}}}}(0) \approx -\sum_{\alpha\beta} \left[\underline{\hat{\boldsymbol{V}}}_\alpha, \left[\underline{\hat{\boldsymbol{V}}}^*_\beta, \underline{\tilde{\hat{\boldsymbol{\sigma}}}}(0) - \underline{\tilde{\hat{\boldsymbol{\sigma}}}}_{eq} \right] \right] \\ \times \int_0^t \int_0^{t'} C_{\alpha\beta}(|t' - t''|) e^{i(\omega_\alpha t' - \omega_\beta t'')} dt'' dt'. \tag{2.139}$$

The correlation functions with $\alpha = \beta$ are termed 'auto-correlation' functions, while those with $\alpha \neq \beta$ are 'cross-correlation' functions. In the following analysis, we consider only auto-correlation functions, however equivalent solutions may be found for cross-correlation functions. For the auto-correlation function, we may solve the integral using the change of variable $t'' \to \tau = t' - t''$, giving:

$$\int_0^t \int_0^{t'} C_{\alpha\alpha}(|t' - t''|) e^{i\omega_\alpha (t' - t'')} dt'' dt' = \int_0^t \int_\tau^t C_{\alpha\alpha}(\tau) e^{i\omega_\alpha \tau} dt' d\tau \tag{2.140}$$

$$= \int_0^t (t - \tau) C_{\alpha\alpha}(\tau) e^{i\omega_\alpha \tau} d\tau. \tag{2.141}$$

Then, assuming $t > \tau$:

$$\int_0^t (t - \tau) C_{\alpha\alpha}(\tau) e^{i\omega_\alpha \tau} d\tau \approx t \int_0^\infty C_{\alpha\alpha}(\tau) e^{i\omega_\alpha \tau} d\tau \tag{2.142}$$

$$\approx \frac{t}{2} \int_{-\infty}^\infty C_{\alpha\alpha}(\tau) e^{i\omega_\alpha \tau} d\tau \tag{2.143}$$

$$\approx \frac{t}{2} J_{\alpha\alpha}(\omega_\alpha), \tag{2.144}$$

where $J_{\alpha\alpha}$ is termed a 'spectral density', and is the Fourier Transform (FT, $\mathcal{F}$) of the correlation function $C_{\alpha\alpha}$:

$$J_{\alpha\alpha}(\omega) = \int_{-\infty}^\infty C_{\alpha\alpha}(\tau) e^{i\omega\tau} d\tau \tag{2.145}$$

$$= \mathcal{F}(C_{\alpha\alpha}(\tau)). \tag{2.146}$$

An analogous procedure can be performed for cross-correlation functions, giving:

$$\int_0^t \int_0^{t'} C_{\alpha\beta}(|t'-t''|)e^{i(\omega_\alpha t' - \omega_\beta t'')}dt''dt' \\ = \frac{1}{2i(\omega_\alpha - \omega_\beta)}\left\{e^{i(\omega_\alpha-\omega_\beta)t}J_{\alpha\beta}(\omega_\beta) - J_{\alpha\beta}(\omega_\alpha)\right\}. \tag{2.147}$$

Typically for large frequency differences (such as heteronuclear dipolar couplings) the $\omega_\alpha - \omega_\beta$ term on the denominator means that cross-correlation is negligible. However, for homonuclear processes this may be significant.

Returning to auto-correlation based relaxation, we can therefore write:

$$\underline{\tilde{\tilde{\boldsymbol{\sigma}}}}(t) - \underline{\tilde{\tilde{\boldsymbol{\sigma}}}}(0) \approx -\frac{t}{2}\sum_\alpha \left[\underline{\hat{\boldsymbol{V}}}_\alpha, \left[\underline{\hat{\boldsymbol{V}}}_\alpha^*, \underline{\tilde{\tilde{\boldsymbol{\sigma}}}}(0) - \underline{\tilde{\tilde{\boldsymbol{\sigma}}}}_{eq}\right]\right] J_{\alpha\alpha}(\omega_\alpha), \tag{2.148}$$

and so, assuming that t is small:

$$\frac{d\underline{\tilde{\tilde{\boldsymbol{\sigma}}}}(t)}{dt} \approx \frac{\underline{\tilde{\tilde{\boldsymbol{\sigma}}}}(t) - \underline{\tilde{\tilde{\boldsymbol{\sigma}}}}(0)}{t} \tag{2.149}$$

$$\approx -\frac{1}{2}\sum_\alpha \left[\underline{\hat{\boldsymbol{V}}}_\alpha, \left[\underline{\hat{\boldsymbol{V}}}_\alpha^*, \underline{\tilde{\tilde{\boldsymbol{\sigma}}}}(0) - \underline{\tilde{\tilde{\boldsymbol{\sigma}}}}_{eq}\right]\right] J_{\alpha\alpha}(\omega_\alpha). \tag{2.150}$$

This equation relates the time-evolution of the density matrix to the value of the spectral density evaluated at a given frequency. In the case of physical motion giving rise to relaxation, this value is interpreted as being related to the amount of motion occurring at a given frequency. A final simplification is to drop the $\alpha\alpha$ from the spectral density $J_{\alpha\alpha}$ and correlation functions $C_{\alpha\alpha}$, as it has been shown that, for an isotropic powder sample, each of these (J_{00}, J_{11}, J_{22} / C_{00}, C_{11}, C_{22}) are functionally equivalent:[146]

$$\frac{d\underline{\tilde{\hat{\boldsymbol{\sigma}}}}(t)}{dt} \approx -\frac{1}{2}\sum_{\alpha}\left[\underline{\hat{\boldsymbol{V}}}_{\alpha},\left[\underline{\hat{\boldsymbol{V}}}^{*}_{\alpha},\tilde{\sigma}(0)-\tilde{\sigma}_{eq}\right]\right]J(\omega_{\alpha}). \tag{2.151}$$

We may then use this expression to generate equations for relaxation rates for different spins, as:

$$\frac{d\langle\underline{\hat{\boldsymbol{Y}}}\rangle}{dt} = \frac{d}{dt}\text{Tr}(\underline{\hat{\boldsymbol{Y}}}\underline{\tilde{\hat{\boldsymbol{\sigma}}}}(t)) \tag{2.152}$$

$$= \text{Tr}\left(\underline{\hat{\boldsymbol{Y}}}\frac{d\underline{\tilde{\hat{\boldsymbol{\sigma}}}}(t)}{dt}\right), \tag{2.153}$$

where $\underline{\hat{\boldsymbol{Y}}}$ is the state being considered. While these are not evaluated here, derivations may be found in several references including 'Protein NMR relaxation: theory, applications and outlook' by Fischer *et al*. (1998),[145] 'The nuclear magnetic resonance relaxation data analysis in solids: General $R_1/R_{1\rho}$ equations and the model-free approach' by Kurbanov *et al*. (2011),[146] and 'Relaxation Processes in a System of Two Spins' by Solomon (1955).[147] The resulting expressions are:

$$R_1^{II} = \frac{3}{4}\omega_D^2(J(\omega_{obs}) + 4J(2\omega_{obs})) \tag{2.154}$$

$$R_1^{IS} = \frac{1}{4}\omega_D^2(J(\omega_{obs}-\omega_{neigh}) + 3J(\omega_{obs}) + 6J(\omega_{obs}+\omega_{neigh})) \tag{2.155}$$

$$R_{1\rho}^{II} = \frac{3}{8}\omega_D^2(3Q(\omega_1) + 5J(\omega_{obs}) + 2J(2\omega_{obs})) \tag{2.156}$$

$$R_{1\rho}^{IS} = \frac{1}{8}\omega_D^2(4Q(\omega_1) + J(\omega_{obs}-\omega_{neigh}) + 3J(\omega_{obs}) + 6J(\omega_{neigh}) + 6J(\omega_{obs}+\omega_{neigh})) \tag{2.157}$$

$$R_1^{CSA} = \frac{1}{3}\delta_{CSA,obs}^2 J(\omega_{obs}) \tag{2.158}$$

$$R_{1\rho}^{CSA} = \frac{1}{18}\delta_{CSA,obs}^2(4Q(\omega_1) + 3J(\omega_{obs})), \tag{2.159}$$

noting that $Q(\omega)$ is the spinning frequency corrected spectral density:

$$Q(\omega) = \frac{1}{6}\left(J(\omega_1 + 2\omega_r) + 2J(\omega_1 + \omega_r) + 2J(\omega_1 - \omega_r) + J(\omega_1 - 2\omega_r)\right), \quad (2.160)$$

and $\delta^2_{CSA,obs}$ is given by:

$$\delta^2_{CSA,obs} = (\omega_{obs} \times 10^{-6})^2(\sigma^2_{xx} + \sigma^2_{yy} + \sigma^2_{zz} - \sigma_{xx}\sigma_{yy} - \sigma_{xx}\sigma_{zz} - \sigma_{yy}\sigma_{zz}). \quad (2.161)$$

where $\sigma_{xx,yy,zz}$ are the CSA tensor components defined in Section 2.1.2.3.

2.2.2 Correlation Functions

Several methods have been developed for analysing NMR relaxation data in terms of underlying motions. Here, three of these will be discussed; namely, spectral density mapping,[148] discrete approaches (*e.g.*, model-free[115] and IMPACT[149]), and continuous approaches (*e.g.*, detectors[150]).

Spectral density mapping based methods do not directly assume any form of the underlying correlation function.[148,151,152] Rather, they make use of sets of experiments performed at the same magnetic field, such that the resulting relaxation rates are different linear combinations of the same spectral density function evaluated at the eigenfrequencies of the system. Performing such analysis at a range of different fields can sample the spectral density at multiple different frequencies and allow for quantitative analysis of the underlying form of the spectral density.[153] However, such an approach is limited in its application to solid-state NMR. In order for the system of linear equations to be well-posed there must be at least as many relaxation rates measured as there are spectral density components to be determined. In solution-state NMR, this is feasible: it is possible to measure spin-lattice relaxation (R_1), spin-spin relaxation (R_2), and the steady-state heteronuclear nuclear

Overhauser effect (nOe), and therefore determine three components of the spectral density (typically, for $^{15}\mathrm{N}-^{1}\mathrm{H}$ analysis, these would be $J(0)$, $J(\omega_{\mathrm{H}})$, and $J(\omega_{\mathrm{N}})$). In the solid state, however, it is not generally practical to determine steady-state nOes owing to limited sensitivity[154] and the influence of incoherent spin diffusion (Chapter 4 investigates this in more detail), and, as such, performing a similar analysis is typically infeasible.

Both discrete and continuous approaches rely on consideration of the correlation function and spectral density more generally. By substituting equation 2.125 into equation 2.138, we can write:

$$C_{\alpha\beta}(\tau) = \langle D^{2}_{\alpha 0}(\Omega(0)) D^{2,*}_{\beta 0}(\Omega(\tau)) \rangle. \tag{2.162}$$

In the case of auto-correlated relaxtion, we have that $\alpha = \beta$, that is,

$$C_{\alpha\alpha}(\tau) = \langle D^{2}_{\alpha 0}(\Omega(0)) D^{2,*}_{\alpha 0}(\Omega(\tau)) \rangle. \tag{2.163}$$

As noted previously for equation 2.151, these correlation functions do not depend on the index α. Then, using the addition theorem of spherical harmonics,[155] this can then be written as:

$$C(\tau) = \frac{1}{5} \langle P_2(\bar{\boldsymbol{\mu}}(0) \cdot \bar{\boldsymbol{\mu}}(\tau)) \rangle, \tag{2.164}$$

where $\bar{\boldsymbol{\mu}}$ is a unit vector in a global frame.

To proceed with this correlation function, we firstly decompose it into two correlation functions representing 'overall motion' ($C_{\text{overall}}(t)$) and 'internal motion' ($C_{\text{internal}}(t)$):

$$C(t) = \frac{1}{5} C_{\text{overall}}(t) C_{\text{internal}}(t). \tag{2.165}$$

Assuming that the overall motion may be represented by a stationary Markovian process and is isotropic, its correlation function will have the form of an exponential decay:

$$C_{\text{overall}}(t) = e^{-\frac{t}{\tau_M}}, \tag{2.166}$$

where τ_M is the correlation time for overall tumbling. In the solid-state, the restriction of overall motion due to sample packing means that this tumbling is typically negligible, and may be ignored (*e.g.*, $C_{\text{overall}}(t) = 1$). The internal motion correlation function may be expressed as

$$C_{\text{internal}}(\tau) = \langle P_2(\bar{\boldsymbol{\mu}}_i(0) \cdot \bar{\boldsymbol{\mu}}_i(\tau)) \rangle, \tag{2.167}$$

where the subscript i indicates that these unit vectors, $\bar{\boldsymbol{\mu}}_i$, are rigidly attached to the overall tumbling body. From this, we can find that

$$C_{\text{internal}}(0) = \langle P_2(1) \rangle = 1, \tag{2.168}$$

which is to say that the internal correlation function is unitary normalised. Further, we can take $C(\infty)$ to be the square of the generalised order parameter, S, such that $C(\infty) = S^2$. Next, we make the assumption that the internal motions are stationary and Markovian, and continuous in their effective timescale. Then, we can express a correlation function over a continuous distribution of timescales of motion using the Laplace transform of $\theta(\tau)$:

$$C_{\text{internal}}(t) = S^2 + \int_{-\infty}^{\infty} \theta(\tau) e^{-\frac{t}{\tau}} d\log(\tau), \tag{2.169}$$

where $\theta(\tau)$ is the 'density of motions' (*i.e.*, how much motion occurs on any given timescale) occurring, with

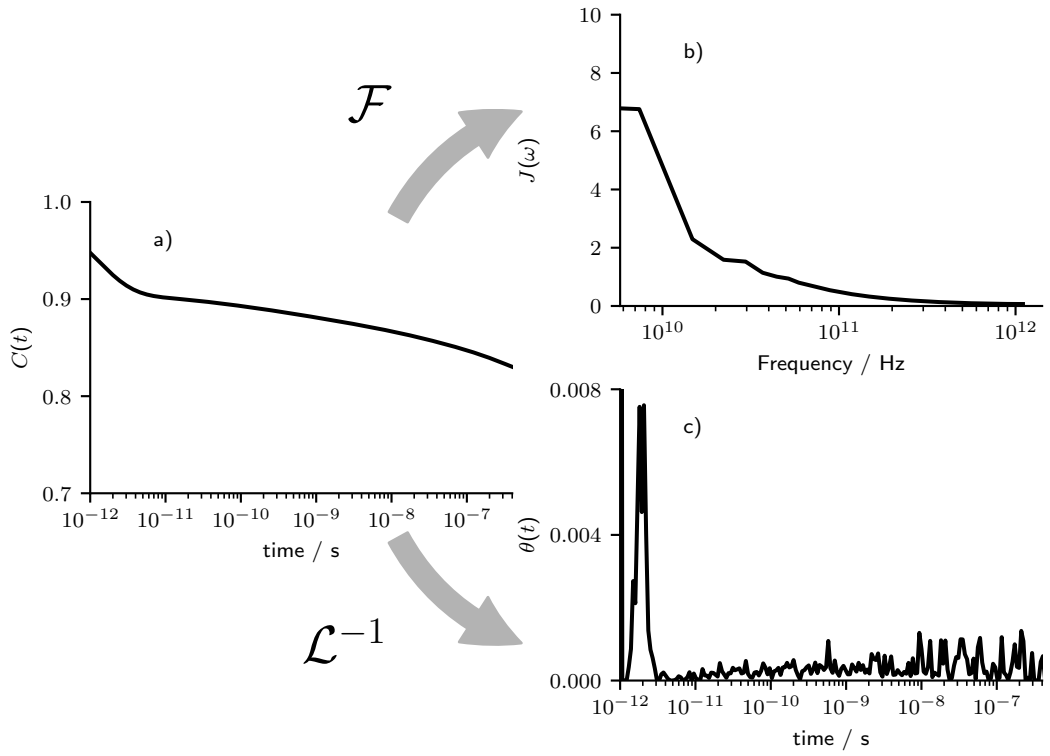

Figure 2.6: Illustration of how the correlation function ($C(t)$, a), spectral density ($J(\omega)$, b), and distribution of motions ($\theta(t)$, c) are related. Note that owing to the ill-posed nature of the inverse Laplace transform, here the $\theta(t)$ has been taken as the ground truth from which the correlation function (via Laplace transform, $\mathcal{L}$) and spectral density (via subsequent Fourier transform, $\mathcal{F}$) have been calculated.

$$\int_{-\infty}^{\infty} \theta(\tau) d\log(\tau) = 1 - S^2. \tag{2.170}$$

Figure 2.6 shows how the correlation function, spectral density, and density of motions are related. The aim of dynamical analysis is to characterise this density of motions. Historically, the majority of methods for performing this in both solution- and solid-state NMR has been to assume some discretised form of the density of motions. More recently, an approach has been introduced which allows the continuous nature of this to be maintained explicitly. Here, discrete models of this will be introduced first, followed by the continuous approach.

2.2.2.1 Discrete Density of Motion Methods

In discrete approximations of the density of motions, the integral in equation 2.169 is replaced with a summation:

$$C_{\text{internal}}(t) \approx S^2 + \sum_i A_i e^{-\frac{t}{\tau_i}} \tag{2.171}$$

$$\sum_i A_i = 1 - S^2, \tag{2.172}$$

where A_i is the amplitude of motion at a correlation time of τ_i. One common version of this discrete approximation is the 'model-free' model ('simple model-free', SMF), first introduced by Lipari and Szabo (1982).[115,116] In the original formulation of this model, the internal correlation function was taken as:

$$C_{\text{SMF, internal}}(t) = S^2 + (1 - S^2)e^{-\frac{t}{\tau}}, \tag{2.173}$$

for which the corresponding spectral density function is

$$J_{\text{SMF, internal}}(\omega) = \frac{(1 - S^2)\tau}{1 + (\omega\tau)^2}. \tag{2.174}$$

It was later found that for many systems, at least two timescales of motion are required to adequately model the internal motions. This led to the introduction of the 'extended model-free' model (EMF):[156,157]

$$C_{\text{EMF, internal}}(t) = S^2 + (1 - S_f^2)e^{-\frac{t}{\tau_f}} + S_f^2(1 - S_s^2)e^{-\frac{t}{\tau_s}} \tag{2.175}$$

$$J_{\text{EMF, internal}}(\omega) = \frac{(1 - S_f^2)\tau_f}{1 + (\omega\tau_f)^2} + \frac{S_f^2(1 - S_s^2)\tau_s}{1 + (\omega\tau_s)^2} \tag{2.176}$$

$$S^2 = S_s^2 S_f^2, \tag{2.177}$$

where τ_f and τ_s refer to fast and slow timescales, respectively, and S_f^2 and S_s^2 to the fast and slow order parameters. A key limitation of extending these discrete models to multiple timescales in the solid state is that the overall amplitude of motion ($\sum_i A_i$) must be constrained by an experimentally measured order parameter, the accuracy of which can then have a large impact on the resulting amplitudes of motion.[158] As a result, the application of these methods is hindered for systems with poor sensitivity, for which the accurate determination of good quality dipolar order parameters is not feasible (see Chapter 5) or for nuclei where the relaxation is dominated by non-dipolar mechanisms, such as carbonyls (see Chapter 6).

In both SMF and EMF (and derived model-free models), there exists the issue that the models are trying to parameterise a likely complex and continuous density of motions with a very small number of timescales. As a result, the interpretation of the timescales of motion (τ for SMF, τ_s and τ_f for EMF) is complicated. It has been found by Smith *et al*. (2017) that, when practically applied, these timescales will fit to where the relaxation rates are most sensitive.[150] One final discrete technique, Interpretation of Motions by Projection onto an Array of Correlation Times (IMPACT),[149] is less affected by this biasing.[159] In IMPACT, the discrete correlation function (equation 2.171) is used directly,

$$C_{\text{IMPACT, internal}}(t) = S^2 + \sum_i A_i e^{-\frac{t}{\tau_i}} \tag{2.178}$$

$$J_{\text{IMPACT, internal}}(\omega) = \sum_i \frac{A_i \tau_i}{1 + (\omega\tau_i)^2}, \tag{2.179}$$

where the τ_i are a predetermined and logarithmically spaced array of correlation times. By not including the timescales in the fitting process, this model is less biased towards where the relaxation rates are sensitive. This model has been found to be particularly useful in the study of intrinsically disordered regions (IDRs) and intrinsically disordered proteins (IDPs), for which the assumption of distinctly

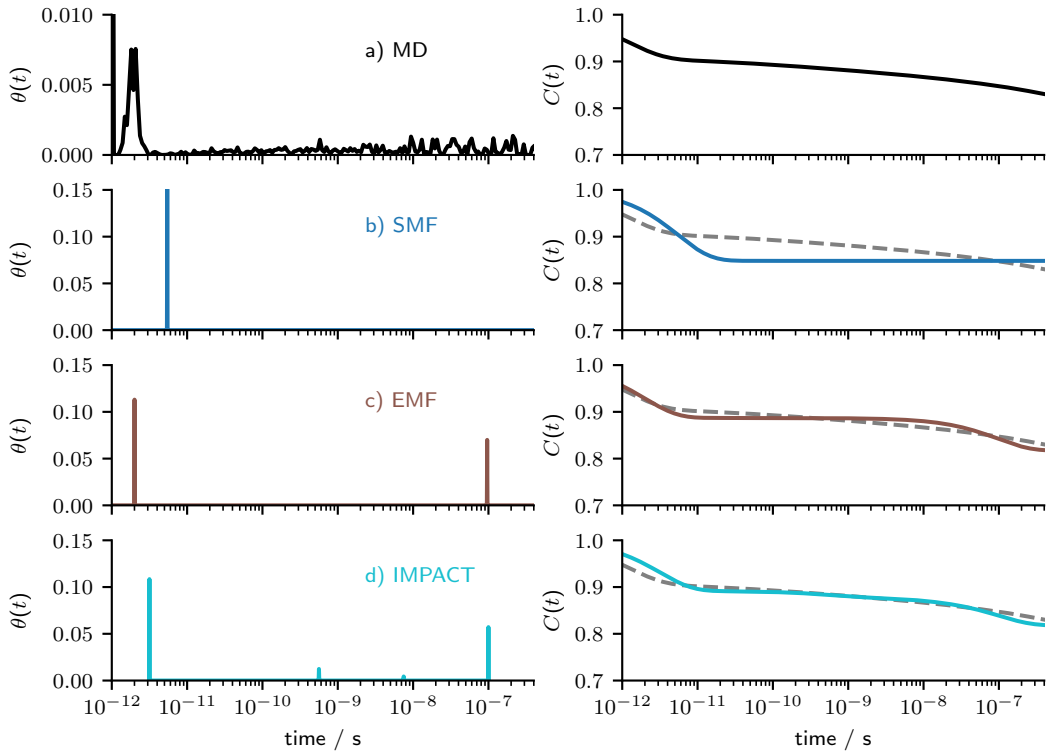

Figure 2.7: Comparison of Model Free methods of parameterising the correlation function. The effective modelled distribution of motions is shown on the left, with the corresponding correlation function on the right. (a) Distribution of motions and correlation function derived from 1 μs of MD of a supercell containing 108 GB1 monomers. (b) Result of fitting a single timescale 'Simple Model Free' model of dynamics to the MD derived correlation function (shown as a dashed line). (c) Result of fitting a two timescale 'Extended Model Free' model to the MD derived correlation function. (d) Result of fitting a 5 timescale 'Interpretation of Motion by Projection onto an Array of Correlation Times' model to the MD derived correlation function.

separated timescales of motion is less justifiable than in rigid proteins.[149] Figure 2.7 shows a comparison of different methods assuming a discrete density of motions. Note, however, that, in this case, these have been fit to a known 'true' density of motions, and the performance for experimental relaxation data will be poorer owing to the limited sensitivity of these rates.

2.2.2.2 Continuous Density of Motion Methods

The issue of timescale biasing, which has been found to potentially lead to significant misrepresentation of real motions,[150] led to the development of methods which

assume a continuous density of motions.[160,161] By taking the Fourier transform of the continuous representation of the correlation function given in equation 2.169, we get:

$$J_{\text{internal}}(\omega) = 2\int_{-\infty}^{\infty} \frac{\theta(\tau)\tau}{1+(\omega\tau)^2} d\log(\tau). \tag{2.180}$$

The corresponding overall spectral density function (*c.f.* equation 2.165) is then:

$$J(\omega) = \frac{2}{5}\int_{-\infty}^{\infty} \frac{\theta(\tau)\tau}{1+(\omega\tau)^2} d\log(\tau). \tag{2.181}$$

Previously, it was shown that the evolution of the density matrix may be expressed as a linear combination of spectral density function contributions (see Section 2.2.1). Following from this, it should be noted that any relaxation rate may also be expressed as a linear combination of spectral density function contributions:

$$R = \sum_i c_i J(\omega_i), \tag{2.182}$$

where R represents any arbitrary relaxation rate composed of a sum of contributions from the spectral density probed at different frequencies (ω_i), weighted by c_i. Substituting the continuous form of the spectral density given in equation 2.180 into equation 2.182, we get

$$R = \sum_i c_i \int_{-\infty}^{\infty} \frac{\theta(\tau)\tau}{1+(\omega_i\tau)^2} d\log(\tau), \tag{2.183}$$

which can be rearranged to give

$$R = \int_{-\infty}^{\infty} \theta(\tau) \sum_i c_i \frac{\tau}{1 + (\omega_i \tau)^2} d\log(\tau) \tag{2.184}$$

$$= \int_{-\infty}^{\infty} \theta(\tau) s(\tau) d\log(\tau). \tag{2.185}$$

Following this rearrangement, it can be seen that the relaxation rate is now the integral of the product of two functions: one unknown ($\theta(\tau)$), and one known ($s(\tau)$). This known function is referred to as the 'sensitivity' of the relaxation rate, and can be easily calculated given knowledge of the coefficients c_i for a given relaxation rate, and the corresponding eigenfrequencies ω_i of the system:

$$s(\tau) = \sum_i c_i \frac{\tau}{1 + (\omega_i \tau)^2}. \tag{2.186}$$

Given a model of the relaxation at a given site, we can therefore calculate the sensitivity of a given relaxation rate to motions occurring on different timescales. Figure 2.8 illustrates this using a known MD-derived density of motions. Ideally, however, we would like to gain greater insight into motions occurring on a specific range of timescales. While the relaxation rate sensitivities are well-defined, they are typically poorly resolved with significant areas of overlap. Smith *et al*. (2018) introduced a method of forming linear combinations of relaxation rates, 'detectors', with well-defined sensitivities optimized to obtain useful properties, such as sensitivity to a specific timescale of motion.[160] Later, they introduced a method using singular value decompositions (SVD) to more readily optimise these linear combinations.[161] This SVD based method will be briefly introduced here, however this will be explored in more detail in Chapters 5 and 6.

In this analysis, it should be noted that the relaxation rates and relaxation rate sensitivities used have been normalised according to the maximum of the sensitivity. That is to say,

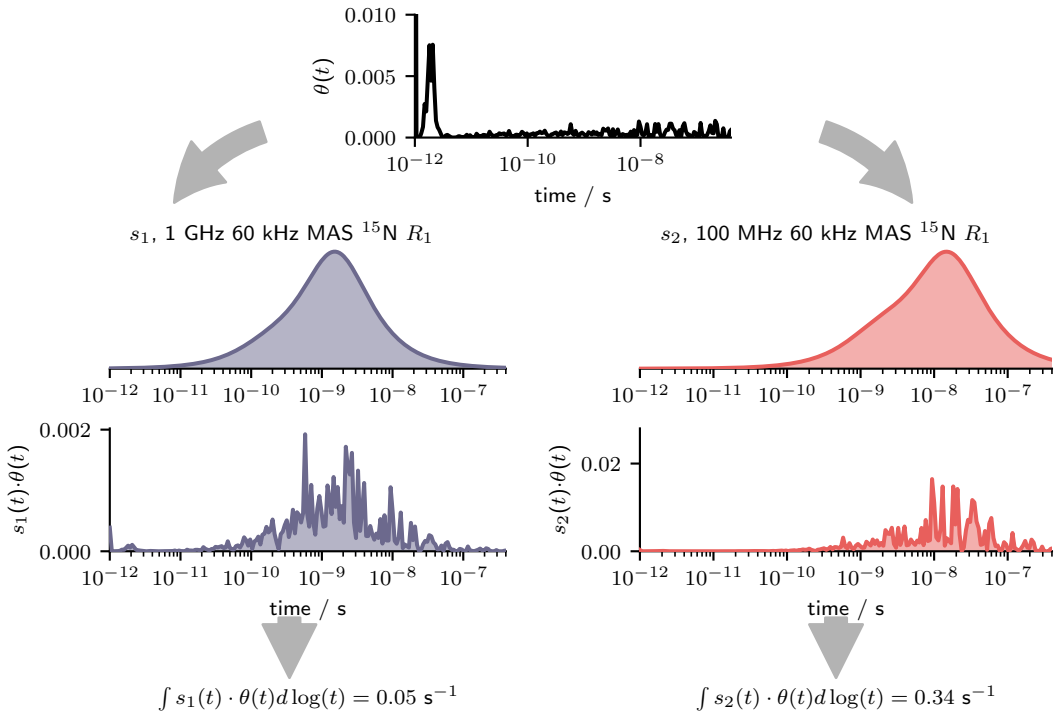

Figure 2.8: Illustration of how relaxation rates may be obtained from the density of motions profile. Each relaxation rate has a 'sensitivity'. The resulting relaxation rate is the integral of the product of this sensitivity with the density of motions.

$$\Re_i = \frac{R_i}{\max(s_i(\tau))} \tag{2.187}$$

$$S_i(\tau) = \frac{s_i(\tau)}{\max(s_i(\tau))}. \tag{2.188}$$

This normalization is performed because the maximum of the unnormalized sensitivities may vary significantly between relaxation rates which may cause problems of numerical stability. It additionally allows for direct comparison between R_1 and $R_{1\rho}$ relaxation rates. We may express a detector, ρ_n, as a linear combination of N relaxation rates

$$\rho_n = \sum_{c=1}^{N} y_{c,n}\Re_c \tag{2.189}$$

where $y_{c,n}$ is a coefficient denoting how much $\Re_c$ contributes to the detector ρ_n. This detector will then have an associated 'detector sensitivity', $P_n(\tau)$:

$$P_n(\tau) = \sum_{c=1}^{N} y_{c,n} S_c(\tau). \tag{2.190}$$

The aim is then to optimise the coefficients $y_{c,n}$ such that the sensitivities $P_n(\tau)$ have the desired properties. Typically, this will be that the detectors are well defined in time, with narrow sensitivities such that each is maximally sensitive to a particular timescale of motions.

To perform the optimization of these detectors, an $N \times m$ matrix $\underline{\boldsymbol{M}}$ describing the sensitivities of our N relaxation rates may be composed by discretising $S_c(\tau)$ with a certain number of points, m, to give the discretised sensitivity $\boldsymbol{S}_c$ with components $S_{c,\mu}$ (μ being an index $1 \ldots m$). The number of points is effectively arbitrary; more points lead to longer calculations, fewer points give reduced accuracy. The matrix $\underline{\boldsymbol{M}}$ is then:

$$\underline{\boldsymbol{M}} = \begin{bmatrix} \boldsymbol{S}_1 \\ \vdots \\ \boldsymbol{S}_N \end{bmatrix} \tag{2.191}$$

$$= \begin{bmatrix} S_{1,1} & \cdots & S_{1,m} \\ \vdots & \ddots & \vdots \\ S_{N,1} & \cdots & S_{N,m} \end{bmatrix}. \tag{2.192}$$

Taking the SVD of this will give an orthogonal matrix $\underline{\boldsymbol{U}}$ (dimension $N \times N$), a rectangular diagonal matrix $\underline{\boldsymbol{\Sigma}}$ (dimension $N \times m$), and an orthogonal transpose matrix $\underline{\boldsymbol{V}}^{'}$ (dimension $m \times m$)

$$\underline{\boldsymbol{M}} = \underline{\boldsymbol{U}\boldsymbol{\Sigma}\boldsymbol{V}'}. \tag{2.193}$$

The N diagonal elements of the $\underline{\boldsymbol{\Sigma}}$ matrix are termed the singular values, σ. Much like eigenvalues and eigenvectors of square matrices, each singular value in $\underline{\boldsymbol{\Sigma}}$ will have a corresponding singular vector, $\boldsymbol{v}$, in $\underline{\boldsymbol{V}}$. The magnitude of a real σ value relates to the extent to which the corresponding singular vector, $\boldsymbol{v}$, contributes to the matrix $\underline{\boldsymbol{M}}$. It has been found that taking the highest k singular values and vectors enables the optimisation of $\approx k$ well-behaved detectors.[129] As we do not know *a priori* how many detectors we can form given our relaxation rate dataset, we perform the optimisation for a range of k values and then determine which gives the best fit to the experimental relaxation rate data. Firstly, the SVD is truncated

$$\underline{\tilde{\boldsymbol{M}}} = \underline{\boldsymbol{U}}_k \underline{\boldsymbol{\Sigma}}_k \underline{\boldsymbol{V}}'_k. \tag{2.194}$$

To find suitable detectors, linear programming algorithms are used to optimize linear combinations of the orthogonal singular vectors in $\underline{\boldsymbol{V}}'_k$ to create detectors with specific properties. This optimisation is performed to identify linear combinations for which $P_{n,\mu} = 1$ for $\mu = q$, and $P_\mu = 0$ otherwise, where q is iterated from 1 to m. This optimization then defines a transformation matrix, $\underline{\boldsymbol{Q}}$, for which each row defines a linear combination of the singular vectors in $\underline{\boldsymbol{V}}'_k$ yielding a well-defined detector. The SVD may then be expanded as

$$\underline{\tilde{\boldsymbol{M}}} = \underline{\boldsymbol{U}}_k \underline{\boldsymbol{\Sigma}}_k \underline{\boldsymbol{Q}}^{-1} \underline{\boldsymbol{Q}} \underline{\boldsymbol{V}}'_k. \tag{2.195}$$

The matrix product $\underline{\boldsymbol{Q}} \underline{\boldsymbol{V}}'_k$ is thus composed of the optimized well-defined detectors. The product $\underline{\boldsymbol{U}}_k \underline{\boldsymbol{\Sigma}}_k \underline{\boldsymbol{Q}}^{-1}$ therefore defines the linear combination of these detectors to obtain the original rates. The linear combination of detectors comprising a relaxation rate is termed a 'detection vector', which are the columns of the matrix $\underline{\boldsymbol{r}}$ calculated as:[129]

$$\underline{\boldsymbol{r}} = \underline{\boldsymbol{U}}_k \underline{\boldsymbol{\Sigma}}_k \underline{\boldsymbol{Q}}^{-1}. \tag{2.196}$$

Once detectors have been optimised, the detector responses may be calculated using these detection vectors ($\boldsymbol{r}_\mu = [r_{0,\mu}, \ldots, r_{k-1,\mu}]$, defining the detector make-up of relaxation rate μ, $1 \leq \mu \leq N$), relaxation rates ($\boldsymbol{\Re} = [\Re_1, \ldots, \Re_N]$), and relaxation rate errors ($\boldsymbol{\epsilon} = [\epsilon_1, \ldots, \epsilon_N]$). This is typically performed as a non-negative least squares fit as

$$\boldsymbol{\rho} = \begin{bmatrix} \frac{\boldsymbol{r}_1}{\epsilon_1} \\ \vdots \\ \frac{\boldsymbol{r}_N}{\epsilon_N} \end{bmatrix}^{-1} \left(\frac{\boldsymbol{\Re}}{\boldsymbol{\epsilon}} \right), \tag{2.197}$$

where the relaxation rates (and corresponding detector vectors) are divided by the respective error to prioritize the fitting of good quality data. In the case that a relaxation rate was missing from a given dataset (for example, due to overlap), the relaxation rate $\Re_i$ was set to 0 and the respective error to $\epsilon_i = 10^5$, effectively removing that relaxation rate from the fit. Sites for which ≥ 5 relaxation rates were missing were removed from fitting entirely. The non-negative least squares fit was performed using the scipy[162] NNLS function.

The error on the detector responses was estimated using a Monte-Carlo approach. From the initial $\boldsymbol{\rho}$, back-calculated relaxation rates ($\boldsymbol{\Re}_{bc}$) were obtained as

$$\boldsymbol{\Re}_{bc} = \begin{bmatrix} \boldsymbol{r}_1 \\ \vdots \\ \boldsymbol{r}_N \end{bmatrix} \boldsymbol{\rho}. \tag{2.198}$$

To each of these back-calculated relaxation rates, normally distributed pseudo-random noise was added according to their respective standard deviations. The resulting set of relaxation rates was then used to obtain detector responses again according to equation 2.197. This procedure was then repeated 200 times, with the value of the detector response reported taken as the median of the repeats. Errors were taken at the 5% and 95% percentiles. The median response was then used

again to back-calculate the relaxation rates to ensure consistency.

This detector approach has found utility in studying the dynamics occurring within a range of systems, including both proteins,[129,160] viral capsids,[163] and lipid membranes.[128] As a new technique, however, a number of questions and challenges remain. For example, the technique relies strongly on having a suitable model for the relaxation rate of interest. While, for ^{15}N relaxation, it is well known that the ^{15}N – ^{1}H interaction dominates, and for ^{13}C′ that the CSA dominates, the application of this to different nuclei may require investigation of the relative contributions of different interactions. Further, the optimisation of these detectors may be challenging in the case that there is one interaction which dominates the sensitivity but, owing to the underlying density of motions, does not dominate the relaxation. Finally, the treatment of other factors such as temperature dependence and other contributing relaxation effects is not obvious in the use of detectors.

Chapter 3

Experimental Techniques

This chapter will introduce the NMR experiment: how do we generate and interconvert nuclear spin coherence? Section 3.1 will introduce some simple NMR experiments and considerations. Initially, the simplest FT-NMR experiment will be shown in Section 3.1.1, with the concepts of Free-Induction Decay (FID) and quadrature detection being introduced. This will be followed by the introduction of Cross-Polarisation (CP) in Section 3.1.2, which is then used to introduce the concept of Multidimensional NMR in Section 3.1.3. Following this, a brief introduction to coherence order and phase cycling will be given in Section 3.1.4. Then, Section 3.2 will expand further into the nature of the RF pulses used and how the nature of a pulse relates to its frequency response. Relaxation experiments will then be introduced in Section 3.3; first as the underlying principles of relaxation measurement in Section 3.3.1, and then with the actual experiments utilised in this thesis in Section 3.3.2. Finally, Section 3.3.3 will discuss the different nuclei and relaxation rates accessible at different MAS frequencies owing to the influence of coherent evolution and spin diffusion.

3.1 General Experimental Methodology

3.1.1 Free-Induction Decay

NMR experiments rely upon the generation, and subsequent detection, of the non-equilibrium coherences generated in nuclear spin systems. The generation of such states relies on the external manipulation of the spin system by the experimentalist. In the early days of NMR, this manipulation was performed by measuring the absorption of a continuously applied weak oscillating RF field.[20–22] By sweeping either the frequency of oscillation of this field, or the magnetic field strength it was possible to identify resonance conditions in which the frequency of the RF applied and the resonant frequency of a nuclear spin were equal, and so the RF was absorbed. This form of NMR is termed 'CW-NMR', for Continuous-Wave NMR. However, as this technique only excites a single frequency at a time it faces poor sensitivity. Additionally, two-dimensional NMR spectroscopy is not practical using CW-NMR.

The development of faster computers and better algorithms[26] in the 1950s and 60s led to the introduction of Fourier Transform (FT)-NMR by Ernst *et al*. in 1966.[25] In this, broadband pulses of RF are used to excite and interconvert magnetic coherence states. As well as the gain in sensitivity from exciting all spin states simultaneously, the use of short 'hard' pulses* to excite and interconvert coherences, combined with the slow relaxation of coherences in NMR, later enabled the development of multiple pulse methods and multi-dimensional techniques. The nature of the RF pulses used to excite these will be discussed more in Section 3.2.

The simplest possible FT-NMR experiment is shown in Figure 3.1a. In this, a 90° hard pulse (shown as a rectangular box) is applied about the x-axis. This causes the nuclear spin magnetisation to nutate around the x axis from equilibrium along the z-axis until it reaches the transverse plane along the y axis. Following this, the transverse plane magnetisation evolves, precessing at its Larmor frequency. The

*'Hard' pulses being where the nutation frequency is much greater than the resonance offset (defined in equation 2.87).

precessing magnetic moment induces a current in the RF coil. In the case of a single isolated spin-1/2 nucleus with a Larmor frequency of ω_0 and a spin-spin relaxation time of T_2, this induced current will be of the form:

$$S(t) \propto \cos(\omega_0 t) \exp^{-\frac{t}{T_2}} . \tag{3.1}$$

The frequency of this response (*e.g.*, ω_0), however, is on the order of MHz and therefore cannot be easily digitised directly. Instead, this resulting frequency is 'mixed' (multiplied) with a synthesised signal applied at the 'receiver reference frequency', ω_{rref} (note that this is typically, though not necessarily, the same as the RF pulse frequency, ω_{rf}). The mixing of these two signals produces an output signal containing the sum and difference of the detected signal and the reference frequency:

$$\begin{aligned} S^{\text{real}}_{mix}(t) &= S(t) \times \cos(\omega_{rref} t) && (3.2)\\ &\propto \cos(\omega_0 t) \exp^{-\frac{t}{T_2}} \cos(\omega_{rref} t) && (3.3)\\ &\propto [\cos((\omega_0 + \omega_{rref})t) + \cos((\omega_0 - \omega_{rref})t)] \exp^{-\frac{t}{T_2}} && (3.4)\\ &\xrightarrow{\text{HP filter}} [\cos((\omega_0 - \omega_{rref})t)] \exp^{-\frac{t}{T_2}}, && (3.5) \end{aligned}$$

with the high-frequency sum term ($\cos((\omega_0 + \omega_{rref})t)$) being omitted using a high-pass (HP) filter and the difference ($\cos((\omega_0 - \omega_{rref})t)$) being a detectable signal, typically on the order of kHz. However, owing to the symmetry of the cosine function ($\cos(x) \equiv \cos(-x)$), we have no way of determining whether $\omega_0 - \omega_{rref} > 0$ or < 0. In order to determine the sign of this resulting signal, we therefore need to acquire the response along both the $x-$ and $y-$ axes; this is termed 'quadrature detection'. To do this, we additionally mix a receiver reference frequency 90° out of phase:

$$S_{mix}^{\text{imag}}(t) = S(t) \times \cos\left(\omega_{rref}t + \frac{\pi}{2}\right) \tag{3.6}$$

$$\propto \cos(\omega_0 t)\exp^{-\frac{t}{T_2}}\cos\left(\omega_{rref}t + \frac{\pi}{2}\right) \tag{3.7}$$

$$\propto -\cos(\omega_0 t)\exp^{-\frac{t}{T_2}}\sin(\omega_{rref}t) \tag{3.8}$$

$$\propto [-\sin((\omega_0 + \omega_{rref})t) + \sin((\omega_0 - \omega_{rref})t)]\exp^{-\frac{t}{T_2}} \tag{3.9}$$

$$\xrightarrow{\text{HP filter}} [\sin((\omega_0 - \omega_{rref})t)]\exp^{-\frac{t}{T_2}}, \tag{3.10}$$

where the resulting difference signal is now sine modulated. These resulting cosine and sine modulated signals can then be digitised, and combined to give a complex Free Induction Decay (FID):

$$FID(t) = S_{mix}^{\text{real}}(t) + iS_{mix}^{\text{imag}}(t) \tag{3.11}$$

$$\propto [\cos((\omega_0 - \omega_{rref})t) + i\sin((\omega_0 - \omega_{rref}))]\exp^{-\frac{t}{T_2}} \tag{3.12}$$

$$= \exp^{i(\omega_0 - \omega_{rref})t}\exp^{-\frac{t}{T_2}}. \tag{3.13}$$

To obtain the frequency domain spectrum we then take the Fourier Transform of this resulting signal. The result is the complex frequency domain signal:

$$S(\omega) \propto \frac{1/T_2}{(1/T_2)^2 + (\omega - \omega_0 + \omega_{rref})^2} - i\frac{\omega - \omega_0 + \omega_{rref}}{(1/T_2)^2 + (\omega - \omega_0 + \omega_{rref})^2} \tag{3.14}$$

$$= A(\omega) - iD(\omega), \tag{3.15}$$

where $A(\omega)$ and $D(\omega)$ are termed the absorptive and dispersive lineshapes (Figure 3.1b). The absorptive lineshape is narrower and gives better resolution, and so to ensure that this is the lineshape displayed a phase correction is applied to the FID to change the relative combinations of the real and imaginary parts to ensure pure

absorptive lineshapes.

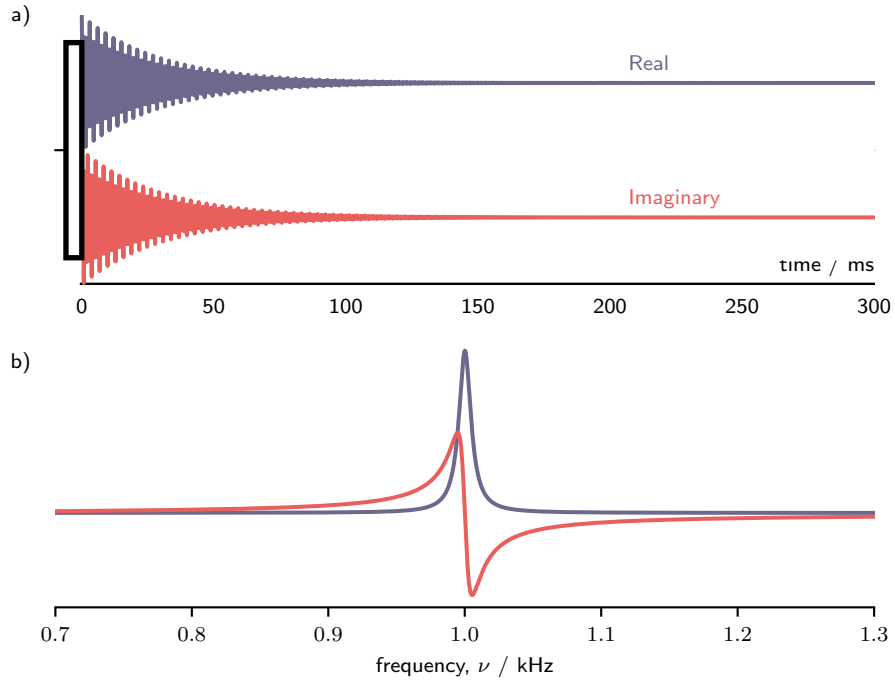

Figure 3.1: (a) Transverse magnetisation generated by the application of an RF pulse precesses and induces a current in the receiver coil. (b) Fourier transform of this gives a spectrum with both a 'real' and 'imaginary' component, with absorptive and dispersive lineshapes, as defined in equation 3.14.

3.1.2 Cross Polarisation

Hydrogen is ubiquitous in biological systems, composing ≈50% of all atoms in proteins numerically. The most abundant isotope of hydrogen, ^{1}H, making up 99.99% of all hydrogen, is the nucleus with the second highest gyromagnetic ratio (exceeded only by the unstable, rare, and radioactive tritium ^{3}H). Additionally, ^{1}H is generally a reasonably fast relaxing nucleus (relative to other isotopes present in biological systems, such as ^{13}C and ^{15}N). ^{1}H is therefore the most sensitive NMR nucleus. This abundance and high magnetic sensitivity, however, give rise to substantial homonuclear (and hence homogeneous) dipolar couplings (see equation 2.100). While MAS can reduce the line-broadening resulting from these, it is still significant even at the fastest MAS rates attainable today. This line-broadening, coupled with the small chemical shift dispersion (≈10–20 ppm), typically gives rise to very crowded and

poorly resolved ^{1}H spectra with many overlapping peaks.

Other spin-active isotopes such as ^{13}C and ^{15}N are also present in biological systems. These nuclei both have substantially lower gyromagnetic ratios, at approximately 25% and 10% of proton respectively. While these exhibit larger chemical shift dispersion (typically on the order of 200 ppm for ^{13}C) and narrower lines owing to their weaker dipolar couplings, they face issues of sensitivity owing to their low natural abundance and low gyromagnetic ratios, and also generally significantly longer required recycle delays (typically on the order of tens of seconds for ^{13}C, and minutes for ^{15}N). While the sensitivity may be aided by isotopic enrichment of the sample, these issues substantially reduce the favourability of NMR spectroscopy to these nuclei.

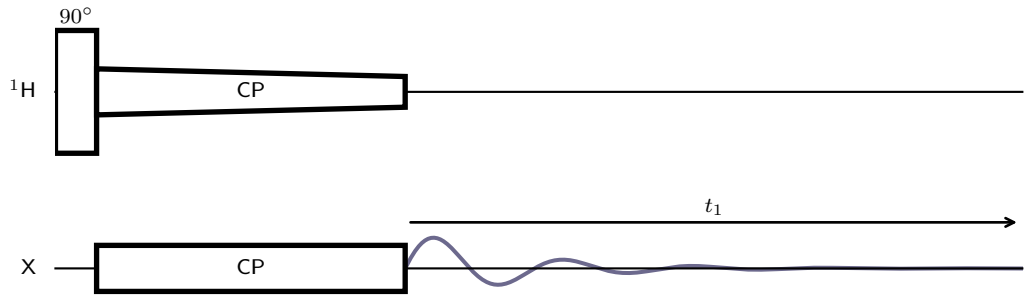

Figure 3.2: Depiction of a cross polarisation experiment. The CP spin lock applied on ^{1}H here is a ramp CP, shown by the slope in the block.

Ideally, we would like to combine the high sensitivity and fast relaxation of ^{1}H with the wider chemical shift dispersion and resolution of these other spin-active isotopes. Cross Polarisation (CP)[164,165] is a method by which the simultaneous application of RF to two channels enables the transfer of magnetisation between them. Figure 3.2 shows a simple CP experiment to transfer magnetisation from the ^{1}H channel to the X channel (where X may be any other spin-active nucleus[§]). Recoupling is achieved by setting the nutation frequencies of the RF spin-lock pulses applied on the two channels such that they meet the Hartmann-Hahn condition,[164]

[§]Typically spin-1/2. Cross-polarisation methods may also be used with quadrupolar nuclei (*e.g.* ref 166), however generally other recoupling methods are more suitable in these cases (*e.g.* ref 167).

$$\nu_1(^1\mathrm{H}) \pm \nu_1(\mathrm{X}) = n\nu_r, \tag{3.16}$$

where $\nu_1(^1\mathrm{H})$ and $\nu_1(\mathrm{X})$ are the nutation frequencies on the ^{1}H and X channels respectively, n is an integer, and ν_r is the MAS frequency. It should be noted that CP may either go via a Zero-Quantum (ZQ) or Double-Quantum (DQ) mechanism depending on whether the sum or difference of nutation frequencies is used[†]; as such, conditions where both of these are met should be avoided as they will give no magnetisation transfer (for instance, at $\nu_r = 60$ kHz spin lock pulses with $\nu_1(^1\mathrm{H}) = 80$ kHz and $\nu_1(\mathrm{X}) = 20$ kHz (ZQ) or $\nu_1(^1\mathrm{H}) = 40$ kHz and $\nu_1(\mathrm{X}) = 20$ kHz (DQ) may be used; however, $\nu_1(^1\mathrm{H}) = 90$ kHz and $\nu_1(\mathrm{X}) = 30$ kHz will not, as this would meet both a positive and negative condition). The difficulty in exactly meeting these Hartmann-Hahn conditions led to the introduction of Ramped-Amplitude CP,[168] whereby the nutation frequency on one channel is linearly varied; this enables slight imperfections in the exact setting of this condition to be accounted for. It should be assumed that, unless specified otherwise, all experiments using CP in this thesis were performed using a ramp. In pulse sequence figures in this thesis, the ramp is represented by a change in the amplitude across the block (*e.g.*, Figure 3.2).

3.1.3 Multidimensional NMR

Higher dimensionality techniques are useful for several purposes; for example, they can enable correlations between nuclei to be observed which provide information on bonding and connectivity (for J-based methods) or spatial arrangement (for dipolar coupling-based methods). By spreading the peaks into multiple dimensions, significantly greater resolution can be attained, allowing for site-specific resolution of resonances within even large biological systems. The primary type of multidimensional experiment used in the work underpinning much of this thesis is the ^{15}N – ^{1}H inverse CP experiment, shown in Figure 3.3a. This experiment is of partic-

[†]See Section 3.1.4 for detail on the difference between ZQ and DQ.

ular utlity in studying protein systems, as these possess N–H amide groups along their backbone. The chemical shift of these groups is sensitive to the local protein secondary structure. Correlating these two nuclei gives a fingerprint spectrum (Figure 3.3b), where cross peaks indicate directly bonded ^{15}N–^{1}H (for short CP contact times). The key facets of many higher dimensional experiments applied to biological systems in the solid state are represented in this experiment.

Reading the two channels of the pulse program in Figure 3.3a from left to right, we begin with the application of a 90° pulse applied to ^{1}H. This nutates the bulk ^{1}H magnetisation from along the longitudinal z-axis into the transverse plane. This transverse magnetisation is then transferred to ^{15}N via a ramped-CP, giving transverse magnetisation on ^{15}N. During the time t_1, this magnetisation is allowed to freely evolve and so encode the ^{15}N Larmor frequency (with decoupling applied to the ^{1}H channel). This free evolution period is then followed by MISSISSIPPI,[169] a water suppression method. First, the ^{15}N magnetisation is placed along the z-axis. The ^{1}H magnetisation is then completely saturated, to kill off any magnetisation which may have recovered during the free evolution time (*e.g.*, water). Once this signal has been fully suppressed, the ^{15}N magnetisation is recovered back into the transverse plane and transferred via CP back to the ^{1}H, where it is detected during t_2. This entire sequence is then repeated several times, with t_1 being incremented sequentially such that the signal detected during t_2 has the free evolution during t_1 encoded as a second 'indirect' dimension. The 2D FT of this resulting 2D FID then gives the complete spectrum shown in the lower panel.

Previously, in Section 3.1.1, quadrature detection was introduced as a method for sign discrimination in 1D spectra. Multidimensional spectra similarly face the issue of sign discrimination. In the spectra presented in this thesis, sign discrimination in the indirect dimension was achieved using the 'States-TPPI' method.[170] This is a combination of the 'States' method with Time-Proportional Phase Incrementation (TPPI). In the States method, each indirect time point requires the acquisition of two spectra, where the phase of the preparation pulse for the evolution in the indirect

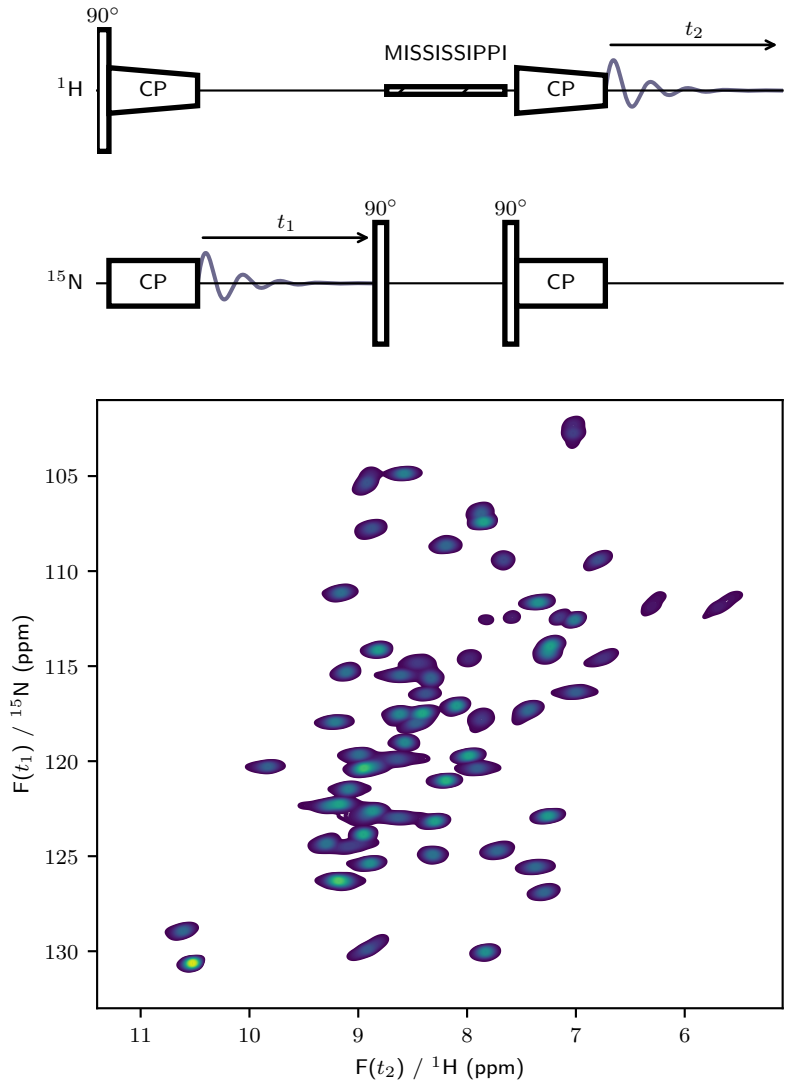

Figure 3.3: Depiction of an inverse cross-polarisation (CP) two-dimensional ^{15}N – ^{1}H experiment. Top: pulse sequence. Magnetisation is generated by an excitation pulse on ^{1}H, transferred to ^{15}N by cross-polarisation, and allowed to evolve on ^{15}N during t_1. MISSISSIPPI water suppression is then used, followed by cross-polarisation back to ^{1}H and detection during t_2. Bottom: An example of a resulting spectrum. The resulting 2D FID is Fourier transformed in each direction. The spectrum shown here is of U-[^{13}C, ^{15}N]-GB1 (uniformly ^{13}C, ^{15}N labelled) at 100 kHz magic-angle spinning at a ^{1}H Larmor frequency of 1 GHz. The outbound ^{1}H→^{15}N CP contact time was 2 ms, while the return ^{15}N→^{1}H CP contact time was 800 μs.

dimension (in Figure 3.3, this is the outbound CP pulse on ^{15}N) is adjusted relative to the receiver such that one of the spectra is cosine modulated and the other sine modulated with respect to the indirect evolution.[171] These may then be combined and transformed in the same manner as the quadrature detection, thereby enabling

sign discrimination. One issue with this method is that artefactual signals which do not get modulated may appear with zero-frequency; typically, the transmitter offset is set such that these zero-frequency artefacts would appear undesirably in the middle of the experimental spectrum. In TPPI, the phase of the preparation pulse and receiver is inverted for every indirect time point such that these zero-frequency artefacts are modulated at the sampling Nyquist frequency, and therefore appear on the edge of the spectrum where there is less chance of this interfering with the desired spectrum.[172] The combination of these two methods in States-TPPI therefore allows for indirect sign discrimination without significant interference from artefacts.

3.1.4 Coherence Order and Phase Cycling

Different product operator states (*e.g.*, $\hat{\underline{\boldsymbol{I}}}_z$, $\hat{\underline{\boldsymbol{I}}}_+\hat{\underline{\boldsymbol{S}}}_-$) may be classified according to how they acquire phase under a rotation about the z axis. For example, taking the $\hat{\underline{\boldsymbol{F}}}_z$ operator as one which rotates any given operator about the z axis, an $\hat{\underline{\boldsymbol{I}}}_+$ state will acquire phase as:

$$e^{-i\phi\hat{\underline{\boldsymbol{F}}}_z}\hat{\underline{\boldsymbol{I}}}_+e^{i\phi\hat{\underline{\boldsymbol{F}}}_z} = e^{-i\phi}\hat{\underline{\boldsymbol{I}}}_+, \tag{3.17}$$

while an $\hat{\underline{\boldsymbol{I}}}_+\hat{\underline{\boldsymbol{S}}}_-$ state will acquire phase as:

$$\begin{aligned} e^{-i\phi\hat{\underline{\boldsymbol{F}}}_z}\hat{\underline{\boldsymbol{I}}}_+\hat{\underline{\boldsymbol{S}}}_-e^{i\phi\hat{\underline{\boldsymbol{F}}}_z} &= e^{-i\phi}e^{i\phi}\hat{\underline{\boldsymbol{I}}}_+\hat{\underline{\boldsymbol{S}}}_- && (3.18)\\ &= e^{i0}\hat{\underline{\boldsymbol{I}}}_+\hat{\underline{\boldsymbol{S}}}_- && (3.19)\\ &= \hat{\underline{\boldsymbol{I}}}_+\hat{\underline{\boldsymbol{S}}}_-. && (3.20) \end{aligned}$$

The response of an operator to this rotation is termed the 'coherence order'. A state with a coherence order of p will rotate as:

$$e^{-i\phi\hat{\underline{\boldsymbol{F}}}_z}\hat{\underline{\boldsymbol{\sigma}}}^{(p)}e^{i\phi\hat{\underline{\boldsymbol{F}}}_z} = e^{-ip\phi}\hat{\underline{\boldsymbol{\sigma}}}^{(p)}. \tag{3.21}$$

Operators with $p = 0$ (*e.g.*, $\hat{\underline{\boldsymbol{I}}}_+\hat{\underline{\boldsymbol{S}}}_-$) are termed 'zero-quantum' operators, while operators with $p = \pm 1$ (*e.g.*, $\hat{\underline{\boldsymbol{I}}}_+$) are 'single-quantum' operators. Higher order coherence orders are possible.

NMR pulse sequences are designed to achieve certain coherence transfers. For example, the aim of the CP pulses introduced in Section 3.1.2 is to transfer single-quantum coherence on ^{1}H to single-quantum coherence on X. However, the RF pulses applied are indiscriminant with regards to the types of coherence transfer which will be induced. They therefore generate other undesirable coherence states, which will compete and interact with the desired coherence transfer pathway, resulting in uninterpretable spectra.

Phase cycling is a technique which can enable the desired coherence transfer pathway to be isolated from competing pathways.[173,174] Using phase cycling, the phase of the pulses applied (see Section 2.1.2.2) and the detector (see Section 3.1.1) can be systematically varied across several repeated experiments such that desired coherence transfer pathways sum together while undesirable coherence transfer pathways cancel out. The design of a phase cycle for a given experiment is aided by the application of the following rules:

- Shifting the phase of a pulse by an amount $\Delta\phi$ will lead to a change in phase of a coherence order transfer Δp by an amount $-\Delta p\Delta\phi$.
- An N step phase cycle, involving a full rotation of the phase and selecting a change in coherence order Δp, will also select pathways giving a change in coherence order $\Delta p \pm nN$ where n is a real integer.

3.2 RF Pulses

The theoretical background of RF pulses was introduced in Section 2.1.2.2. Here, experimental considerations of such pulses will be discussed. An RF pulse is defined by a transmitter frequency (ω_{rf}), a phase (ϕ), and nutation frequency (ω_1). On a modern spectrometer any of these properties may be varied as a function of time, enabling a range of shaped pulses which can be tuned to have different properties and excitation bandwidths. The transmitter frequency determines which spins are being interacted with; as in equation 2.86 (repeated here), the effective rotating frame Hamiltonian for evolution of an $\hat{\underline{\boldsymbol{I}}}_x$ state under an applied pulse is:

$$\tilde{\hat{\underline{\boldsymbol{H}}}}_{RF}(t) = \omega_1 e^{i(\Omega t+\phi)\hat{\underline{\boldsymbol{I}}}_z} \hat{\underline{\boldsymbol{I}}}_x e^{-i(\Omega t+\phi)\hat{\underline{\boldsymbol{I}}}_z}, \tag{3.22}$$

where $\Omega = \omega_0 - \omega_{rf}$ and is the frequency offset between the applied pulse and the Larmor frequency of the spin of interest. The application of this pulse 'on-resonance' to a nuclear spin causes the nuclear spin magnetisation to nutate about the axis of the pulse (defined by the phase, ϕ) at the nutation frequency. As such, the length of time for which an RF pulse must be applied for depends both on the nutation frequency and the desired angle of rotation, β, as

$$\beta = \omega_1 \tau, \tag{3.23}$$

where τ is the pulse length and ω_1 is in angular frequency units (rad s^{-1}). For example, a pulse applied with a nutation frequency of 100 kHz ($\omega_1 = 2\pi \times 10^5$ rad s^{-1}) for 2.5 μs would cause the magnetisation to nutate $\pi/2$ rad from *e.g.*, along the z axis to the transverse plane. A lower powered pulse with a nutation frequency of 1 kHz ($\omega_1 = 2\pi \times 10^3$ rad s^{-1}) would require 250 μs to nutate the same amount. This longer nutation has consequences for the bandwidth of the applied pulse. The effect may be considered by calculating the first-order average Hamiltonian,[‡] with

[‡]Note explicitly that this is approximate to first-order, and higher-order terms do contribute

$\tau = \frac{\pi}{2\omega_1}$ and $\phi = 0$:

$$\underline{\tilde{\hat{\boldsymbol{H}}}}_{RF}^{(1)} = \frac{1}{\tau}\int_0^{\tau} \underline{\tilde{\hat{\boldsymbol{H}}}}_{RF}(t)dt \tag{3.24}$$

$$= \frac{2\omega_1^2}{\pi}\int_0^{\frac{\pi}{2\omega_1}} e^{i\Omega t\underline{\hat{\boldsymbol{I}}}_z}\underline{\hat{\boldsymbol{I}}}_x e^{-i\Omega t\underline{\hat{\boldsymbol{I}}}_z}dt. \tag{3.25}$$

The effective Hamiltonian along $\underline{\hat{\boldsymbol{I}}}_x$ is then given by the trace of the resulting first-order average Hamiltonian with the $\underline{\hat{\boldsymbol{I}}}_x$ operator. Analytically, to first-order, this gives an effective RF amplitude scaling as a function of offset of

$$\frac{\omega_1'(\Omega)}{\omega_1} = \frac{\sqrt{2}\omega_1}{\pi\Omega}\sin\left(\frac{\Omega\pi}{\sqrt{2}\omega_1}\right), \tag{3.26}$$

where $\omega_1'(\Omega)$ is the offset-dependent effective nutation frequency, and all other terms are as defined above. The effective RF amplitude therefore has a sinc dependence on the frequency offset. From this, it can be seen that when the RF is applied perfectly on resonance ($\Omega \to 0$), the RF amplitude is ω_1. As the RF pulse moves off-resonance, the effective nutation frequency decreases. As a result, for broadband excitation, high nutation frequencies ($\omega_1 \gg \Omega$) are required to excite the spectrum evenly. The offset dependence of these pulses is visualised in Figure 3.4, for nutation frequencies of 10, 50, and 100 kHz. In general, the nutation frequency used for these hard pulses is limited by the hardware; the power required scales as the square of the nutation frequency, such that a 100 kHz pulse requires $4\times$ the power (in watts) of a 50 kHz pulse. Faster spinning probes, with their smaller rotor sizes and consequently smaller RF coils, can achieve greater power density in the coil and therefore can typically achieve higher nutation frequencies with lower power.

The offset dependence of the excitation of a pulse enables the use of these for selective excitation. Often, it is useful to be able to interact specifically with either a single resonance, or with a set of resonances in a specific range of chemical shifts.

significantly; this approximation is used here to illustrate the offset dependence.

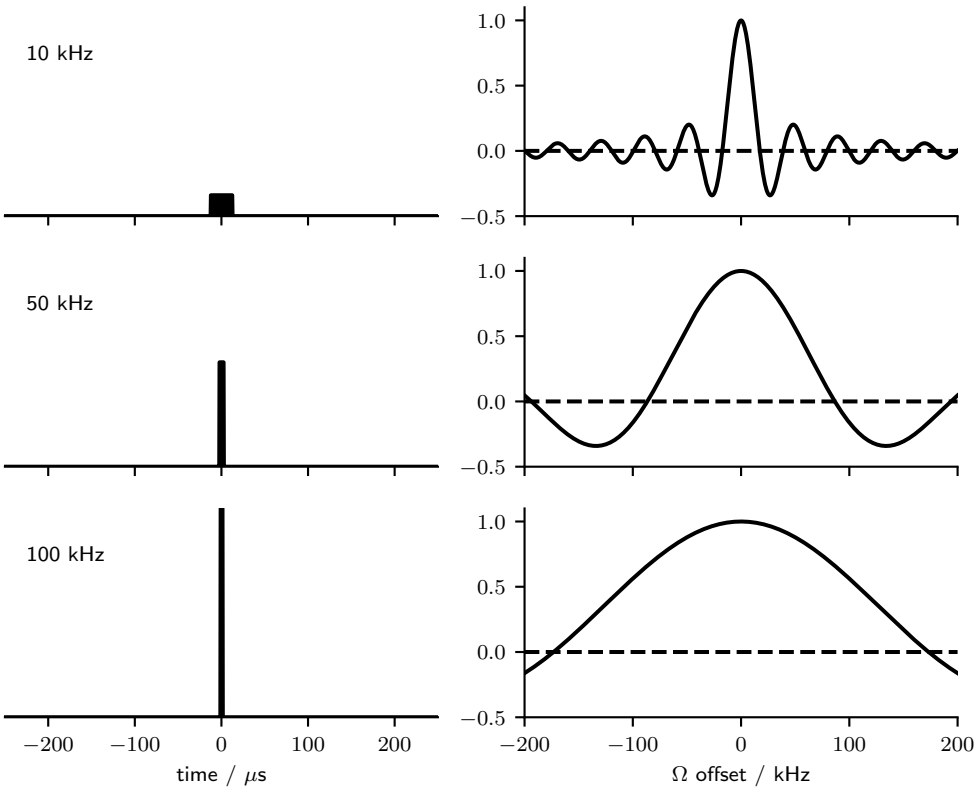

Figure 3.4: Pulses visualised in time domain (left) and frequency domain (right) for different pulse lengths and nutation frequencies for broadband excitation pulses. The frequency domain responses here have been calculated numerically, and as such may differ from the first-order analytical expression in equation 3.26.

By using a low-powered excitation pulse, such as those shown on the left side of Figure 3.5, it is possible to interact selectively with specific resonances. However, as these are rectangular pulses, their corresponding frequency response is characterised by a sinc wave, as shown on the right of Figure 3.5. While these sinc wobbles are typically not a concern with hard broadband pulses (where we would aim to include all resonances of interest within the broadband response), they can cause issues for selective pulses by interacting with other spins. The 'ideal' pulse for selective excitation would be to apply a sinc wave in the time domain; the corresponding frequency response would then analogously be a rectangular spectral response. However, to include sufficient sinc wobbles to have such a nicely well-defined spectral response would require such a pulse to be unfeasibly long.

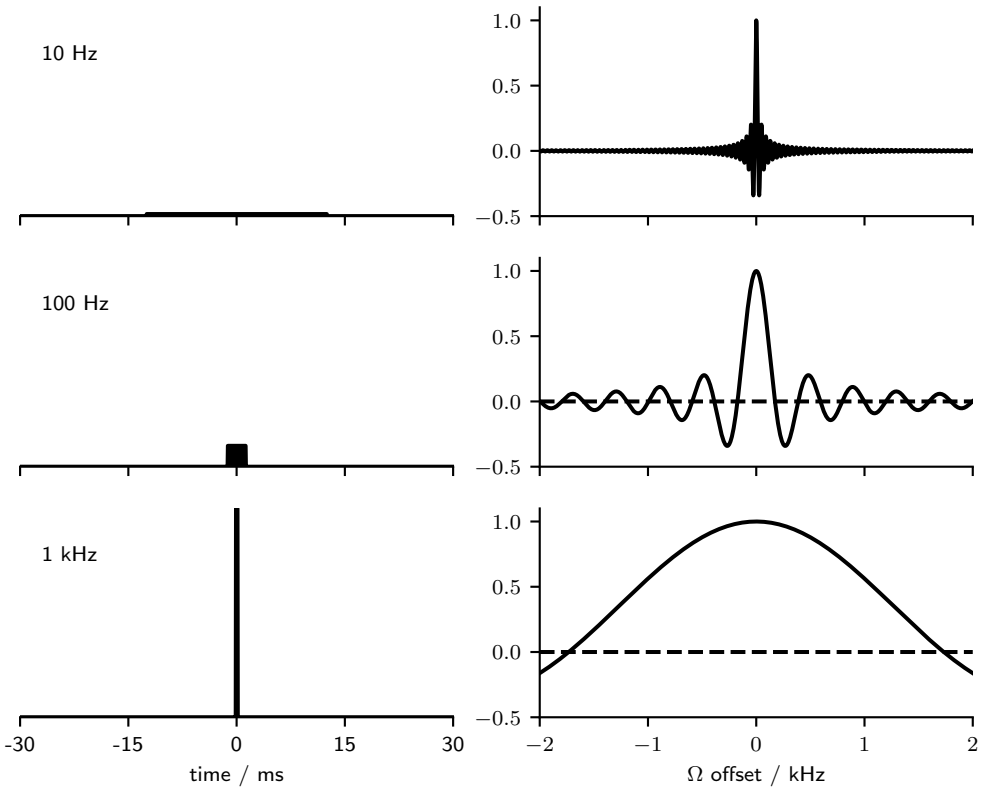

Figure 3.5: Pulses visualised in time domain (left) and frequency domain (right) for different pulse lengths and nutation frequencies for selective excitation pulses. The frequency domain responses here have been calculated numerically, and as such may differ from the first-order analytical expression in equation 3.26.

To account for this, a number of different selective pulses have been introduced, such as Gaussian pulses[175,176] and DANTE pulses.[177] In the case of a Gaussian pulse, the amplitude of the RF is varied as a Gaussian. The FT of a Gaussian is a Gaussian, and therefore the resulting spectral response is a well-defined Gaussian. Gaussian pulses will be used in Section 4.5 to selectively saturate and invert specific resonances in resolved spectra.

3.3 Relaxation Experiments

As discussed previously in Section 2.2, relaxation is the phenomenon by which a perturbed spin-order will return to its equilibrium magnetisation. Quantifying the rate at which nuclear spins recover to equilibrium can provide a wealth of

information as to their local motions and environment. The general premise of a relaxation experiment is to perturb or excite a spin away from its bulk equilibrium magnetisation. This is then followed by a variable delay, during which the spin is allowed to relax. The delay is then followed by excitation (if required for detectable coherence) and, finally, detection of the resulting signal, where the intensity of the signal reflects the extent to which the spin was able to relax back to equilibrium. By varying the delay during which the spin is allowed to relax, a graph can be plotted to show this recovery. Despite this rather simple basis, there are several different approaches to measuring these rates. In Section 3.3.1, three such approaches for measuring R_1 relaxation will be introduced, with their respective advantages and disadvantages discussed. For simplicity, $R_{1\rho}$ relaxation will not be considered in this section. This will then be followed by a discussion of the experiments specifically used in this thesis to measure ^{13}C and ^{15}N R_1 and $R_{1\rho}$ relaxation rates in Section 3.3.2. Finally, Section 3.3.3 will discuss factors which must be considered when applying these relaxation experiments in order to allow for adequate quantification of dynamics.

3.3.1 Principles of Relaxation Rate Measurement

Proteins undergo motions over several orders of magnitude of timescale. Simple bond librations may occur with characteristic timescales on the order of picoseconds, while larger domain motions may take microseconds to complete. As a result, a range of experimental methodologies have been developed to study different types of motion. Figure 3.6 outlines the different types of motion and the timescales on which they occur, and different NMR experiments which can be performed to study these varied motions. This thesis will focus entirely on solid-state relaxation analysis.

Three of the most common methods of measuring spin-lattice (T_1) relaxation are shown in Figure 3.7. These are saturation recovery (a), inversion recovery (b), and the Torchia method (c,d). Their resulting relaxation recovery graphs are shown in

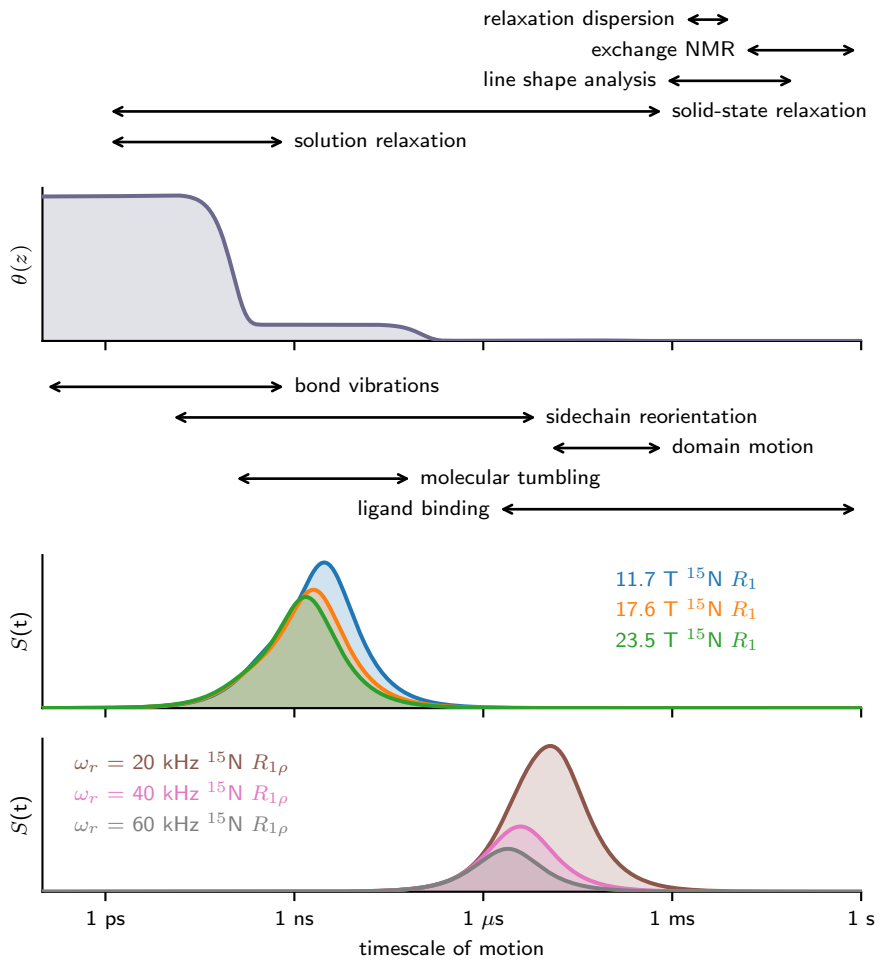

Figure 3.6: Depiction of the timescales of motion in proteins. From top to bottom: types of NMR experiments which are sensitive to motion on the given timescales; A depiction of a possible distribution of motions; Motions which are expected to occur on this timescale; Sensitivities of ^{15}N R_1 rates to motion on these timescales over different magnetic fields; Sensitivities of ^{15}N $R_{1\rho}$ rates to motion on these timescales at different spinning frequencies. The first and third panes were inspired by Figure 1 in ref 178.

Figure 3.8, and will be discussed here.

In a saturation recovery experiment (Figure 3.7a), the magnetisation on the spin of interest (shown as X) is 'saturated' (dashed block). Saturation occurs when RF is applied to equilibrate the spin-up and spin-down energy levels in such a manner that there is no bulk magnetic moment, which is to say that a vector denoting the bulk magnetic moment has no magnitude. As a result, at the end of this saturation pulse the magnetisation along the z-axis is 0. This is then followed by a relaxation

delay, τ_{relax}, during which the magnetisation is allowed to recover to the equilibrium polarisation. Following this, the z magnetisation is excited to the transverse plane using a 90° pulse, and the resulting FID recorded. The amplitude of the resulting signal is proportional to the amount of z magnetisation which is allowed to recover during this τ_{relax} period; by varying this, a profile of the relaxation may be built up, as shown in Figure 3.8a.

The principle behind inversion recovery (Figure 3.7b) is very similar. In this, a hard inversion pulse is applied, such that the bulk magnetic moment is placed along $-z$. This out of equilibrium magnetisation then recovers during τ_{relax}, before being excited to the transverse plane by a 90° pulse. As in saturation recovery, the amplitude of the resulting FID and therefore spectrum is dependent on the extent to which the magnetisation has recovered along the z axis. The resulting relaxation curve, Figure 3.8b, is very similar again.

While both inversion recovery and saturation recovery can be used to acquire good quality relaxation data, they face several limitations. For reasons which will be discussed in Section 3.3.3, we are normally interested in recording relaxation rates of ^{13}C and ^{15}N for proteins and other biological systems. As was discussed previously in Section 3.1.2, these nuclei are characterised by low sensitivity and slow relaxation. Both inversion recovery and saturation recovery rely purely on the magnetisation recovered on these nuclei for their signal; as such, they cannot be performed using CP to enhance their sensitivity. Furthermore, inversion recovery requires that the magnetisation has adequately recovered along the $+z$ axis after the FID has been recorded; a consequence of this is then that the recycle delay between scans is limited by the (often slow) relaxation of the nuclei being observed. While saturation recovery does not require this, it typically requires high-powered saturation pulses which owing to the duty cycle of the probe may reduce the scan rate which may be used.

The Torchia method enables the use of CP to enhance the sensitivity of these relaxation experiments.[179] This method involves the application of the pulse programs

shown in Figures 3.7c,d, which are identical except that the phase of the first 90° pulse on the X channel has been shifted by 180°. Firstly, the ^{1}H magnetisation is excited into the transverse plane; this magnetisation is then transferred via CP to the X channel. The issue with then performing an experiment analogous to inversion recovery at this point is that this magnetisation is hyper-polarised; after the relaxation period, the magnetisation would not recover back to this hyper-polarised state, which means that the final equilibrium magnetisation to which the experiment will recover is unknown. The Torchia method bypasses this by switching the phase of the 90° pulse applied on the X channel to bring the magnetisation along the z axis; as a result, in half of the scans the hyper-polarised magnetisation is placed along $-z$ and recovers to normal polarisation z, while in the other half the hyper-polarised magnetisation is placed along z and recovers to normal polarisation z. As these scans are accumulated, the difference is taken such that the normal polarisation recovery cancels out. The resulting relaxation decay profile, shown in Figure 3.8c, is then characterised by a decay from the hyper-polarised state to 0 magnetisation, which can more readily be quantified.

The use of the Torchia method is then beneficial for several reasons. The use of ^{1}H magnetisation enables hyper-polarisation of the X spins, giving greater sensitivity. The transfer of magnetisation from ^{1}H additionally allows the recycle delay of the ^{1}H to be used instead of that of the X channel nuclei, typically giving a faster repeat time. A limitation of this method is that it requires the presence of ^{1}H or another abundant high sensitivity nuclei in the sample. For biological systems, however, this is generally the case.

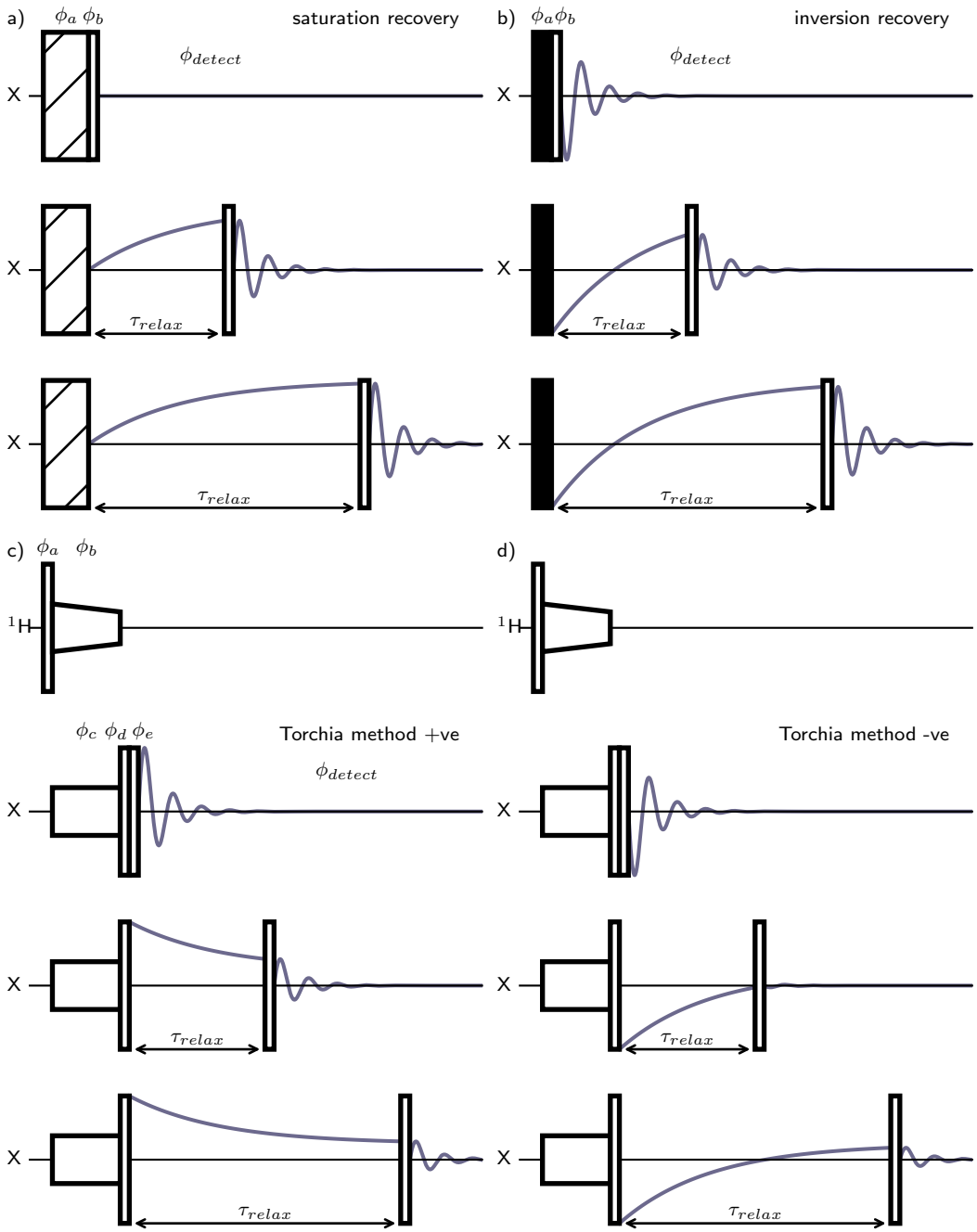

Figure 3.7: Different types of experiment for measuring relaxation rates. (a) Saturation recovery, (b) Inversion recovery, (c,d) Torchia method (positive and negative, noting that it is the difference of the resulting decays which is used in this case.). Saturation pulses are shown as a block with diagonal lines, 90° pulses and 180° are shown as empty and full tall rectangles respectively, and CP pulses are shown as longer shorter rectangles. Typically phase cycles are as follows: (a) ϕ_a: $\{+x\}$, ϕ_b :{+x, +x, -x, -x, +y, +y, -y, -y},ϕ_{detect}: $\{+x, +x, -x, -x, +y, +y, -y, -y\}$; $(b)\phi_a$: $\{+x, -x\}$, ϕ_b: $\{+x, +x, -x, -x, +y, +y, -y, -y\}$, ϕ_{detect}: $\{+x, +x, -x, -x, +y, +y, -y, -y\}$; (c): ϕ_a: $\{+y\}$, ϕ_b: $\{+x\}$, ϕ_c: $\{+x\}$, ϕ_d: $\{-y, +y\}$, ϕ_e: $\{+x, +x, -x, -x, +y, +y, -y, -y\}$, ϕ_{detect}: $\{+x, -x, -x, +x, +y, -y, -y, +y\}$ (note that for (c), the combined phase cycle for $+$ve and $-$ve mode is shown).

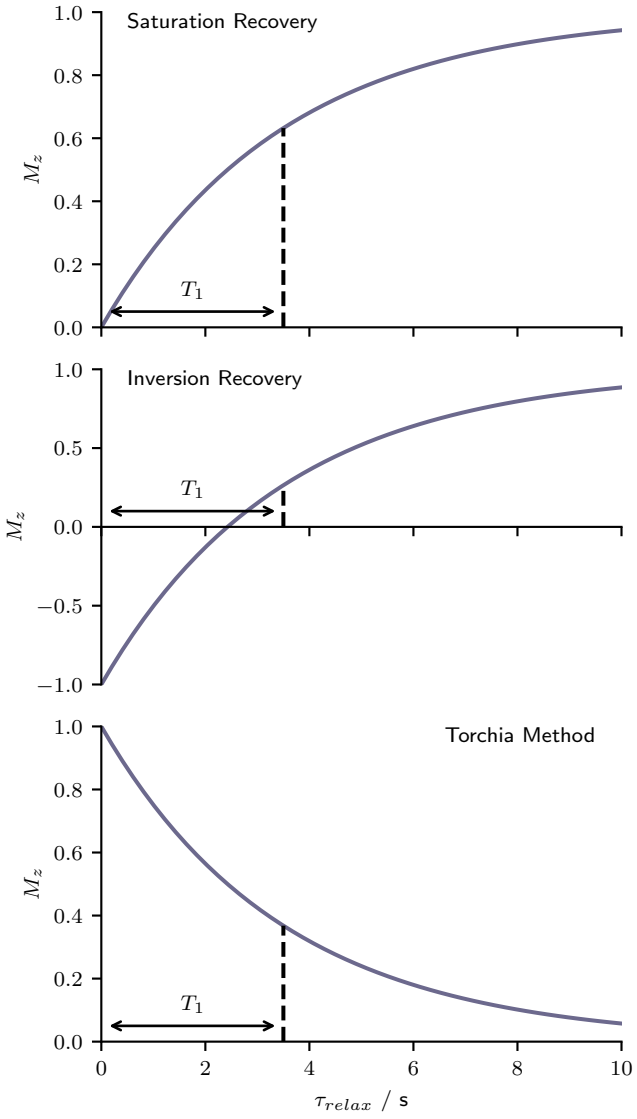

Figure 3.8: z-Magnetisation as a function of variable delay (τ_{relax}) for different relaxation experiments.

3.3.2 Relaxation Rate Experiments

In this thesis, four different types of relaxation rates have been recorded: ^{13}C′ R_1, $R_{1\rho}$; ^{15}N R_1, $R_{1\rho}$. In each case, these have been measured using detection in a ^{15}N – ^{1}H 2D spectrum to allow for site-specific relaxation quantitation. For the R_1 measurements, the Torchia method was used[§].

Figure 3.9 shows the experiments used for R_1 quantitation on ^{15}N (a) and ^{13}C′ (b). The ^{15}N experiment is analogous to the 2D ^{15}N – ^{1}H CP experiment shown in Section 3.1.3, with the exception that the transverse relaxation on ^{15}N generated by the CP is nutated to the z axis for a relaxation period, before being returned and allowed to evolve as normal. The ^{13}C′ experiment is different; in this case, the ^{1}H transverse magnetisation is instead transferred via CP to the ^{13}C spins. Following nutation to the z axis and relaxation, this magnetisation is then transferred from ^{13}C to ^{15}N via CP to be allowed to evolve and be spin labelled on ^{15}N. Spin labelling on ^{15}N enables the ^{13}C relaxation rate to be measured through the same ^{15}N-^{1}H spectrum.

$R_{1\rho}$ relaxation is measured in a similar manner. $R_{1\rho}$ relaxation relates to the decay of signal which has been spin-locked in the transverse plane. Pulse programs for measuring this are shown in Figure 3.10, where it may be seen that in both cases, after the transverse magnetisation is transferred to the nuclei of interest, it is spin-locked for a variable delay. During this period, the transverse magnetisation decays. This is then followed by ^{15}N evolution in the indirect dimension, and then finally recovery and detection on ^{1}H.

[§]For clarity, this is not shown explicitly in the pulse sequence.

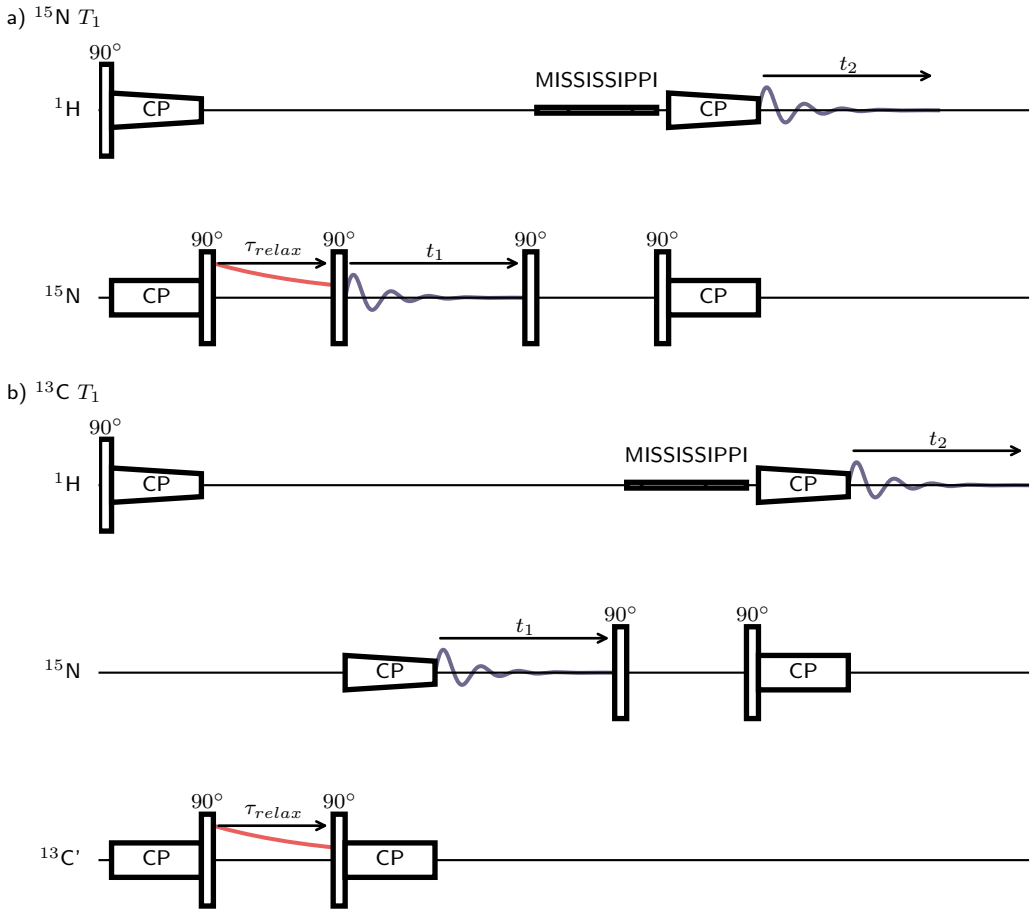

Figure 3.9: Experiments used in this thesis to measure (a) ^{15}N and (b) ^{13}C′ T_1 relaxation rates with detection in a ^{15}N – ^{1}H 2D NMR experiment.

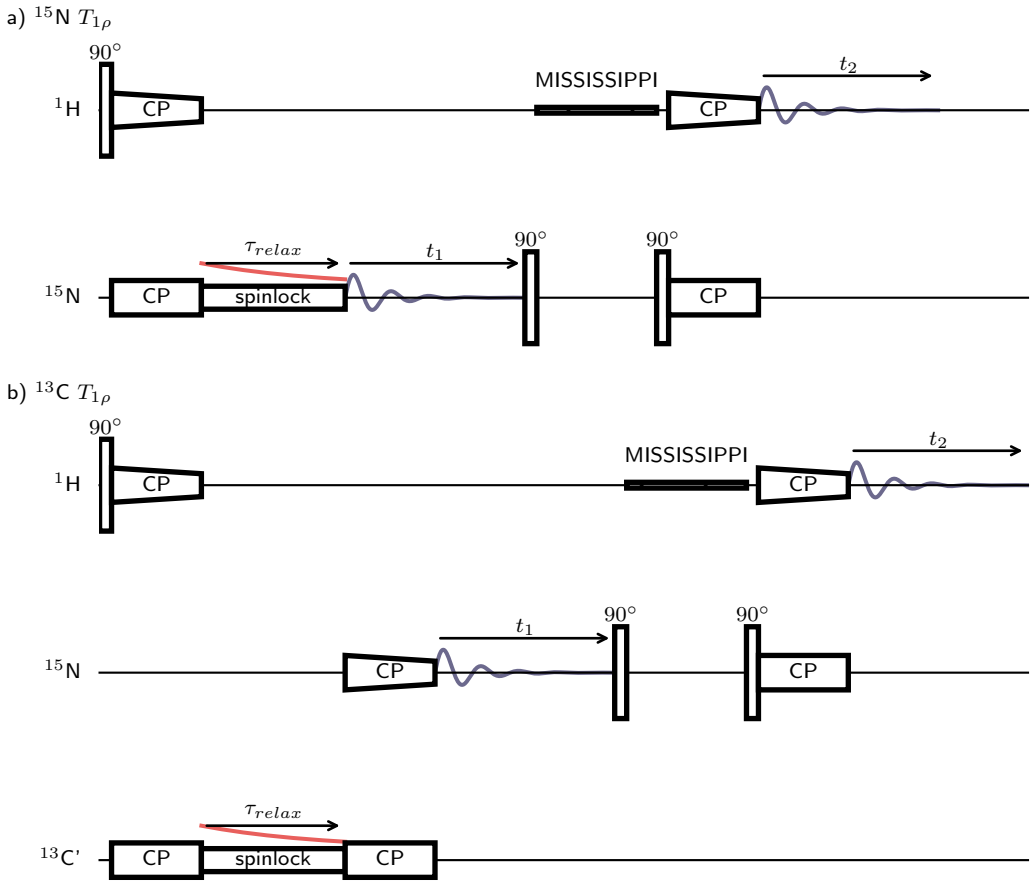

Figure 3.10: Experiments used in this thesis to measure (a) ^{15}N and (b) ^{13}C′ $T_{1\rho}$ relaxation rates with detection in a ^{15}N – ^{1}H 2D NMR experiment.

3.3.3 Experimental Considerations for Measuring Relaxation Rates

As has been alluded to previously, the nuclei we typically use for dynamical quantitation are the amide ^{15}N and the carbonyl ^{13}C′. The question may then be asked why we do not consider the ^{1}H relaxation, the $^{13}C\alpha$, or the sidechain ^{13}C sites. The primary reason for this is the presence of significant spin diffusion between these nuclei. For ^{15}N, typically the nearest homonuclei will be the next amide ^{15}N at a distance of $\approx 3-4$ Å; this, combined with the low gyromagnetic ratio and weak dipolar couplings between these nuclei strongly limits the rate of spin diffusion between these. This enables quantitation of ^{15}N relaxation even in fully protonated samples at ≈ 50 kHz. On the other hand, for ^{1}H relaxation there are often very dense strongly coupled networks of neighbouring protons; as a result, relaxation is rapidly averaged between these sites and therefore cannot be interpreted in a site specific manner. Table 3.1 illustrates the minimum MAS frequencies required for quantitation of R_1 and $R_{1\rho}$ rates for a range of possible nuclei of interest in both perdeuterated and fully protonated systems; this has been adapted from LeManchard *et al*. (2022).[125] It should be noted that these are for fully ^{13}C, ^{15}N labelled systems; samples which are not isotopically enriched in ^{15}N and ^{13}C will very rarely have strongly coupled homonuclear interactions owing to the low density of these spin active nuclei, therefore allowing their relaxation rates to be measured at lower spinning rates.

Table 3.1: Approximate minimal MAS frequencies required for site-specific quantification of incoherent relaxation. Adapted from ref 125.

Nuclei	Rate	Perdeuterated Min / kHz	Protonated Min / kHz
^{15}N	R_1	50	50
^{15}N	$R_{1\rho}$	27	45
^{13}C′	R_1	≈ 50	60
^{13}C′	$R_{1\rho}$	≈ 45	45
$^{13}C\alpha$	R_1	unknown	>80
$^{13}C\alpha$	$R_{1\rho}$	unknown	>80
^{1}H	R_1	>150	>150
^{1}H	$R_{1\rho}$	>150	>150

For recording $R_{1\rho}$ relaxation rates, consideration must be given to the applied spin lock field. It is necessary to apply a sufficiently high nutation frequency to ensure that all sites of interest are spin locked. Additionally, at low spin lock frequencies, Bloch-McConnell Relaxation Dispersion (BMRD) may lead to an increase in the measured $R_{1\rho}$ owing to the presence of exchange interactions.[51,180,181] Similarly, the application of high nutation frequencies approaching the MAS frequency will lead to NEar Rotary Resonance Dispersion (NERRD).[180,181] BMRD and NERRD have found utility in the study of slow microsecond exchange and dynamical processes.[51,121,180,181]

Consideration must also be given to cross-correlation effects. For example, in the case of ^{15}N relaxation, both the ^{15}N CSA and ^{15}N – ^{1}H dipolar interactions transform with the same symmetry. As a result, there is the potential that cross-correlation effects could arise between the two mechanisms for relaxation. A result of this would be that the measured relaxation rate would be different depending on whether the ^{1}H adjacent to the ^{15}N was in the $|+\frac{1}{2}\rangle$ or $|-\frac{1}{2}\rangle$ state. However, in the solid state, it has been found that the presence of strong dipolar couplings and rapid spin diffusion causes these states to interconvert and so self-decouple, such that these cross correlation effects are negligible.[182,183]

Chapter 4

Spin Diffusion

This chapter is based on work published in B. P. Tatman, W. T. Franks, S. P. Brown, J. R. Lewandowski, Nuclear spin diffusion under fast magic-angle spinning in solid-state NMR, **J. Chem. Phys.**, 2023, **158**, 184201.

4.1 Introduction

Spin diffusion is a reversible and coherent process through which spin order may be transferred via dipolar couplings in the solid state. In ^{1}H solid-state NMR at slow magic-angle spinning (MAS) frequencies, spin diffusion occurs in a manner analogous to macroscopic diffusion owing to the nucleus's low chemical shift dispersion and strong dipolar couplings. The spatial diffusional nature of this transfer has led to it being applied to the study of systems from materials[184] and biomaterials,[185,186] to small molecules[73,74,187] and proteins.[71,188] Additionally, spin diffusion plays an important role in dynamic nuclear polarisation NMR (DNP-NMR).[189–194] Recently, experimental methods relying on selective pulses to exploit the increased resolution at faster MAS and higher fields have been introduced. For example, selective pulses have found use in reducing t_1 noise,[195] in increasing the rate of experimental acquisition,[196] and in selectively investigating pharmaceuticals in the presence of excipients.[197] In addition, low power pulses with narrow bandwidth were used for

implementing chemical exchange saturation transfer (CEST) in the solid state[45,198] where spin diffusion may be an alternative mechanism to chemical exchange that needs to be considered.[124] Modelling spin diffusion transfer is of key importance to understanding the results of such experiments.

The spin dynamics at slow spinning frequencies have been shown to be adequately reconstructed using diffusion-based perturbation-theory simulation approaches.[72–74,80] In these studies, perturbation theory is used to derive rate expressions which are then used to model the system as a diffusive process.[75,76] It has even been shown that such models are able to solve crystal structures from known unit cell parameters to excellent precision.[72] However, with the increase in resolution obtained using higher MAS frequencies and higher magnetic fields, the assumption that spin diffusion may be treated in an entirely spatial manner begins to break down.[75,76,199] As an energy conserving process, it follows that spin diffusion between spins with dissimilar energy level separations (*i.e.*, different chemical shifts) is only possible if interacting with a spin energy bath, such as that provided by a dense dipolar coupled proton spin network. The decrease in spectral overlap with higher spinning frequencies arises because these dipolar coupling networks are more effectively averaged, and this combined with the larger energy level separations at higher magnetic fields means that spin diffusion becomes strongly dependent on the resonance offset between two spins. The importance of this resonance offset dependence was recently exemplified by Agarwal (2019),[200] where it was shown that, in proton spin-diffusion spectra of L-histidine HCl H_2O, negative cross peaks may be observed which relate to the interaction of four spins simultaneously, where the difference in differences between pairs of spins lead to a $n = 0$ rotational resonance transfer with inverse sign.

This four spin interaction effect would not arise in perturbation theory-/diffusion-based approaches, with the exception of qualitative models intended explicitly to study the effect.[201] Indeed, the majority of such models published to date either include the resonance offset through an exponential or gaussian approximation of a

zero-quantum lineshape,[80] or exclude it entirely.[72,74] Computational calculations in which the spin evolution of the density matrix is simulated under the spin Hamiltonian would, in theory, accurately reconstruct the coherent spin dynamics. Unfortunately, owing to their exponential scaling (the matrices scale $\propto 2^n$, where n is the number of spins), such simulations are typically restricted to systems with fewer than 12 spins.[80,202] As a result, they are unable to accurately model spin diffusion for which interactions with many more spins must be considered.

One approach which has been used to remedy this scaling problem is the use of restricted basis sets.[77,78,82,84,85] In such approaches, the number of basis sets states for which the evolution must be considered are drastically reduced by omitting those which can be assumed to contribute negligibly to the evolution of the spin system. Restricted basis set methods have been shown to enable accurate simulation of spin systems containing thousands of interacting spins.[190,203] Dumez *et al*. (2010)[78] introduced the Low-order Correlations in Liouville space (LCL) method, where only zero-quantum operators are considered, and product states are limited to those containing at most q interacting spins. Such an algorithm scales polynomially as n^q, and allows for the number of spins in simulations to be drastically increased. The LCL method was further developed by Perras and Pruski (2019) who introduced local restriction (LR-LCL),[85] where only the N closest spins to each spin were considered to be interacting resulting in a linear scaling algorithm ($\propto n \times N^{q-1}$). Such an approach has been applied to modelling DNP in systems containing thousands of atoms.[190,204] LR-LCL simulations are, however, considered to be accurate up to only ≈ 40 kHz MAS frequencies. This limitation arises due to the aforementioned increasing dependence on resonance offset and the chemical anisotropy. Though resonance offset was included in the LR-LCL model introduced by Perras *et al*. (2020),[190] this was included solely as an isotropic chemical shift.

Here, a new method for basis set selection is introduced and the method developed to include both isotropic and anisotropic chemical shift (chemical shift anisotropy, CSA). The effects of the full chemical shift, MAS frequency, magnetic field, and

dynamics on the evolution of the spin system are considered. Then, in Section 4.5, the impact of these findings on experimental spin diffusion is studied through the use of two case studies. Experimental results are shown for the dipeptide β-aspartyl L-alanine (β-AspAla), for which agreement with the simulated trends is found, but confounded by the presence of additional temperature-dependent behaviour, which may be indicative of an incoherent ^{1}H-^{1}H homonuclear nuclear Overhauser effect. Finally, it is shown that, in the case of a deuterated fully back-exchanged protein at 60 kHz MAS, the polarization transfer by spin diffusion is dominated by resonance offset.

4.2 Methods

4.2.1 Density Functional Theory

The crystal structure of β-AspAla (CCDC: FUMTEM)[205] was geometry optimized by DFT using CASTEP 16.1.[206–208] CASTEP implements density functional theory using a plane-wave basis set. The default CASTEP 16.1 ultrasoft pseudopotentials were used. The Perdew-Burke-Ernzerhof (PBE) implementation of the generalized gradient approximation was used as the exchange-correlation functional.[209] Plane waves up to 700 eV were used. The same cut-off energies were then used to determine magnetic resonance parameters using the GIPAW method[210–214] under the same DFT conditions to determine the CSA tensors, which were then extracted using Magresview.[215]

4.2.2 Spin-Diffusion Simulations

The 'Tourbillon' software introduced by Dumez *et al*. (2010)[77] was extended to include the basis-set selection method which will be introduced in Section 4.3.2, and to implement the use of an unordered map to store the density states as introduced by Perras and Pruski (2019).[85] Additionally, isotropic and anisotropic chemical shift evolution was implemented, along with the ability to output zero-quantum

lineshapes.

Spin diffusion simulations were performed using a complete unit cell of β-AspAla (4 molecules in the unit cell and 12 ^{1}H per molecule, *i.e.*, $n = 4 \times 12 = 48$ spins) using periodic boundary conditions. Unless otherwise stated, all simulations began with the inversion of all carboxylic acid protons (the site with the most separated ^{1}H NMR resonance), for which the interatomic distances and resonance offsets are shown in Table 4.1. This system is illustrated in Figure 4.1, where the spins of particular interest are color coded: Asp Hα (orange), the spatially closest proton to COOH; Ala NH (green), the closest in chemical shift to COOH; and Ala CH_3 (purple), for which there is particularly interesting spin evolution. In the case of the alanine CH_3, only one of the protons (labelled 12 in Table 4.1) was considered when plotting the trajectories as the evolution differs slightly between non-symmetrically equivalent sites. The spins are numbered 1–48, where the protons are numbered sequentially for each individual β-AspAla molecule, *i.e.*, molecule 1 is numbered 1–12, molecule 2 is numbered 13–24, etc. Experimental isotropic chemical shifts were used,[216] but the CSA tensors were calculated as described in Section 4.2.1. The rotational motion of the NH_3 and CH_3 groups was considered by assuming averaging of the chemical shift tensors in the molecular frame prior to conversion into the interaction frame for both of these sites, though no explicit averaging of dipolar couplings was considered unless indicated explicitly; the effect of dynamics on spin diffusion will be considered in Section 4.4.3.

Simulations were performed for $t_{\text{mix}} = 100$ ms (see Figure 4.2) using a REPULSION-48 set of crystallite orientations[217] and a timestep of 0.2 μs. Simulations were performed using the University of Warwick Scientific Computing Research Technology Platform (SCRTP) High Performance Computing clusters, on nodes consisting of two Intel Xeon 24 core processors giving 48 cores per node. Parallelism was implemented with each crystallite running in an individual thread using OpenMP. 192 GB of RAM was present per node, however in the case of some larger models, high memory nodes were used with up to 1.5 TB of RAM. Additional simulations using

Table 4.1: Nearest neighbour distances and resonance offsets between the carboxylic acid proton (COOH) and the other sites in β-AspAla. Spins of particular interest are in bold.

	Environment	Nearest distance to COOH /	Resonance Offset from COOH / ppm
1	Ala COOH	0.00	0.0
2	Asp NH_3^+	2.43	5.2
3	Asp NH_3^+	3.12	5.2
4	Asp NH_3^+	2.67	5.2
5	**Ala NH**	**4.04**	**4.6**
6	**Asp Hα**	**2.44**	**8.6**
7	Asp Hβ_2	4.06	9.9
8	Asp Hβ_3	3.45	10.6
9	Ala Hα	3.48	7.7
10	Ala CH_3	2.88	11.7
11	Ala CH_3	3.24	11.7
12	**Ala CH_3**	**3.96**	**11.7**

a REPULSION-128 set of crystallite orientations were performed using the HPC Midlands Tier 2 High Performance Computing cluster Sulis, on nodes containing two AMD EPYC 7742 (Rome) 2.25 GHz 64 core processors, giving 128 cores and 512 GB of RAM per node. There was no additional benefit to using more crystallites (see Figure 4.3).

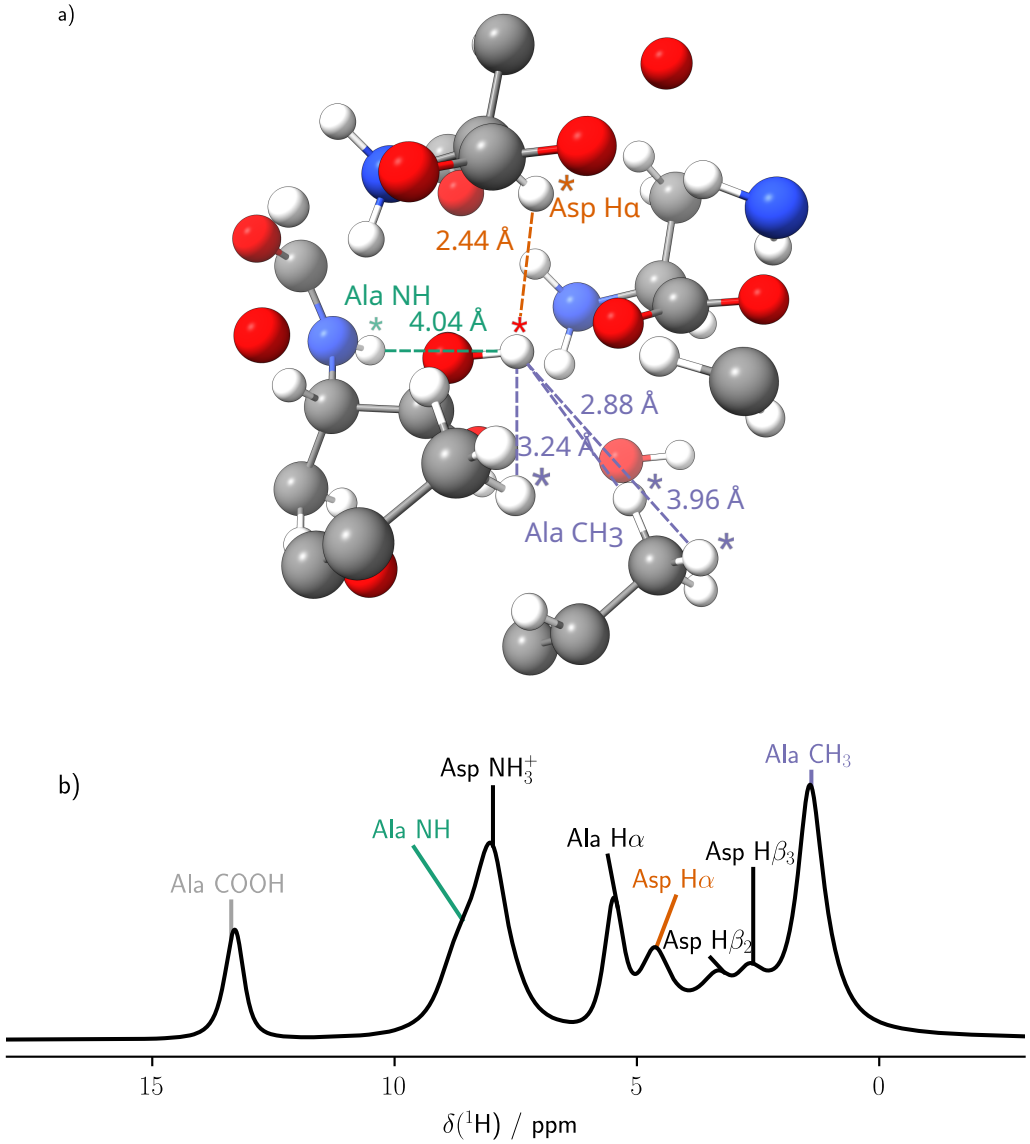

Figure 4.1: β-aspartyl L-alanine (β-AspAla), the model system used here. The spins of interest are highlighted in their respective colours. (a) a representation of the DFT (CASTEP) geometry-optimized structure, centered on one of the carboxylic acid protons. (b) a ^{1}H one-pulse MAS NMR spectrum acquired at a spinning frequency of 55 kHz and a ^{1}H Larmor frequency of 600 MHz. These spins were chosen to best illustrate various principles of this system: the Ala COOH (grey) is the most isolated resonance in the spectrum, and so the easiest to selectively invert/saturate experimentally without interfering with other sites; the Ala NH (green) site is the closest in chemical shift to Ala COOH; the Asp Hα (orange) is the closest in space to Ala COOH; the Ala CH_3 (purple) experiences 'inverse sign spin diffusion'.

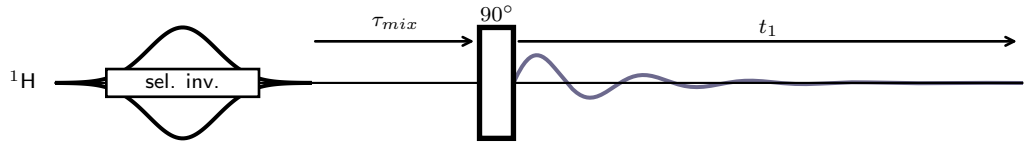

Figure 4.2: Effective pulse sequence used for simulations. In this, the first selective inversion pulse inverts one nuclear spin such that this is aligned along $-z$. During the mixing period, τ_{mix}, this longitudinal spin-order then diffuses between all spins involved in the simulation. After the 90° pulse, this magnetisation is then rotated along the transverse plane such that any spin-order formerly along $-z$ at the time of the 90° pulse would give a negative peak.

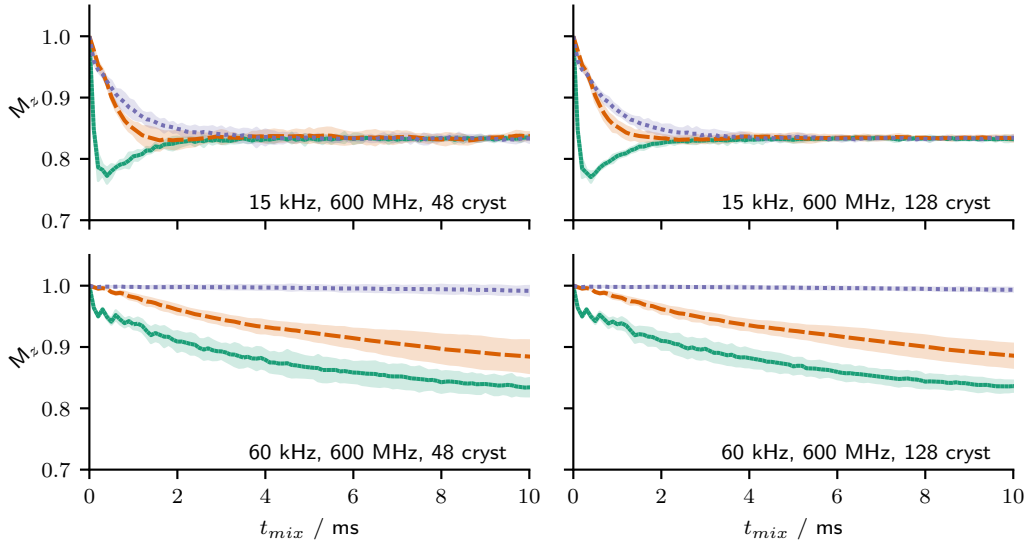

Figure 4.3: Comparison of the magnetisation transfer, monitored according to the ratio of the instantaneous calculated magnetisation to the equilibrium magnetisation (M_z), for models run with 48 and 128 crystallites. The rate at which spin diffusion from the inverted COOH to the respective sites (coloured as in Figure 4.1) may be seen by the rate at which the 'fully averaged' magnetisation of 83.3 % is achieved; for instance, it is apparent that there more rapid spin diffusion from the COOH to the Ala NH (green, solid) than the Ala CH_3 (purple, dotted) in all cases. Models were run with CSA at 60 kHz and 600 MHz. 48 crystallite simulations were performed using a HPC resource with 48 cores per node (2 Intel Xeon Platinum 8268 24-core processors), while 128 crystallite simulations were performed using 128-core nodes (2 AMD EPYC 7742 (Rome) 64-core processors).

4.2.3 Experimental Methods

4.2.3.1 Case Study 1: Incoherent Nuclear Overhauser Effect in β-aspartyl L-alanine (β-AspAla)

β-AspAla was purchased from Bachem (Switzerland) and packed as received into a 1.3 mm zirconia rotor. Spin diffusion experiments were performed using a 1.3 mm HXY probe operating in double resonance mode spinning at 55 kHz at a ^{1}H Larmor frequency of 599.5 MHz with a Bruker Avance Neo console. 1D proton spin diffusion (PSD) experiments[218] were performed in a manner analogous to saturation transfer difference methods in the solution-state,[219,220] using variable length 'trains' of gaussian inversion (180°) pulses for the saturation of the highest ppm resonance, the carboxylic acid resonance, at 13.1 ppm. Gaussian inversion pulses were optimized for a pulse length of 1.1 ms. Hard pulses were applied to ^{1}H with a nutation frequency of 100 kHz, corresponding to a 90° pulse length of 2.5 μs. The pulse sequence for this is shown in Figure 4.4. The number of inversion pulses applied was varied linearly from 0 to 100, with 8 coadded transients acquired per increment. A recycle delay of 2 seconds was used. The resulting data were then analysed by taking the intensities of each peak. Spectra were referenced according to the resonance offset for the methyl group used for simulations at 1.4 ppm.[216] Temperatures were calibrated using the chemical shift dependence on temperature of the ^{79}Br resonance in KBr.[221] 2D proton spin diffusion experiments were additionally performed at 60 kHz MAS at a ^{1}H Larmor frequency of 1 GHz with an Avance Neo console.

β-AspAla was also packed as received into a 1.6 mm zirconia rotor. Prior to inserting the top cap, a small 'plug' of KBr was inserted for temperature reference. Spin diffusion experiments were performed using a Phoenix 1.6 mm HXY probe operating in double resonance (^{1}H, ^{79}Br) mode spinning at 55 kHz at a ^{1}H Larmor frequency of 850 MHz with an Bruker Avance Neo console. Experiments were performed using inversion of the COOH, followed by a delay and then a background-compensated pulse sequence.[222] A pulse sequence for this is shown in Figure 4.5. At lower

temperatures the ^{1}H relaxation rate decreased and therefore longer recycle delays were required. A combination of this, the limited experimental time available, and the requirement for a background compensated pulse sequence,* means that the resulting data is significantly noisier than for the 600 MHz data also presented here.

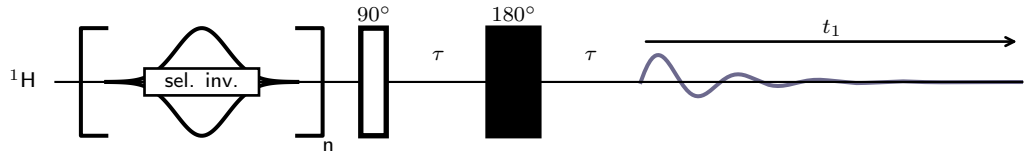

Figure 4.4: The pulse sequence used experimentally to probe spin diffusion in the 1.3 mm 1 GHz experiments. In this pulse sequence, the initial train of selective inversion pulses causes the magnetisation at the selected site (in this case, the Ala COOH) to tend to zero. During this period, spin diffusion causes magnetisation to transfer from other spins to the spin being saturated, and so the longitudinal magnetisation on these interacting spins will decrease. This is then followed by a 90° excitation and spin-echo, such that the intensity of the peaks in the resulting spectrum reflects the remaining longitudinal magnetisation on each site. The phase cycle was as follows: gaussian pulse $\{+y\}$, 90° $\{+x, -x\}$, 180° $\{+x, -x, +y, -y\}$, detect $\{+x, -x, -x, +x\}$.

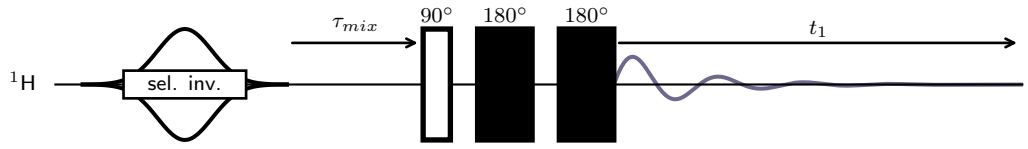

Figure 4.5: The pulse sequence used experimentally to probe spin diffusion in the 1.6 mm Variable Temperature 850 MHz experiments. In this pulse sequence, the selective inversion pulse inverts the longitudinal equilibrium magnetisation of a single site such that the ensemble magnetisation is aligned along $-z$. During the mixing period, τ_{mix}, spin diffusion causes spin order from interacting sites to transfer to this inverted site, leading to a reduction in their longitudinal magnetisation, M_z. Following this, a 90° pulse is applied to transfer this magnetisation into the transverse plane, followed by two phase cycled 180° pulses for background suppression. Finally, the signal is detected, where the intensity of each peak reflects the longitudinal magnetisation at the time of the 90° pulse. The phase cycle was as follows: gaussian pulse $\{+x\}$, 90° $\{4\{+x\}, 4\{+y\}, 4\{-x\}, 4\{-y\}\}$, 1st 180° $\{+x, +y, -x, -y\}$, 2nd 180° $\{4\{+x\}, 4\{-x\}, 4\{-y\}, 4\{+y\}\}$, detect $\{+x, -x, +x, -x, +y, -y, +y, -y\}$.

Recorded experimental spectra were integrated using a python script using both

*The probe experienced a significant ^{1}H background which could be removed by using a series of phase-cycled 180° pulses.

nmrglue[223] and lmfit[224] to fit a polynomial background and Lorentzian lineshapes to each peak. Following the optimization of the offset on the first slice, the offsets were fixed and only the peak height and width were allowed to vary.

4.2.3.2 Case Study 2: 600 MHz Spin Diffusion in U-[^{2}H,^{13}C,^{15}N]-GB1 at 60 kHz

Perdeuterated U-[^{2}H,^{13}C,^{15}N] GB1[†] with 100% back-exchanged amide ^{1}Hs was prepared as described in ref 225, and packed into a 1.3 mm zirconia rotor, sealed with silicon glue. Experiments were performed using the 1.3 mm HXY probe operating in triple resonance HCN mode spinning at 60 kHz. Cooling was applied to achieve a sample temperature of ≈ 300 K, as calibrated using the difference in shift between DSS and H_2O.[226] 2D ^{15}N-^{1}H-detected ^{1}H spin-diffusion experiments were performed in a manner analogous to saturation transfer difference methods in the solution-state[219,220] or CEST experiments.[198] Low powered (≈100 Hz) bandwidth saturation was applied for 500 ms, both on resonance with various N – H sites and off resonance. The pulse sequence for this is shown in Figure 4.6. 32 coadded transients were acquired for each of 128 t_1 FIDs, using States-TPPI in F_1 for sign discrimination and a 2 s recycle delay. Except for the saturation pulse, the ^{1}H transmitter was placed at 2.46 ppm with a spectral width of 39.7 ppm. The ^{15}N transmitter was placed at 120 ppm, with a spectral width of 54.9 ppm. Hard pulses were applied to ^{1}H with a nutation frequency of 100 kHz, corresponding to a 90° pulse length of 2.5 μs. On ^{15}N, hard pulses had a nutation frequency of 50 kHz, corresponding to a 90° pulse length of 5 μs. Cross-polarisation (CP) was applied with a 70:100% linear ramp[168] on ^{1}H, meeting the Hartmann-Hahn condition with 45 kHz on ^{1}H and 15 kHz on ^{15}N. This was applied for 800 μs for the ^{1}H – ^{15}N CP, and for 600 μs for the ^{15}N – ^{1}H CP. 100 ms MISSISSIPPI water saturation using 10 kHz ^{1}H irradiation was used.[169] Spectra were referenced according to DSS at 0 ppm, with ^{15}N referenced indirectly to liquid NH_3 at 0 ppm using the IUPAC recommended frequency ratio.[226,227] Low-powered ($\nu_1 = 10$ kHz) waltz-16 heteronuclear decoupling was applied to the ^{1}H channel

[†]The β_1 domain of Protein G, a 56 residue protein.

during ^{15}N evolution, and again to the ^{15}N channel during ^{1}H acquisition.[89] Peaks in 2D experimental spectra were integrated using CARA.[228] Assignments were taken from ref 169.

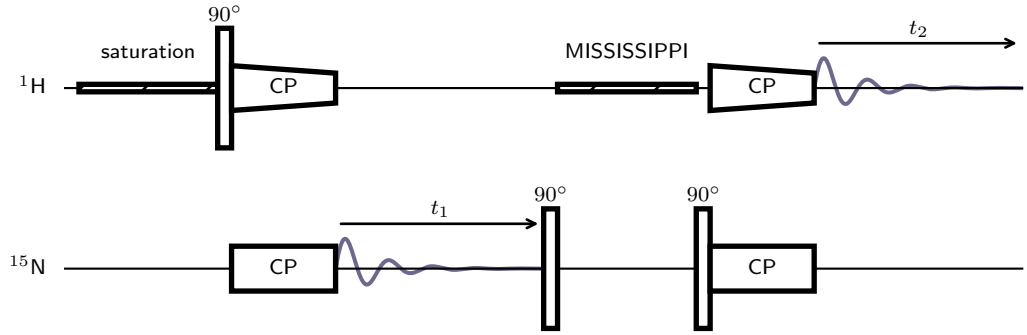

Figure 4.6: Pulse program used for experiments on protein samples where the additional ^{15}N dimension was necessary for resolution of different sites.

4.3 Theory

4.3.1 Low-Order Correlations in Liouville Space

A brief introduction to the LCL approach is given here, based on that presented by Brüschweiler *et al*. (1997),[229] Dumez *et al*. (2010),[77] and Perras and Pruski (2019).[85] For clarity, a full list of symbols and associated descriptions is given in Table 4.2. In Liouville space, the density matrix for a set of n spin-1/2 nuclei may be represented as a 4^n vector, consisting of elements

$$\hat{\boldsymbol{B}}_r = 2^{q-1} \prod_{i=1}^{n} \hat{\boldsymbol{I}}_{i,r}, \tag{4.1}$$

where $\hat{\boldsymbol{I}}_{i,r}$ represent single spin operators $\hat{\boldsymbol{I}}_{i,r} \in \left\{ \hat{\boldsymbol{E}}_i, \hat{\boldsymbol{I}}_{iz}, \hat{\boldsymbol{I}}_{i+}/\sqrt{2}, \hat{\boldsymbol{I}}_{i-}/\sqrt{2} \right\}$, and q represents the order of the product operator, that is, the number non-identity operators in the product operator, corresponding to the number of interacting spins.

The density matrix, $\hat{\boldsymbol{\sigma}}\left(t_{mix}\right)$ after a mixing time t_{mix}, is then a combination of these

Table 4.2: List of symbols used in this chapter.

Symbol	Meaning
q	Order of product operator (*i.e.*, number of non-identity operators in a product operator), corresponding to the number of interacting spins
$q_{\max}$	Maximum value of q considered in a model
n	Number of spins in a simulated system
N	Number of neighbour spins
$N_{\max}$	Maximum number of neighbour spins
N_{avg}	Average number of neighbour spins
$\hat{\underline{\boldsymbol{L}}}$	Liouvillian superoperator
t_{mix}	Length of simulation, corresponding to PSD mixing time (see Figure 4.2)
Δt	Length of an individual timestep
P	Number of timesteps (*i.e.*, $t_{mix}/\Delta t$)
S	Order parameter (*e.g.*, the S in S^2)
M_z	Ratio of z-magnetisation to equilibrium z-magnetisation
$\hat{\boldsymbol{I}}_{i,r}$	Single spin operator, *e.g.* one of $\hat{\boldsymbol{E}}_i, \hat{\boldsymbol{I}}_{iz}, \hat{\boldsymbol{I}}_{i+}/\sqrt{2}, \hat{\boldsymbol{I}}_{i-}/\sqrt{2}$
$\hat{\boldsymbol{\sigma}}$	Density matrix
$\hat{\boldsymbol{B}}_r$	Arbitrary product operator, defined as in equation 4.1

elements

$$\hat{\boldsymbol{\sigma}}(t_{mix}) = \sum_r b_r(t_{mix})\hat{\boldsymbol{B}}_r, \tag{4.2}$$

which may be propagated under the action of the Liouvillian superoperator, $\hat{\underline{\boldsymbol{L}}}$

$$\hat{\boldsymbol{\sigma}}(t_{mix}) = \exp\left(-i\int_0^t \hat{\underline{\boldsymbol{L}}}(t_{mix})dt\right)\hat{\boldsymbol{\sigma}}(0). \tag{4.3}$$

This propagation may be approximated by considering the Liouvillian to be piecewise time independent

$$\hat{\boldsymbol{\sigma}}(t_{mix}) = \prod_{p=0}^{P-1} \exp\left(-i\Delta t\hat{\underline{\boldsymbol{L}}}(p\Delta t)\right)\hat{\boldsymbol{\sigma}}(0), \tag{4.4}$$

where Δt is a small step such that $P \times \Delta t = t_{mix}$.

The low-order correlation in Liouville (LCL) method relies on basis set reduction

by excluding certain terms.[77–79,230] For the simulation of spin diffusion the most obvious terms to omit are those which are not zero-quantum since spin diffusion is fundamentally a zero-quantum process.[75,76] Further basis set reduction can be performed, as considered below in Section 4.3.2.

Owing to the very large size of the full Liouvillian, $\hat{\underline{\underline{\boldsymbol{L}}}}$, the first-order Suzuki-Trotter algorithm[231] was used, as utilized by both Dumez *et al*. (2010)[77] and Perras and Pruski (2019)[85] This enables the density matrix evolution to be calculated piecewise, without requiring storage of the full Liouvillian. Namely,

$$\hat{\boldsymbol{\sigma}}_{p+1}(\tau+\Delta t) = \left(\prod_{i=1}^{n} \prod_{j=\text{neighbour}(i)}^{\text{neighbours},j>i} \exp\left(i\hat{\underline{\underline{\boldsymbol{L}}}}_{i,j}(p\Delta t)\Delta t \right) \right) \hat{\boldsymbol{\sigma}}(\tau), \tag{4.5}$$

where the inner product represents the product over all states considered to be 'neighbours' of spin i, noting that, in the case of the basis set methods used here, these are not necessarily the most spatially proximate sites (see Section 4.3.2). Higher-order Suzuki-Trotter algorithms were not applied since these double the computational time and were found not to change the results of the simulation.

The $\exp\left(i\hat{\underline{\underline{\boldsymbol{L}}}}_{i,j}(p\Delta t)\Delta t \right)$ terms in equation 4.5 are evaluated sequentially using the cog-wheel approach of Brüschweiler and Ernst (1997).[229] Under a dipolar coupling, $\omega_{D,i,j}(t)$, subspaces of the form $\left\{ \hat{\boldsymbol{I}}_{iz}\hat{\boldsymbol{B}}_r,\ \hat{\boldsymbol{I}}_{jz}\hat{\boldsymbol{B}}_r, \hat{\boldsymbol{I}}_{i+}\hat{\boldsymbol{I}}_{j-}\hat{\boldsymbol{B}}_r, \hat{\boldsymbol{I}}_{i-}\hat{\boldsymbol{I}}_{j+}\hat{\boldsymbol{B}}_r \right\}$ (where $\hat{\boldsymbol{B}}_r$ does not include spins i or j, and must be such that the total product operator formed is zero-quantum in nature) evolve under the effect of the following rotation

$$\hat{\underline{\underline{\boldsymbol{R}}}}_{0,i,j} = \frac{1}{2} \begin{bmatrix} 1+c & 1-c & -is & is \\ 1-c & 1+c & is & -is \\ -is & is & 1+c & 1-c \\ is & -is & 1-c & 1+c \end{bmatrix}, \tag{4.6}$$

where $c = \cos(\omega_{D,i,j}(p\Delta t)\Delta t)$ and $s = \sin(\omega_{D,i,j}(p\Delta)t\Delta t)$. An example subspace may be $\left\{ \hat{\boldsymbol{I}}_{1z}\hat{\boldsymbol{I}}_{3z}, \hat{\boldsymbol{I}}_{2z}\hat{\boldsymbol{I}}_{3z}, \hat{\boldsymbol{I}}_{1+}\hat{\boldsymbol{I}}_{2-}\hat{\boldsymbol{I}}_{3z}, \hat{\boldsymbol{I}}_{1-}\hat{\boldsymbol{I}}_{2+}\hat{\boldsymbol{I}}_{3z} \right\}$, where $\hat{\boldsymbol{B}}_r = \hat{\boldsymbol{I}}_{3z}$,

which would evolve under the rotation $\hat{\hat{\underline{\boldsymbol{R}}}}_{0,1,2}$. Subspaces of the form $\left\{\hat{\boldsymbol{I}}_{i\pm}\hat{\boldsymbol{B}}_r,\ \hat{\boldsymbol{I}}_{j\pm}\hat{\boldsymbol{B}}_r, \hat{\boldsymbol{I}}_{i\pm}\hat{\boldsymbol{I}}_{jz}\hat{\boldsymbol{B}}_r, \hat{\boldsymbol{I}}_{iz}\hat{\boldsymbol{I}}_{j\pm}\hat{\boldsymbol{B}}_r\right\}$ evolve under the rotation

$$\hat{\hat{\underline{\boldsymbol{R}}}}_{\pm,i,j} = \begin{bmatrix} cch & -ssh & \mp isch & \mp icsh \\ -ssh & cch & \mp icsh & \mp isch \\ \mp isch & \mp icsh & cch & -ssh \\ \mp icsh & \mp isch & -ssh & cch \end{bmatrix}, \tag{4.7}$$

where the additional trigonometric functions on $\Delta t/2$ are distinguished by 'h' for half as $ch = \cos(\omega_{D,i,j}(p\Delta t)\Delta t/2)$, $sh = \sin(\omega_{D,i,j}(p\Delta t)\Delta t/2)$. For example, $\left\{\hat{\boldsymbol{I}}_{1+}\hat{\boldsymbol{I}}_{3-},\ \hat{\boldsymbol{I}}_{2+}\hat{\boldsymbol{I}}_{3-}, \hat{\boldsymbol{I}}_{1+}\hat{\boldsymbol{I}}_{2z}\hat{\boldsymbol{I}}_{3-}, \hat{\boldsymbol{I}}_{1z}\hat{\boldsymbol{I}}_{2+}\hat{\boldsymbol{I}}_{3-}\right\}$, where $\hat{\boldsymbol{B}}_r = \hat{\boldsymbol{I}}_{3-}$, would evolve under the rotation $\hat{\hat{\underline{\boldsymbol{R}}}}_{+,1,2}$. It should be noted that this rotation would not be performed were $\hat{\boldsymbol{B}}_r = \hat{\boldsymbol{I}}_{3z}$, as this would form non-zero-quantum product operators. The same operator may evolve under several rotations; it is the sequential application of these rotations which gives rise to the variation in evolution for symmetrically equivalent sites in the model here (which has been used as an estimate of numerical uncertainty).

Under MAS, the dipolar coupling is calculated in a time dependent fashion as

$$\omega_{D,i,j}(t) = R_{DD,i,j} \sum_{m=-2}^{2} \sum_{m'=-2}^{2} D^2_{0,m}(\Omega_{PC}) D^2_{m,m'}(\Omega_{CR}) D^2_{m',0}(\Omega_{RL}(t)), \tag{4.8}$$

where Ω_{PC} is the change in orientation going from the principal axis system of the dipolar interaction to the crystallite frame, and Ω_{CR} relates this crystallite frame to the rotor frame (that is, the powder crystallites). Finally, $\Omega_{RL}(t)$ is the time dependent (under rotation) conversion from the rotor frame to the laboratory frame. The dipolar coupling constant, $R_{DD,i,j}$, is given in equation 2.100, repeated here:

$$R_{DD,i,j} = -\left(\frac{\mu_0}{4\pi}\right)\left(\frac{\gamma_i\gamma_j h}{2\pi}\right)\langle r^{-3}_{i,j}\rangle, \tag{4.9}$$

in units of rad s^{-1}. The evolution under chemical shift (see Section 2.1.2.3) is treated in an analogous manner. The time-dependent chemical shift is calculated as

$$\delta_{CS,i}(t) = \delta_{iso} + \sqrt{\frac{2}{3}} \sum_{l=-2}^{2} \delta_{CS,i}^{(l)} \sum_{m=-2}^{2} \sum_{m'=-2}^{2} D_{l,m}^{2}(\Omega_{PC}) D_{m,m'}^{2}(\Omega_{CR}) D_{m',0}^{2}(\Omega_{RL}(t)), \tag{4.10}$$

with

$$\delta_{CS,i}^{(p)} = \begin{cases} -\frac{1}{2}\eta\delta_{aniso} & \text{if } p = \pm 2 \\ 0 & \text{if } p = \pm 1 \\ \sqrt{\frac{3}{2}}\delta_{aniso} & \text{if } p = 0 \end{cases}, \tag{4.11}$$

where δ_{iso} is the isotropic chemical shift (in ppm), δ_{aniso} the anisotropic chemical shift (in ppm), and η is the chemical shift anisotropy.[81,232] These are obtained from the diagonalised chemical shift tensor $\underline{\boldsymbol{\delta}}$ components, δ_{xx}, δ_{yy}, and δ_{zz} as given in equation 2.94 and discussed in Section 2.1.2.3.

The evolution under the chemical shift is then considered for any product operator of the form $\hat{\boldsymbol{I}}_{i\pm}\hat{\boldsymbol{B}}_r$, as

$$b_{i\pm,r}(\tau + \Delta t) = \exp(\pm i 2\pi \delta_{CS,i}(\tau) B_{Hz/ppm} \Delta t) b_{i\pm,r}(\tau), \tag{4.12}$$

where $B_{Hz/ppm}$ is the magnetic field strength in units of Hz ppm^{-1}, *e.g.* 599.5 Hz ppm^{-1} for a ^{1}H Larmor frequency of 599.5 MHz, and $b_{i\pm,r}(t)$ is the contribution of the product operator $\hat{\boldsymbol{I}}_{i\pm}\hat{\boldsymbol{B}}_r$ to the density matrix as defined in equation 4.2. Computationally, these were implemented sequentially such that, for each timestep, the dipolar evolution under equations 4.6 and 4.7 was applied first, followed by the chemical shift evolution under equation 4.12.

4.3.2 Basis Set Selection

Ideally, all spin interactions would be included within the basis-set. Such a simulation, akin to a full density matrix treatment as implemented by SIMPSON[81,233,234] and SpinEvolution,[235] would scale exponentially ($\propto 2^{3n}$ assuming Hilbert space simulations).[234] To reduce the complexity of the problem, the simulation can be approximated using a reduced basis set. Edwards *et al*. (2014)[203] introduced three basis sets for the solution state which aim to reduce the number of terms which must be included: IK-0, in which only product operator states consisting of a given number of spins are considered; IK-2, in which only product operator states containing spins which are close in proximity are included; and IK-1, where both criteria are applied. In the solid state, the analogous restricted basis sets used by Dumez *et al*. (2010) correspond to an IK-0 basis set.[77] The local restriction introduced by Perras and Pruski (2019) further develops this into an IK-1 basis set.[85] The computational complexity of the locally restricted low-order correlations in Liouville space model is approximately given by

$$\text{complexity} \ \propto P \times n \times N_{\max}^{q-1} \tag{4.13}$$

where P ($= t_{mix}/\Delta t$) represents the number of time steps which must be calculated, n is the number of spins in total, and $N_{\max}$ is the number of spin neighbours considered per spin. In the case of the original LCL algorithm (*i.e.*, $N_{\max} \rightarrow n - 1$), the complexity goes as n^q, that is, it will scale polynomially. On the other hand, introducing local restriction ensures that $N_{\max}$ is independent of n. The complexity then scales linearly in n. The choice of $N_{\max}$ is important for such linear scaling models because including too few spin pairs will lead to the simulation not adequately recreating the dynamics of a larger model, while including too many will not be an efficient use of computational time. In Figure 4.7a, it can be seen that at least 16 spin pairs per spin are required to recreate the spin dynamics, while in Figure 4.7b, increasing the average number of spin neighbours (note N_{avg}; the

difference between this and $N_{\max}$ will be discussed below in the description of the computational implementation) leads to a polynomially greater computational time. Therefore, on average 16 spin pairs per spin have been included, in good agreement to the 15 found to be optimal by Perras and Pruski (2019) who found that ≈15 spin pairs per spin were able to recreate spin diffusion well in their system, a linear alkane.[85]

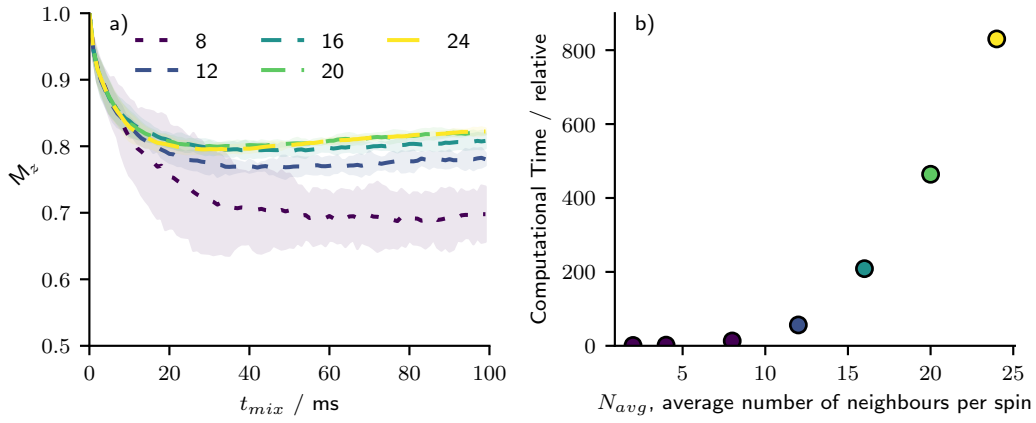

Figure 4.7: Simulations of the pulse sequence in Figure 4.2 applied to the β-AspAla unit cell (n = 48) at $\nu_r = 60$ kHz, $\nu_0(^1\text{H})$ = 600 MHz, with a variable basis set size (N_{avg}, approximate number of neighbours per spin). (a) The evolution of the z magnetisation, M_z, for one of the Asp NH_3 spins after inversion of the carboxylic acid proton. The spread about the lines indicates twice the standard deviation for all symmetry equivalents. (b) The computational time required to run a model of each size, relative to the model with $N_{avg} = 2$. The simulated z-magnetisation evolution rapidly converges, with a basis set consisting of on average 16 spin neighbours per spin approximating well a system containing an average of 24 spin neighbours. Only up to a spin system containing 24 spin neighbours per spin were considered, as above this was not computationally feasible.

In the modelling here, product operator states were limited to those containing at most $q = 4$ spins, an upper limit which has been shown to allow for accurate simulation when compared to exact simulation at slower spinning.[79] While a larger value of $q_{\max}$ may model the spin evolution better,[77,78] such a larger basis set is infeasible. The faster spinning frequencies modelled here mean that the rotor cycle time is shorter and therefore more steps are required to sample the rotation adequately for any given time, and additionally the slower rate of spin diffusion means that longer times must be simulated. A significantly larger absolute number

of steps, P, therefore needs to be calculated. As such, given the exponential scaling nature of q (see equation 4.13) it is not feasible to simulate with larger product operators included.

A method for selecting which spin pairs contribute significantly is necessary to perform a basis set reduction in spin space. It has been shown that applying spatial restrictions (*i.e.*, selecting the $N_{\max}$ closest spins) to the choice of spin states to include is valid[82,85,203] when the evolution of the spin dynamics are determined predominantly by through-bond J-couplings (as in solution-state NMR) or dipolar couplings in the presence of a strongly coupled spin bath (as at slow spinning frequencies). However, this assumption begins to fail for solid-state NMR in the fast-spinning regime. At attainable fast spinning frequencies, the dipolar couplings are not averaged to zero as in the solution-state, but are averaged sufficiently to make the transfer of magnetisation strongly truncated by resonance offset. To consider this transition from slow to fast MAS, here a method is introduced in which a short simulation is performed including all spin pairs, where the basis set is restricted to product operators containing $q \leq 4$ spins. A score is then calculated for each spin pair, based on the population of all spin operators which include both spins

$$\text{score}_{i,j} = W_2 \sum b_{i,j}(t) + W_3 \sum_k b_{i,j,k}(t) + W_4 \sum_{k,l} b_{i,j,k,l}(t), \tag{4.14}$$

where W_n is a weighting to ensure that all spin orders contribute equally, and $b_p(t)$ refers to the population of spin states made up of the spins within the set p.[‡] Weighting is necessary, as there are n times as many four-spin states as there are three-spin states, and n times as many three-spin states as two-spin states. While, in principle, the relative contribution of these is also a function of the spinning frequency, this is an emergent property of the simulation and so had not been considered in the calculations here. Figure 4.8 shows that the contributions of these states no longer significantly vary such that they would lead to different spin interactions giving a

[‡]Note that the summation is over all matching spin states. For example, the first term ($\sum b_{i,j}$) is the sum over all i,j two-spin zero-quantum operators — $\hat{\underline{\boldsymbol{I}}}_{iz}\hat{\underline{\boldsymbol{I}}}_{jz}$, $\hat{\underline{\boldsymbol{I}}}_{i+}\hat{\underline{\boldsymbol{I}}}_{j-}$, $\hat{\underline{\boldsymbol{I}}}_{i-}\hat{\underline{\boldsymbol{I}}}_{j+}$.

greater contribution after 0.1 ms; in the modelling performed here, these simulations were performed for 0.2 ms. Our selection method corresponds to ordering the spin pairs from the highest score to lowest score and selecting the $n \times N_{avg}$ highest scoring spin pairs to include in the basis set, thereby including only the states which contribute the most to the spin evolution. These spin pairs which contribute the most are not necessarily those closest in proximity; Figure 4.9 shows the magnitude of the score in equation 4.14 as a function of distance and resonance offset for a methyl group proton (spin-10 in Table 4.1), where there is no clear dependence on either parameter. The spatial arrangement of these included spins are then shown in Figure 4.10 for this methyl group proton at $\nu_r = 20$ kHz and $\nu_0(^1\text{H})$ = 600 MHz.

Note here that the average number of spin neighbours per spin (N_{avg}) is used, as opposed to a fixed number of spin neighbours per spin ($N_{\max}$). This is because, when ordering the spin pairs by score, it is found that some spins are generally more important to the evolution of other spins; for example, the carboxylic acid protons are inverted at the start of the simulations and, as a result, have the greatest magnetisation gradient with their neighbours and therefore tend to have a much larger contribution to many other spins. This is seen in Figure 4.11, where generally the carboxylic acid protons (grey) are found to contribute more to the spin evolution of far more other spins than is the case for the CH_3 protons (purple). This is also evident in Figure 4.9 where the biggest circles (highest scores) are at the greatest resonance offset. At faster magic-angle spinning frequencies, the relative spin pair scores change, as shown in Figure 4.9, leading to a different basis set selection thereby making different spin pairs contribute more or less as in Figure 4.11. For example, two spins which are spatially proximate but well separate in resonance frequency will contribute more at lower spinning frequencies, but with the truncation of resonance offset at faster spinning frequencies will consequently contribute less, and therefore be less likely to be included. This has important consequences for the evolution of the spin system, as will be discussed in the following sections.

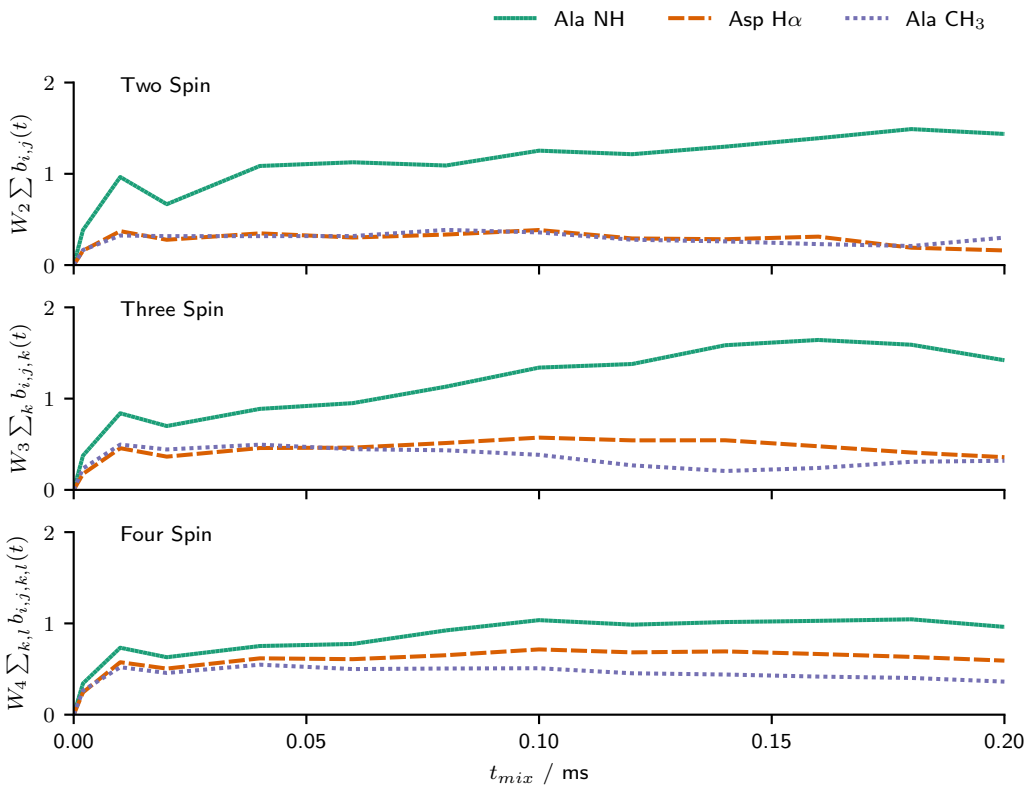

Figure 4.8: Spin-pair interaction scores as calculated using equation 4.14 over a representative simulation of the pulse sequence in Figure 4.2 including all spin pairs at $\nu_r = 60$ kHz, $\nu_0(^1\text{H})$ = 600 MHz, beginning with inversion of the carboxylic acid proton. LCL simulations without restriction are run for 1000 steps (0.2 ms), with the weighted population of two, three, and four spin states plotted above. Spin pairs involving the COOH and the Ala NH, Asp Hα, and Ala CH_3 in β-AspAla are shown in green (solid), orange (dashed), and purple (dotted), respectively (see Figure 4.1 and Table 4.1). Beyond approximately 0.1 ms, the contribution of the 2, 3, or 4 spin states no longer significantly change such that the ordering of which spin interactions to include is likely fixed at this point.

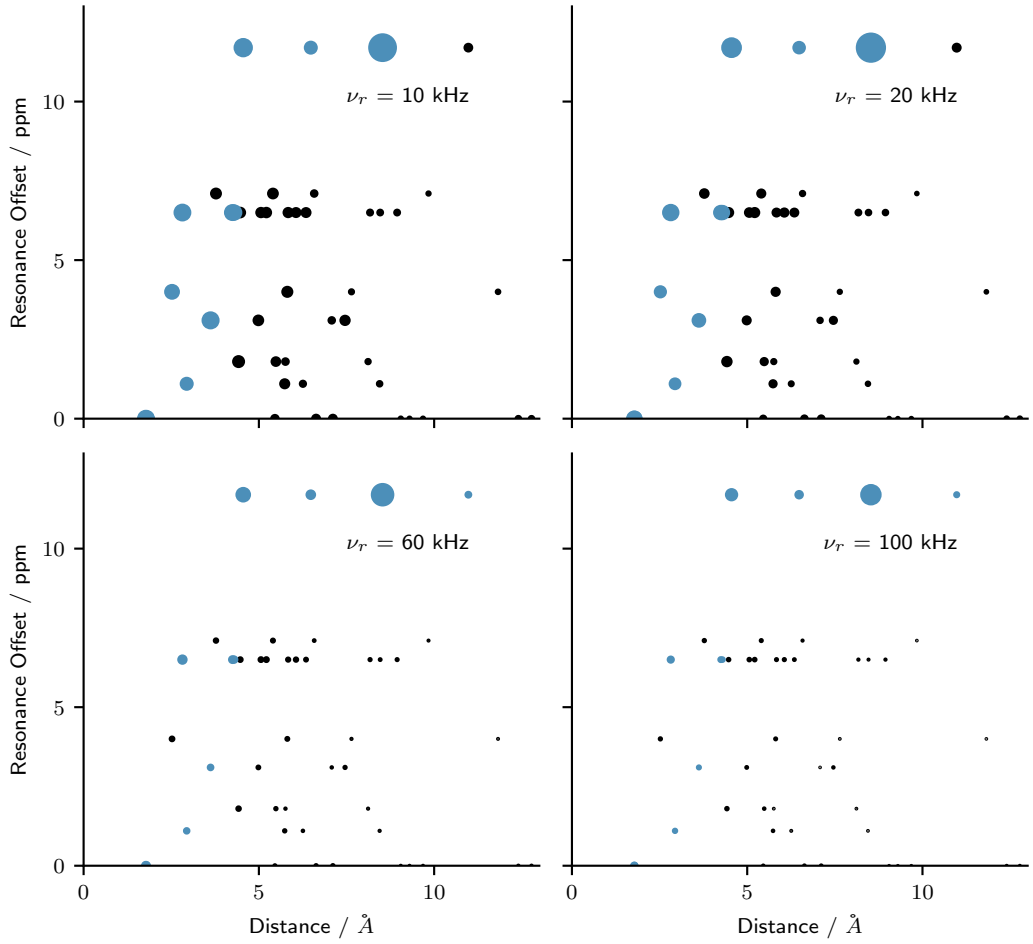

Figure 4.9: Basis set selection according to the method outlined in Section 4.3.2 for the pulse sequence in Figure 4.2 starting with COOH resonance inversion at the indicated spinning frequencies ($\nu_0(^1\text{H})$ = 600 MHz), as a function of their resonance offset and distance from spin-10, a CH_3 proton in molecule 1. The size of each point represents the score as in equation 4.14, *i.e.*, the sum of the weighted 2, 3, and 4 spin terms. Spins which were included as 'neighbours' to the spin of interest by restricting the the average number of spin neighbours per spin, N_{avg}, to 16 are shown highlighted in blue, while spins which were not included as neighbours are shown in black. The number of 'neighbours' included per spin are shown in Figure 4.11. The spatial arrangement of the spin pairs included for the 20 kHz simulation are shown in Figure 4.10.

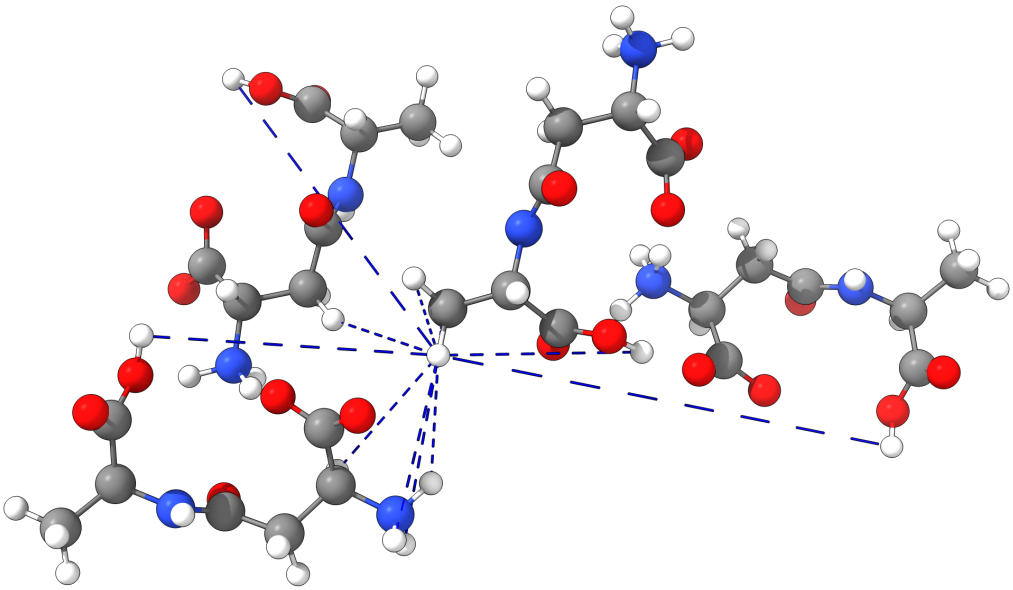

Figure 4.10: Spin interactions included in simulation involving spin-10, a CH_3 proton in molecule 1 (see Table 4.1), at $\nu_r = 20$ kHz and $\nu_0(^1H)$ = 600 MHz. These correspond to spins highlighted in blue in panel 2 of Figure 4.9.

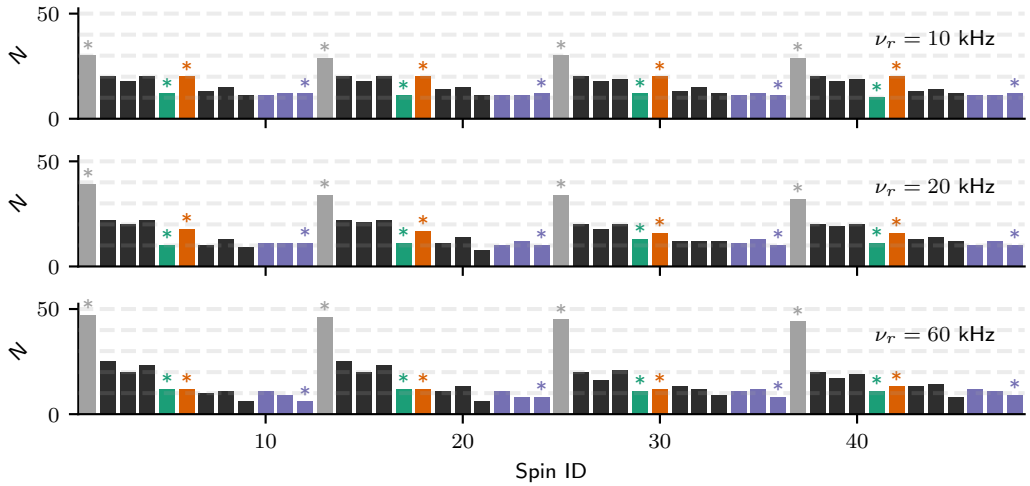

Figure 4.11: Number of neighbouring spin pairs selected for $N_{avg} = 16$ as a function of the Spin ID of interest for three different spinning frequencies, for simulations of the pulse sequence in Figure 4.2 at 600 MHz, beginning with inversion of the carboxylic acid proton resonance (grey), with chemical shift anisotropy included and no dipolar averaging. Colours are as in Figure 4.1, and sites with asterisks are those which are used in the following plots. The spin IDs are as given in Table 4.1, noting that the unit cell contains 4 symmetry equivalent molecules (1–12, 13–24, 25–36, 37–48).

4.4 Results and Discussion

4.4.1 Effect of Resonance Offset on Spin Diffusion

The chemical shift of a spin relates to how the local environment changes the effective magnetic field experienced by that spin, and therefore the change in the difference in energy between the spin-up and spin-down states. Spin diffusion, being an energy conserving diffusion of spin order between sites, is therefore truncated by the offset between two resonances, corresponding to two chemically distinct sites in the solid-state structure. Dipolar couplings to the large proton bath provide an external reservoir of energy to allow for spin diffusion to occur, as apparent by the broad overlapping peaks in ^{1}H solid-state NMR spectra. In the limit of low magnetic fields and low spinning frequencies, the contribution from this spin bath is sufficient to ensure that the rapid magnetisation transfer between different spins occurs in an approximately spatial manner (*i.e.* that the efficiency of the polarisation transfer is approximately related to the distance between spins).[72,80]

With faster magic-angle spinning and higher magnetic fields, however, the spatial nature of this transfer begins to break down. Figure 4.12 shows the effect of including both isotropic and anisotropic chemical shift in the spin diffusion model presented here. It is notable that, in the absence of isotropic or anisotropic chemical shift (red dashed lines), the reduction in the rate of spin diffusion is negligible as higher spinning frequencies are attained, as seen by comparing with the blue dotted lines for purely dipolar spin diffusion. This suggests that truncation by resonance offset dominates the reduction in spin diffusion as opposed than the direct averaging of the dipolar couplings.

Figure 4.12 further exemplifies the importance of including not only the isotropic component of the chemical shift tensor, but also the anisotropic component. In the absence of anisotropic chemical shift, it appears that the rate of spin diffusion is further reduced as the anisotropic component of the chemical shift tensor commutes with the homonuclear dipolar interactions and so aids the spin diffusion. The

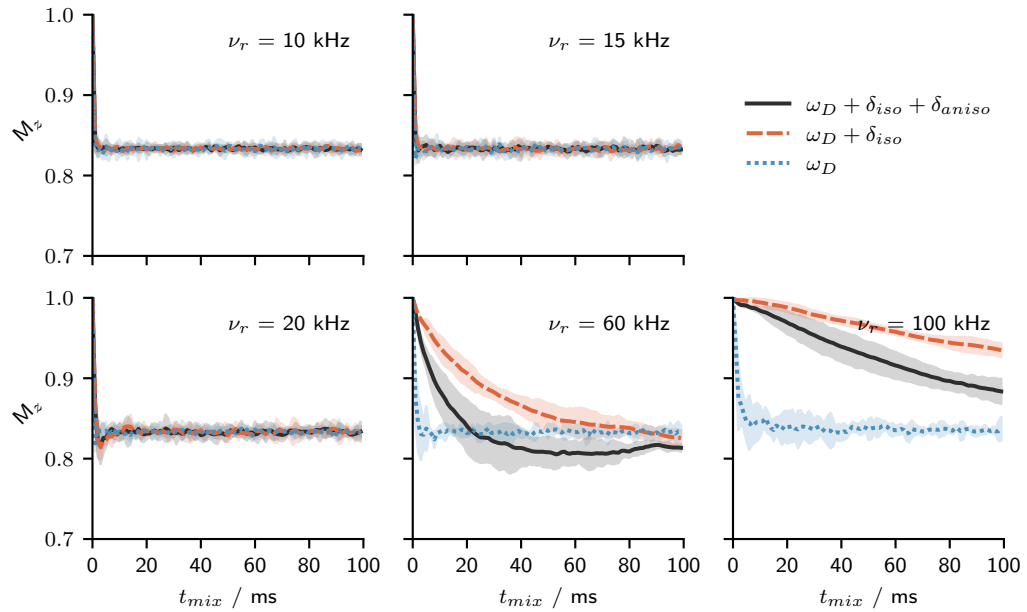

Figure 4.12: Simulated effect of adding both isotropic and anisotropic chemical shift to the employed LCL model, as a function of spinning frequency, at $\nu_0(^1\text{H})$ = 600 MHz, for a unit cell of β-AspAla ($n = 48$) with periodic boundary conditions. The evolution of the ratio of the instantaneous magnetisation to the equilibrium magnetisation, M_z, is shown for the Ala NH (spin 5 in Table 4.1), after inversion of the COOH proton resonance (see pulse sequence in Figure 4.2).

increasing dependence of spin diffusion on resonance offset between sites may also be seen in Figure 4.13. Here, the transfer of magnetisation for the Ala NH (4.6 ppm offset from COOH), Asp Hα (8.6 ppm offset), and an Ala CH_3 proton (11.7 ppm offset) is shown as a function of spinning frequency (10 to 150 kHz) and magnetic field (^{1}H Larmor frequencies of 100 MHz, 600 MHz, and 1 GHz). At 100 MHz, it may be seen that there is little truncation due to offset even for high spinning frequencies ($\approx$ 60 kHz) indicating little isotropic chemical shift resolution even at these higher spinning frequencies. This is exemplified by comparison between 20 kHz MAS at 1 GHz and 60 kHz MAS at 100 MHz, where the rate of transfer appears qualitatively similar. At 1 GHz, spinning frequencies greater than 100 kHz would be expected to severely truncate coherent spin diffusion.

Coherent inverse-sign spin diffusion, as observed in L-histidine HCl H_2O at 60 kHz at 500 and 700 MHz,[200] is also seen. In these simulations, such spin diffusion is

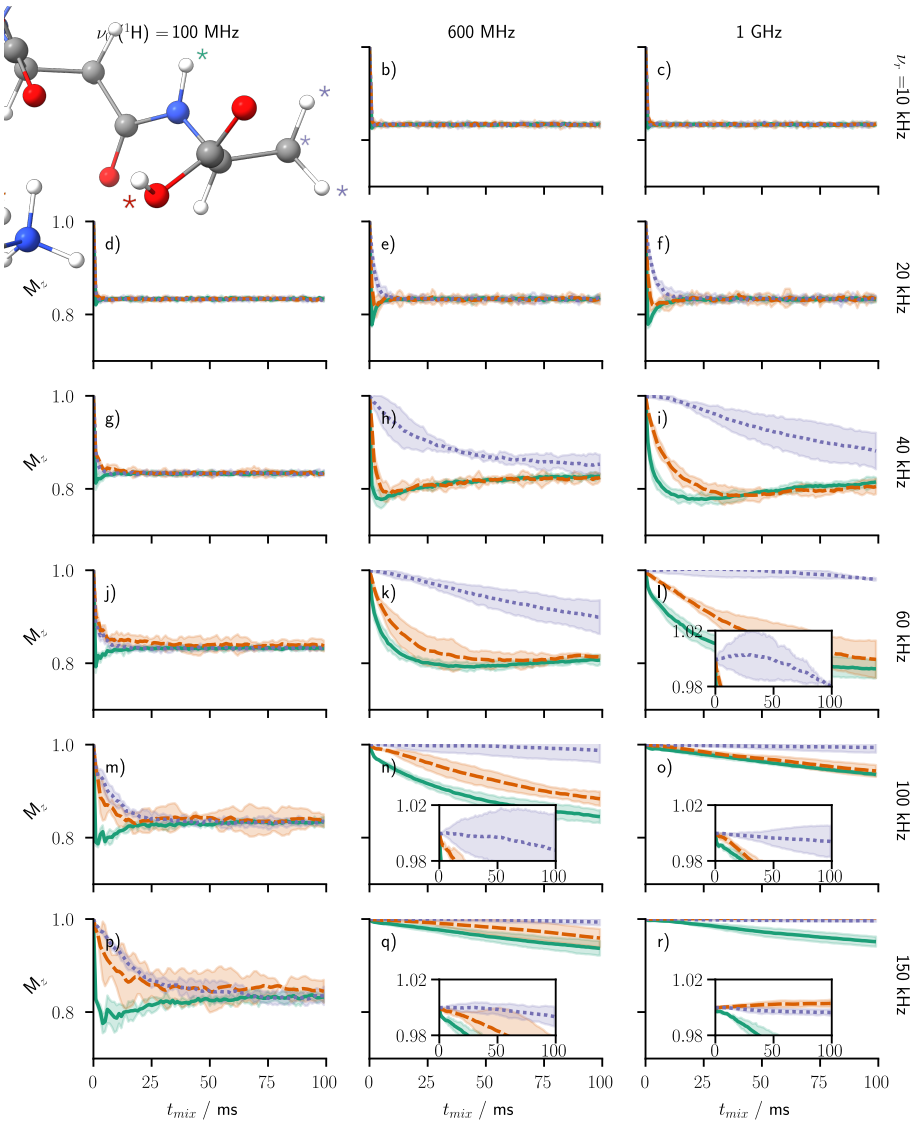

Figure 4.13: Simulated effect of the spinning frequency and applied magnetic field (given as ^{1}H Larmor frequency) on the rate of spin diffusion after inversion of the COOH proton (see pulse sequence in Figure 4.2). Simulations were performed for a full unit cell of β-AspAla ($n = 48$), with periodic boundary conditions, in the absence of dipolar averaging. Colours are matched with Figure 4.1, *i.e.*, solid green (Ala NH), dashed orange (Asp Hα), dotted purple (Ala CH_3) (see also Table 4.1). Left to right: $\nu_0(^1H)$ = 100 MHz, 600 MHz, 1 GHz. Top to bottom: $\nu_r = 10$ kHz, 20 kHz, 40 kHz, 60 kHz, 100 kHz, 150 kHz. The spread around each line corresponds to twice the standard deviation of all four equivalent spins in the system. This error increases at higher spinning frequencies likely due to faster MAS giving shorter rotor cycle times and therefore sparser sampling of the evolution of anisotropic chemical shift and dipolar couplings under MAS (noting that a timestep of 0.2 μs was used for all simulations).

manifested by the magnetisation associated with a site increasing, *e.g.* $M_z > 1$, as is evident for the inset axes on Figure 4.13 (l, n, o, q, and q). This is expected to occur when four interacting spins, I, S, R, and P, meet a resonance condition of $(\omega_I - \omega_S) - (\omega_R - \omega_P) = 0$. In this system, it is likely that the Ala COOH (13.1 ppm), Ala NH (8.5 ppm), Ala Hα (5.4 ppm), and Ala CH_3 (1.4 ppm) protons meet this four-spin resonance condition, as $8.5 - 1.4 = 7.1 \approx 13.1 - 5.4 = 7.7$. It is found to be particularly relevant in this system for the methyl protons (purple) at spinning frequencies >60 kHz at 1 GHz, and >100 kHz at 600 MHz; a more thorough analysis will be discussed in Section 4.4.3 and Section 4.5.1.

4.4.2 Relation to Perturbation Approaches

Whilst the restricted basis set low-order correlation in Liouville space model used here is orders of magnitude faster than simulating the complete evolution of the full density matrix, it is still far slower than perturbation theory diffusion equation-based approaches. As such, relating the resonance offset dependence here to these methods is of interest to the broader applicability of such models at faster spinning frequencies. Kubo and McDowell (1988) give an equation for the dependence of the rate of spin diffusion on the dipolar couplings and the resonance offset (via the 'zero-quantum lineshape') under MAS (their equation 25).[76] Their equation is reproduced here:

$$R_{SD}^{D} = \frac{1}{T_{SD}^{D}} \tag{4.15}$$

$$= \frac{R_{DD,i,j}^{2}}{15} \left\{ \left[K_{R_y}(\omega_r) + K_{R_y}(-\omega_r) \right] + \frac{1}{2} \left[K_{R_y}(2\omega_r) + K_{R_y}(-2\omega_r) \right] \right\}, \tag{4.16}$$

where $K_{R_y}(\omega)$ represents the zero-quantum lineshape function (note the similarity with the form of equations 2.154–2.159, and especially equation 2.160) and $R_{DD,i,j}$ is the dipolar coupling as defined in equation 4.9. This equation, or its equivalent equations, form the basis of most diffusion-based simulations of spin diffusion. The

zero-quantum lineshape function arises from the evolution of zero-quantum coherence (*e.g.*, ZQT = I_+S_-).[236] In such models, the dependence of spin diffusion on both spinning frequency and resonance offset arises via this lineshape function. As such, understanding the nature of this function has been of interest.[83,237] Typically, however, this has been done using convolutions of single-quantum lineshapes[83] or through master equation based modelling.[237] By comparison, here, simulations are presented in Figures 4.14, 4.15, and 4.16, in which the evolution of the I_+S_-, $I_+S_-R_z$, and $I_+S_-R_zQ_z$ states (respectively) is considered for different spinning frequencies during the normal evolution of the system after inversion of the carboxylic acid proton resonance.

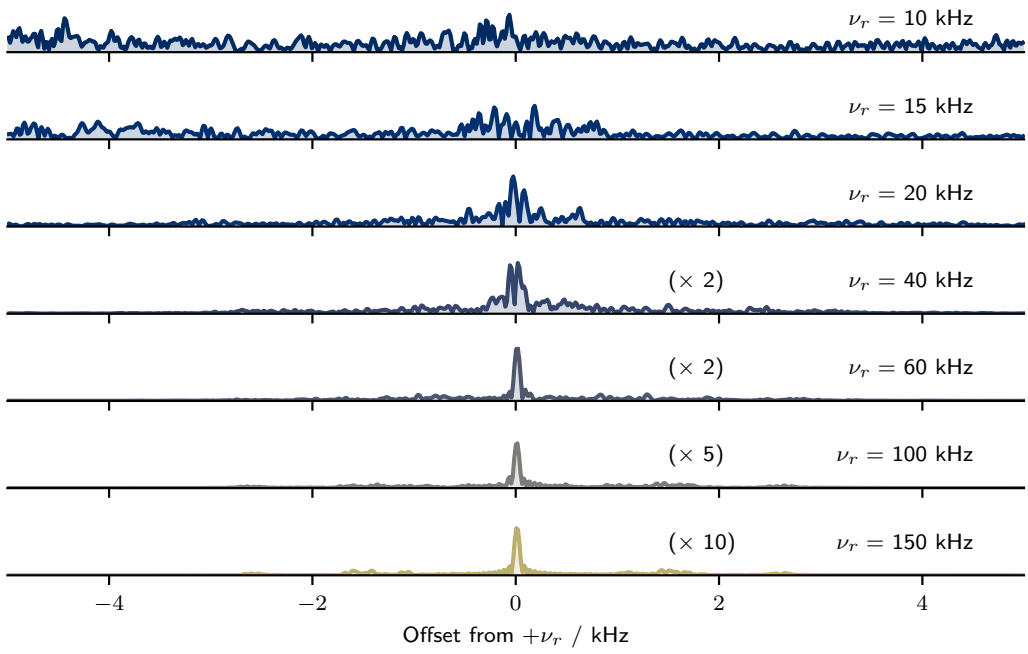

Figure 4.14: Simulated zero-quantum lineshapes at the first spinning sideband as obtained from evolution of the I_+S_- ZQT coherence after inversion of the carboxylic acid proton resonance. Simulations were performed with $\nu_0(^1\text{H})$ = 600 MHz and variable ν_r, for a full unit cell of β-AspAla ($n = 48$) with periodic boundary conditions. The interactions between spin-2 and spin-5 are shown where spin-2 is one of the NH_3^+ protons of molecule 1, and spin-5 is the Ala NH proton (see Table 4.1).

Specifically, the zero-quantum lineshapes of the first spinning sideband between the carboxylic acid proton and Ala NH protons of molecule 1 extracted from the model are shown in Figures 4.14, 4.15, and 4.16 for a range of spinning frequencies

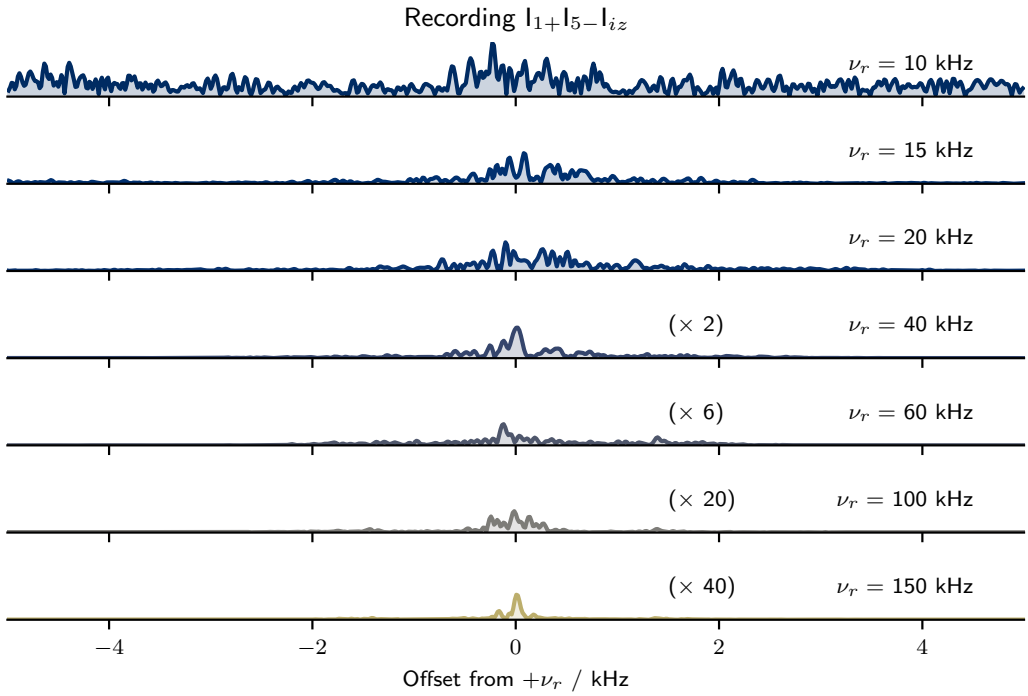

Figure 4.15: Simulated zero-quantum lineshapes at the first spinning sideband as obtained from evolution of the $I_+S_-R_z$ ZQT coherences after inversion of the carboxylic acid proton resonance. Simulations were performed with $\nu_0(^1\text{H})$ = 600 MHz and variable ν_r, for a full unit cell of β-AspAla ($n = 48$) with periodic boundary conditions. In this, spin I is spin-2, spin S is spin-5 (see Table 4.1), and spin R was summed over all spins which were neighbours of both I and S.

considering different zero-quantum coherences. At spinning frequencies $\nu_r = 15$ kHz, the lineshapes are broadened such that it is not possible to identify a single peak, which suggests that spin diffusion in this regime will have little dependence on the exact form of this function. As the spinning frequency increases, however, the lineshapes narrow significantly. It is also noted that the intensity of the spinning sidebands is significantly reduced with higher MAS frequencies, reflecting the reduction in spin diffusion rate with spinning frequency.

A result of this zero-quantum line narrowing is that spin diffusion would be expected to occur only within a well-defined range of resonance offsets, with relayed transfer slightly broadening this by allowing magnetisation to transfer between rather more separated spins. Modelling this line narrowing in the manner utilized here may enable the development of perturbation theory approaches at faster

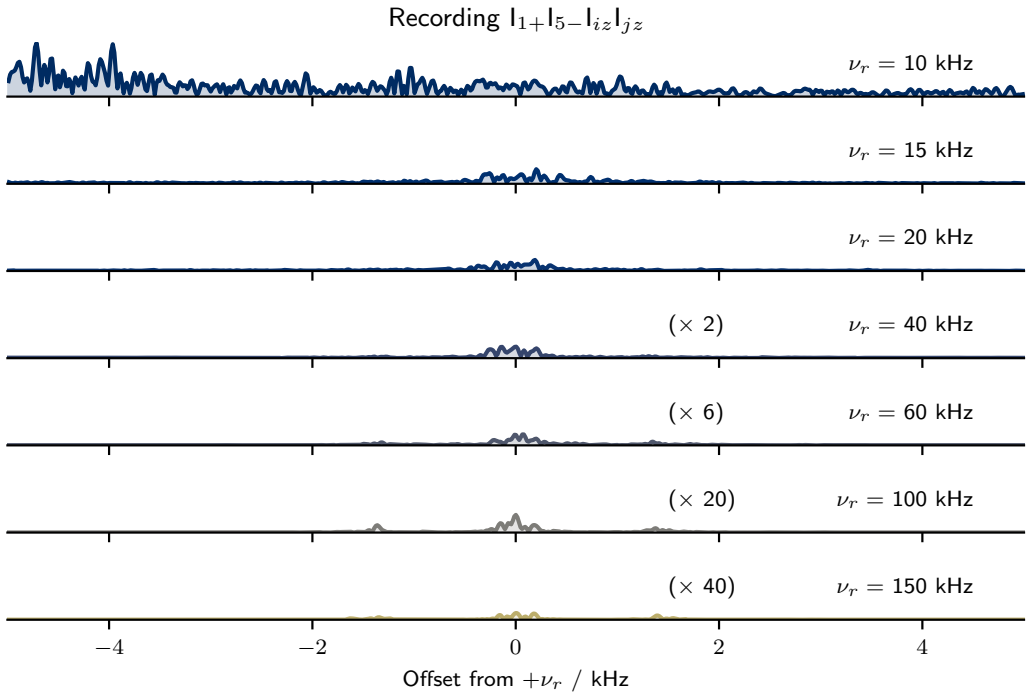

Figure 4.16: Simulated zero-quantum lineshapes at the first spinning sideband as obtained from evolution of the $I_+S_-R_zQ_z$ ZQT coherences after inversion of the carboxylic acid proton resonance. Simulations were performed with $\nu_0(^1\text{H})$ = 600 MHz and variable ν_r, for a full unit cell of β-AspAla ($n = 48$) with periodic boundary conditions. In this, spin I is spin-2, spin S is spin-5 (see Table 4.1), and spins R and Q were summed over all spins which were neighbours of both I and S

MAS frequencies by accounting more directly for the change in ZQT lineshape rather than approximating this effect with a decaying exponential as is typically performed.

4.4.3 Effect of Dynamics on Spin Diffusion

Many of the systems of interest for characterisation with spin-diffusion based techniques exhibit dynamics.[238,239] Dynamic motions affect the coherent evolution in spin space by leading to averaging of dipolar couplings and CSA tensors.[115,240] Even in crystalline solid samples, it is known that significant motions may be present.[240–245] Of particular importance are rotational motions of axially symmetric groups such as methyl groups, primary amines, and phenyl groups, which are typically fast on the NMR timescale and with limited energetic barriers.[246,247]

Motions occurring at frequencies coincident with various spin interactions can give rise to relaxation. In the case of interacting proton spins, motion could lead to incoherent cross relaxation and the nuclear Overhauser effect. Such an effect would interfere with the coherent spin evolution. A relaxation super-operator based treatment[113] of such effects is beyond the scope of this chapter, where the interest is solely in the coherent evolution of the system. In the model here, dynamics is included through two parameters. Overall motion is reflected by an order parameter S, which applies a linear scaling to all dipolar couplings between spins. C_3 rotation of the NH_3^+ and CH_3 groups was modelled by averaging the dipolar couplings between protons within the same group by $P_2(\cos\theta) = \frac{1}{2}(3\cos^2\theta - 1)$, where θ is the angle between the rotational axis and the interaction of interest. The angle is usually taken to be 90° so that the averaging factor is 0.5. As mentioned previously, the CSA tensors were averaged between all protons within a given CH_3 or NH_3^+ group in the molecular frame prior to rotation into the interaction frame.[83] The spin evolution as shown in Figure 4.17 (60 kHz MAS, 600 MHz) appears relatively insensitive to the overall motion order parameter. Under CH_3 or NH_3^+ rotation, however, the dynamics significantly change. Given that six of the twelve protons in each molecule of β-AspAla are within these axially symmetric groups, this is unsurprising.

Of important note is the behaviour of the inverse-sign spin diffusion ($M_z > 1$) apparent for the methyl (purple) group. As was noted by Agarwal (2019), this inverse transfer is aided by scaling the couplings involved.[200] For this effect to occur, the four-spin third order Hamiltonian contribution must dominate over the two- and three-spin Hamiltonians. While at such fast-spinning frequencies, the two-spin terms are effectively completely averaged, relayed transfer may still come to dominate over the four-spin interactions at long simulation times, hence giving the short lifetime of the effect observed in Figure 4.17e in the absence of methyl rotation. When these relaying interactions are further averaged by the methyl rotation, however, the four-spin term can dominate for far longer as seen in

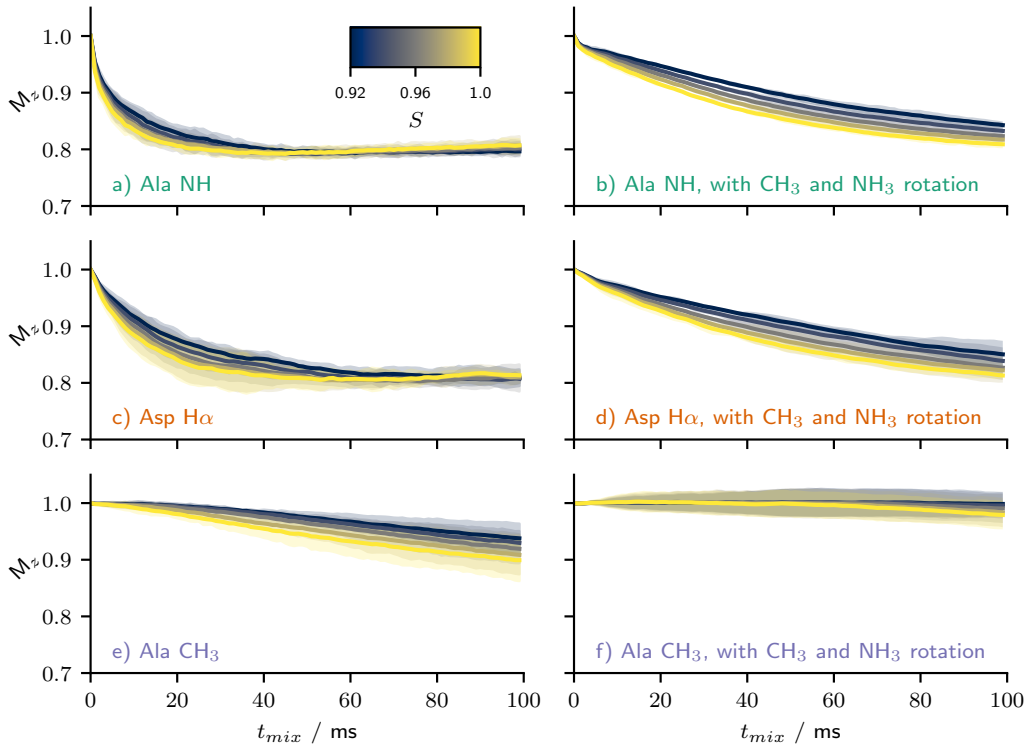

Figure 4.17: Simulated variation in spin diffusion for the Ala NH, Asp Hα, and Ala CH_3 sites after inversion of the carboxylic acid resonance (see pulse sequence in Figure 4.2) under different models of dynamical averaging. All dipolar couplings within each system were scaled by the parameter S to reflect overall dynamical motion. In (b,d,f), all dipolar interactions within a CH_3 or NH_3^+ group were additionally scaled by 0.5 to represent their axial rotation. Simulations were performed with $\nu_0(^1H)$ = 600 MHz and $\nu_r = 60$ kHz, for a full unit cell of β-AspAla ($n = 48$) with periodic boundary conditions

Figure 4.17f.

4.5 Experimental Case Studies

In the previous discussion, it was found, in agreement with prior work,[75,76] that spin diffusion may become truncated by the resonance offset between spins. As a result, the spatial nature of coherent spin diffusion breaks down. In this section, the experimental impacts of this truncation will be discussed. First, experimental spin diffusion in the dipeptide β-aspartyl L-alanine is shown, for which qualitative agreement is found with the simulated trends. However, an additional temperature-dependent behaviour is observed which may be indicative of an incoherent ^{1}H-^{1}H homonuclear nuclear Overhauser effect. Second, the efficiency of polarisation transfer via ^{1}H spin diffusion in perdeuterated U-[^{2}H,^{13}C,^{15}N] GB1 with 100% ^{1}H back-exchange at 60 kHz is found to be dominated by resonance-offset truncation.

4.5.1 Case Study 1: Incoherent Nuclear Overhauser Effect in β-aspartyl L-alanine (β-AspAla)

Experimental spin diffusion results obtained at 55 kHz MAS and 600 MHz are presented in Figure 4.18, with the six plots corresponding to the resolved ^{1}H resonances (see Figure 4.1b and Table 4.1). In these experiments, variable length trains of selective gaussian inversion pulses were applied selectively to the carboxylic acid proton peak (see Figure 4.4), and the corresponding intensity of all other sites recorded in a manner analogous to saturation transfer difference experiments conducted in the solution state.[219,220,248] Under these conditions, it is expected that the transfer of spin order will occur via spin diffusion with the saturated site acting as a magnetisation sink. A saturation type experiment was applied because experimentally influence from incoherent relaxation processes would be expected, which would lead to a fast recovery of the COOH spin making analysis of the behaviour in an inversion-type experiment more complex. On the other hand, under saturation the system would evolve towards a 'steady-state' and so the rate at which this occurs may be more readily quantified. Additionally, mis-set inversion pulses may not completely invert the site, meaning that the initial state would not be along -1, while saturation

would cause this site to approach 0 even for imperfect inversion.

While a comparison with simulation is presented in Figure 4.18, it should be noted that the presence of incoherent auto- and cross- relaxation means that this comparison is not necessarily ideal. Experimentally the spin diffusion is a combination of incoherent and coherent processes, while the computational modelling here is purely coherent.

It is observed that, under saturation, there is a strong resonance offset dependence with regards to the magnetisation change under saturation. Figure 4.18 is ordered with the site highest in chemical shift (closest in resonance offset to the carboxylic acid) at the top, with the chemical shift progressively getting lower (with greater resonance offset) on moving down the figure. Interestingly, the Ala CH_3 group experiences significant inverse sign spin diffusion similar to that which has been seen in other systems,[200,201,249] with an enhancement of ≈20%. This is significantly greater than any inverse-sign spin diffusion observed within the simulations (the maximum seen being 1.82%, in Figure 4.17f with $S = 0.94$). Moreover, this effect exhibits a significant temperature dependence, with an increase in the amount of inverse sign spin diffusion at higher temperatures. This observation is in contrast to the similar effect observed for L-histidine HCl H_2O by Agarwal (2019), and suggests that this effect may be dominated by an incoherent cross relaxation effect.[200]

In Figure 4.19, the calculated nuclear Overhauser effect (nOe) enhancement is shown as a function of temperature for this system. The temperature dependence of the timescale was approximated using an Arrhenius relation,[250]

$$\tau(T) = \tau(300\text{K}) \exp\left(\frac{E_a}{R}\left[\frac{1}{T} - \frac{1}{300}\right]\right), \tag{4.17}$$

with the activation energy, E_a, assumed to be 17.4 kJ mol^{-1} and the timescale at 300 K, $\tau(300\text{K}) = 200$ ps, though it should be noted that these values are approximated from the solution state[247] and are likely somewhat different in this system.[246,251] Approximating the spectral density as a single timescale Lorentzian function:

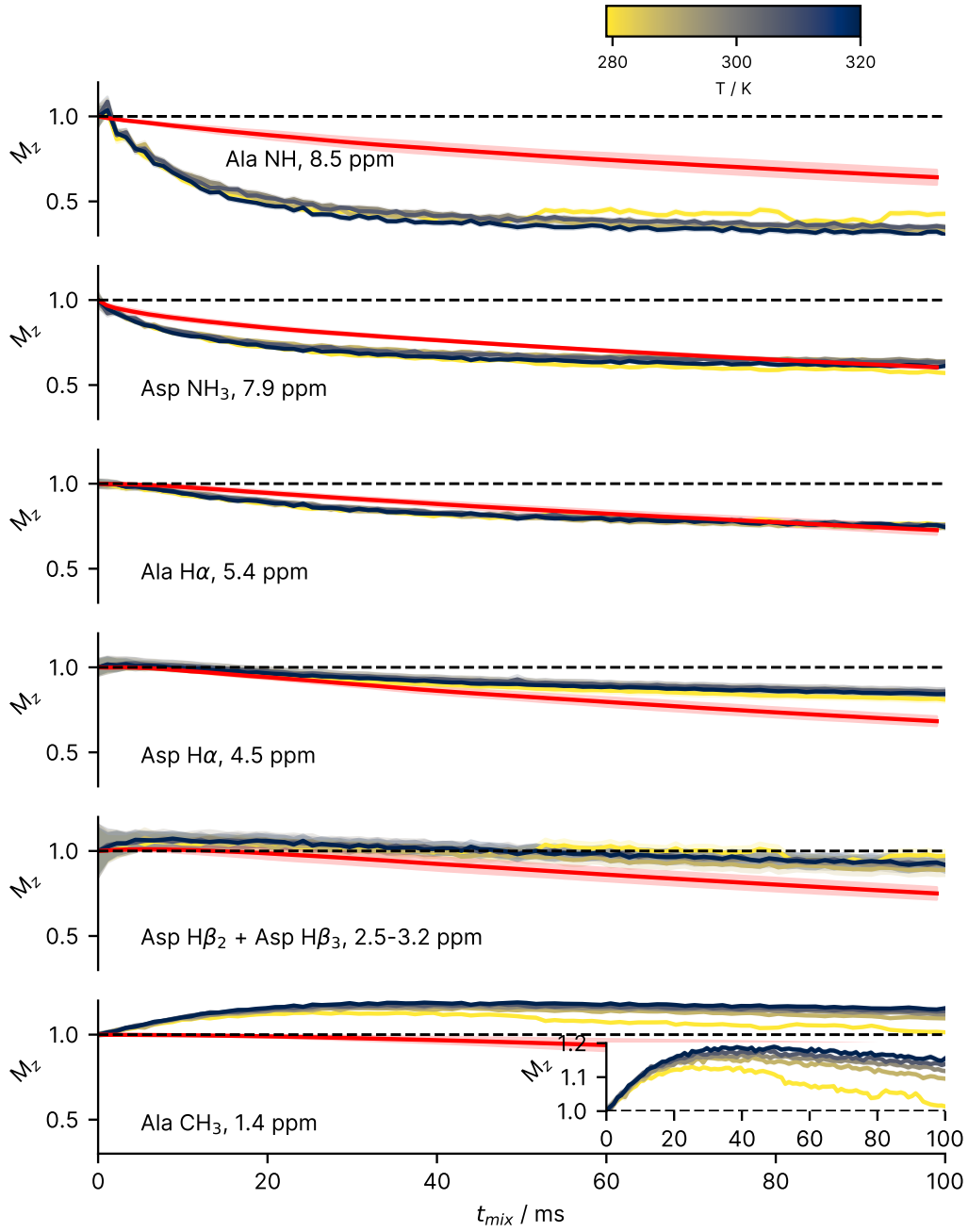

Figure 4.18: Experimental spin diffusion curves under saturation of the COOH proton resonance for β-AspAla at 55 kHz MAS and a ^{1}H Larmor frequency of 600 MHz, at temperatures of 279–320 K (calibrated using KBr). There is a significant difference in the spin diffusion observed under each temperature condition. Errors are shown as twice the standard error from voigt lineshape fitting with lmfit. Simulated spin diffusion curves under the same conditions are shown in red.

$$J(\omega) = \frac{1}{1 + (\omega\tau)^2}, \tag{4.18}$$

the nuclear Overhauser effect is then calculated as

$$\eta = \frac{6J(2\omega_0) - 1}{1 + 3J(\omega_0) + 6J(2\omega_0)}, \tag{4.19}$$

with ω_0 being the ^{1}H Larmor frequency as defined in equation 2.25. Note that the spectral density function in principle has an orientation dependence, however here this prefactor is omitted as for the calculation of nOe it would cancel out. At a ^{1}H Larmor frequency $\omega_0 = 600$ MHz, it is expected that a positive nOe would be observed and hence a positive enhancement in the resultant signal over this temperature range.

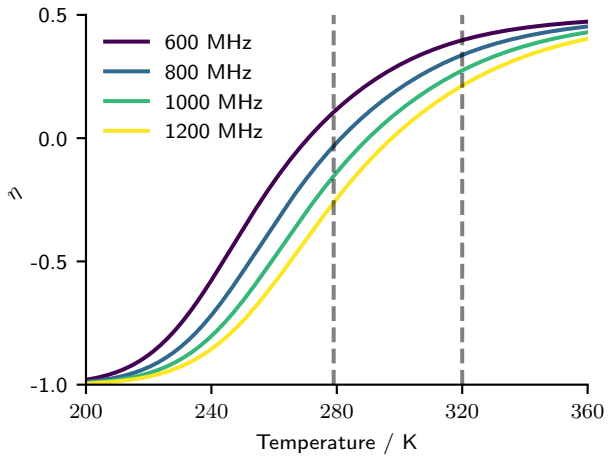

Figure 4.19: Calculated nOe (see equations 4.17–4.19) as a function of temperature at a range of magnetic field strengths. This was calculated assuming an Arrhenius dependence of timescale on temperature, with an activation energy of 17.4 kJ mol^{-1}, and a correlation time of 200 ps, though these are approximate.[246,247,251] Temperatures of 279 K and 320 K are shown using vertical lines.

In order to further investigate this apparent nuclear Overhauser effect in Section 4.5.1 further variable temperature experiments were performed over a range of temperatures. The 1.3 mm HXY probe, however, was limited in that it could only reach from 240–330 K. Using a Phoenix 1.6 mm probe it was possible to record a wider range of temperatures from 170 K to 365 K. At each temperature, a series of 1D spectra was recorded at different time delays after inversion of the COOH. The average intensity of the CH_3 resonance from 22–32 ms after inversion was recorded relative to the

intensity immediately after inversion. Figure 4.20 shows the resulting intensity achieved as a function of temperature (170.9–363.9 K). The trend in general agrees with that expected of a nuclear Overhauser effect (*c.f.* Figure 4.19), with the coldest temperature (170.9 K) having a reduction in the intensity. A model of the nuclear Overhauser effect (equations 4.17–4.19) has been fit, identifying a correlation time of 140 ± 30 ps and an activation energy of 1.9 ± 1.0 kJ mol^{-1}. While the correlation time is in good agreement with prior solution state studies,[247] this activation energy is significantly lower.

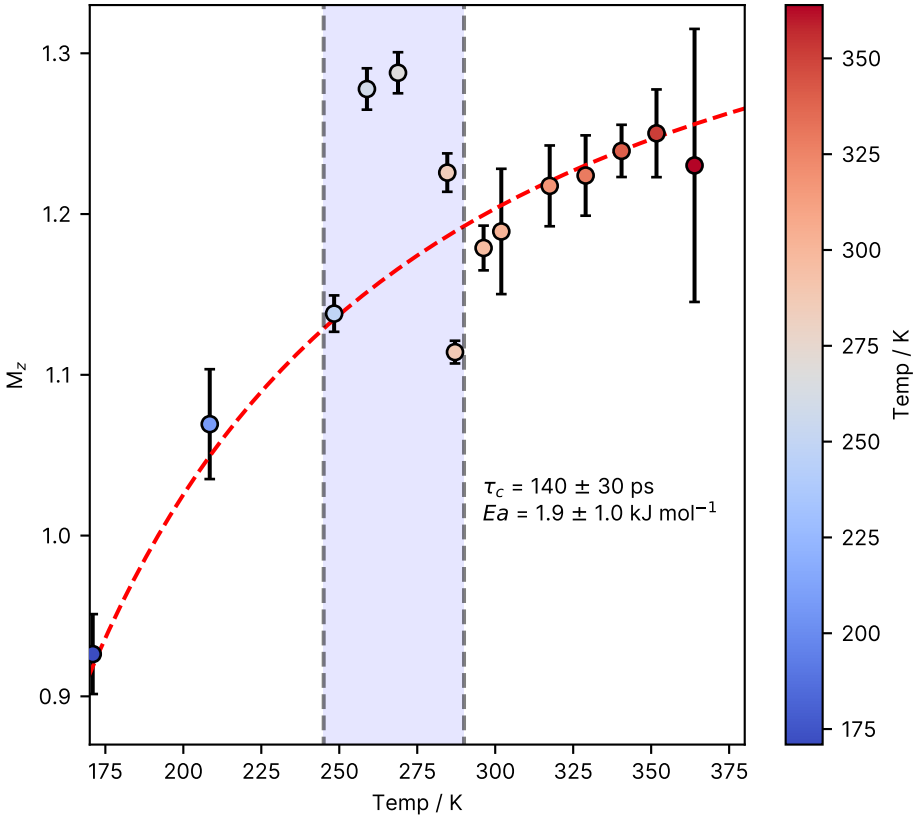

Figure 4.20: Deconvoluted integral of the CH_3 resonance measured as the average for t_{mix} between 22–32 ms after inversion of the COOH resonance in β-AspAla, measured at a ^{1}H Larmor frequency of 850 MHz spinning at 40 kHz in a 1.6 mm rotor. Error bars are shown at two standard deviations. A model of the nOe enhancement (see equations 4.17–4.19) was fit (red dashed line, data between 245–290 K were omitted during the fit), with the correlation time of the methyl group being found to be approximately 140 ± 30 ps with an activation energy of 1.9 ± 1.0 kJ mol^{-1}.

Interestingly, the measurements around 260–270 K do not fit the general trend. In

the variable temperature 1D ^{1}H spectra (Figure 4.21), the NH_3^+ resonance is not observed below this temperature. This indicates that 260–270 K represents the coalescence temperature for the rotation of the NH_3^+. That the coalescence of the NH_3^+ occurs at a similar temperature to the divergence in Figure 4.20 suggests that the two effects may be related, however more study into this effect is required.

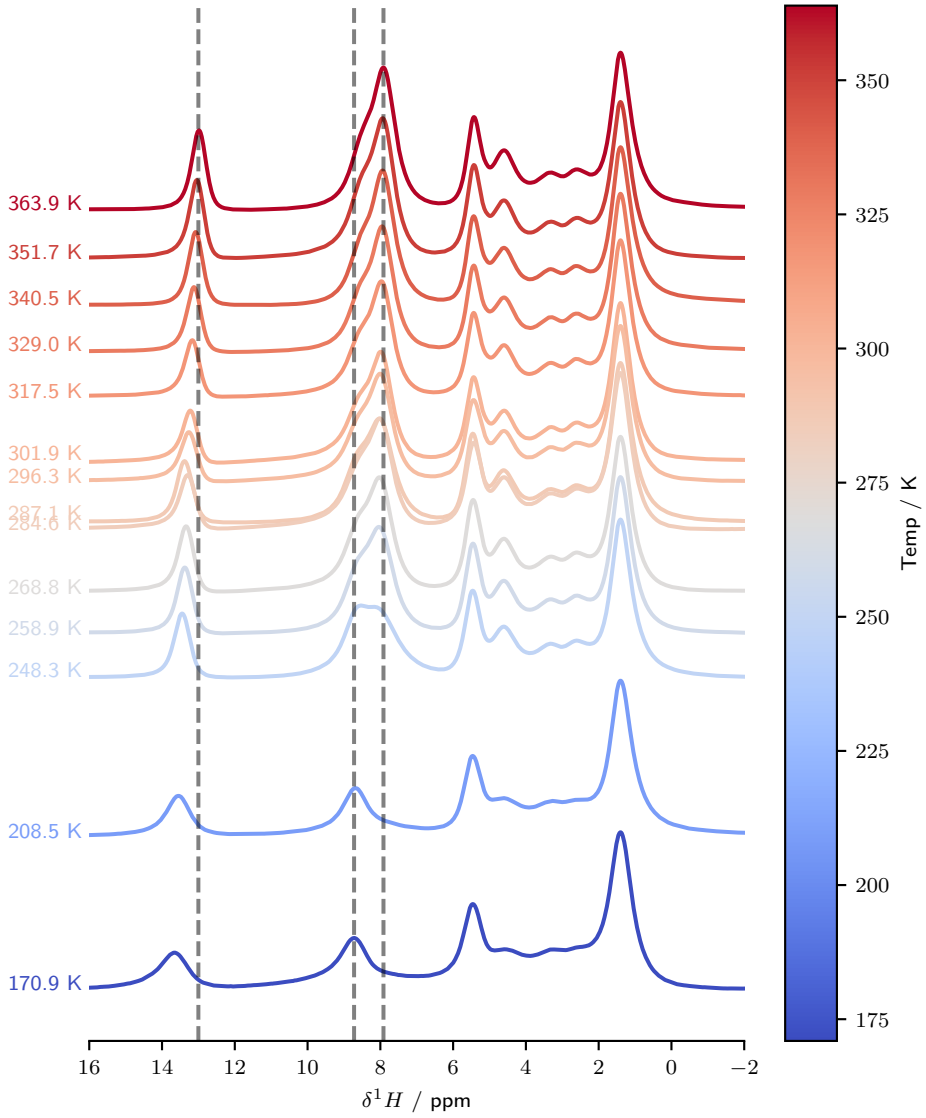

Figure 4.21: Variable temperature ^{1}H 1D spectra of β-AspAla measured at a ^{1}H Larmor frequency of 850 MHz at 40 kHz MAS

As a final verification of this being an incoherent nuclear Overhauser effect, a 2D ^{1}H – ^{1}H proton spin diffusion spectrum with a MAS frequency of 60 kHz and

a ^{1}H Larmor frequency of 1 GHz was recorded. This is shown in Figure 4.22. While the general pattern of resonance offset dependent spin diffusion is apparent, the existence of negative cross peaks between the methyl group and three other resonances (Ala NH, Ala Hα, Ala COOH) is observed. This indicates that this effect is indeed dominated by an incoherent process; in the case of a four spin inverse-sign coherent spin-diffusion effect, only a single negative cross peak would be expected, as the other two spins involved (Ala NH, Ala Hα) would give positive cross peaks.

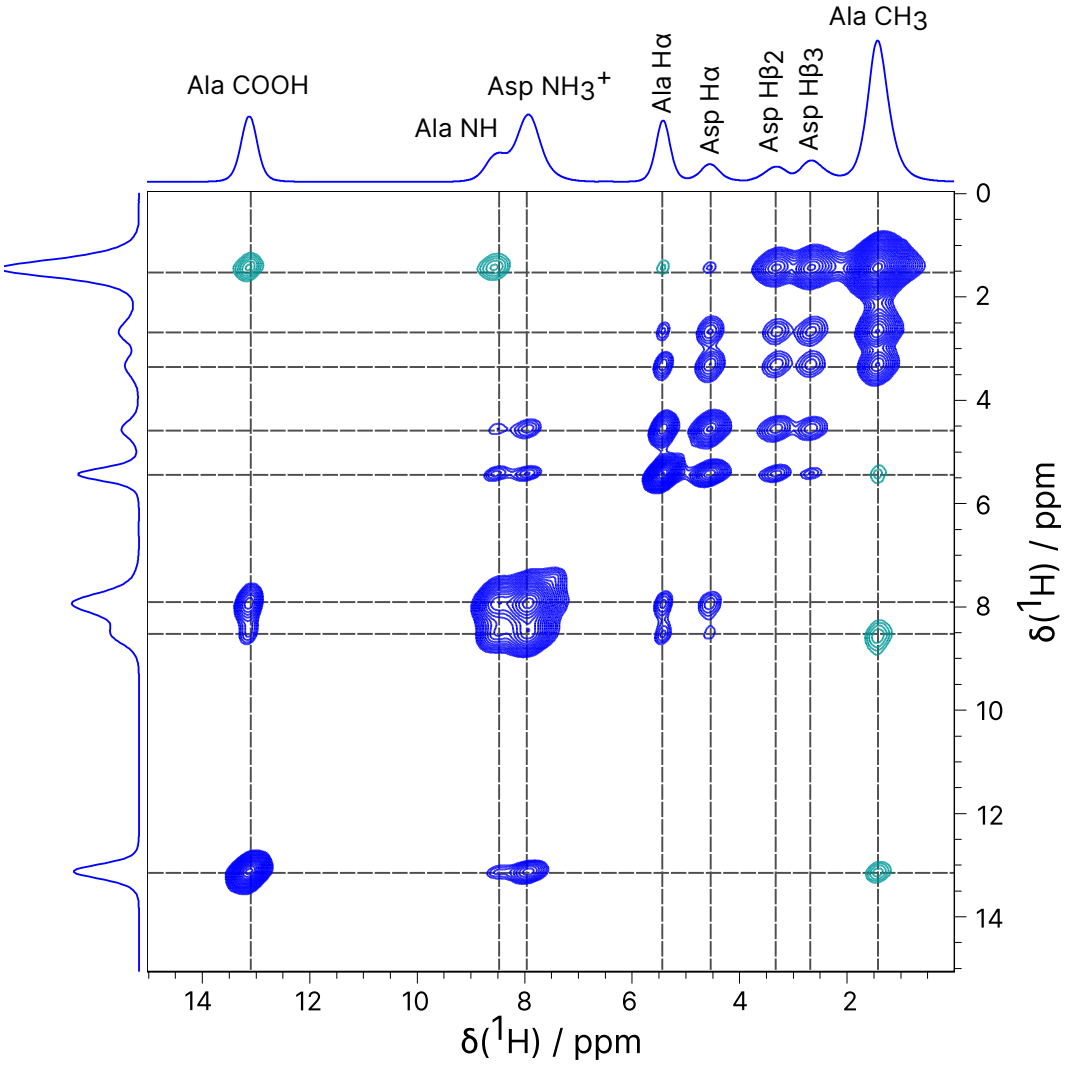

Figure 4.22: 2D PSD spectrum of β-AspAla recorded at 1 GHz ^{1}H Larmor frequency and 60 kHz MAS. The base contour level was set at 2.1%. A mixing time of 50 ms was used. 4 coadded transients were acquired for each of 512 t_1 FIDs, using States-TPPI in F_1 for sign discrimination.

While both homonuclear[252] (^{11}B) and heteronuclear nOes[154,253–255] (^{1}H$-^{13}$C, ^{1}H$-^{15}$N) have been observed before in the solid-state, few ^{1}H$-^{1}$H solid-state nOes have been reported. A solid-state nOe was observed in a study of hydrogen-π interactions with trapped water molecules.[256] Another such example is the suggestion that a ^{1}H$-^{1}$H homonuclear nOe is responsible for the difference between ^{1}H$-^{1}$H SD and ^{1}H$-^{1}$H fp-RFDR spectra occurring in a study of bone at 110 kHz MAS.[257] However, in light of the results of this study it is more likely that what was observed in the bone study was not actually a nuclear Overhauser effect, rather it was the result of resonance-offset truncation in spin diffusion.

The presence of this temperature-dependent incoherent effect may suggest that at fast spinning frequencies and high magnetic fields, the spin terms responsible for coherent spin evolution are sufficiently truncated by resonance offset such that there may be a competing influence of incoherent effects.

4.5.2 Case Study 2: 600 MHz Spin Diffusion in U-[^{2}H,^{13}C,^{15}N]-GB1 at 60 kHz

Following the observation of strong resonance-offset dependence for spin diffusion in a protonated sample at fast MAS, the effect of this phenomenon on a system with a more dilute proton network was studied. It has been found for several crystalline protein systems that the combination of perdeuteration and fast MAS leads to excellent resolution with narrow protein linewidths (< 50 Hz).[125] This is the case for the β_1 domain of Protein G, GB1, a protein commonly used in solid-state NMR. Selective saturation ($\approx$100 Hz bandwidth, 500 ms) was applied to several resolved sites in GB1, and the ratio of the intensities of all other resolved resonances under saturation on resonance and off resonance was recorded as a function of the resonance offset from the saturation transmitter. Specifically, Lys$_{10}$ NH, Ala$_{20}$ NH, Trp$_{43}$ Hϵ_1, and Asn$_{37}$ Hδ_{21} were saturated. These sites are highlighted in a 2D ^{1}H$-^{15}$N spectrum of perdeuterated GB1 in Figure 4.23. Note that not all of these saturation sites are 'perfect', and so they may overlap with other sites which could

influence the resulting saturation profile.

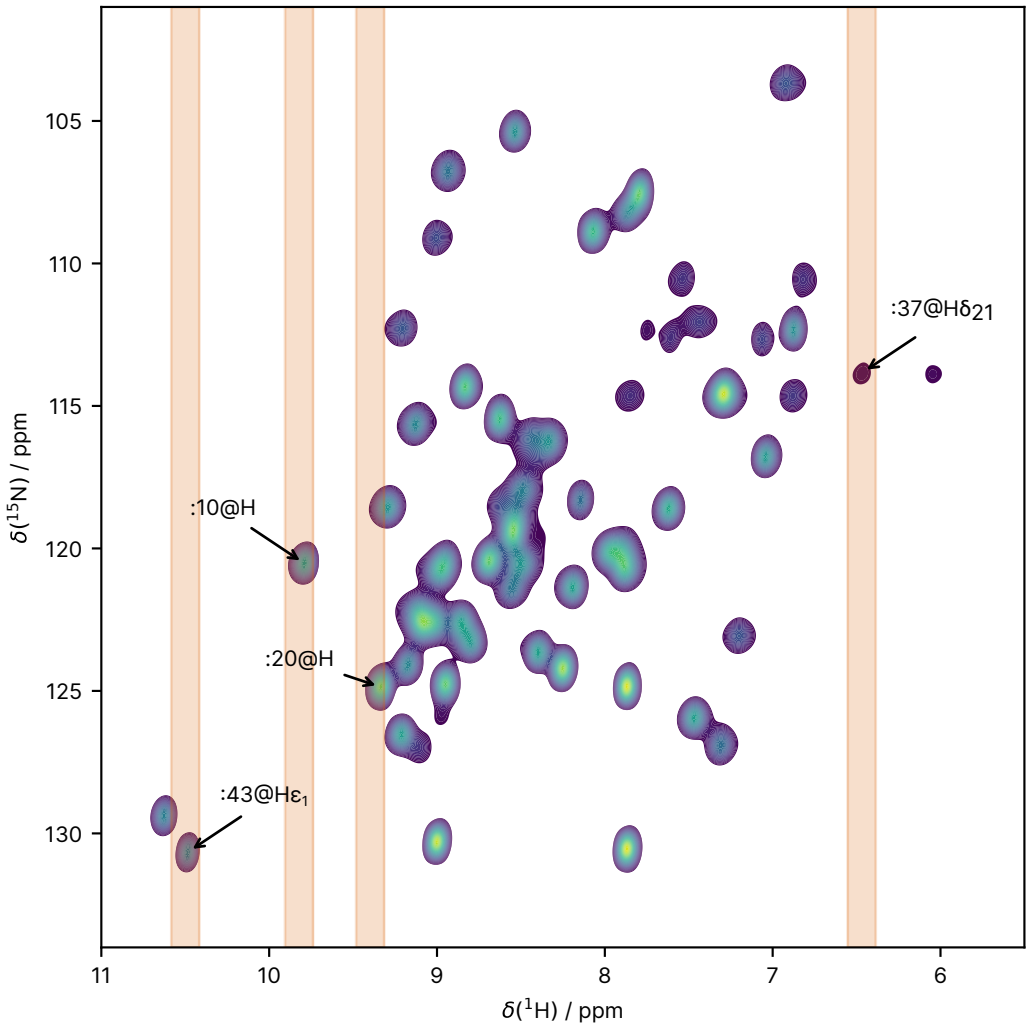

Figure 4.23: A 2D $^{1}H-^{15}N$ spectrum of perdeuterated U-[^{2}H,^{13}C,^{15}N] GB1 recorded at 60 kHz MAS, 600 MHz ^{1}H Larmor frequency. The sites which were targeted with saturation have been annotated (using selection algebra notation), with the approximate bands of saturation shown (the frequency of saturation $\pm$50 Hz).

For all sites under saturation, a strong dependence of magnetisation change on resonance offset was observed, yet negligible to no dependence on distance. This is illustrated in Figure 4.24. Thus, under these conditions considering the intensity of peaks as even very rough indicator of spatial proximity may lead to wrong conclusions without careful consideration of the chemical shift.

Figure 4.25 shows 1D spectra under 500 ms of saturation of the different labelled

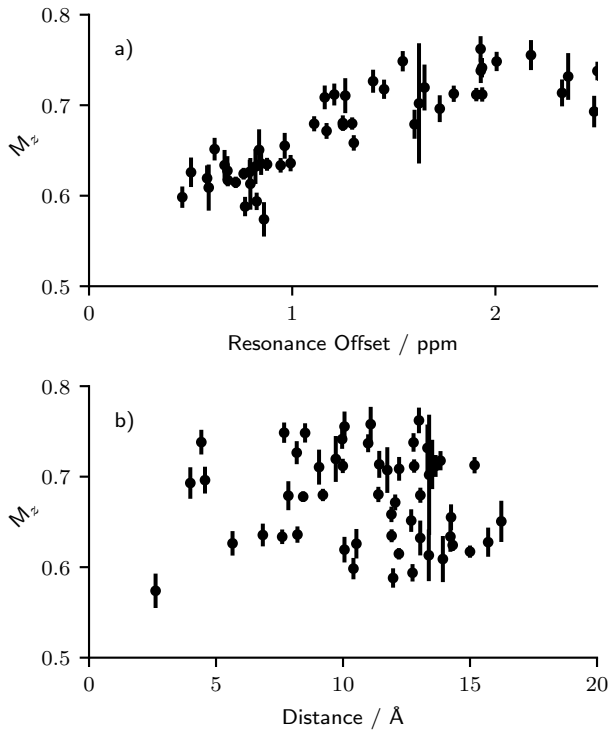

Figure 4.24: Saturation was applied for 500 ms to the resolved Lys_{10} NH resonance. The resulting intensity of the other sites, relative to off-resonance saturation, is shown as a function of (a) their resonance offset and (b) their spatial proximity.

points. On top of these, the ratio of the intensity with and without saturation is shown, displaying a strong resonance-offset dependence.

An additional consideration is whether the rate at which the saturation transfer occurs varies as a function of saturation site. For example, Trp_{43} Hϵ_1 is only close in resonance offset to a single site, Phe_{52} NH; as a result, very little transfer occurs to the other sites. However, it is of interest whether the rate at which this magnetisation transfer occurs is dependent on the site being saturated, or whether it is a property of the system as a whole. In Figure 4.26, the transfer of saturation from Ala_{20} NH to Thr_{17} NH under different saturation times is shown. This follows an exponential decay:

$$M_z(t_{sat}) = A + Be^{-k_{sat}t_{sat}}, \tag{4.20}$$

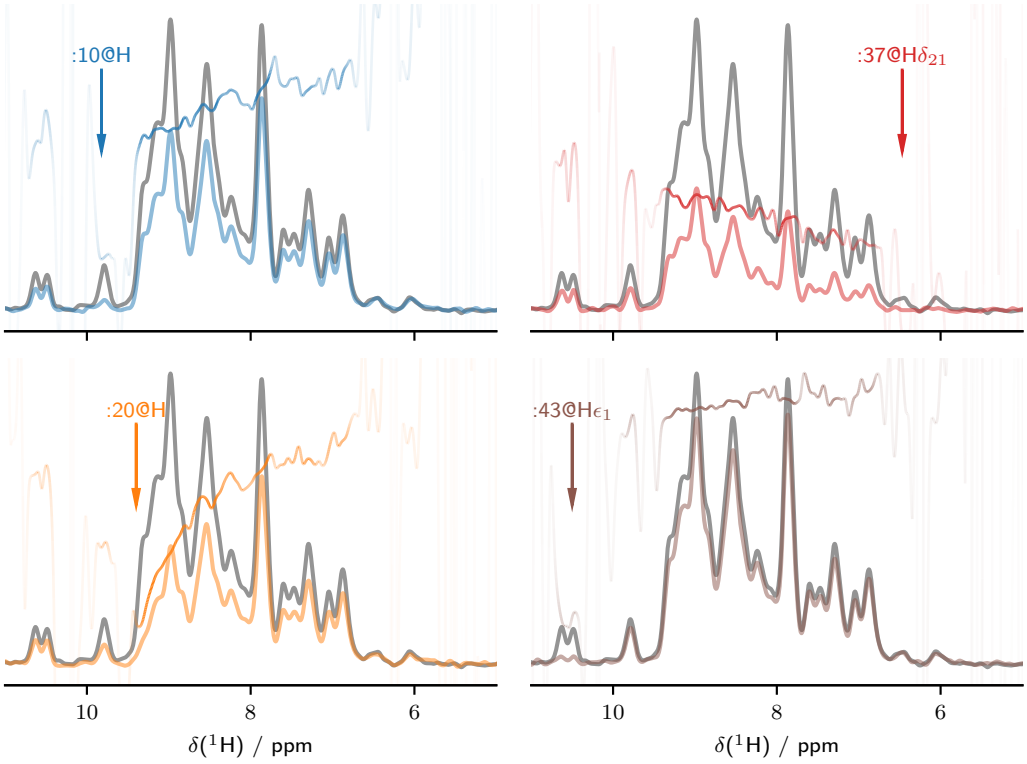

Figure 4.25: 1D projections of perdeuterated GB1 under saturation of different sites, as recorded with $\nu_r = 60$ kHz at $\nu_0(^1\text{H}) = 600$ MHz are shown as coloured spectra. The equivalent spectra with off-resonance saturation is shown in grey. 500 ms of saturation with $\nu_1 = 100$ Hz was applied at the points indicated. Projections were calculated by summing rows. Also shown is the saturation ratio, calculated as the intensity under saturation divided by the intensity under off-resonance saturation. This has been coloured according to the intensity of the off-resonance saturation, as the ratio in the noise is not meaningful.

where A and B relate to the degree to which saturation is transferred, and k_{sat} to the rate at which this transfer occurs. Such curves have been fit to the transfer of magnetisation between each pair of points, which is shown in Figure 4.27 as a function of resonance offset and spatial proximity. While the values of A and B are very dependent on the point of saturation, it is found that the rate of saturation transfer, k_{sat}, is independent of the saturation point and follows a strong dependence on the shift offset. There is no discernible dependence of this on the spatial distance between sites.

In conclusion, it has been found that in a perdeuterated U-[^{2}H,^{13}C,^{15}N] GB1 with

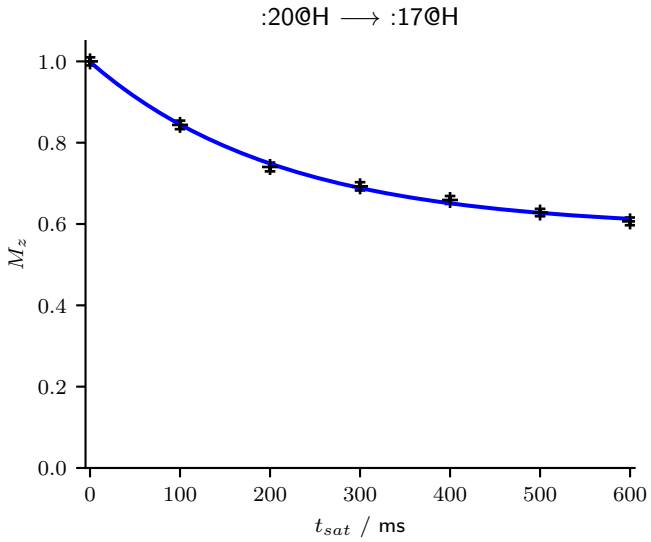

Figure 4.26: Plot showing the transfer of magnetisation from Ala_{20} N-H to Thr_{17} N-H under variable mixing times of saturation. An exponential decay curve (equation 4.20) has been fit in blue.

100% back-exchange at 60 kHz MAS, the spin diffusion is almost entirely dominated by the resonance offset between sites. The rate at which this transfer occurs is dependent principally on the resonance offset between sites, and this dependence is consistent between saturation sites.

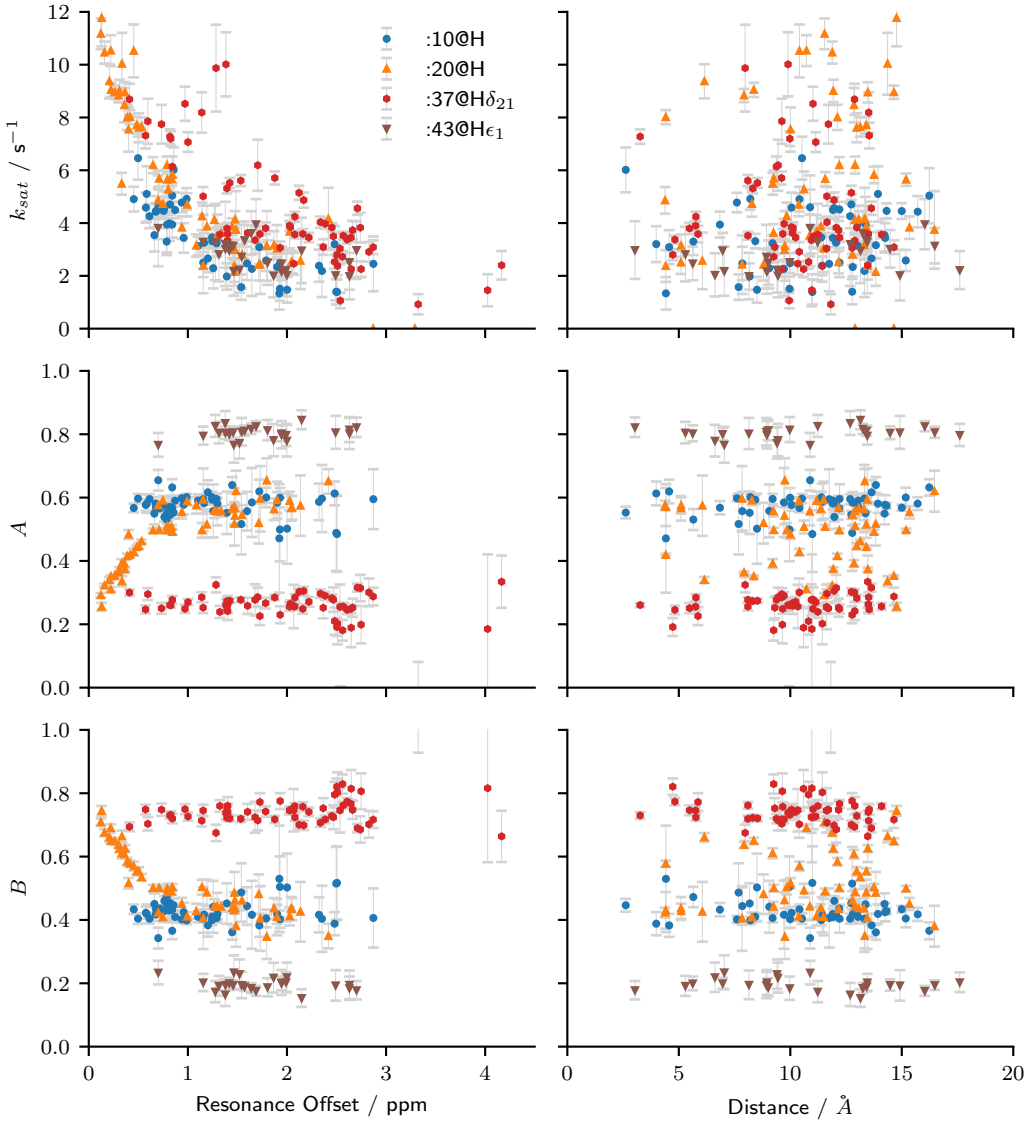

Figure 4.27: Variation in the fit exponential decay parameters, k_{sat}, A, and B (see equation 4.20), as a function of resonance offset and distance for each of the saturation points considered here.

4.6 Conclusions

As faster magic-angle spinning and higher magnetic fields become routine for accessing higher resolution in ^{1}H solid-state NMR, understanding the behaviour of spin-diffusion becomes more important for designing experimental methods in which spin diffusion is utilised or where it is a competing effect to, *e.g.*, chemical exchange like in CEST. Specifically, as ^{1}H sites become better resolved, the transfer of

spin order between them via spin diffusion becomes increasingly dependent on their resonance offset. Here, it was shown that the inclusion of chemical shift evolution, and specifically chemical shift anisotropy, is of key importance for simulating how these systems evolve. The effect of dynamics was also investigated and found to play an important role in the coherent evolution of the system.

In Section 4.5.1, it was found that for crystalline β-AspAla the resonance-offset truncation is sufficient both to ensure almost entirely offset dependent transfer, and to enable a possible incoherent nuclear Overhauser effect to become competitive. The truncation was also studied in a sample of microcrystalline perdeuterated GB1 in Section 4.5.2, where the transfer becomes entirely resonance-offset dependent. These suggest that under such conditions, experiments relying on coherent ^{1}H–^{1}H spin diffusion should be avoided. However, it may also open up new avenues for exploration. For example, the resonance-offset truncation has the effect that for some sites, there is effectively negligible coherent ^{1}H spin diffusion; for example, the saturation of Trp_{43} $\mathrm{N}\epsilon_1$ led to very little transfer to other sites (see Figure 4.25). In this case, cross-relaxation incoherent processes likely become strongly competitive. There exist solid-state systems which possess significant microsecond dynamics (for select examples, see ref 163, ref 121, ref 258, and Chapter 5). In such systems, a positive enhancement nuclear Overhauser effect would be expected which may enable these well-resolved sites to be used as structural probes.

While here only direct proton to proton spin diffusion has been considered, it should be noted that the consequences and features observed likely affect other experiments. For example, CHHC[80,259] experiments as commonly applied at slower spinning rates will suffer the same resonance offset dependence under fast MAS as the proton spin bath relied upon for transfer becomes increasingly more resolved. This analysis highlights the importance of application of active recoupling under fast magic angle spinning conditions to collect spatial structural constraints.[260–266] On the other hand, better understanding of proton spin diffusion at fast MAS has implications for our ability to measure site-specific ^{1}H relaxation and quantification of ^{1}H CEST in the

solid state.

Chapter 5

Investigating Protein Dynamics in the Presence of Paramagnetic Dopants

The relaxation rate dataset used in this chapter includes both previously published data (see Table 5.1 and 5.3 for lists) and newly recorded data (Table 5.2). This new data was recorded entirely by myself. The method used for the analysis of the relaxation data presented here was performed and developed by myself.

5.1 Introduction

NMR has found an important role in experimentally quantifying and understanding the local dynamics of proteins.[128,130,149,163,225,267–272] However, most of these studies have only observed proteins in an single-component context, when it is known that many of their biological roles arise through the interactions between proteins and other molecules.[273–278] While, in principle, solid-state NMR is a powerful tool to access information on motions in multicomponent systems, it often faces issue of limited sensitivity. Long experimental times are required due to the multiplicity of experiments and necessary signal averaging, hindering direct relaxation-based

dynamic analyses.

Most of the time in an NMR experiment is spent waiting for the nuclear spins to relax to equilibrium.[279–282] This is particularly the case when measuring relaxation rates, for which the experiment is additionally lengthened by the requirement to wait for the relaxation of the nuclei being studied. In the case of ^{15}N T_1 measurements, this can lead to extremely long experimental times owing to the slow relaxation of this nuclei (^{15}N T_1s are typically dozens of seconds long). This intrinsic T_1 barrier may be reduced through the addition of paramagnetic species which give rise to a paramagnetic relaxation enhancement (PRE). PRE may be exploited by doping samples with paramagnetic agents such as Gd(DTPA-BMA) or CuEDTA, and has been shown to allow for rapid acquisition of structural information.[50,283–289] For relaxation measurements, PRE helps to shorten the overall experimental time not only by reducing the ^{1}H T_1, and thus the repetition rate of experiment, but also by reducing the measured relaxation times and consequently the required variable relaxation delays.[279,284,288,290]

Though the PRE can aid structural studies, it does this by affecting the nuclear spin relaxation. As such, it is no longer possible to directly interpret the measured nuclear spin relaxation rates in terms of their underlying dynamics without quantifying the additional PRE.[51,284] Recently, several models for this paramagnetic term for structural analysis have been investigated.[286,291–293] In cases where the position of the paramagnetic centre is well defined (*e.g.*, in metalloproteins) these models can be used to determine the paramagnetic contribution and subtract this from the experimental relaxation rates to allow for dynamical analysis.[294–296] However, there are currently no general protocols to quantify local dynamics based on relaxation data in the presence of PREs. While the paramagnetic contribution to the relaxation is typically significant, it usually does not completely dwarf the dynamical contribution in the applicable regime. Typically, when the paramagnetic contribution is significantly greater than the dynamical contribution, the broadening due to excess of paramagnetic dopant becomes too large to allow site-specific measurements.

As such, if the paramagnetic contribution were adequately quantified it would be possible to access the underlying dynamic contribution to relaxation, and thereby investigate the local dynamics.

One such system in which dynamical analysis is limited owing to the poor sensitivity of the sample is the complex formed by GB1 and Immunoglobulin G (IgG) (GB1:IgG, shown in Figure 5.1a). The intermolecular interaces for this system have been characterised both by considering fragments[297–300] and the full-length antibody.[49,50,258] The characterisation of the local dynamics and interactions within this system is challenging because the labelled U-[^{2}H, ^{13}C, ^{15}N]-GB1 makes up only $\approx$10% of the sample weight by volume,[49] a result of which is that $\approx 100\times$ as much experimental time is required for the same quality data relative to the same datasets measured on microcrystalline GB1.* As a result, experimental times required to obtain the requisite set of relaxation rates for the analysis of dynamics can run into several months (see Figure 5.1b, noting that several of each type of relaxation rate would be required). Consequently, the analysis of the dynamics within the GB1:IgG complex to date has been limited to qualitative comparison of relaxation rates[258] or the quantitative analysis of relaxation dispersion where the separation of the paramagnetic and exchange contributions to relaxation is straightforward.[51] The technique introduced here, COncerted Motion and PAramagnetic Dynamics RElaxation analSis (CoMPaDReS), attempts to obtain separation of dynamic and paramagnetic contributions to relaxation in samples which have been doped with paramagnetic species. This separation enables the quantification of both the local dynamics and the paramagnetic interaction. This approach improves the feasibility and practicality of solid-state NMR relaxation analysis for sensitivity limited large biomolecular complexes.

This chapter will begin by introducing the theory and methodology behind the technique. The CoMPaDReS method will then be applied to paramagnetically-doped microcrystalline GB1, for which the resulting dynamical profile will be compared

*Owing to the square root dependence of signal to noise on the number of scans. $10\times$ more signal to noise requires $100\times$ as many scans.

to a more traditional analysis on undoped microcrystalline GB1. Following this, the CoMPaDReS method will be applied to the paramagnetically-doped GB1:IgG complex, where the resulting dynamics will be compared with those arising from a limited undoped dataset, from molecular dynamics simulations, and from the microcrystalline form of GB1. Finally, the size of the relaxation rate dataset required for this analysis will be discussed, with a key focus on the potential for saving experimental time.

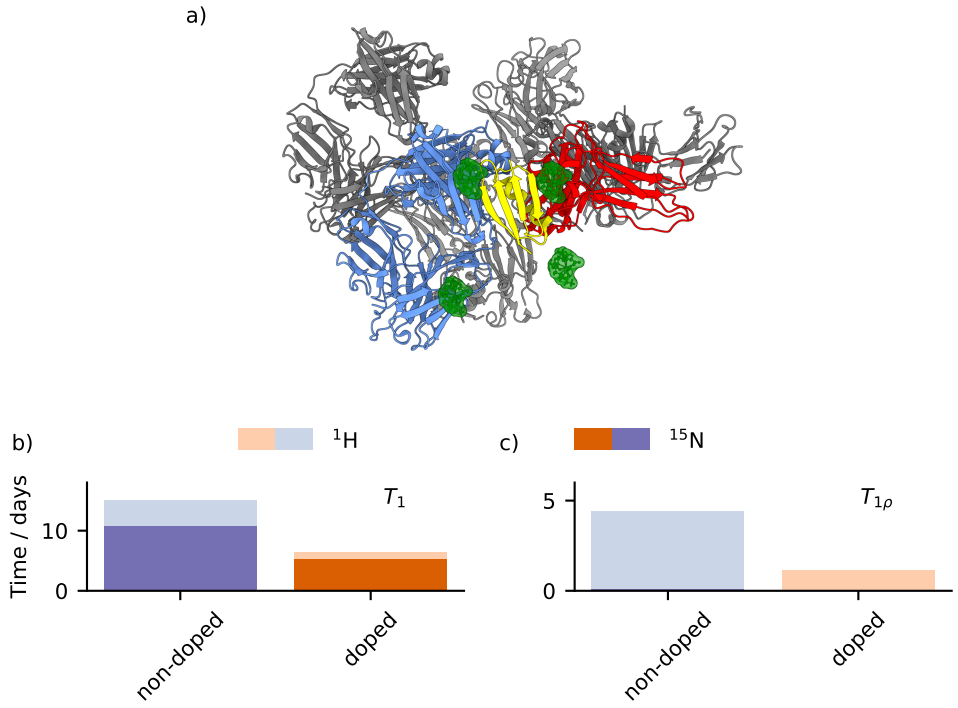

Figure 5.1: (a) Depiction of the GB1:IgG complex studied here. The Fab and Fc domains of the Immunoglobulin G (IgG) protein which were simulated are shown in blue and red respectively. The GB1 is shown in yellow. Representative models of the Gd^{3+} complex are shown in green. Note that for molecular dynamics modelling, only the coloured parts of the protein complex were simulated. (b,c) Example comparison of calculated approximate experimental times (see Section 5.3.3) for the measurement of a ^{15}N R_1 (b) (calculated using the average R_1 measured at a ^{1}H Larmor frequency of 600 MHz and a MAS frequency of 60 kHz, both with and without 3.5 mM [Gd^{3+}]) or $R_{1\rho}$ (c) (calculated using the average $R_{1\rho}$ measured at a ^{1}H Larmor frequency of 700 MHz, a spin lock field of 10 kHz, and a MAS frequency of 60 kHz, both with and without 3.5 mM [Gd^{3+}]). These experimental times are shown divided into contributions from the relaxation of ^{15}N (*e.g.*, the relaxation delays), shown in dark colour, and the ^{1}H (*e.g.*, the recycle delay), shown in a light colour.

5.2 Methods

5.2.1 Solid-State NMR

Much of the relaxation data used in this study has been published previously.[50,51,258] Table 5.1 outlines the datasets which have been obtained from prior studies for the GB1:IgG complex, which include R_1 and $R_{1\rho}$ rates at different concentrations of Gd(DTPA-BMA)[†] obtained at ^{1}H Larmor frequencies from 600 to 850 MHz. To supplement this, and to better quantify the slow microsecond motions apparent in this system,[258] additional relaxation rates have been measured as outlined in Table 5.2, which include R_1 and $R_{1\rho}$ at 1 GHz ^{1}H Larmor frequency in the presence of 3.5 mM Gd(DTPA-BMA) and ^{15}N NEar Rotary Resonance Dispersion (NERRD) at 700 MHz ^{1}H Larmor frequency. These additional rates were measured using the same conditions as the previous studies, including using the same samples (For sample preparation see ref 49). While experimental dipolar order parameters have been previously published for this system,[301] owing to the considerable error in these they have not been included in this analysis. These could be included as in previous detector-based analysis of dynamics.[160] In all cases, a sample temperature of ≈300 K was used as monitored with the difference in chemical shift between the DSS peak and the water peak.[227]

Table 5.1: Previously published relaxation rates measured for the 100% back-exchanged U-[^{2}H,^{13}C,^{15}N]-GB1:natural abundance IgG complex.

Field / T	Type	[Gd^{3+}] / mM	ν_1 / kHz	ν_r / kHz	Citation
14.1	R_1	0.0[‡], 3.5, 5.0, 7.5	—	60	ref 50
16.4	$R_{1\rho}$	0.0, 1.0, 2.0, 3.5	10.0	60	ref 50
16.4	$R_{1\rho}$	3.5	10.0	60	ref 51
20.0	R_1	0.0	—	60	ref 258
20.0	$R_{1\rho}$	5.0	10.2, 15.5, 20.4	60	ref 51
20.0	$R_{1\rho}$	0.0	17.0	60	ref 258
20.0	$R_{1\rho}$	0.0	13.1	45, 52	ref 258

In order to better verify the method on a system for which equivalently good data

[†]In the text, Gd(DTPA-BMA) will be used when reference is made to the full species while Gd^{3+} will be used to refer the paramagnetic centre.

[‡]All 0 mM data was only used for undoped detector calculations.

Table 5.2: Additional data recorded for the 100% ^{1}H back-exchanged U-[^{2}H,^{13}C,^{15}N]-GB1:natural abundance IgG complex. The same samples were used as for the data recorded in previous studies.

Field / T	Type	[Gd^{3+}] / mM	ν_1 / kHz	ν_r / kHz
16.4	R_1	2.0, 3.5	—	60
16.4	$R_{1\rho}$	3.5	13.0, 18.0, 23.0, 32.0, 39.0	60
23.5	R_1	3.5	—	60
23.5	$R_{1\rho}$	3.5	11.0	60

could be obtained on both a diamagnetic and a paramagnetically doped sample, previously recorded relaxation data for microcrystalline GB1 has been used. The datasets used for this analysis are shown in Table 5.3.

Table 5.3: Previously published relaxation rates measured for microcrystalline GB1.

N	Field / T	Type	[Gd^{3+}] / mM	ν_1 / kHz	ν_r / kHz	Citation
1	14.1	R_1	0.0	—	60	ref 225
2	14.1	R_1	2.0	—	60	ref 50
3	14.1	$R_{1\rho}$	0.0	17.0	60	ref 225
4	14.1	$R_{1\rho}$	2.0	10.4	60	ref 51
5	16.4	R_1	0.0	—	100[§]	ref 302
6	16.4	$R_{1\rho}$	0.0	5.0	100[¶]	ref 302
7	16.4	$R_{1\rho}$	2.0	10.0	60	ref 51
8	20.0	R_1	0.0	—	60	ref 225
9	20.0	$R_{1\rho}$	0.0	17.0	60	ref 225

For the analysis of diamagnetic microcrystalline GB1, datasets 1, 3, 5, 6, 8, and 9 were used (highlighted in blue); for the analysis of paramagnetically doped microcrystalline GB1, datasets 2, 4, 5, 7, 8, and 9 were used (highlighted in magenta). Datasets used for both are highlighted in teal.

While here Gd(DTPA-BMA) has been used as the paramagnetic dopant, this technique should be applicable to other paramagnetic species. Gd(DTPA-BMA), and other Gd^{3+} complexes, however, are particularly suited to this kind of analysis. Having an electron spin of 7/2, significantly lower concentrations are required compared to some other dopants such as Cu^{2+}.[258,303] The relatively long electron spin

[§]this was fully protonated microcrystalline GB1
[¶]this was fully protonated microcrystalline GB1

relaxation time, T_{1e}, of these complexes,[284,304] combined with the high magnetic fields used in this study, means that the correlation time of the paramagnetic interaction (τ_{para}) is dominated by the rotational diffusion of the agent, and is therefore both field independent, and on a similar order of magnitude to the inverse of the nuclear Larmor frequencies probed here (≈10–100 MHz, corresponding to ≈10–100 ns).[305–307] As such, there is sufficient variation in the paramagnetic effect with field that the paramagnetic interaction can be characterised both temporally and spatially. This may not be as simple with faster relaxing species, which may still be field dependent under these experimental conditions. Another benefit of using Gd^{3+} complexes is the isotropic g-tensor, meaning it does not produce a paramagnetic contact shift (PCS).[284] The presence of PCS may affect CSA relaxation pathways, or relaxation dispersion. Finally, the Gd(DTPA-BMA) species used here does not specifically bind to the protein,[303] which means that this does not need to be accounted for when interpreting the modelling results.

5.2.2 Relaxation Modelling

In the following analysis, it is assumed that the paramagnetic agent causes no changes to the internal dynamics or to the coherent spin evolution. This assumption is reasonable both because the local backbone dynamics are unlikely to interact with the non-binding Gd(DTPA-BMA) complex,[303] and because the correlation time of the paramagnetic interaction is substantially faster than the rate of spin diffusion (*vide infra*). A given relaxation rate may then be expressed as a linear combination of terms considering the local dynamics, the paramagnetic interaction, and coherent spin diffusion as

$$R_X = R_X^{dyn} + R_X^{para} + \rho_X, \tag{5.1}$$

with R_X^{dyn}, R_X^{para}, and ρ_X representing the dynamic, paramagnetic, and coherent contributions respectively. As discussed in Section 3.3.3, it has been shown previ-

ously that at spinning frequencies ≥ 50 kHz the coherent contribution (ρ_X) to the ^{15}N relaxation rates measured here is negligible.[123,308]

Many models for the contribution of paramagnetic species to relaxation have been proposed.[50,291,292,303,309,310] In this analysis, these interactions are modelled assuming only point-dipole-dipole relaxation (Solomon-Bloembergen-Morgan relaxation) as this is the primary cause of the PRE effect for an isotropic paramagnetic species with a slow electron relaxation time (relative to other dopants), as in the Gd^{3+} species used here.[304] Curie relaxation has been shown to be of minimal importance in the solid-state.[311] As all of the relaxation rates used here were measured in the high-field limit, the paramagnetic contribution has been modelled using a simple two parameter model[291,312]

$$J^P(\omega) = \frac{C_N \times 6.022 \times 10^{-7} \times \tau_{para}}{1 + (\omega\tau_{para})^2} \tag{5.2}$$

$$Q^P(\omega) = \frac{1}{6}\left(J^P(\omega_1 + 2\omega_r) + 2J^P(\omega_1 + \omega_r) + 2J^P(\omega_1 - \omega_r) + J^P(\omega_1 - 2\omega_r)\right) \tag{5.3}$$

$$R_1^{para}(\omega_{obs}) = \frac{2}{15}\omega_P^2 S(S+1)\left[3J^P(\omega_{obs})\right] \tag{5.4}$$

$$R_{1\rho}^{para}(\omega_{obs}) = \frac{1}{15}\omega_P^2 S(S+1)\left[Q^P(0) + 3J^P(\omega_{obs})\right], \tag{5.5}$$

where C_N is the concentration of the paramagnetic agent in mM, ω_P is the hyperfine coupling between ^{15}N and e^- at 1 Å in rad s^{-1}, τ_{para} is the paramagnetic interaction correlation time, and S is the electron spin quantum number (for Gd^{3+}, 7/2). The factor 6.022×10^{-7} is a conversion from concentration in mM to number density per $Å^3$. The spectral density terms including the electron Larmor frequency have been assumed negligible and omitted.[286] It should be noted that the electron-spin relaxation rate is field dependent,[305–307] and therefore in theory so is the paramagnetic correlation time τ_{para}. However, as the relaxation measurements are all from high field ($(\omega_S\tau_R)^2 \gg 1$, where τ_R is the rotational correlation time of the Gd(DTPA-

BMA) complex and ω_S the Larmor frequency of the electron) it is expected that the effective electron spin relaxation time will be on the order of microseconds, and therefore the correlation time for the paramagnetic interaction will be dominated by the field-independent rotational diffusion of the paramagnetic dopant.

For the analysis, relaxation rate sensitivities were calculated with both dynamic and paramagnetic components. Relaxation rates and their sensitivities were normalized such that the maximum value of the dynamical region of the rate sensitivity was unitary, as described in equation 2.187. The dynamic contribution was obtained using the relaxation rate expressions given in equations 2.154–2.159. Computationally, the sensitivities were defined by combining the dynamic sensitivity (discretised using 100 time points from 10^{-13} to 10^{-3} seconds) and the paramagnetic sensitivity (a single point). Detectors were then formed from these sensitivities using the SVD method outlined in Section 2.2.2.2, with the key modification of instructing the linear programming algorithm to optimize linear combinations such that the paramagnetic component of the sensitivity was equal to zero for non-paramagnetic detectors.

To determine how many detectors should be used, the number of singular values included was varied from 2 to 10. For each value of k the optimal paramagnetic timescale, τ_{para}, was determined by generating and fitting detectors over a logarithmically spaced range of 200 τ_{para} from $\tau_{para} = 100$ picoseconds to 1 microsecond, and then calculating the average χ^2 value of the back-calculated relaxation rates over all residues. The best fit value was taken as the value of τ_{para}. Then, models with different values of k were compared using the median reduced χ^2 values. The reduced χ^2 was calculated for each value of k on a per-residue basis as

$$\text{reduced}\chi^2 = \frac{1}{N_{\text{rates}} - N_{\text{detectors}} - 1} \sum_i \left(\frac{\Re_i - \Re_{bc,i}}{\sigma_i} \right)^2, \tag{5.6}$$

where N_{rates} is the number of relaxation rates, and $N_{\text{detectors}}$ is the number of detectors generated. The model selection was then performed using the median value

of the reduced χ^2, $\hat{\chi}^2$, across all of the residues for which models were fit for each value of k.

5.2.3 Molecular Dynamics and Computational Methods

Molecular dynamics simulations of the GB1:IgG complex were performed using AMBER 20.[313,314] A model of GB1:IgG was produced by combining PDB: 2GI9[315] (GB1), 1FCC[299] (GB1 + Fc domain of human-derived IgG), 1IGC[298] (GB3 + Fab domain of mouse-derived IgG), and 6P9I[316] (Fab domain of human-derived IgG) using ChimeraX.[317] Note that only part of the complex shown in Figure 5.1a was simulated, comprising a single Fab domain, a single Fc domain, and a single GB1. The structure was protonated according to a pH of 5.5 using the PlayMolecule ProteinPrepare webserver.[318] The structure was then neutralised with Na^+ and Cl^-, with additional salt ions added up to a concentration of 50 mM. The ff19SB force field[319] was used, solvated with a 10 Å octahedral box of explicit OPC water.[320] Following minimisation and heating to a temperature of 300 K, two repeats of 500 ns of classical MD (cMD) were performed. For each step, a 2 fs timestep was used with a cut-off of 11 Å for non-bonded interactions. Temperatures were maintained using a Langevin thermostat, with the SHAKE algorithm[321] applied to all bond lengths involving a hydrogen atom. Anisotropic pressure scaling was used with periodic boundary conditions.

The structure was then aligned to remove the overall tumbling. Correlation functions were extracted using cpptraj.[322] These were inverse Laplace transformed according to a previously published method for detector analysis,[161] using 199 decaying exponentials with correlation times ranging logarithmically from 1 ps to 250 ns, and an additional decaying exponential to represent the limit using a correlation time of 1 ms. The MD detector responses were then calculated by integrating the product of the detector sensitivity, and the ILT profile. To investigate the relationship between the paramagnetic detector and the electron-nucleus distance, molecular surfaces were then calculated for frames extracted every 200 ps using MSMS,[323]

with a probe radius of 3.5 Å to represent the paramagnetic dopant.

5.3 Results and Discussion

5.3.1 Application to Microcrystalline GB1

In order to determine whether adequate separation of paramagnetic and dynamical contributions to relaxation could be achieved using this method, the analysis was firstly performed on microcrystalline GB1. Good quality experimental data can be obtained in a reasonable experimental time for both diamagnetic (undoped) and paramagnetically doped samples of microcrystalline GB1, for which the underlying dynamical contributions should be equivalent. In the diamagnetic case, six relaxation rates measured in the absence of Gd^{3+} were used. In the paramagnetic case, three relaxation rates measured in the presence of Gd^{3+} were used in addition to three relaxation rates measured in the absence of Gd^{3+}. The datasets were chosen such that the dynamical responses in the paramagnetic case would be reliant on incorporating the doped relaxation data, and therefore the resulting dynamics would be dependent on the quality of the separation of dynamic and paramagnetic sensitivities.

Owing to the non-linear dependence of the relaxation rate on the paramagnetic correlation time, this was treated as a global fitting parameter and was varied logarithmically from 100 picoseconds to 1 microsecond in 200 steps. For each step, detectors were formed from a truncated singular value decomposition using the first $k = 2 - 10$ singular values. Figure 5.2 shows how the average χ^2 varies as a function of the paramagnetic correlation time, τ_{para}, for the paramagnetic case. Only k and τ_{para} values for which detectors could be formed are shown.[||] It is found for $k = 3$ and $k = 4$ that the paramagnetic correlation time is $\approx 43 - 47$ ns. Table 5.4 gives the reduced $\hat{\chi}^2$ as a function of the number of included singular values, k,

[||] Noting that compared to typically detector optimization, the additional constraint that the response of a dynamical detector to paramagnetic effects be zero causes this optimization to fail in cases that this is not possible.

for both the diamagnetic and paramagnetic cases. The value of $\hat{\chi}^2$ lowest in the paramagnetic case was $k = 3$, giving two dynamic detectors and one paramagnetic detector. In the diamagnetic case, the lowest $\hat{\chi}^2$ value was $k = 2$, composed of two dynamical detectors.

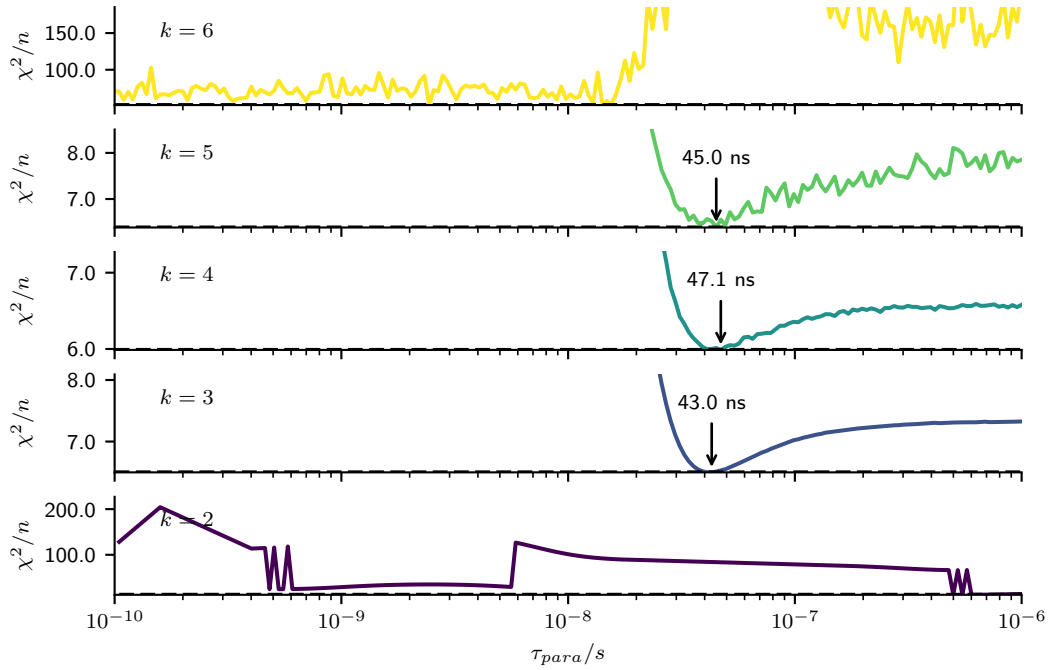

Figure 5.2: Average χ^2 values as a function of paramagnetic correlation time and the number of included singular values for microcrystalline GB1. The value of τ_{para} giving the minimum average χ^2 value is annotated for $k = 3 - 5$.

Table 5.4: Summary statistics for microcrystalline GB1 models.

k	diamagnetic $\hat{\chi}^{2**}$	paramagnetic $\hat{\chi}^2$	τ_{para} / ns
2	**135.6**	17.5	547.9
3	150.5	**14.6**	43.0
4	315.9	26.1	47.1

The resulting dynamical responses for both the diamagnetic and paramagnetic cases in microcrystalline GB1 are shown in Figure 5.3. There is overall very good agreement between the dynamic responses for the diamagnetic and paramagnetic cases, indicating that adequate separation of paramagnetic and diamagnetic contributions to relaxation was achieved.

**Median reduced χ^2

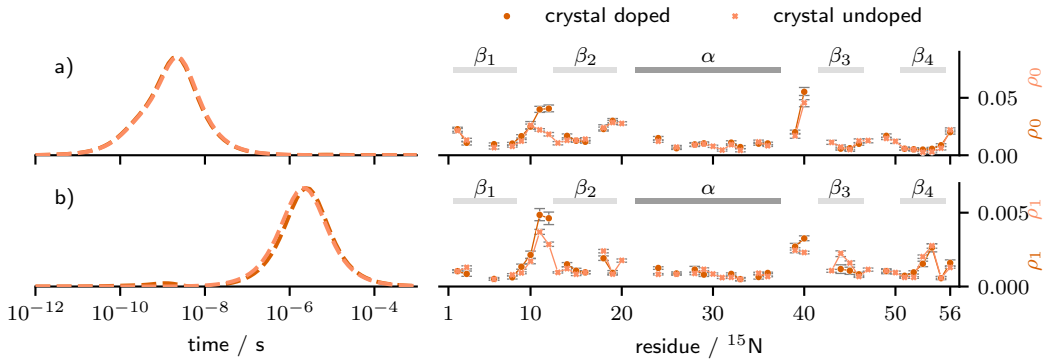

Figure 5.3: Comparison of the resulting dynamical detectors produced for the paramagnetically-doped microcrystalline GB1 dataset (noting that this dataset contained some undoped data) and the diamagnetic microcrystalline GB1 datasets. Very good agreement is found.

5.3.2 Application to GB1:IgG Complex

Following the analysis on microcrystalline GB1, the technique was applied to the GB1:IgG complex. The analysis was performed using 19 relaxation rates, measured Gd^{3+} concentrations ranging from 1.0–7.5 mM. As in the microcrystalline GB1 case, the paramagnetic correlation time τ_{para} was treated as a global fit parameter and was varied logarithmically from 100 picoseconds to 1 microsecond in 200 steps. Detectors were formed using the SVD method for each timestep using the first $k = 2 - 10$ singular values. Figure 5.4 shows how the average χ^2 value varies as a function of τ_{para} for each value of k. Substantial discontinuities are observed for $k = 2$, likely owing to there being only two detectors to consider three relatively separate relaxation contributions (fast and slow motions, paramagnetic interaction); depending on the value of τ_{para}, the model may fit any two of these relatively well, which will lead to sudden variation in the average χ^2. For $k = 3$ to 5, well-defined profiles of τ_{para} are observed with minima of $\approx 25 - 27$ ns. For $k \geq 6$ the τ_{para} becomes overwhelmed by noise suggesting overfitting.

In order to determine how many k values should be included in the following analysis, both average χ^2 (χ^2/n, where n is the total number of relaxation rates for all residues) and median reduced χ^2 ($\hat{\chi}^2$) values were calculated for each value of k

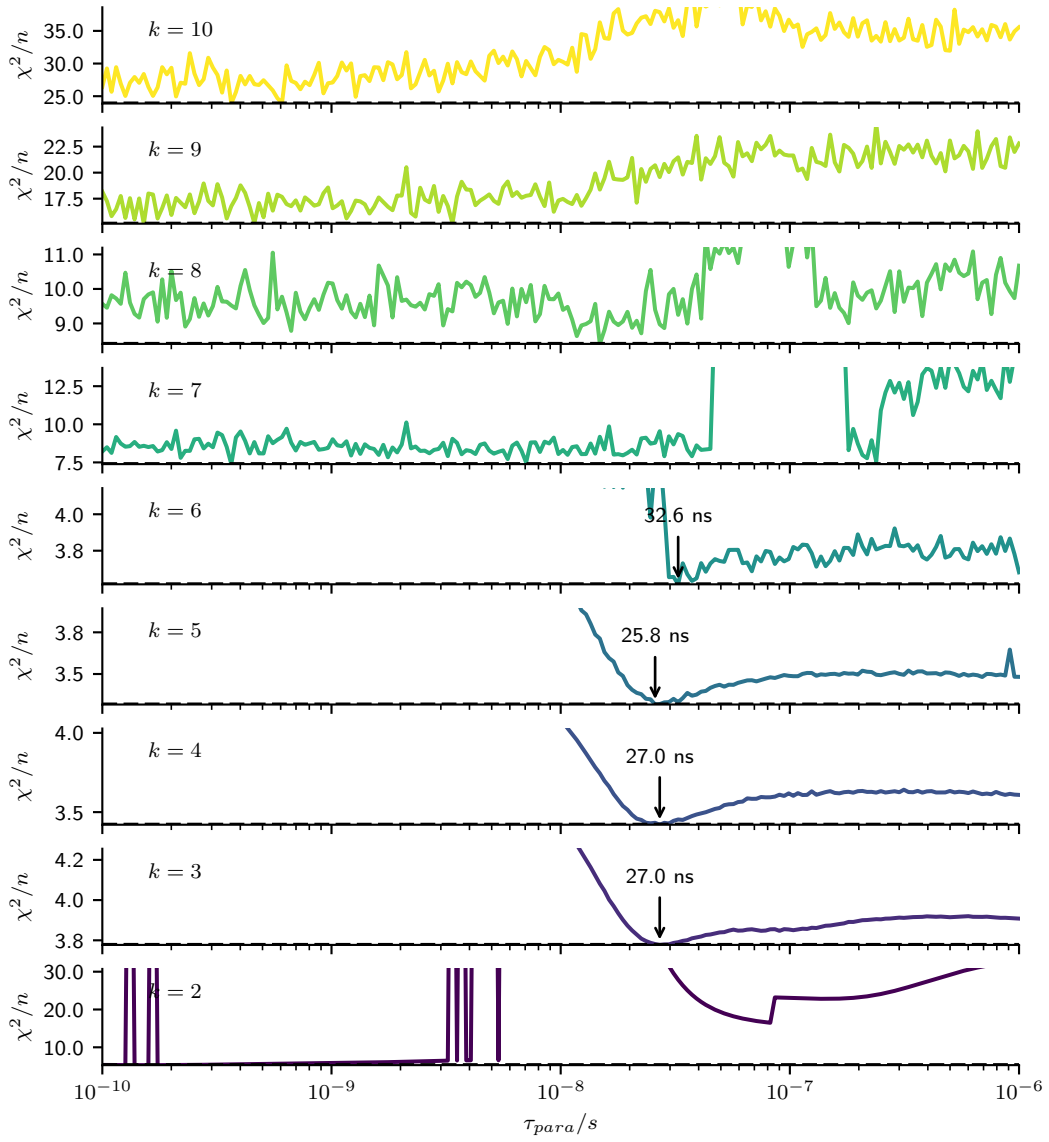

Figure 5.4: Average χ^2 values over all residues as a function of paramagnetic correlation time and the number of included singular values. The value of τ_{para} giving the minimum reduced χ^2 value is annotated for $k = 3 - 6$.

using the respective optimal values of τ_{para} obtained from Figure 5.4. The reduced χ^2, denoted as $\hat{\chi}^2$, was calculated on a per-residue basis with the median value taken for each value of k. The resulting summary statistics are outlined in Table 5.5.

As in Figure 5.4, the fit quality (χ^2/n) improves as k increases from 2 to 5, before rapidly declining as k increases. For minimum value of $\hat{\chi}^2$ indicates $k = 4$ as the most parsimonious fit. The model with $k = 4$ was therefore used for further

analysis, calculated using $\tau_{para} = 27.0$ ns. It should be noted, however, that the dynamic and paramagnetic responses do not vary significantly for different values of k; Appendix A shows the detectors and responses arising from analysis with $k = 3$ and $k = 5$, which show very similar profiles of motions to those obtained with $k = 4$ shown here.

Table 5.5: Summary statistics for GB1:IgG dynamic/paramagnetic model fitting.

k	χ^2/n[††]	$\hat{\chi}^2$[‡‡]	τ_{para} / ns
2	5.28	5.66	0.16
3	3.72	4.72	27.0
4	3.42	**4.47**	27.0
5	3.33	4.70	25.8
6	3.52	5.37	32.6
7	8.65	13.65	— [§§]
8	8.78	13.00	—
9	16.54	27.84	—
10	28.27	50.50	—

5.3.2.1 Paramagnetic Correlation Times

Before moving on to look at the detector responses, it is interesting to consider the values of the paramagnetic correlation times obtained here. The paramagnetic correlation times in theory contain contributions from electron spin relaxation (T_{1e}), chemical exchange (τ_M), and molecular tumbling (τ_r):

$$\frac{1}{\tau_{para}} = \frac{1}{T_{1e}} + \frac{1}{\tau_M} + \frac{1}{\tau_r}. \tag{5.7}$$

The electron spin relaxation time of the Gd^{3+} complex used here is highly dependent on magnetic field. In the high-field limit, it has been shown to be proportional to the square of the magnetic field.[305] It would therefore be expected to be on the order of microseconds under the experimental conditions used here. This paramagnetic correlation therefore likely relates to molecular tumbling of the Gd^{3+}

[††]Average χ^2 over all residues, where n is the number of relaxation rates across all residues.
[‡‡]Median reduced χ^2
[§§]$k \geq 7$ were too noisy to determine τ_{para}

complex, which would occur on a much faster timescale and therefore dominate the correlation time.[324] This molecular tumbling correlation time arises from rotational diffusion[115]

$$\tau_r = \frac{1}{6D_r}, \tag{5.8}$$

where D_r is the rotational diffusion coefficient. Assuming that the Gd^{3+} can be modelled as an isotropic sphere, this rotational diffusion coefficient may be approximated using the Stokes-Einstein-Debye equation[325,326]

$$\tau_r \approx \frac{4\pi\eta r^3}{3kT}, \tag{5.9}$$

where η represents the solvent viscosity, r the spherical radius of the Gd^{3+} (approximately 3.5 Å[327]), k the Boltzmann coefficient, and T temperature. In the microcrystalline GB1 case τ_{para} was found to be ≈ 45 ns (Table 5.4), while in the complex it is found to be ≈ 27 ns (Table 5.5). The same paramagnetic dopant and temperature was used in both cases, suggesting that the difference in the resulting correlation time arises due to a difference in viscosity between the two samples. Table 5.6 gives approximate viscosities for the two samples assuming the above relations, with comparison to liquid water at 293.15 K and atmospheric pressure.[328,329] It should be noted, however, that the local water environment surrounding the proteins would likely be highly heterogeneous.

Table 5.6: Viscosities calculated using the calculated paramagnetic correlation times. Errors on the calculated viscosities are likely on the order of 100–200 mPa s.

sample	τ_{para} / ns	η / mPa s
water[328,329]	—	1.0016
GB1:IgG complex	≈ 27	≈ 600
microcrystalline GB1	≈ 45	≈ 1000

The viscosity in the protein systems is significantly greater than that of the water, likely due to the crowded environment and protein-protein interactions.[326] The

higher viscosity in the case of microcrystalline GB1 may indicate greater crowding in this system compared to the complex.

5.3.2.2 Dynamic and Paramagnetic Detector Responses

The 4 detectors formed, and their responses, are shown in Figure 5.5. One is mostly sensitive to picosecond-nanosecond dynamics: ρ_0 (primarily composed of R_1 rates and with similar pattern of responses). Two are mostly sensitive to nanosecond-microsecond motions: ρ_1, ρ_2. (primarily composed of $R_{1\rho}$ rates and again with a similar pattern of responses). One is sensitive to the paramagnetic interaction: ρ_3. These responses are calculated simply as linear combinations of the contributing relaxation rates, weighted according to the SVD optimized detector vectors (see Section 2.2.2.2). For example, ρ_0 is calculated as:

$$
\begin{aligned}
\rho_0 = {} & 0.185 \times \Re_1(\text{600 MHz, 60.0 kHz, 0.0 kHz, 3.5 mM}) \\
& -0.020 \times \Re_1(\text{600 MHz, 60.0 kHz, 0.0 kHz, 5.0 mM}) \\
& -0.362 \times \Re_1(\text{600 MHz, 60.0 kHz, 0.0 kHz, 7.5 mM}) \\
& 0.035 \times \Re_{1\rho}(\text{700 MHz, 60.0 kHz, 10.0 kHz, 1.0 mM}) \\
& 0.018 \times \Re_{1\rho}(\text{700 MHz, 60.0 kHz, 10.0 kHz, 2.0 mM}) \\
& -0.009 \times \Re_{1\rho}(\text{700 MHz, 60.0 kHz, 10.0 kHz, 3.5 mM}) \\
& 0.018 \times \Re_{1\rho}(\text{700 MHz, 60.0 kHz, 10.0 kHz, 2.0 mM}) \\
& -0.022 \times \Re_{1\rho}(\text{850 MHz, 60.0 kHz, 15.5 kHz, 5.0 mM}) \\
& -0.020 \times \Re_{1\rho}(\text{850 MHz, 60.0 kHz, 20.4 kHz, 5.0 mM}) \\
& -0.023 \times \Re_{1\rho}(\text{850 MHz, 60.0 kHz, 10.2 kHz, 5.0 mM}) \\
& 0.289 \times \Re_1(\text{700 MHz, 60.0 kHz, 0.0 kHz, 3.5 mM}) \\
& 0.013 \times \Re_{1\rho}(\text{1000 MHz, 50.0 kHz, 11.2 kHz, 3.5 mM}) \\
& 0.465 \times \Re_1(\text{1000 MHz, 50.0 kHz, 0.0 kHz, 3.5 mM}) \\
& -0.008 \times \Re_{1\rho}(\text{700 MHz, 60.0 kHz, 14.2 kHz, 3.5 mM})
\end{aligned}
$$

$$
\begin{aligned}
&-0.006 \times \Re_{1\rho}(\text{700 MHz, 60.0 kHz, 19.8 kHz, 3.5 mM}) \\
&-0.003 \times \Re_{1\rho}(\text{700 MHz, 60.0 kHz, 25.2 kHz, 3.5 mM}) \\
&\;\;0.001 \times \Re_{1\rho}(\text{700 MHz, 60.0 kHz, 32.1 kHz, 3.5 mM}) \\
&\;\;0.006 \times \Re_{1\rho}(\text{700 MHz, 60.0 kHz, 39.2 kHz, 3.5 mM}) \\
&\;\;0.450 \times \Re_{1}(\text{700 MHz, 60.0 kHz, 0.0 kHz, 2.0 mM})
\end{aligned} \tag{5.10}
$$

where the parameters of each relaxation rate are ^{1}H Larmor frequency (MHz), MAS frequency (kHz), Spin Lock frequency (kHz), and [Gd^{3+}] (mM). The dynamical responses (ρ_0, ρ_1, ρ_2) show no sensitivity to the paramagnetic interaction, indicating that good separation has been achieved. The paramagnetic response shows very slight sensitivity to slow motions, however this is expected to comprise only a very small proportion of the total response.[¶¶]

As expected, larger amplitude ps-ns motions were observed for loops and edges of β-strands. The responses for microsecond motions are much flatter but again mostly elevated in the loops between $\beta_2 - \alpha$ and $\beta_3 - \beta_4$. Note also that there is a correlation between the paramagnetic response (ρ_3) and the fast motion dynamics response (ρ_0), likely because greater solvent exposure enables greater mobility.[330]

Using these detector responses, the separated dynamic and paramagnetic relaxation contributions were back-calculated for several relaxation rates by setting either the paramagnetic or dynamic responses to 0 prior to calculation. Figure 5.6 and 5.7 show the relative contributions of the dynamic and paramagnetic relaxation to a series of R_1 and $R_{1\rho}$ (respectively) rates measured with varying concentrations of [Gd^{3+}]. These illustrate that for the concentrations of [Gd^{3+}] used here, the dynamic and paramagnetic contributions to relaxation are on a similar order of magnitude for both R_1 and $R_{1\rho}$ relaxation rates. It should be noted that the analysis presented here for the paramagnetic terms is similar to previous solvent paramagnetic relaxation enhancement (sPRE);[50,291,293,331] in both cases, it is effectively the difference in

[¶¶]Note that for $k = 5$, full separation is achieved.

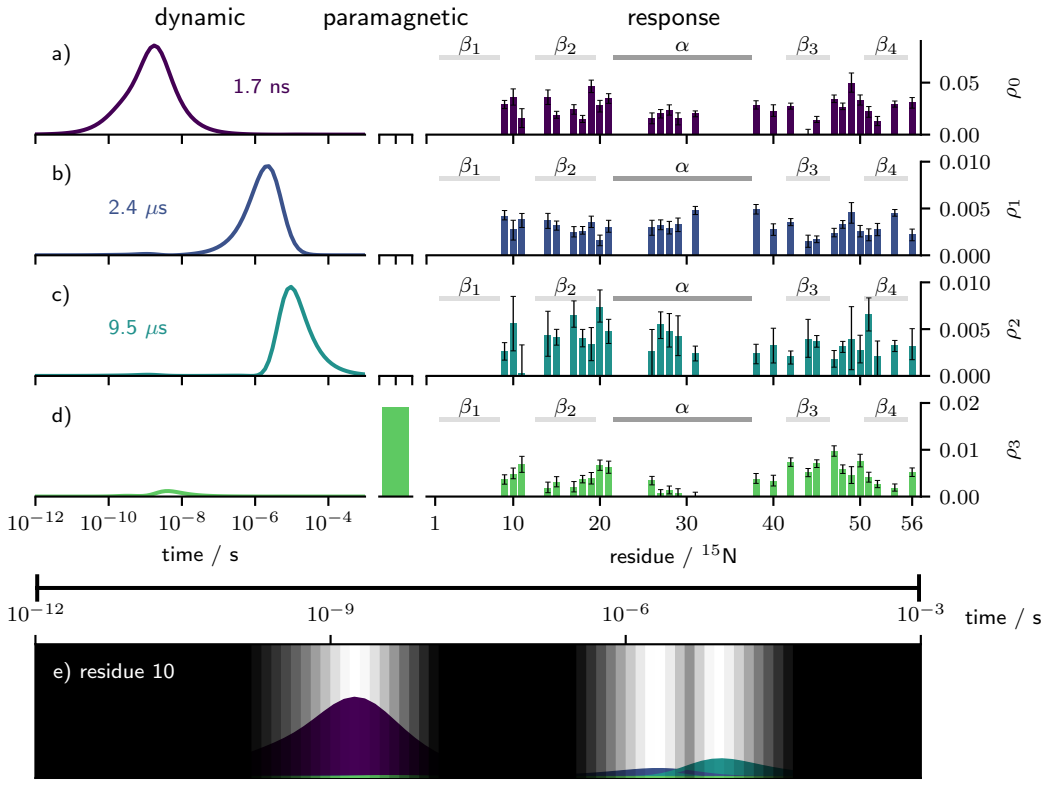

Figure 5.5: Detector sensitivities and their responses. (a-d) Detectors and responses produced from GB1:IgG complex analysis. The leftmost panel shows the detector sensitivity to local dynamics, where for detectors with no paramagnetic response the timescale corresponding to the maximum of the sensitivity is given. The middle panel shows the detector sensitivities to the paramagnetic interaction. The rightmost panel shows the resulting detector responses arising from these detectors. In the rightmost panel, the horizontal bars refer to the secondary structure of the protein; light grey indicating β-strand and dark grey α-helix. Residues for which overlap prevented site-specific relaxation rate measurement for more than 5 relaxation rates have been omitted. (e) Depiction of the timescales of motion for residue 10. Detectors are shown scaled by their integral normalized responses to give an indication of the timescales over which motion is occurring. Regions where the relaxation rate is insensitive are shaded out.

relaxation rate with different concentrations of paramagnetic dopant which allows for the PRE to be quantified. One benefit of this method, among others, is that by simultaneously quantifying the dynamics and dynamical sensitivity the variation in several relaxation rates under different conditions with the paramagnetic dopant concentration is used, thereby giving greater accuracy in the resulting paramagnetic response.

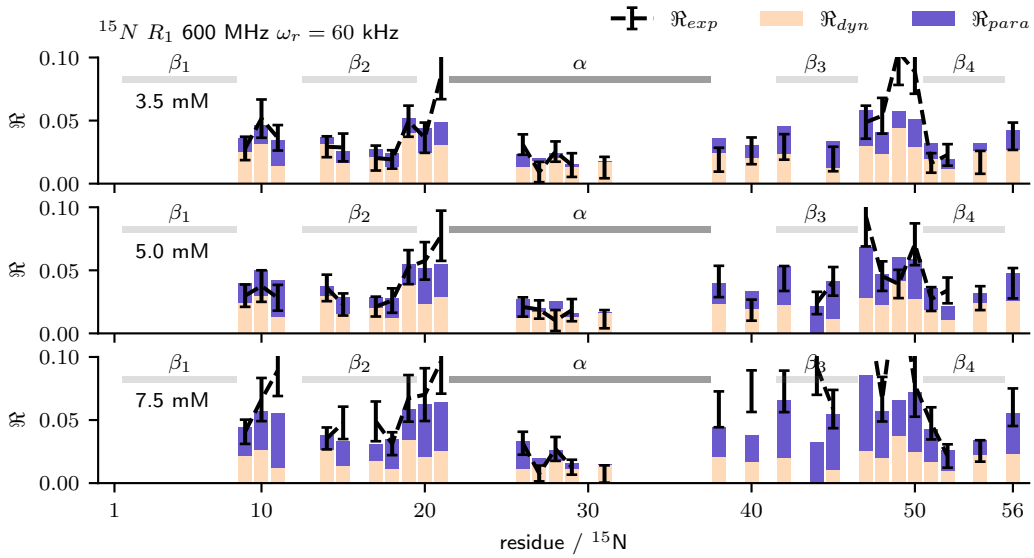

Figure 5.6: The relative contributions of dynamic ($\Re_{dyn}$) and paramagnetic ($\Re_{para}$) relaxation to the overall relaxation rates are shown for ^{15}N R_1 relaxation rates measured at $\nu_0(^1\text{H})$ = 600 MHz and a MAS frequency of 60 kHz, using a range of concentrations of $[Gd^{3+}]$. Note that $\Re$ indicates that these relaxation rates have been normalized such that the sensitivity of the rate is unitary, as in equation 2.187.

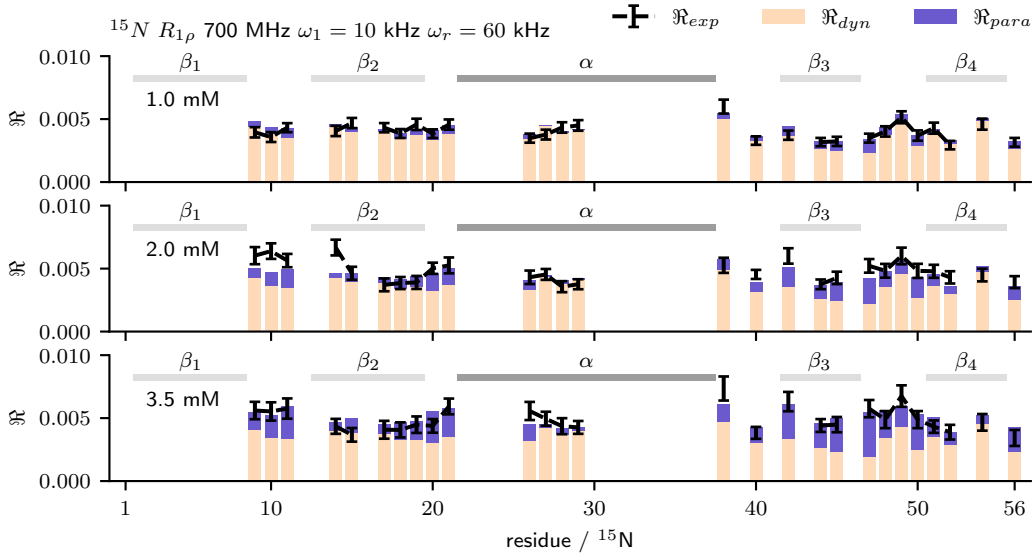

Figure 5.7: The relative contributions of dynamic ($\Re_{dyn}$) and paramagnetic ($\Re_{para}$) relaxation to the overall relaxation rates are shown for ^{15}N $R_{1\rho}$ relaxation rates ($\nu_0(^1\text{H})$ = 700 MHz, ν_1 = 10 kHz, ν_r = 60 kHz) recorded at a range of $[Gd^{3+}]$. Note that $\Re$ indicates that these relaxation rates have been normalized such that the sensitivity of the rate is unitary, as in equation 2.187.

5.3.2.3 Comparison with Undoped GB1:IgG complex

Previously, six relaxation rates have been recorded for the complex in the absence of paramagnetic dopant. Due to the poor sensitivity of the complex, coupled with the requirement for long relaxation delays, these are of significantly poorer quality than those measured on the doped data. A comparison between the responses obtained from the doped and undoped datasets is shown in Figure 5.8. Owing to the smaller dataset obtained on the undoped dataset only two detectors were able to be produced; a linear sum assignment algorithm was used to pair up the detectors to optimize the pairing to give the greatest total integral overlap. In order to account for the different sensitivities of the paired detectors, the responses in the undoped sample were scaled by the ratio of the integrals. The responses between the doped and undoped samples are similar for the majority of residues. While some differences exist, it is likely these are related to the poor quality of the undoped dataset.

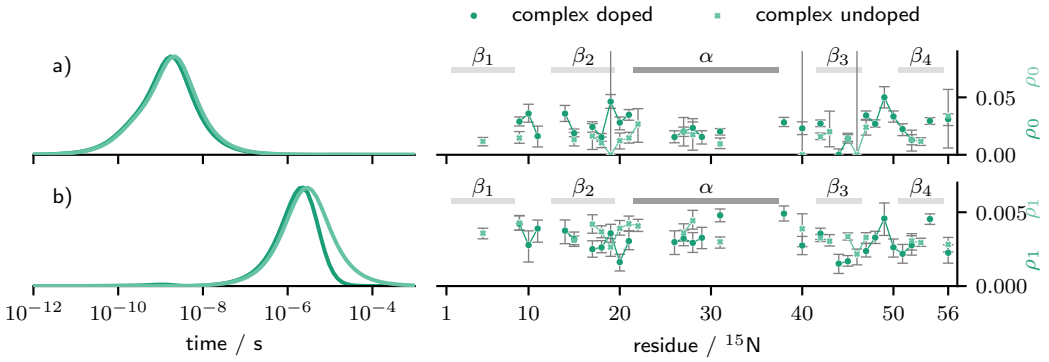

Figure 5.8: Comparison of the dynamical profiles arising from analysis of doped GB1:IgG (dark green) and undoped GB1:IgG (light green).

5.3.2.4 Comparison with Molecular Dynamics

To further explore the dynamical profile obtained here, molecular dynamics simulations were performed. Since as it has previously been demonstrated that the general interfaces defined by studies of GB1-like domains with fragments of IgG are very similar to what is found in the full construct (with small differences),[49,258] a

truncated complex reflecting those interactions was simulated by combining crystal structures of subdomains of IgG with GB1(/GB3), which were aligned relative to a crystal structure of GB1 (PDB:2GI9[315]) (the coloured protein in Fig. 5.1a).

Firstly, the response of the paramagnetic detector, ρ_3 was examined by way of comparison with MD. Frames were taken from each of the two 500 ns classical MD sampled every 200 picoseconds, with a molecular surface calculated for each frame assuming a probe radius, r_{probe}, of 3.5 Å (corresponding to the approximate radius of the Gd^{3+} complex[327]). Using this surface, the distance, $r_{\text{n-n,closest}}$, from each backbone ^{15}N to the closest possible Gd^{3+} site was calculated. The actual closest distance between the ^{15}N nucleus and the interacting electron, $r_{\text{e-n,closest}}$, is calculated by subtracting the ionic radius of the Gd^{3+} ion, $r_{\text{Gd,ionic}}$, taken here to be 1.1 Å.[332] Figure 5.9 illustrates the different distances which will be referred to in this section. As shown in Figure 5.10a there is a good correlation ($R^2 = 0.76$) between the resulting closest distance, $r_{\text{e-n,closest}}$, and the inverse of the paramagnetic detector. The nature of this relationship will be discussed further here.

In the parameterisation of the paramagnetic relaxation enhancement used here, the paramagnetic response should be related to the distance scaling between the ^{15}N nucleus and the unpaired electrons within the Gd^{3+} complex. Formally, the hyperfine coupling is proportional to the cube of the distance between the electron and the nucleus. As a result, the value of the paramagnetic response would be expected to scale as the sixth power of this electron nucleus distance

$$\rho_3 = r_{\text{e-n}}^{-6}. \tag{5.11}$$

However, as the paramagnetic species is in the solvent, it would not be expected to adopt a fixed distance to a given ^{15}N site. Instead, the PRE would reflect an averaged ensemble of different potential distances, characterised by an effective distance, $r_{\text{e-n, eff}}$

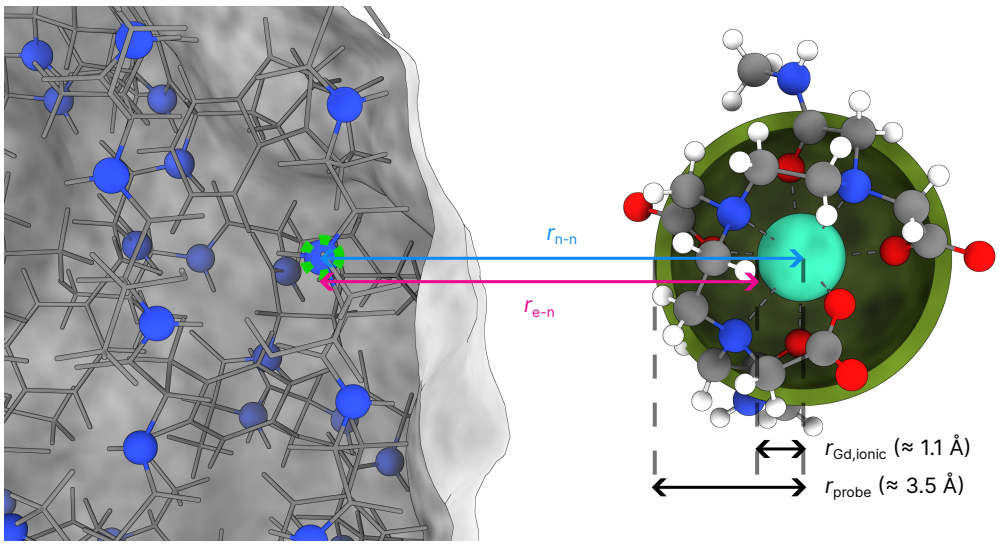

Figure 5.9: Illustration of the distances used in the analysis of the MD. On the left, GB1 is shown. Nitrogen atoms are shown as blue spheres. The surface was calculated using a probe radius, r_{probe}, of 3.5 Å. On the right, the Gd(DTPA-BMA) complex is shown. The outermost green sphere represents the probe radius used in calculations. The inner light green sphere represents the ionic radius of the Gd^{3+} ion. The distance between the selected (highlighted in green) nitrogen atom and the centre of the Gd^{3+} is represented as a blue line, $r_{\text{n-n}}$. The corresponding electron-nucleus distance is given as the pink line, $r_{\text{e-n}}$.

$$\rho_3 = r_{\text{e-n, eff}}^{-6}. \tag{5.12}$$

The ensemble averaged nature of this dependence has been studied in detail by Linser *et al.* (2009).[293] There, the effective distance was expressed by considering it to be an average over a conical volume. Their equation 5 has been included here:

$$r_{\text{e-n, eff}}^{-6} = \int_0^{\infty} \int_0^{\phi_{\text{lim}}} \int_0^{\theta_{\text{lim}}} r_{\text{e-n}}^{-6} r'^2 \sin\theta d\theta d\phi dr' \tag{5.13}$$

$$r_{\text{e-n}} = \sqrt{r_{\text{e-n, closest}}^2 + r'^2 + 2r_{\text{e-n, closest}} r' \cos\theta}, \tag{5.14}$$

where the integral limits θ_{lim} and ϕ_{lim} relate to the concavity or convexity of the surface at this point; for a planar surface, these would be $\theta_{\text{lim}} = \pi/2$ and $\phi_{\text{lim}} = 2\pi$. $r_{\text{e-n, closest}}$ represents the shortest possible distance between the electron and the

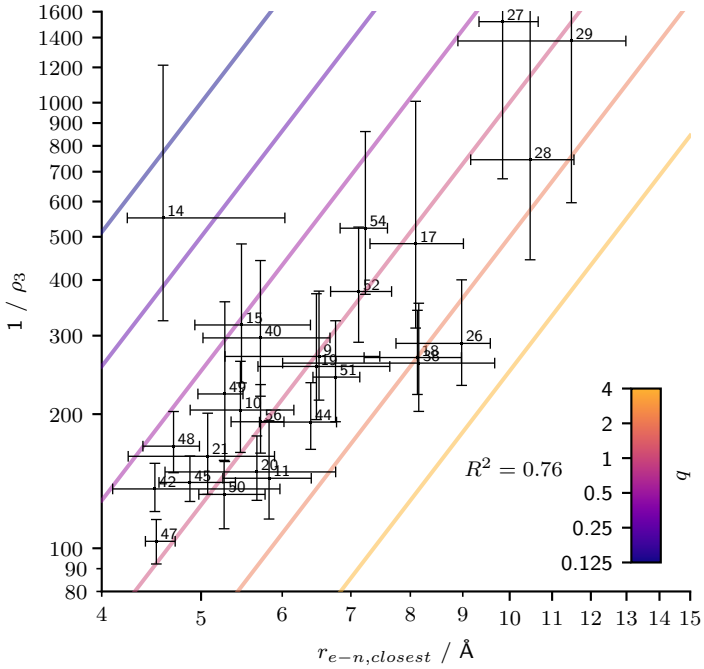

Figure 5.10: Comparison of the MD derived closest electron-nucleus distances ($r_{\text{e-n,closest}}$) for a model of the complex and the inverse of the paramagnetic detector response. Lines are plotted according to equation 5.17 for varying values of q.

nucleus. This integral is approximated well by

$$r^{-6}_{\text{e-n, eff}} = \frac{q}{r^{3}_{\text{e-n, closest}}}, \tag{5.15}$$

where the value of the proportionality constant q is dependent on the specifics of the protein surface at that point. For instance, a ^{15}N site buried inside a protein interface may only be accessible to the solvent, and hence the paramagnetic species, from a very specific orientation. As a result, q for this site would be expected to be lower, such that the effective distance is increased.

To relate this discussion to the paramagnetic analysis here, equation 5.15 may be substituted into equation 5.12. The paramagnetic response is then expected to be

$$\rho_3 = q r^{-3}_{\text{e-n, closest}}. \tag{5.16}$$

To aid visualisation, the inverse of the detector has been taken such that

$$\frac{1}{\rho_3} = \frac{1}{q} r^3_{\text{e-n, closest}}. \tag{5.17}$$

This equation has been plotted on alongside the experimental and MD comparison in Figure 5.10. The majority of sites fall along $q = 1$. Notable exceptions include Gly_{14}, which appears shifted to a higher value of q, possibly indicating lower angular solvent accessibility, and Thr_{18}, Ala_{26}, Gly_{38}, which appear shifted to a lower value of q, which may indicate greater angular accessibility.

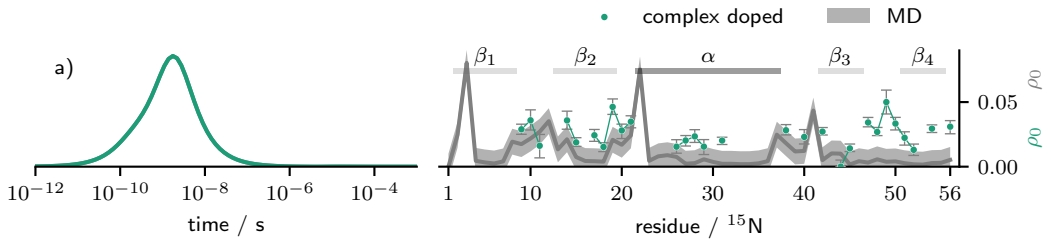

Figure 5.11: Comparison of detector responses for GB1 in the complex (green) with responses derived from $2\times$ 500 ns-molecular dynamics simulations (grey bars). The error bars on the MD responses have been estimated at ± 0.01.

Figure 5.11 compares the detector responses for GB1 in the complex with those calculated from an MD simulation of the complex fragment corresponding to the blue, red and yellow parts in Fig. 5.1a. Reasonable agreement between responses calculated from relaxation data and MD simulations is found for most of the polypeptide chain except for the $\beta_3 - \beta_4$ loop, which is much more mobile on fast ps-ns time scale based on the experimental data. While two repeats of the MD were performed, note that it is unlikely these will have fully sampled the dynamics; for comparison, consider the range of responses found in the 108 protein repeats in Figure 6.12 (see Chapter 6), where the range of possible responses from the MD is substantial. Interestingly, the ps-ns responses for the $\beta_3 - \beta_4$ loop calculated from the model of the complex are similar to the experimental responses for that region in microcrystalline GB1. Notably, the model of the complex uses conformation of GB1

found in crystals for which the $\beta_3 - \beta_4$ loop is stabilised by a network of backbone to backbone and side chain to backbone hydrogen bonds. The difference in the case of the complex may indicate that this hydrogen bond network is disrupted owing to interactions with the IgG.

5.3.2.5 Comparison with Microcrystalline GB1

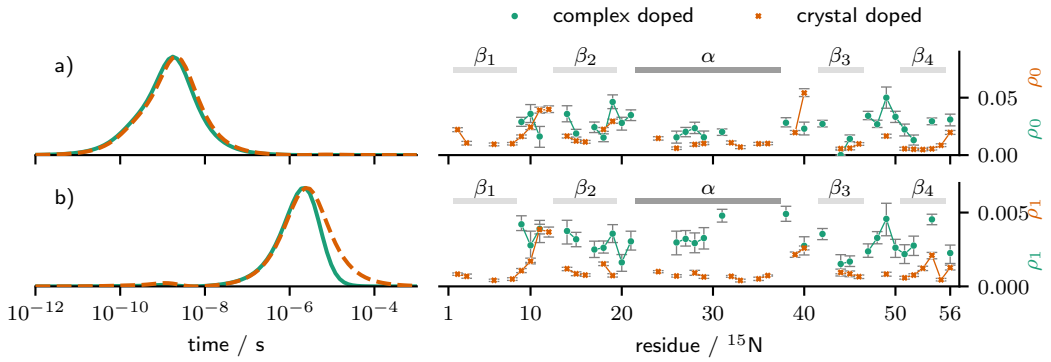

Figure 5.12: Comparison of detector responses for GB1 in the complex (green, solid) with (doped) microcrystalline GB1 (orange, dashed). These detectors have been matched to find the most optimal pairing (closest corresponding time scale), as the different datasets give rise to different sets of detectors.

Structurally, the microcrystalline and complex forms of GB1 are expected to differ only in their intermolecular interfaces, with the intramolecular fold of the GB1 protein being retained in both cases. As a result, a comparison of the local dynamics in each case may provide insight as to the effect of intermolecular interactions on the local protein dynamics.

Figure 5.12 compares detector responses from microcrystalline GB1 (the doped case from Section 5.3.1) and those in the complex. Owing to the different sensitivities of the rates used for these two analyses, these have been paired such that the timescales best correspond to one another. The microcrystalline responses have been scaled by the ratio of their respective sensitivity integrals to allow for direct comparison. For the fast motion detectors, ρ_0 (crystal) and ρ_0 (complex), there exists reasonable agreement from the *N*-terminus to the end of the α-helix. Poorer agreement for the fast ps-ns motions between microcrystalline GB1 and GB1 in the complex with

IgG is seen in the part of the polypeptide stretching from $\beta_3 - \beta_4$. A reduction in motional amplitudes for Asp_{40} is observed in the complex relative to the crystal, which is consistent with reduced solvent accessibility for this region in the complex. A relative increase in fast ps-ns mobility in the $\beta_3 - \beta_4$ loop in the complex is also noted. The reduced ps-ns mobility of the $\beta_3 - \beta_4$ loop may be related to the presence of a stabilising network of hydrogen bonds which may be disrupted in the complex as discussed previously in Section 5.3.2.4.

The β_2 strand is involved in an extended intermolecular β sheet in both the complex[297] and microcrystalline forms.[333] Figure 5.13 compares the fast (ρ_0, ps-ns) motional profiles arising in β_2 more closely for the two forms. A notable feature in both microcrystalline GB1 and in the complex is a stretch of 3–4 amino acids for which a reduction in detector response is observed (Glu_{15}-Thr_{18} in the complex, Lys_{13}-Thr_{16} for the microcrystalline form). This reduction likely relates to the formation of both inter- and intra-molecular $\beta - \beta$ hydrogen bonds, which would inhibit relaxation-active motion of the $^{15}N-^{1}H$ dipole (see Chapter 6). However, there exists an offset in which residues show this effect in the two forms, which may indicate a difference in the intermolecular contact in the two forms of GB1.

Returning to Figure 5.12, greater microsecond detector responses (ρ_1) are observed for GB1 in the complex relative to the microcrystalline form. Previously, Krushelnitsky *et al*. (2018) presented a NERRD analysis of the microcrystalline form of GB1 averaged over the whole protein (*i.e.* using bulk rather than site-specific rates) and found a very high effective order parameter (0.9995),[121] indicating there is very little overall microsecond motion. On the other hand, both relaxation dispersion studies[51] and qualitative $R_{1\rho}$ comparisons[258] have suggested significant microsecond motions in the GB1:IgG complex. The relatively uniformly elevated detector responses for these microsecond motions shown here for the complex suggest that for GB1 in the complex these microsecond motions may be predominantly composed of overall whole-body rocking motions (as suggested previously in ref 258), whereas in the crystal these may be more local domain microsecond motions.

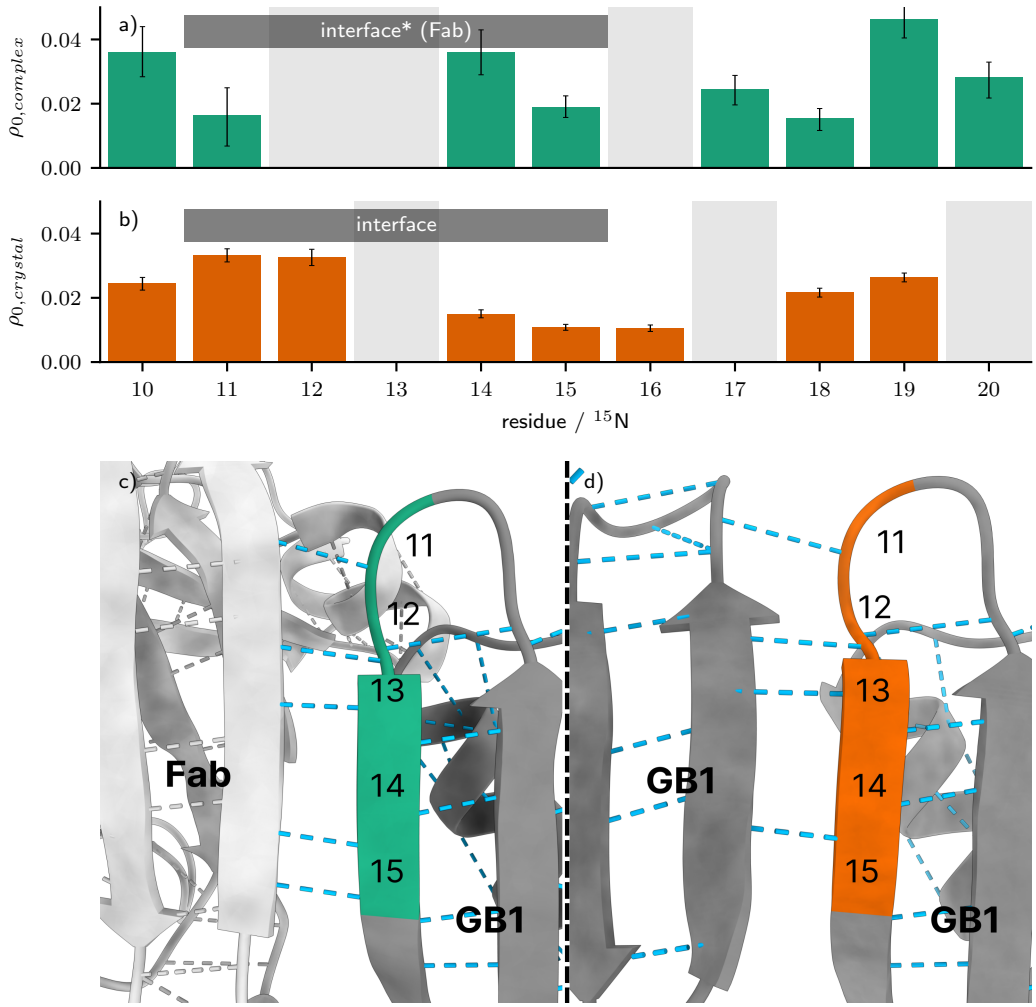

Figure 5.13: (a,b) Fast (ns) motion detector responses for GB1 in the complex with IgG (a) and microcrystalline GB1 (b) for β_2. (c,d) Structure of the interfaces at β_2 in the complex (c) and in the microcrystalline form (d). The hydrogen bonding interfaces to neighbouring proteins are highlighted in (a) and (b), and are coloured in (c) and (d). (Note that the interface for the complex is taken from a structure of the Fab domain with GB3,[297] and may not correctly reflect the interface with the full-length construct[49,50]).

5.3.3 Reduced Datasets and Time Savings

Quantification of dynamics in the presence of paramagnetic dopants necessitates recording more experiments compared to quantification of dynamics in their absence because of the need to additionally characterise the paramagnetic contribution to relaxation. The time savings due to shortening both recycle delay and relaxation delays (due to the reduction of the relaxation times) can compensate for need to

measure additional experiments (see Figure 5.1b,c). However, recording such a large relaxation rate dataset still requires a substantial time investment. The use of smaller datasets was therefore investigated, as these could provide insight into the dynamics in the presence of paramagnetic dopant while saving additional experimental time. In the case of these smaller datasets, a residue was omitted if any relaxation rates were missing from the dataset.

The relaxation rates used in this analysis were recorded over several years under different experimental conditions. To allow for comparison of the experimental time of each, standardised experimental times were calculated for each of them assuming a standard set of conditons;

- 364 coadded transients, for each of 64 indirect FIDs
- the recycle delay was taken as 2 s for undoped samples, 1 s for $0 < [\mathrm{Gd}^{3+}] \leq 1.5$ mM, 0.5 s for $[\mathrm{Gd}^{3+}] > 1.5$ mM
- 8 relaxation delays were used, placed at $1\times$, $1/2\times$, $1/4\times$, $1/8\times$, $1/16\times$, $1/32\times$, $1/64\times$, and $1/128\times$ the mean experimentally determined T_1 or $T_{1\rho}$ time.

Using these calculations, the 19 doped relaxation rates used for the bulk of the analysis in this chapter would take a total of 52.9 days. In contrast, the 6 undoped relaxation rates used in Figure 5.8 would require 48.3 days. While the information content of the 19 doped relaxation rates is greater than the 6 undoped relaxation rates (4 detectors were formed with the doped dataset, while 6 good quality undoped rates would be expected to only give at most 3 detectors (*c.f.* Table 5.4)), 52.9 days of experimental time is still a significant undertaking.

To determine which rates should be include in these reduced datasets, the 19 relaxation rates were ordered by their contributions to the detectors determined using the full set. To do this, the Root-Sum of Squares of the Contributions (RSSC) of each normalized relaxation rate to the resulting detectors was calculated:

$$\text{RSSC}_c = \sqrt{\sum_{n=1}^{N} y_{c,n}^2}, \tag{5.18}$$

where $y_{c,n}$ is the contribution of relaxation rate c to detector n, as defined in equation 2.189. A reduced dataset of r relaxation rates is then obtained by taking the first r relaxation rates in an ordered list of RSSC_i. Note that this is not necessarily the only way to produce reduced datasets; there are ${}_NC_r$ possible ways of choosing a subset of r relaxation rates from N relaxation rates, and it would not be feasible to test all 524,287 possible combinations. This ordered list is shown in Table 5.7. Interestingly, spin-lattice R_1 relaxation rates are generally those which have the greatest RSSC. This is likely because the paramagnetic contribution to R_1 is dominated by a spectral density term which probes the ^{15}N Larmor frequency, which in the case of the measurements used here is close to the inverse of the paramagnetic correlation time; as a result, these R_1 measurements are likely more influential in the parameterisation of the paramagnetic response here, as well as being highly sensitive to the fast motions occurring.

The results of these reduced datasets are summarised in Table 5.8, where N_{rates} and $N_{\text{detectors}}$ refer to the number of relaxation rates included and the number of detectors formed. A reduced dataset of 5 relaxation rates (25.8 days equiv.) is capable of producing three detectors; this is shown in Figure 5.14. Increasing this set to 11 relaxation rates (43.8 days equiv.) generates four detectors, as in Figure 5.15.

Table 5.7: Ordered list of relaxation rates by RSSC_i for GB1:IgG complex.

N	Type	Field / T	$[Gd^{3+}]$ / mM	ν_1 / kHz	ν_r / kHz	RSSC
1	^{15}N R_1	23.5	3.5	—	50.0	3.20
2	^{15}N R_1	14.1	3.5	—	60.0	1.87
3	^{15}N R_1	16.4	2.0	—	60.0	1.43
4	^{15}N $R_{1\rho}$	16.4	3.5	39.2	60.0	1.32
5	^{15}N R_1	14.1	7.5	—	60.0	1.24
6	^{15}N R_1	14.1	5.0	—	60.0	0.73
7	^{15}N $R_{1\rho}$	16.4	3.5	32.1	60.0	0.67
8	^{15}N R_1	16.4	3.5	—	60.0	0.54
9	^{15}N $R_{1\rho}$	16.4	1.0	10.0	60.0	0.39
10	^{15}N $R_{1\rho}$	20.0	5.0	10.2	60.0	0.35
11	^{15}N $R_{1\rho}$	16.4	2.0	10.0	60.0	0.35
12	^{15}N $R_{1\rho}$	16.4	2.0	10.0	60.0	0.35
13	^{15}N $R_{1\rho}$	16.4	3.5	10.0	60.0	0.34
14	^{15}N $R_{1\rho}$	16.4	3.5	14.2	60.0	0.26
15	^{15}N $R_{1\rho}$	20.0	5.0	15.5	60.0	0.25
16	^{15}N $R_{1\rho}$	16.4	3.5	25.2	60.0	0.21
17	^{15}N $R_{1\rho}$	20.0	5.0	20.4	60.0	0.13
18	^{15}N $R_{1\rho}$	23.5	3.5	11.2	50.0	0.12
19	^{15}N $R_{1\rho}$	16.4	3.5	19.8	60.0	0.11

Table 5.8: Number of detectors formed using reduced sets of data, where the reduced sets were taken from Table 5.7 with $N \leq N_{\text{rates}}$.

N_{rates}	k	$N_{\text{detectors}}$	Time / days
3	0	0	20.5
4	2	1	21.6
5	3	3	25.8
6	3	3	32.0
7	3	3	33.1
8	3	3	39.3
9	3	3	41.5
10	3	3	42.7
11	4	4	43.8
12	4	4	45.0
13	4	4	46.1
14	4	4	47.2
15	3	3	48.4
16	3	3	49.5
17	3	3	50.6
18	4	4	51.7
19	4	4	52.9

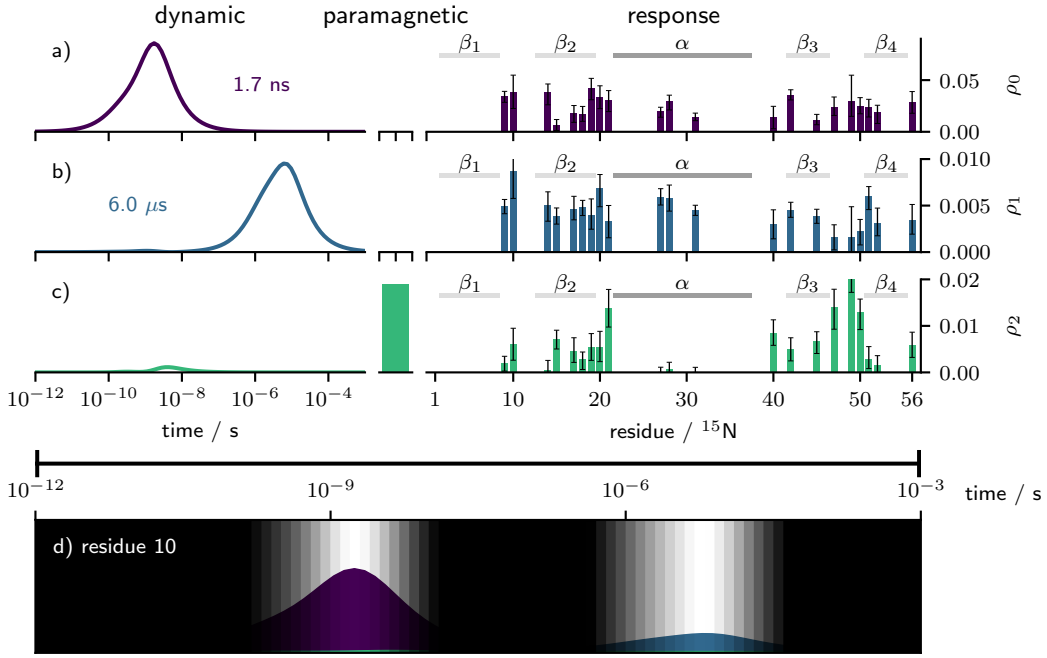

Figure 5.14: Resulting detectors from a reduced set of 5 relaxation rates for GB1:IgG (see Figure 5.5 for figure details).

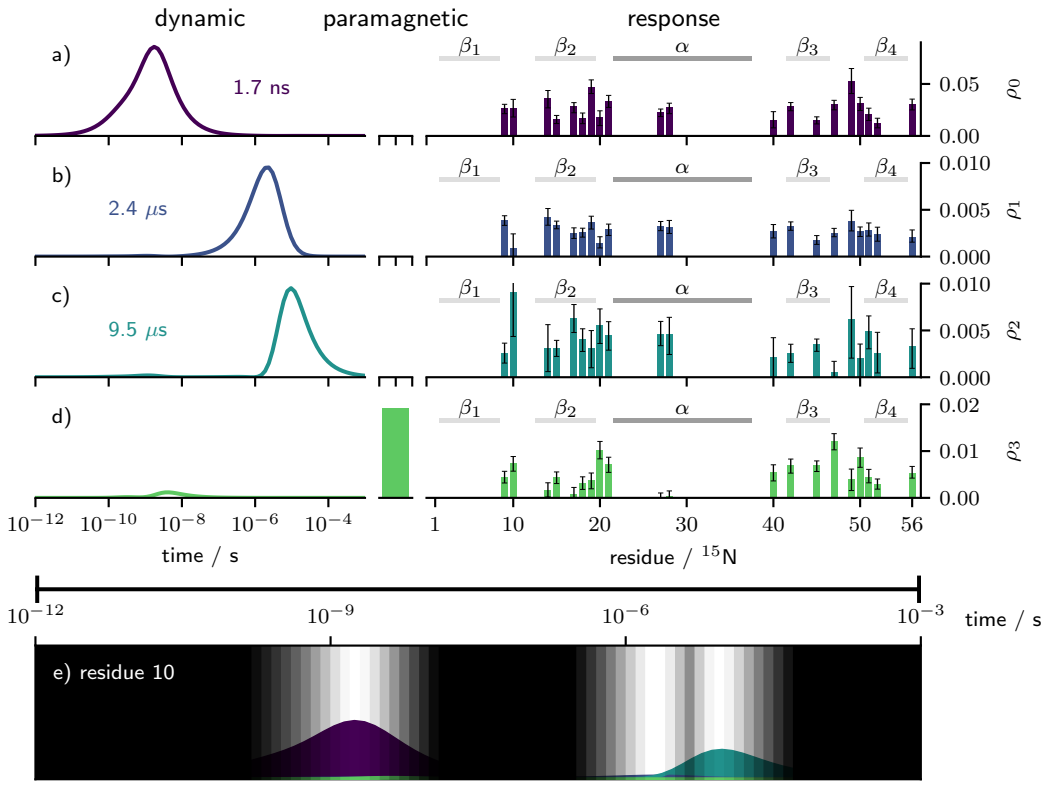

Figure 5.15: Resulting detectors from a reduced set of 11 relaxation rates for GB1:IgG (see Figure 5.5 for figure details).

5.4 Conclusion

In summary, it has been shown to be possible to adequately quantify the local motions of a protein bound in a complex with an antibody in the presence of PRE by simultaneously modelling both the paramagnetic enhancement and the local dynamics. By quantifying the PRE, additional insight can be gained into the local accessibility and tumbling of the paramagnetic dopant.

The CoMPaDReS approach introduced here is also generally applicable to discrete density of motions methods, such as those discussed in Section 2.2.2.1. However, the use of such discrete methods necessitates the recording of good quality dipolar order parameters.[158] Recording such datasets in sensitivity limited systems, such as the GB1:IgG complex studied here, introduces additional difficulty and significant experimental time.[301] Further, such methods have been shown to introduce significant biases into the analyses[150] and as such are unlikely to provide any benefit over the Detectors approach used here. As a result, such alternative methods have not been presented here.

It is hoped that this approach will enable a route towards the investigation of local dynamic of other large complex systems. It is possible that this approach will also find applicability outside of biological NMR; for example, solid-state NMR has found application to the study of local dynamics in pharmaceutical formulations and small organic molecules[244,245,334] and inorganic/material systems.[335–338] In many of these cases, owing to either the natural presence of paramagnetic species, the low natural abundance of unlabelled samples, or the large complexity of the systems, traditional diamagnetic relaxation based dynamical analysis is unfeasible. The ability to combine the study of local motions and paramagnetism simultaneously is likely directly applicable to such systems.

Chapter 6

Developing a Multinuclear Approach to Protein Dynamics

The majority of the large relaxation rate dataset used in this chapter was recorded by previous PhD students and postdocs (specifically, Dr Trent Franks, Dr Jonathan Lamley,[339] Dr Rebecca Stevens[124]). The resulting experimental data was then analysed by Dr Jacqueline Tognetti to obtain relaxation rates. The method for analysis of these relaxation rates was developed and performed by myself, with useful suggestions and insight from Dr Albert Smith-Penzel and Dr Sarah Mann. The variable temperature MD simulations used in this chapter have been previously published in a different context in W. T. Franks, B. P. Tatman, J. Trenouth, J. R. Lewandowski, Dipolar Order Parameters in Large Systems with Fast Spinning, **Front. Mol. Biosci.**, 2021, **8**, 1151.

6.1 Introduction

As NMR is a technique fundamentally sensitive to the local environment around a nuclear spin, it follows that increasing the number of spins being probed can provide a greater resolution as to the local motions. As discussed previously in Section 2.2, for diamagnetic systems in the absence of chemical exchange, relaxation arises due to the incoherent modulation of anisotropic interactions such as dipolar

couplings[340] and chemical shift anisotropy.[341] The relaxation experienced at a specific site is then dependent not only on the timescale and amplitude of motion occurring, but also on the orientation of the motion and how this relates to the anisotropic interaction tensor. For instance, the relaxation of backbone carbonyl sites (here referred to as ^{13}C′) in the presence of fast (ps-ns) motions is significantly dominated by the CSA tensor.[126,342,343] On the other hand, backbone amide (^{15}N) relaxation is dominated by the modulation of the ^{15}N – ^{1}H dipolar coupling. The tensors of these respective interactions are visualised in Figure 6.1. Despite the nuclei being close in proximity, the two dominant relaxation active tensors have distinct orientations and asymmetries and therefore probe different motions, and as a result the relaxation experienced on these two sites could in principle provide information as to the local anisotropy of the motions.[127]

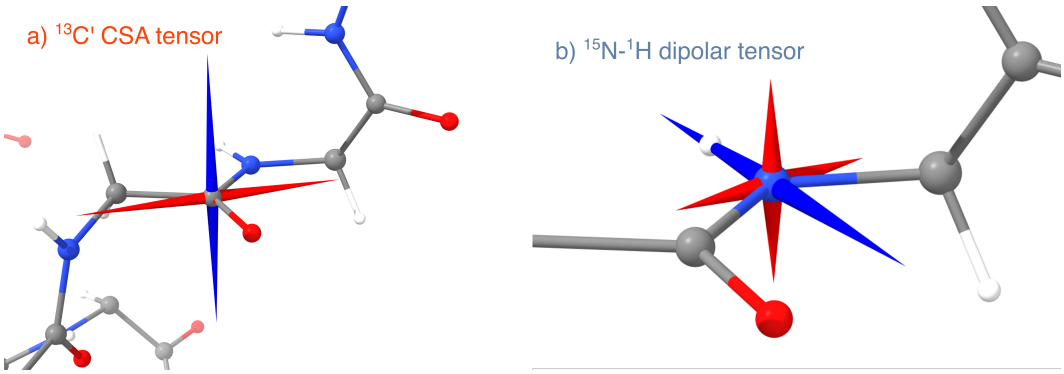

Figure 6.1: Tensor orientations for the dominant interactions for (a) ^{13}C′ and (b) ^{15}N relaxation. Positive values are shown in blue, negative values in red. The size of the vectors is scaled to the eigenvalue of the eigenvector. The CSA of the carbonyl in (a) was taken as having principal components $\sigma_{11} = -74.4$ ppm, $\sigma_{22} = -7.4$ ppm, $\sigma_{33} = 81.8$ ppm, orientated $-72°$ away from the ^{13}C′ – ^{13}Cα axis. This was then converted to Hz assuming a ^{1}H Larmor frequency of 700 MHz. For the dipolar coupling in (b), a ^{15}N – ^{1}H distance of 1.02 Å was assumed.

While several studies in solution state have utilized ^{15}N and ^{13}C′ as complementary probes of motion,[126,342–346] very few combined studies have been attempted in the solid-state.[225] This is likely in part due to site specific ^{13}C′ relaxation rates only becoming feasible at fast magic-angle spinning (MAS) ($\geq$ 50 kHz)[125,225] (see Section 3.3.3) without difficult specific carbonyl labelling schemes, coupled with the difficulty in constraining the overall motion of the ^{13}C′.[158] While techniques such

as COMFORD (CO-Modelfree Fitting Of Relaxation Data) have been introduced to obtain effective order parameters in solution,[342] such approaches are not easily applicable in solids owing to the practical difficulty in measuring spin-spin relaxation rates* (R_2) and nuclear Overhauser effects (nOes).

One approach which has been applied in the solid-state is to assume that the ^{13}C′ and ^{15}N rates from a single peptide plane may be evaluated together. Lamley *et al*. (2015) have shown that ^{13}C′ and ^{15}N relaxation rates may be fit simultaneously to probe a greater range of timescales of motion with higher sensitivity.[225] Implicit in this model is the assumption that the peptide plane containing both nuclear spins is rigid and the motion isotropic, such that the motions at both sites are equivalent and that the ^{15}N dipolar order parameter can constrain both the ^{15}N and the ^{13}C′ sites. Such an approach could be extended along the lines of the 3D-Gaussian Axial Fluctuation (GAF) model introduced in the solution state to look at the local anisotropy of motion.[126,347–349] In such a model, dipolar order parameters could be measured in the peptide plane to constrain the overall motion in the absence of a ^{13}C′ CSA order parameter. However, an approach based on the GAF formalism would face several limitations which are particularly exacerbated in the solid state. Highly accurate measurements of dipolar order parameters would be required to properly constrain the anisotropic amplitudes of different timescales of motion, and these would need to be measured under identical conditions to ensure there is no systematic bias. Further, it is known that the 'peptide plane' is not perfectly planar, with both dynamic[350] and static deviations from planarity.[351,352] As such, the assumption of planarity for dynamics analysis may be misleading, especially in the case of separating the ^{15}N–^{1}H bond motions from the rest of the plane, considering the relative atomic masses of the involved nuclei. Finally, as discussed in Section 2.2.2, it has recently been shown by Smith *et al*. (2017) that the limited sampling of the spectral density function can significantly bias the resulting model-free timescales obtained by such an analysis, which could lead to fitted correlation

*Though with additional approximations these could be substituted with $R_{1\rho}$ relaxation rates.

times and amplitudes being physically misleading.[150]

Here, a new approach to investigate the local anisotropy of motions based on detectors will be introduced. A benefit of detectors is that they do not require dipolar order parameters to constrain the overall amplitude of motion; rather, they need an adequate model for which interactions contribute to the relaxation of a nuclear spin (though order parameters may be included in the analysis[161]). As such, they may be readily applied equivalently to both ^{13}C′ and ^{15}N.

6.2 Methods

6.2.1 Experimental and Relaxation Rate Analysis

NMR experiments were performed on samples of microcrystalline U-[^{2}H,^{13}C,^{15N}]-GB1 (with 100% ^{1}H back-exchange at exchangeable sites) packed into 1.3 mm rotors at four magnetic fields: a Bruker Avance II spectrometer operating at 14.1 T ($\nu_0(^1\text{H}) = 600$ MHz) using a 1.3 mm HXY probe; a Bruker Avance III spectrometer operating at 16.4 T ($\nu_0(^1\text{H}) = 700$ MHz) using a 1.3 mm HXY probe; a Bruker Avance III spectrometer operating at 20.0 T ($\nu_0(^1\text{H}) = 850$ MHz) using a 1.3 mm HFXY probe; and a Bruker Avance Neo spectrometer operating at 23.5 T ($\nu_0(^1\text{H}) = 1000$ MHz) using a 1.3 mm HCN probe. Experiments were performed at a MAS frequency of 50 kHz. Internal temperatures were measured using the ^{1}H chemical shift of water relative to DSS. ^{15}N R_1 and $R_{1\rho}$ rates were recorded using the pulse sequences outlined in Section 3.3.2. Tables 6.1 and 6.2 outline the different experimental conditions for relaxation rate measurements.

For the ^{15}N relaxation rate analysis it was assumed that the primary components were the dipolar ^{15}N – ^{1}H coupling (1.02 Å), ^{15}N CSA (parameterised using chemical shift,[353] assuming an isotropic chemical shift of 120 ppm), ^{15}N – ^{13}C (1.33 Å), and ^{15}N – ^{13}Cα (1.46 Å). For ^{13}C, a composition of ^{13}C CSA (parameterised using chemical shift,[354] assuming an isotropic chemical shift of 170 ppm for detector optimization and site-specific isotropic chemical shift for response calculation),

Table 6.1: Conditions under which relaxation rates were measured for ^{15}N.

Field / T	Type	Temp / K	ν_r / kHz	ν_1 / kHz
14.1	$R_{1\rho}$	259.8	50	7.8
14.1	$R_{1\rho}$	260.6	50	7.8
14.1	R_1	262.4	50	-
14.1	$R_{1\rho}$	270.1	50	7.8
14.1	R_1	273.1	50	-
14.1	$R_{1\rho}$	273.8	50	7.8
14.1	R_1	275.6	50	-
14.1	$R_{1\rho}$	278.1	50	7.8
14.1	$R_{1\rho}$	280.4	50	7.8
14.1	R_1	282.4	50	-
14.1	$R_{1\rho}$	282.4	50	7.4
14.1	R_1	290.1	50	-
16.4	$R_{1\rho}$	278.0	50	10.0
16.4	$R_{1\rho}$	290.0	50	10.0
16.4	$R_{1\rho}$	294.0	50	10.0
16.4	R_1	299.0	50	-
16.4	$R_{1\rho}$	299.0	50	10.0
16.4	$R_{1\rho}$	309.0	50	10.0
20.0	$R_{1\rho}$	278.0	50	10.0
20.0	$R_{1\rho}$	291.0	50	10.0
20.0	R_1	298.0	50	-
20.0	$R_{1\rho}$	299.0	50	10.0
23.5	R_1	302.0	50	-
23.5	$R_{1\rho}$	302.0	50	10.4
23.5	R_1	306.0	50	-
23.5	$R_{1\rho}$	306.0	50	10.4

^{13}C – ^{13}Cα (1.525 Å, 2.49 Å), ^{13}C – ^{15}N (1.33 Å), and ^{13}C – ^{1}H (2.04 Å) was used. Note that as the experiments involved non-selective inversion of ^{13}C the homonuclear dipolar relaxation rate equations have been used for these. In the optimization of detectors the same chemical shift anisotropy was used for all sites as this allowed the same detectors to be used for each site, however owing to the dominance of CSA for ^{13}C′ relaxation, site-specific CSA was used for response calculation in this case, parameterised from isotropic chemical shift as in ref 354. Residues for which more than five relaxation rates for a given nuclei were missing were omitted from the analysis of that nuclei.

Variable temperature NMR experiments were used to increase the range of effective

Table 6.2: Conditions under which relaxation rates were measured for $^{13}C'$.

Field / T	Type	Temp / K	ν_r / kHz	ν_1 / kHz
14.1	$R_{1\rho}$	266.1	50	7.8
14.1	R_1	268.1	50	-
14.1	R_1	270.8	50	-
14.1	$R_{1\rho}$	271.1	50	7.8
14.1	R_1	274.6	50	-
14.1	$R_{1\rho}$	275.4	50	7.8
14.1	$R_{1\rho}$	282.8	50	7.8
14.1	$R_{1\rho}$	284.9	50	7.8
14.1	$R_{1\rho}$	286.9	50	7.8
14.1	R_1	287.6	50	-
14.1	$R_{1\rho}$	290.2	50	7.8
16.4	$R_{1\rho}$	291.0	50	11.0
16.4	$R_{1\rho}$	293.0	50	11.0
16.4	$R_{1\rho}$	299.0	50	11.2
16.4	R_1	303.0	50	-
16.4	$R_{1\rho}$	309.0	50	10.8
20.0	$R_{1\rho}$	276.9	50	10.4
20.0	R_1	282.2	50	-
20.0	$R_{1\rho}$	285.8	50	10.2
20.0	$R_{1\rho}$	289.4	50	10.3
20.0	R_1	290.8	50	-
23.5	$R_{1\rho}$	302.0	50	11.3
23.5	R_1	302.0	50	-
23.5	$R_{1\rho}$	306.0	50	11.3
23.5	R_1	306.0	50	-

timescales accessible. The sensitivity of a given relaxation rate is independent of the temperature; that is, a relaxation rate highly sensitive to motions occurring with a characteristic timescale of 10 ns will be sensitive to those motions regardless of whether it is recorded at 200 K or 400 K. However, the underlying motions are likely to shift in timescale, with higher temperatures causing the motional kinetics to speed up. To aid the analysis here, it is desirable for the temperature sensitivity of the underlying kinetics to be shifted into the sensitivity, to give temperature-dependent effective sensitivities with motions considered relative to a fixed temperature. In this, there is the implicit assumption that the density of motions occurring is approximately the same at any given temperature, just temporally-shifted according to

the temperature. Here, this temporal shift is considered using an Arrhenius factor, calculated as:

$$\tau_{\text{eff}}(T\ \text{K}) = \tau_{300\ \text{K}} e^{\frac{E_a}{R}\left(\frac{300-T}{300T}\right)}, \tag{6.1}$$

where E_a is the activation energy (kJ mol^{-1}), R is the gas constant (kJ mol^{-1} K^{-1}), and $\tau_{300\ \text{K}}$ the timescale at 300 K. The aim of this correction is to convert a timescale-independent sensitivity over temperature-dependent kinetics into a temperature-dependent sensitivity over temperature-independent kinetics. The 'fixed' timescale (*e.g.*, of the temperature-independent kinetics) is taken to be 300 K: ($\tau_{300\ \text{K}}$). This temperature correction to the timescale is illustrated in Figure 6.2. On the left, the temperature-independent sensitivity is shown on a temperature-dependent timescale. On the right, the Arrhenius shift is performed to give a temperature-independent timescale (referenced to that at 300 K) with a temperature-dependent sensitivity. This adjustment makes a number of assumptions; it assumes that all motions are temperature dependent, with the same activation energy E_a, and that this variation is effectively the same across all timescales. A more detailed discussion of the use of temperature dependent timescales, with comparison to previous VT studies of protein dynamics and VT molecular dynamics, is given in Section 6.3.1.

Detectors were produced and responses calculated for each of ^{15}N and ^{13}C′ according to the approach outlined in Section 2.2.2.2. The discretisation of the sensitivity was performed with 200 time points ranging from 10^{-13} to 10^{-3} seconds, with the exception of the variable activation energy models (see Section 6.3.1) for which 100 time points were used to speed up the calculations. Following this, the resulting detectors were paired using a linear sum assignment method to find the combination giving the greatest total overlap integral. This procedure was repeated with different numbers of singular values included ranging from $k = 2 - 10$. In order to determine how many k to include in the analysis here, reduced χ^2 were calculated

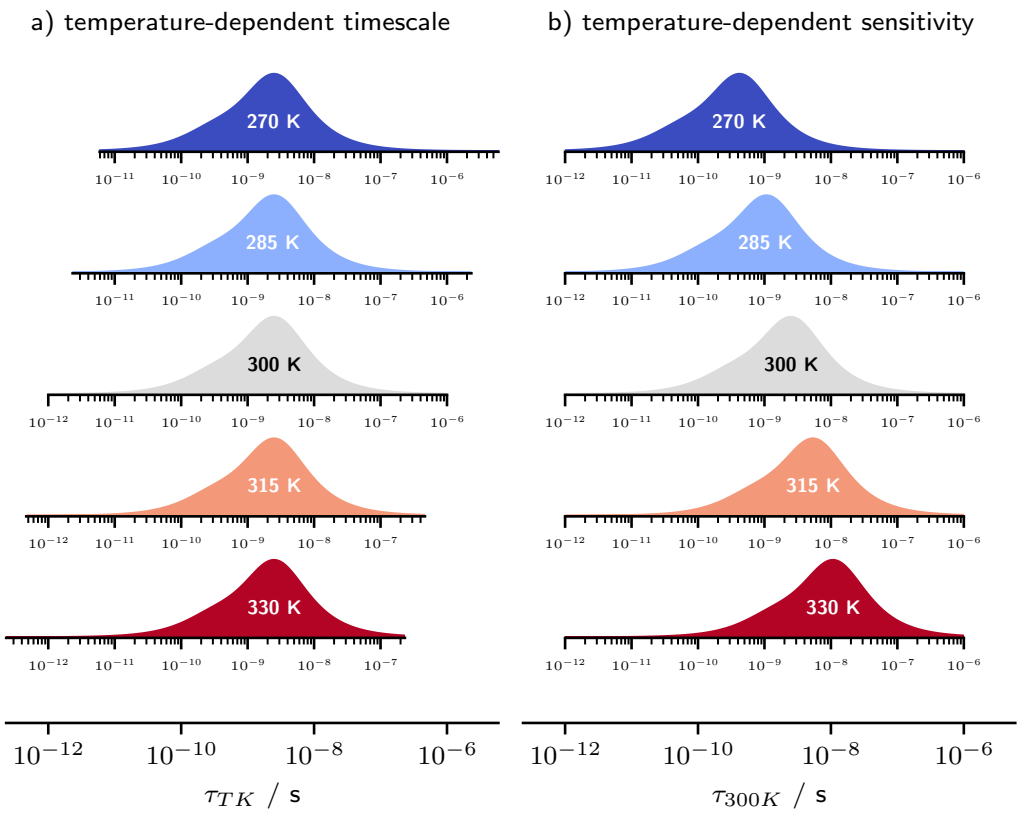

Figure 6.2: Figure showing how the temperature dependence of relaxation was considered in the modelling here. The temperature dependence is modelled here with an activation energy of 40 kJ mol^{-1}, with the sensitivities calculated for a ^{15}N R_1 relaxation rate at 700 MHz and 60 kHz MAS. (a) The relaxation rate sensitivities are calculated according to a temperature-dependent timescale, calculated according to equation 6.1. (b) When the resulting sensitivities are plotted as a function of the timescale at 300 K this leads to a temperature-dependent temporal shift in the sensitivity, which was exploited to enhance the range of timescales which could be accessed.

on a site-specific basis for each value of k. Model selection was then achieved by calculating the median reduced χ^2, $\hat{\chi}^2$, for each value of k, and taking the value of k giving the closest $\hat{\chi}^2$ to 1.

6.2.2 Molecular Dynamics

Molecular dynamics simulations of microcrystalline GB1 were performed using a 3 $\times$ 3 $\times$ 3 supercell of GB1 containing 108 monomers. These were simulated using AMBER 20,[313,355] with the ff19SB protein force-field[319] and OPC water.[320] The

starting conformation was taken from the structure 2GI9,[315] from which a supercell was produced using the UnitCell and PropPDB functionalities in AMBER 20, before adding 108 PO_4^{3-} counter ions (simulated using a GAFF force-field[355]), solvating with 12,852 explicit water molecules and charge balancing with Na^+/Cl^- using TLeap. Following minimization, the system was replicated for each of the seven separate MD simulations: six variable temperature MD simulations at internal temperatures of 260, 270, 280, 290, 300, 310 K for 400 ns, and one longer MD simulation at a temperature of 300 K for 2.28 μs. Following heating to the given temperatures, the systems were simulated for their respective lengths. A 2 fs timestep was used with a cut-off of 11 Å for non-bonded interactions. The SHAKE algorithm was applied to all bond lengths involving a hydrogen atom,[321] and a Langevin thermostat was used to maintain the temperatures. Anisotropic pressure scaling was used with periodic boundary conditions.

cpptraj was used to align Cα atoms between frames.[322] Correlation functions for each N$-$H or C$\alpha\cdots$Cα vector were calculated for each residue in each protein monomer for the 2.28 μs simulation using cpptraj, which were then inverse Laplace transformed and processed using a previously published method for detector analysis,[160] using 199 decaying exponentials with correlation times ranging logarithmically from 1 ps to 1000 ns, and an additional decaying exponential to represent the limit with a correlation time of 1 ms. These were then averaged between each of the 108 protein monomers. The corresponding MD detector response was then calculated by integrating over the product of the detector sensitivity (from the NMR analysis) and this distribution of motion (see Section 2.2.2.2). Analysis of the variable temperature MD simulations was performed equivalently, however the 199 decaying exponentials ranged logarithmically from 1 ps to 200 ns.

6.3 Results and Discussion

6.3.1 Variable Temperature Detectors

Experimentally determined relaxation rates probe the spectral density at the eigenfrequencies of the spin system, that is, specific linear combinations of Larmor frequencies, spin lock frequencies, and magic-angle spinning frequencies. Therefore, to increase the range of timescales probed by NMR experiments one may either vary these eigenfrequencies or manipulate the underlying spectral density function through the experimental conditions. The former may be performed by using a range of magnetic field strengths, which is generally limited by how many spectrometers are available; here, relaxation rates have been recorded at four fields ranging from 600–1000 MHz. Shuttling methods, where the sample is quickly shuttled into a different magnetic field to relax, have found important utility in such relaxometry measurements in solution.[356–358] However, owing to the necessity to spin the samples at fast magic-angle spinning frequencies and the issue of induced eddy currents in a solid rapidly moving through a magnetic field, such an approach has not yet been developed for the solid state.

An alternative method to increase the timescale range probed is to modify the underlying spectral density. Typically, this involves assuming an Arrhenius dependence of motional kinetics on sample temperature, which may then be systematically varied to gain insight into a greater range of timescales. In performing this sort of analysis, however, care must be taken that varying the temperature does not also affect the amplitudes of the motions occurring. Both MD and NMR studies of GB1 in the solid state have demonstrated negligible variation in dipolar order parameters as a function of temperature.[250,301] While a number of solution-state studies of proteins have suggested a significant temperature dependence of amplitude,[342,344,359,360] this may be explained by the temperature dependence of overall tumbling motion which may truncate the observable internal motions and so lead to variation in the model-free order parameters. In this study, it was assumed that the amplitudes of

motion are invariant with changing temperature, and that instead this is purely a kinetic effect.

Previous studies have explored the energetics of the motions occurring in microcrystalline GB1.[250,361,362] These have found the presence of two motional modes with significantly different activation energies of approximately 5 kJ mol^{-1} and 25–35 kJ mol^{-1}. A variable temperature study of Anabaena Sensory Rhodopsin by Good *et al*. (2017) found that analogous motional modes with similar activation energies appear to be associated with picosecond and nanosecond timescales respectively.[43] In the analysis here, it is assumed that the experiments are performed above the 'crossover' temperature, such that the higher activation energy mode is the dominant source of relaxation, and that the lower activation energy mode is fully activated.[250]

One potential limitation of the prior variable temperature energetics studies is the use of the model-free formalism. The activation energies are effectively extracted by considering the temperature dependence of the model-free correlation times. However, as discussed previously (see Section 2.2.2), it has been shown that these correlation times may be substantially biased by the sensitivities of the relaxation rates used in the analysis;[150] in this case, such a bias would be expected to oppose the change in correlation function with timescale, and therefore lead to underestimation of the true activation energy for the motional modes. This effect is visualised in Figure 6.3.

In this study, both molecular dynamics and fitting of the activation energy were used to gain insight into the energetics of the protein dynamics. Firstly, using MD, 400 ns simulations of a $3 \times 3 \times 3$ supercell containing 108 GB1 monomers at temperatures of 260, 270, 280, 290, 300, and 310 K were simulated. Results from some of these simulations have previously been published in ref 301. These were individually inverse Laplace transformed (ILT) to approximate the temporal density of motion, $\theta(t)$. Following this, the cumulative density of motions, $\Theta(t) = \int_0^t \theta(\tau) d\tau$, was calculated. In Figure 6.4 it appears that there is significant variation in the

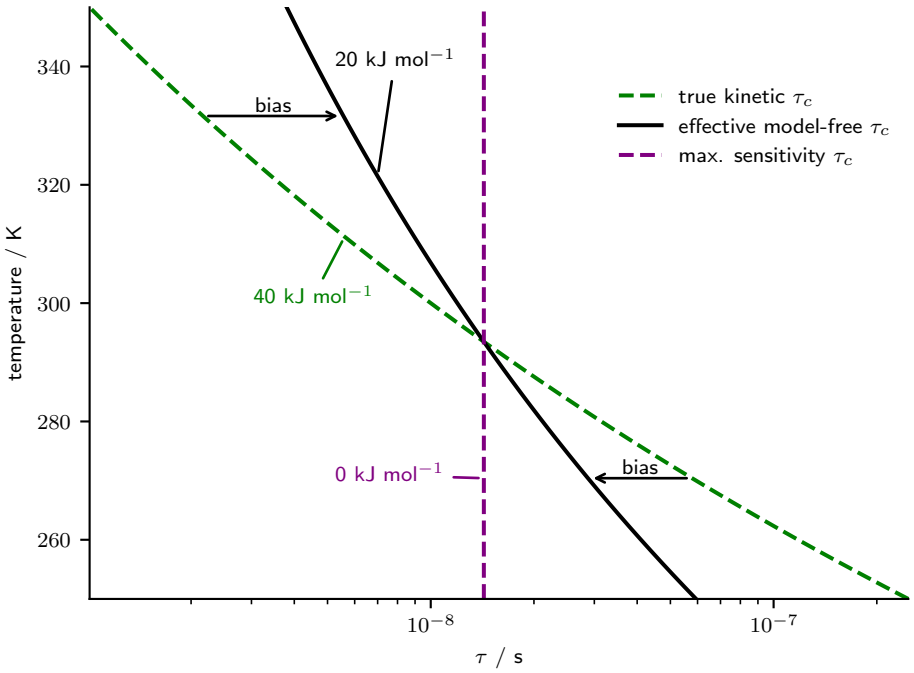

Figure 6.3: Figure showing how the effect of timescale biasing[150] may have consequences for the model-free analysis of energetics. The effective model-free correlation time (black) is biased from the true kinetic correlation time (green) by where the relaxation data is most sensitive (purple). In this model, the effective correlation time has been taken as the logarithmic average of the 'true' kinetic τ_c and the maximum sensitivity τ_c (This is unlikely to be the true relation between the two; here it is used purely for illustrative purposes.) The resulting fit activation energy (20 kJ mol^{-1}) is then an underestimate of the 'true' activation energy (40 kJ mol^{-1}).

amplitude of the motion as a function of temperature, with the order parameters varying significantly across the temperature range. Experimentally, however, it has been shown that there is no significant variation in order parameter as a function of temperature.[301] The discrepancy likely arises due to the short length of the MD simulations here; experimental dipolar order parameters include all motions up to the μs-ms timescale, whereas these simulations probe motions with correlation times of at most 100s of ns. A temperature dependence in the timescale of motion could give rise to the phenomenon seen here.

In order to investigate the energetics of the motions of the different modes in the MD, the ILTs were split into components of timescales ranging from 1 ps to 40 ps, and from 40 ps to 200 ns. For each, the effect of scaling the timescale according to an

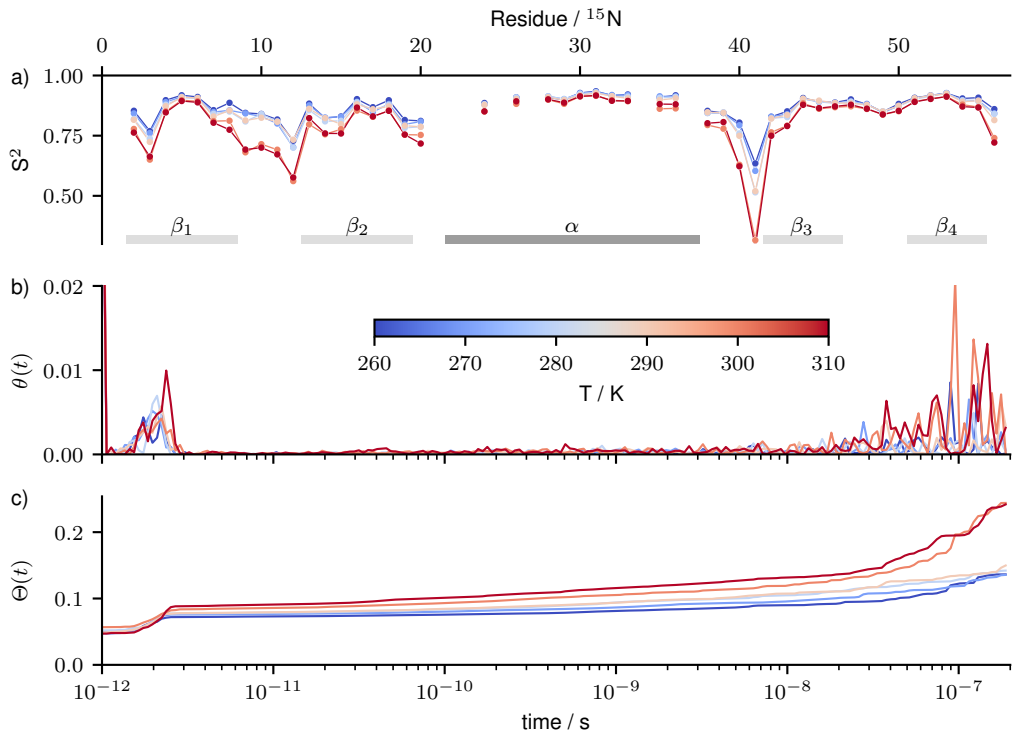

Figure 6.4: Figure showing (a) S^2, the limit of the correlation function, (b) the density of motions for residue 11, and (c) the cumulative density of motions for residue 11 in a $3 \times 3 \times 3$ supercell of GB1 containing 108 GB1 monomers as a function of temperature ranging from 260–310 K. The simulations were each run for 400 ns.

Arrhenius factor was considered:

$$\tau_{\text{eff}}(300\text{ K}) = \tau_{\text{MD}}(T\text{ K})e^{-\frac{E_a}{R}\left(\frac{300-T}{300T}\right)}, \tag{6.2}$$

where $\tau_{\text{MD}}(T\text{ K})$ is the timescale extracted from the MD simulation performed at a temperature of T K, and $\tau_{\text{eff}}(300\text{ K})$ is the equivalent timescale at 300 K assuming an activation energy E_a. The primary assumption underlying this analysis is that the density of motions is only shifted temporally with variation in temperature, such that undoing this shift (using the Arrhenius relation) would lead to essentially the same density of motions at any given temperature. The resulting profiles are shown in Figures 6.5 and 6.6 for the 1–40 ps and 40 ps–200 ns components respectively.[†] The

[†]The choice of this separation is effectively arbitrary; the primary constraint is that the split timescale (here 40 ps) is past the change in gradient in the cumulative distribution of motions — in Figure 6.4, this appears to be at around 3 ps.

faster motion component does not appear to significantly vary with temperature; this may arise either because this motional mode is fully activated at any of the temperatures modelled here,[250] or rather because the MD timestep used (10 ps) is too long to probe the variation of these timescales. With the slower motion component, on the other hand, adjusting the timescales with the inclusion of an activation energy leads to significantly better agreement between the simulations. An activation energy of ≈40 kJ mol^{-1} gives the best agreement for the majority of residues. This figure is in good agreement with the lower bound of 25–35 kJ mol^{-1} found previously experimentally.[250,361,362]

To investigate the effect of varying the activation energy on the detector-based analyses used here, the analysis was performed in which the activation energy was varied linearly in 50 steps from 0 to 60 kJ mol^{-1}. This analysis was performed separately for each nuclei, as the number of included singular values, k, was increased from $k = 2 - 10$. Table 6.3 shows summary statistics for this analysis.

Table 6.3: Summary model statistics for models with different values of k for which the activation energy was allowed to vary.

k	N^o ^{13}C′	N^o ^{15}N	$\frac{\chi^2}{n}$ ^{13}C′‡	$\frac{\chi^2}{n}$ ^{15}N	$\hat{\chi}^2$ ^{13}C′§	$\hat{\chi}^2$ ^{15}N
2	2	2	10.28	54.73	11.45	32.68
3	3	3	8.66	29.08	9.61	18.44
4	4	5	8.33	26.33	9.74	18.24
5	5	5	7.25	22.61	8.54	**15.34**
6	6	7	6.16	20.57	**7.95**	17.08
7	7	7	6.07	19.52	7.98	15.47
8	8	9	5.99	19.00	8.44	17.15
9	9	9	5.78	18.67	8.89	16.94
10	10	10	6.10	18.30	10.29	17.39

Increasing the number of singular values (and hence number of detectors) leads to an improvement in the fit (reduction in the average χ^2). However, the median reduced $\hat{\chi}^2$ indicates that the most parsimonious model for ^{13}C′ has $k = 6$, and for ^{15}N has $k = 5$. On the basis of this, $k = 5$ was taken for further analysis. Figure 6.7 shows how the average χ^2 value varies as a function of the activation energy for the

‡average χ^2 value, calculated over all data

§median reduced χ^2 value, calculated for each individual residue and then the median taken

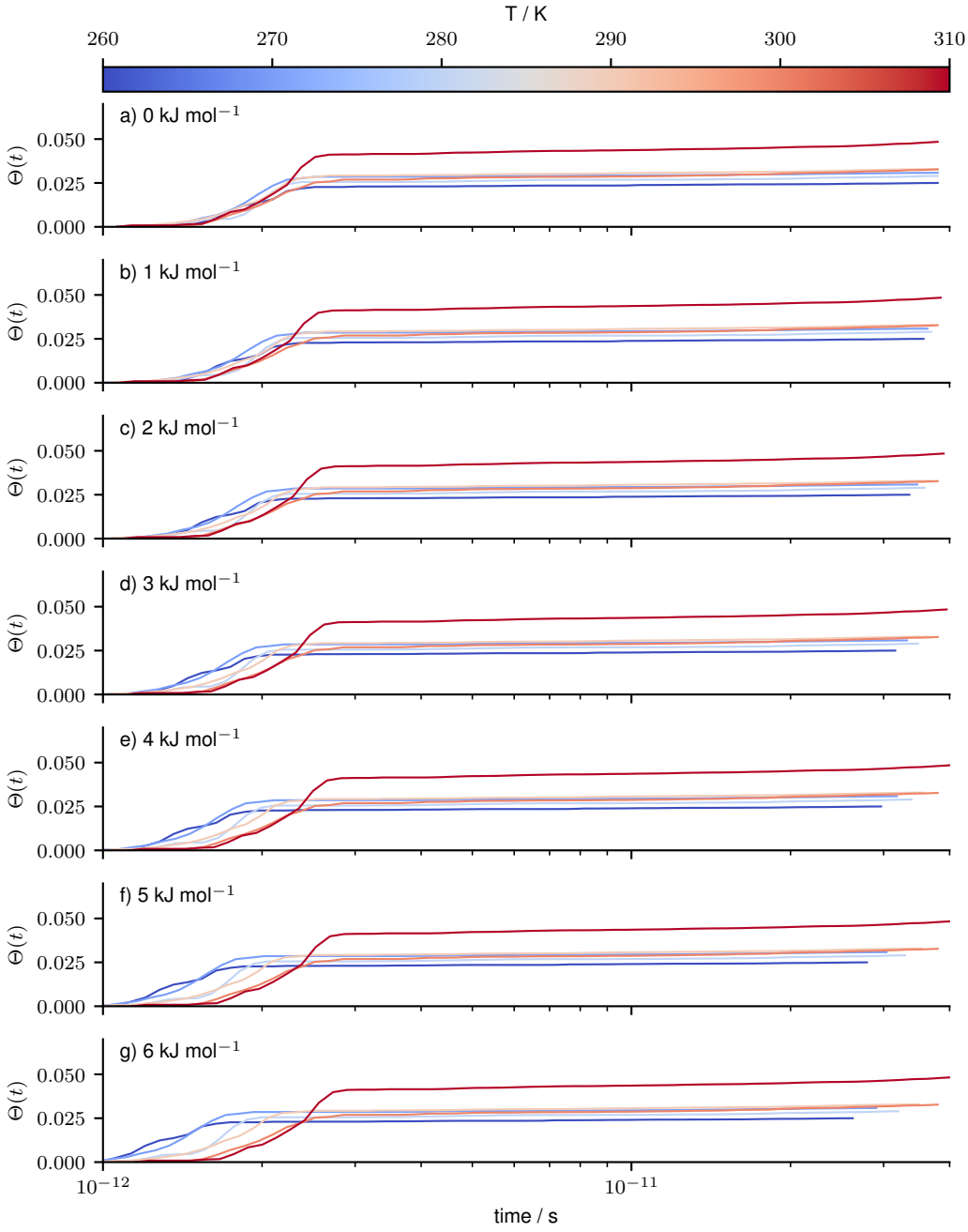

Figure 6.5: Figure showing how inclusion of an activation energy ranging from 0–6 kJ mol^{-1} affects the cumulative density of motions of fast (1–40 ps) motions for residue 11 from variable temperature MD.

$k = 5$ models. In the case of ^{15}N (top), the average χ^2 shows a shallow well centred around 44 kJ mol^{-1}. For ^{13}C′, there is a reduction in average χ^2 which then plateaus for $E_a > 40$ kJ mol^{-1}. The shallow nature of these plots likely relates to the limited

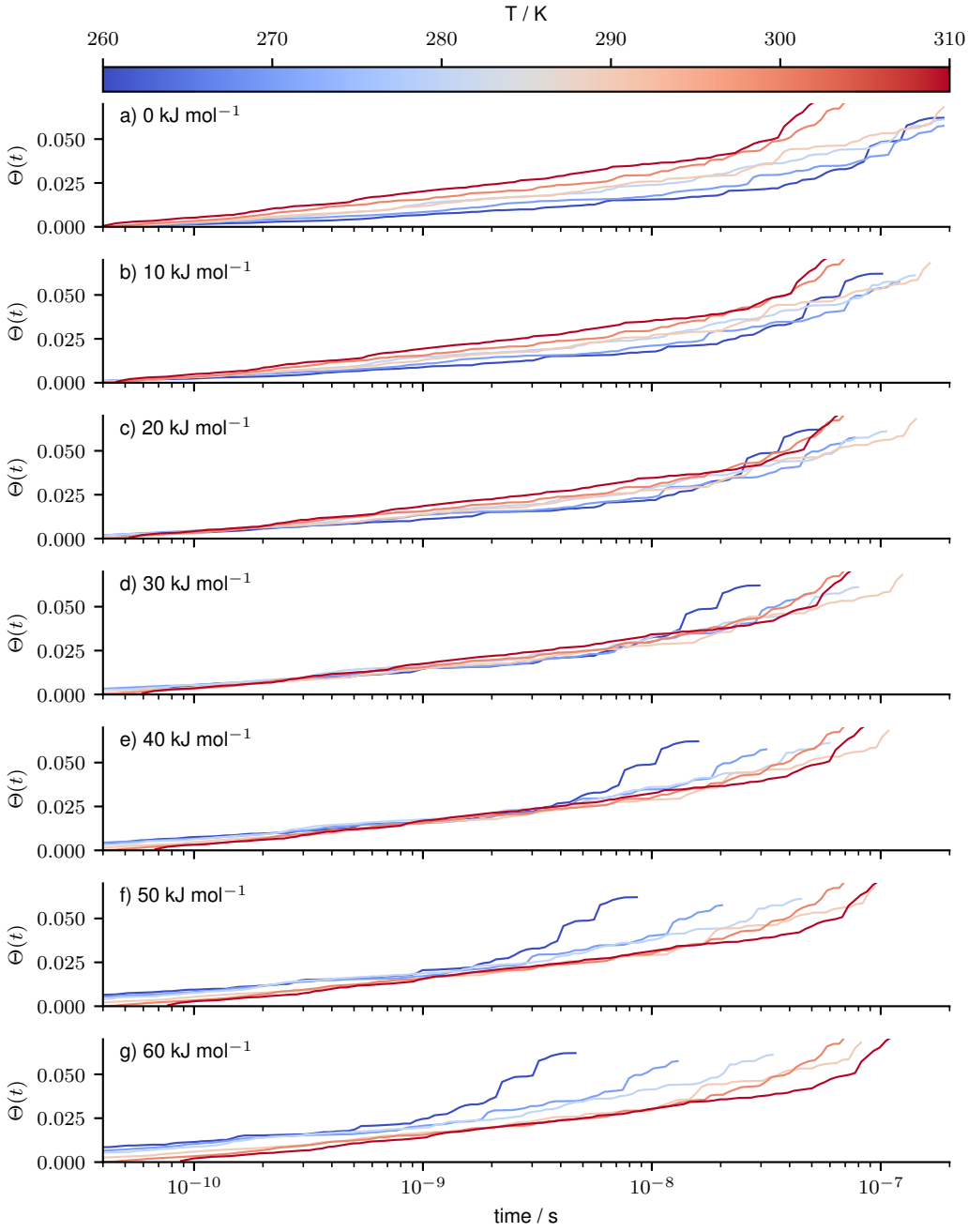

Figure 6.6: Figure showing how inclusion of an activation energy ranging from 0–60 kJ mol^{-1} affects the cumulative density of motions of slower (40 ps–200 ns) motions for residue 11 from variable temperature MD.

range of temperature used in this analysis. The plateau in the case of $^{13}C'$ may be rationalised as follows. Two relaxation rates, recorded equivalently but under different temperatures, will possess the same analytical sensitivity but will differ

in value owing to the changes in the underlying density of motions. Taking the activation energy as 0 kJ mol^{-1} will poorly fit these, as the resulting back-calculated relaxation rate for each will be the same and thus a compromise between the two. Increasing the activation energy will lead to separation of the two rates, such that they may be fit independently. However, there is little to penalise too high of an activation energy, until the slowest fast motion detector begins to overlap with the fastest slow motion detector; this is likely what causes the penalty in the case of ^{15}N. As a result, the most reasonable approximation for the activation energy is likely the lowest activation energy for which the average χ^2 has plateaued.

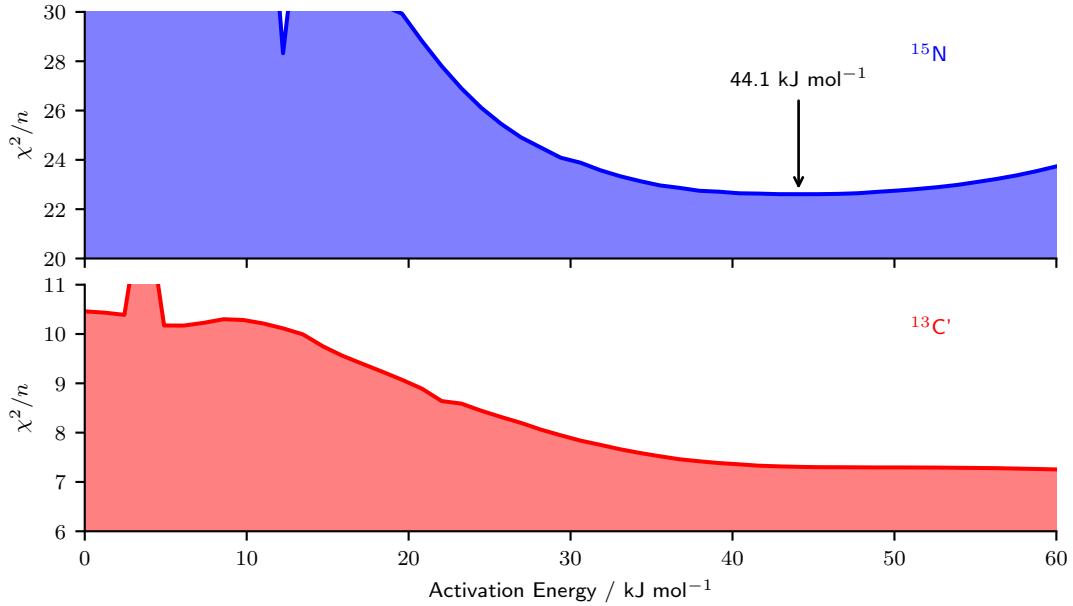

Figure 6.7: Variation in the average χ^2 value as a function of the activation energy for $k = 5$ included singular values.

Following this discussion, the activation energy for the further modelling performed here was taken as 40 kJ mol^{-1}. This value is consistent with the previously published lower bound of 25-35 kJ mol^{-1},[250,361,362] and is in agreement with both molecular dynamics and the detector-based activation energy fitting proposed here. While using a site-specific activation energy was considered, it is expected that the variation in the activation energy with site is significantly lower than the error in the value of this activation energy used here, and as such inclusion of a site-specific activation

energy would lead to over-interpretation of the data. However, it should be noted that the exact choice of activation energy does not lead to a significant change in the profile of dynamics; Appendix B shows equivalent modelling for activation energies of 30 kJ mol^{-1} and 50 kJ mol^{-1}.

6.3.2 Variable Nuclei Responses

Taking the activation energy as 40 kJ mol^{-1}, fitting was performed using truncated sets of singular values with k ranging from $2-10$. The resulting back-calculated rates are shown as a function of k in Figure 6.8. Table 6.4 shows summary statistics for the different models. The model with $k=5$ was chosen for further analysis, as this gave the lowest $\hat{\chi}^2$ value for ^{15}N indicating this was the most parsimonious.[¶] It should be noted, however, that the dynamical profiles do not significantly vary with k. The resulting five detectors for each nuclei were then paired using a linear sum assignment.

Table 6.4: Summary model statistics for models with different values of k with the activation energy fixed at 40 kJ mol^{-1}.

k	N^o ^{13}C′	N^o ^{15}N	$\frac{\chi^2}{n}$ ^{13}C′[||]	$\frac{\chi^2}{n}$ ^{15}N	$\hat{\chi}^2$ ^{13}C′[**]	$\hat{\chi}^2$ ^{15}N
2	2	2	10.35	60.48	11.75	26.08
3	3	3	9.80	30.61	11.30	21.80
4	4	4	9.45	27.59	11.23	19.83
5	5	5	7.37	22.60	8.57	**15.31**
6	6	7	7.06	20.60	**8.49**	17.00
7	7	7	6.85	20.17	9.22	15.85
8	8	9	7.03	19.77	9.78	17.60
9	9	9	7.05	19.58	10.80	17.61
10	10	11	7.62	18.83	13.42	19.63

Figure 6.9 shows the resulting responses for the paired detectors. While there is reasonable agreement between the paired detector responses for the detectors ρ_2 and ρ_3, there appears to be an scaling in the magnitude of the responses for detectors ρ_0, ρ_1, and ρ_4. This scaling likely arises due to the different interaction giving rise

[¶]While the $\hat{\chi}^2$ is lowest for $k=6$ in the case of ^{13}C′, it was chosen to take k to be the same for both to aid in the paired comparative analysis.

[||]average χ^2 value, calculated over all data

[**]median reduced χ^2 value, calculated for each individual residue and then the median taken

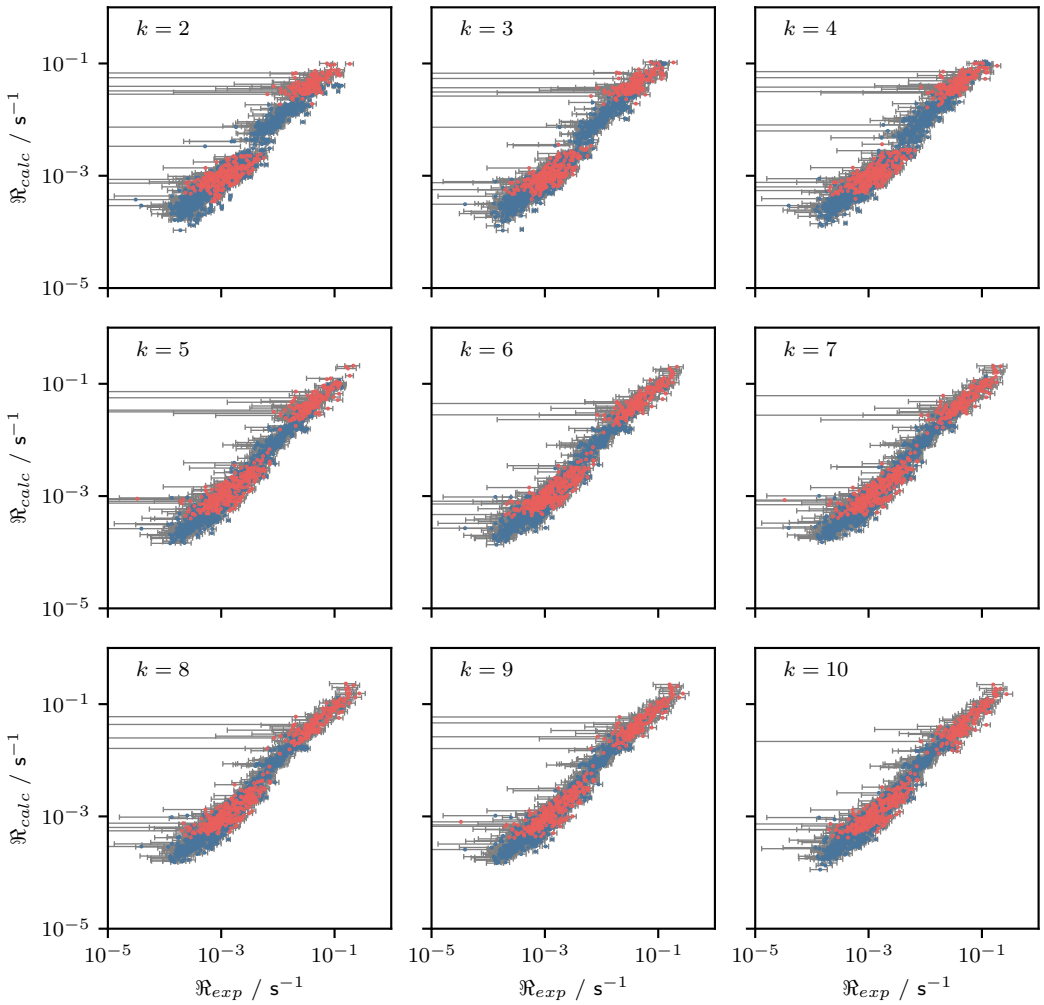

Figure 6.8: Backcalculated goodness of fit plots as a function of number of detectors included, k. ^{15}N data is shown in blue, ^{13}C′ data in red. Note that relaxation rates for which the error was greater than the measured rate have been omitted.

to this relaxation. The relaxation of the amide is dominated by the ^{15}N – ^{1}H dipole; this is invariant under rotation about the axis parallel to this bond, and invariant under translational motion occurring at this site. On the other hand, the carbonyl relaxation is dominated by the CSA tensor, which is both sensitive to all orientations of axial motion but also to translational motion. As a result, the same effective motion occurring at a site will likely modulate the CSA tensor to a greater extent, and therefore give rise to a greater response.[127] This is illustrated in Figure 6.10. To account for this variation, here the responses have been normalized such that the median of the responses for a given pair of detectors are equal. The scaling factors

for these are given in Table 6.5.

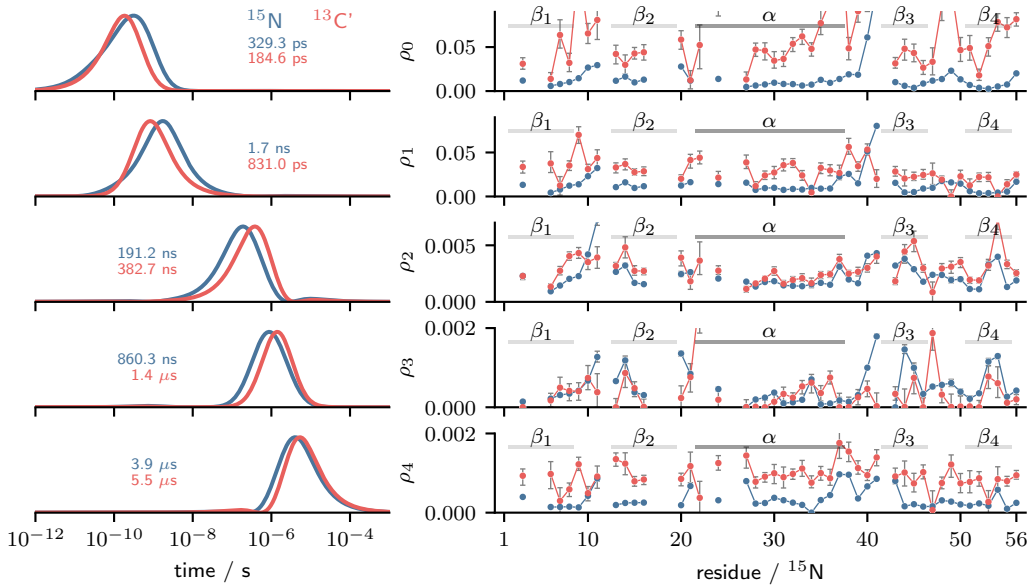

Figure 6.9: Calculated detector responses for ^{15}N and ^{13}C′. Left: Paired detector sensitivities, with the times corresponding to the maximum sensitivity of each detector shown. Right: Paired detector responses.

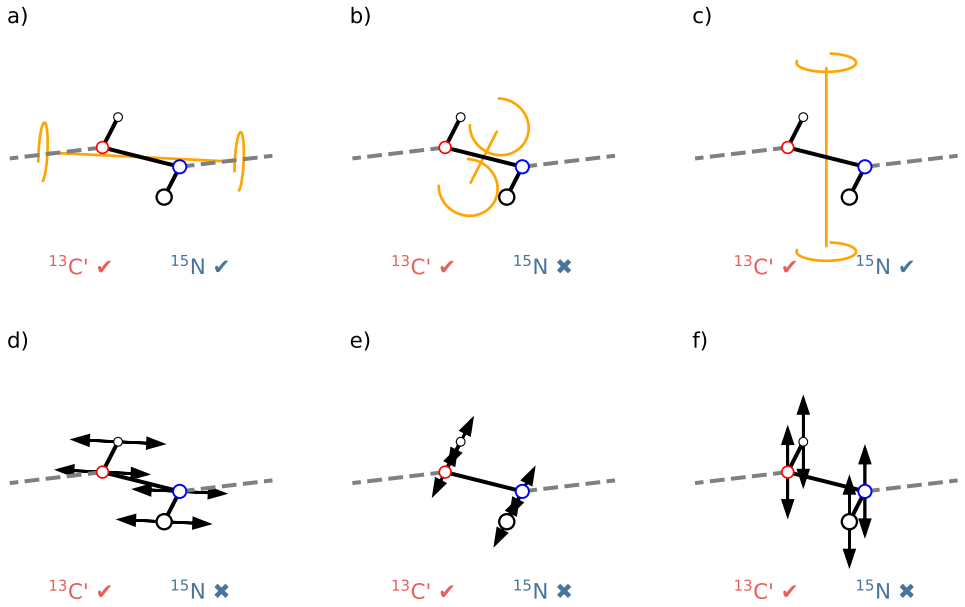

Figure 6.10: Depiction of different rotational (a, b, c) and translational (d, e, f) motion and the whether the dominant relaxation interactions for ^{15}N and ^{13}C′ are sensitive to the different types of motion. The carbonyl and nitrogen are highlighted with red and blue, respectively.

Table 6.5: Scaling factors applied to carbonyl detector responses.

Detector	Scaling Factor
ρ_0	0.26
ρ_1	0.55
ρ_2	0.83
ρ_3	1.55
ρ_4	0.41

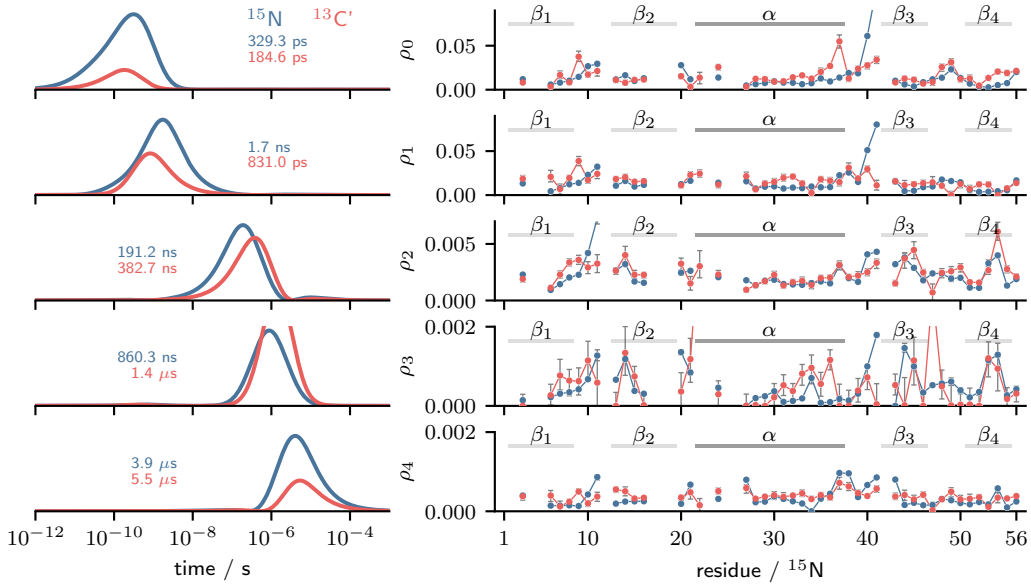

Figure 6.11: Scaled calculated detector responses for ^{15}N and ^{13}C′. Left: Detector sensitivity profiles, with the times corresponding to the maximum sensitivity of each detector shown. Right: Detector responses.

In the scaled responses, Figure 6.11, the carbonyl and amide responses show similar overall profiles of motion. For example, in the two detectors sensitive to faster motions (ρ_0, ρ_1), it is apparent that the amplitude of the motion on both nuclei appears to be reduced in the secondary structure elements relative to the loop regions between them. This is particularly apparent for the $\beta_3 - \beta_4$ region. There are a number of notable differences between the responses derived from the two nuclei, however. For example, the response for ρ_0 around β_4 appears greater on ^{13}C′ than on ^{15}N. The origin of these discrepancies will be discussed further in Section 6.3.4.

6.3.3 Comparison with Molecular Dynamics

In Figure 6.12 the resulting detector responses are compared with molecular dynamics. 2.28 μs of MD was performed for a 108 monomer containing $3 \times 3 \times 3$ supercell of GB1. In order to ensure adequate sampling of the dynamics, the comparison has been restricted to detectors where the sensitivity (see Figure 6.11, left) has decayed to approximately 0 at $t = 1$ μs; this leaves the ρ_0 and ρ_1 detector pairs. The MD detector responses were calculated using the ^{15}N – ^{1}H bond vector individually for each of the 108 GB1s, and are displayed on Figure 6.12 as a grey band showing the 5%, 50%, and 95% percentiles of these responses. In general, very good agreement is seen between the relaxation analysis and the MD derived responses.

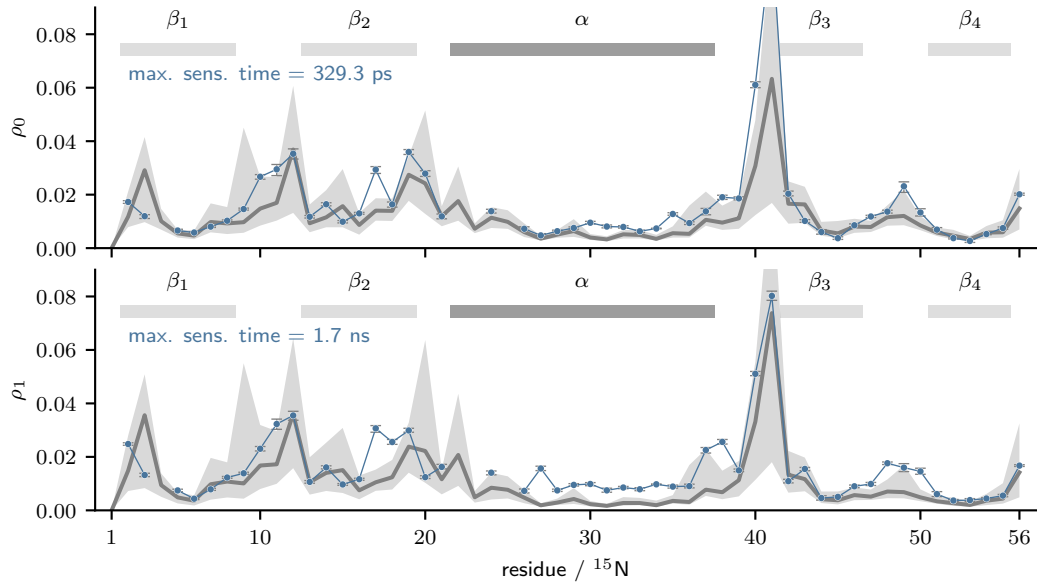

Figure 6.12: Comparison of calculated detector responses for ^{15}N with molecular dynamics. Comparison is shown for detectors covering timescales for which the MD was sensitive to. The time corresponding to the maximum sensitivity of the detector is indicated. MD response is shown as a grey band, with percentiles at 5%, 50%, 95%.

In the case of the carbonyl ^{13}C′, determining an MD derived response is significantly harder. The relaxation of ^{13}C′ is dominated by the CSA tensor. As discussed above, this is sensitive not only to a greater range of axial fluctuations but also to translational fluctuations. While CSA tensors may be calculated computationally

to good accuracy[210,212] they are very computationally expensive and currently unfeasible to perform on a protein sized system.[363] While analytical models of CSA tensors have been developed which could enable approximation of the CSA tensor,[364,365] such analysis as not been attempted here.

6.3.4 Anisotropy of Motions

After scaling the detector responses from the carbonyl, it is still notable that there are significant differences between the responses on ^{15}N and ^{13}C′ for the same peptide plane. This is unsurprising; as discussed previously, relaxation originates through the modulation of anisotropic tensors, and the tensors dominating the relaxation of the ^{13}C′ and ^{15}N are different both in orientation and asymmetry. The different responses between the two may therefore give us insight into the anisotropy and asymmetry of the motions occurring at different sites within the protein. As noted above (see Fig. 6.1 and Fig. 6.10), the ^{15}N – ^{1}H dipolar tensor dominating the relaxation of the amide is most sensitive to axial rotations perpendicular to the bond axis; that is, rotation about the ^{15}N – ^{1}H vector will not be relaxation active, nor will translation of the pair of spins. On the other hand, while the ^{13}C′ CSA tensor is sensitive to rotational motions about all axes and likely also to translation, it is most sensitive to rotational motions about an axis approximately parallel to the ^{15}N – ^{1}H.

To explore the motional anisotropy the natural log of the ratio between the ^{15}N response and the scaled ^{13}C′ response has been calculated for each pair of detectors:

$$\xi_i = \log\left(\frac{\rho_i^{\text{amide}}}{\rho_i^{\text{carbonyl}}}\right), \tag{6.3}$$

which is displayed in Figure 6.13, where a negative number (orange) indicates that the response on the carbonyl is relatively greater than the response on the amide, therefore suggesting that the dominant motion is parallel to the ^{15}N – ^{1}H bond axis,

while a positive number (purple) is a relatively greater response on the amide than the carbonyl, suggesting a dominant motion about an axis perpendicular to the ^{15}N – ^{1}H bond axis.

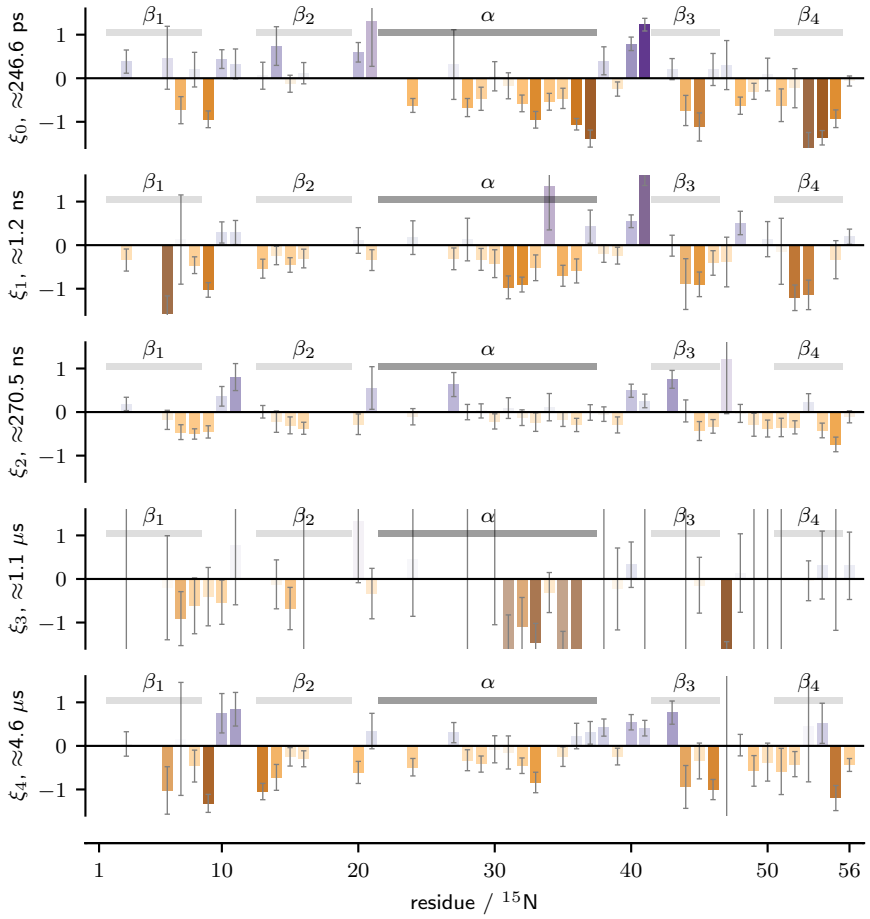

Figure 6.13: Natural log of the ratio between the ^{13}C′ response and the ^{15}N response for each pair of detectors. A negative (orange) value suggests dominant motion parallel to the ^{15}N – ^{1}H bond axis, while a positive (purple) number indicates motion perpendicular to this. The transparency of each bar is related to the scale of the error, with an error of 0 being fully opaque and an error of ≥ 1.5 being fully transparent. The log-average maximum sensitivity time of the pair of detectors is shown.

To relate these dynamical motions to the structure of GB1, Figures 6.14 and 6.15 visualise the responses for detectors ρ_0 and ρ_2 respectively (representative of fast and slow motions). Appendix C contains visualisations for the other three detectors. In these, each residue (for which responses were calculated) is shown as an ellipsoid; these have been aligned to the individual peptide planes and coloured according

to the same scale as in Figure 6.13. As shown in Figure 6.16, a larger axis in one direction indicates greater motion about this axis. As such, a 'rugby ball' shape (Fig. 6.16a) indicates a greater amount of motion about the long axis. As it is not possible to distinguish motion about the $C\alpha_i \cdots C\alpha_{i+1}$ axis and an axis perpendicular to the peptide plane, a greater response on the ^{15}N has been shown as increasing motion about both perpendicular axes (Fig 6.16). As a result, the motions about these axes are partially ambiguous.

The resulting ratios for the slower motion detectors (ξ_{2-4}) show less variation than the faster motion detectors. These slower motions are likely to be more whole body and domain like in nature (see Figure 3.6), and so it is reasonable to expect that they would have less local orientational variation. In the faster motion detectors, on the other hand, there are indications of a substantial degree of anisotropy. In the α helix, β_3, and β_4 there appears to be a dominant motion about the $^{15}N-^{1}H$ dipole, which is likely related to the significant degree of hydrogen bonding in these secondary structure elements; on the other hand, the loop regions between these either observe bias towards motion perpendicular to this dipole (for the loop between α and β_3) or motion which is not biased either way ($\beta_3 - \beta_4$). It should be noted that in the crystal structure, the $\beta_3 - \beta_4$ loop is stabilised by a sidechain-backbone hydrogen bond between Asp_{46} and Ala_{48}, while there is no such stabilisation in the $\alpha - \beta_3$ loop. The observation of bias towards motion about the $^{15}N-^{1}H$ in the β sheet may be analogous to the slow correlated motions observed by Bouvignies *et al*. (2005).[118]

The behaviour around β_2 appears slightly more complicated, with less bias towards motion about the $^{15}N-^{1}H$ axis observed relative to the other β strands. As discussed previously in Chapter 5, β_2 is involved in the recognition of the Fab domain of Immunoglobulin G..[297] It has been identified both in the solution state[118,366,367] and solid state[158,225] as a particularly mobile region of GB1, which may be an evolved characteristic of GB1 to enable it to identify the Fab domain.

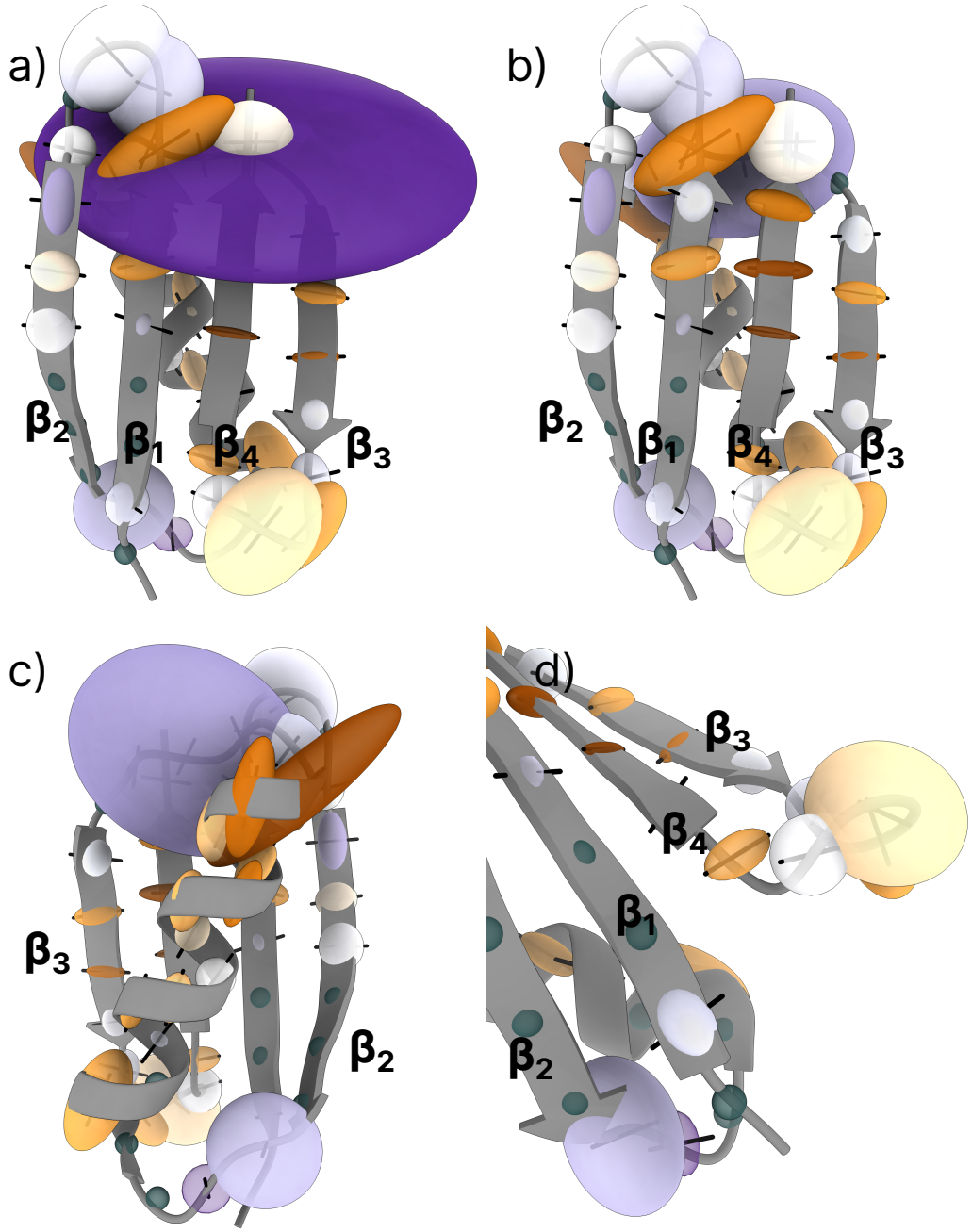

Figure 6.14: Visualisation of the anisotropic motions of detector ρ_0 projected onto the structure of GB1. Motions are shown as ellipsoids as described in Figure 6.16, with the transparency set according to the error as in Figure 6.13. The backbone of the GB1 is shown in grey, with black bars indicating the orientation of the N–H bond vector for each residue. The colours are as in Figure 6.13, with orange suggesting dominant motion parallel to the ^{15}N–^{1}H bond axis, and purple indicating motion perpendicular to this. Sites for which there was insufficient data to perform the analysis are highlighted with grey spheres. (a) Front view of the β-sheet of GB1. (b) Same as (a), but the large response on Gly_{41} has been hidden. (c) View of the α helix. (d) View of the loop regions between $\beta_2 - \alpha$ and $\beta_3 - \beta_4$.

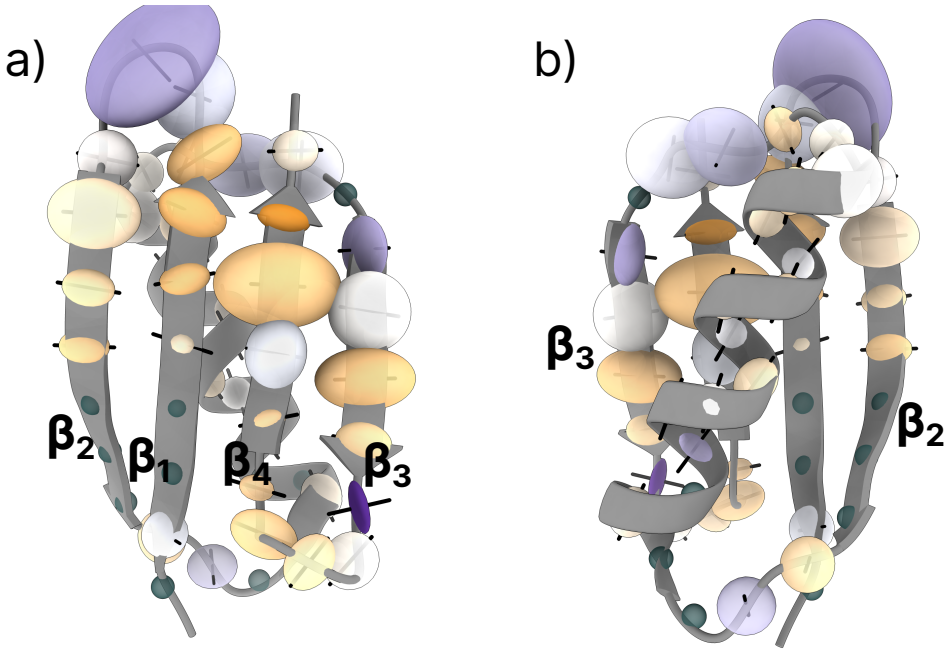

Figure 6.15: Visualisation of the anisotropic motions of detector ρ_2 projected onto the structure of GB1. Motions are shown as ellipsoids as described in Figure 6.16, with the transparency set according to the error as in Figure 6.13. Sites for which there was insufficient data to perform the analysis are highlighted with grey spheres. The backbone of the GB1 is shown as in grey, with black bars indicating the orientation of the N−H bond vector for each residue. (a) View of the β-sheet of GB1. (b) View of the α-helix of GB1. Note that for clarity, the responses have been scaled up $5\times$ relative to those shown in Figure 6.14.

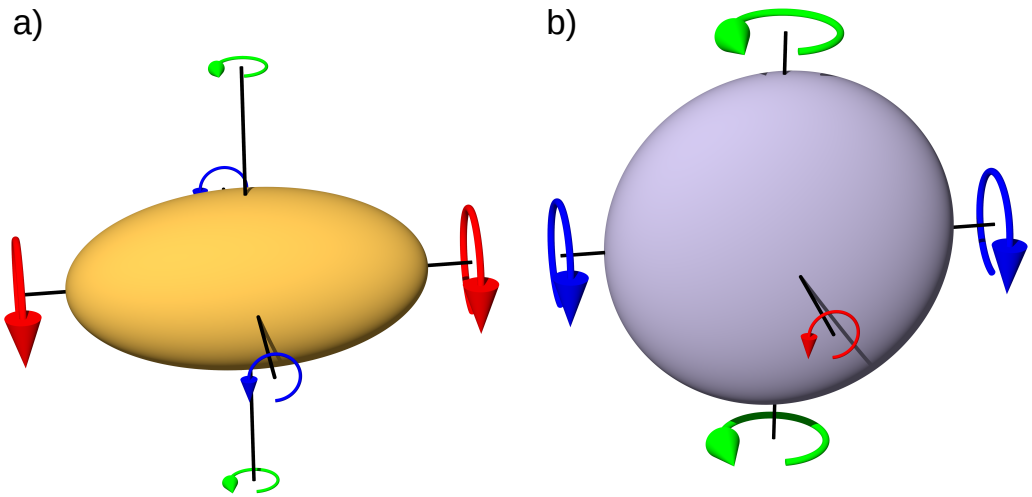

Figure 6.16: Guide to the ellipsoids shown in Figures 6.14 and 6.15. A larger axial length and corresponding larger circular arrow indicates more motion. (a) An orange 'rugby ball' like shape (*e.g.* the response on $^{13}C'$ is greater than that on ^{15}N, indicating motions about the N–H bond vector). (b) A lilac 'disc' like shape (*e.g.* the response on ^{15}N is greater than that on $^{13}C'$, indicating motions perpendicular to the N–H bond vector).

6.4 Conclusion

It has been found possible to form complementary detectors on both $^{13}C'$ and ^{15}N to study the dynamics of proteins with greater resolution. The applicability of detectors to studying variable temperature motions has been discussed, though more work is required. It has been found that the combination of ^{15}N and $^{13}C'$ detectors can enable insight into the anisotropic nature of local motions within a microcrystalline protein over a range of timescales.

The approach presented here to study the energetics and anisotropies of local protein motion may appear to be less expansive and 'precise' compared to the Model-Free[250,361,362] and GAF based methods[43,126,368] presented previously, in the sense that it does not intend to provide a model for the angular rotation, axes orientation, or to give a precise numerical value for the activation energy of the motion occurring. However, this relates to the underlying imprecision in the information provided by the relaxation rates themselves: NMR-based analyses of protein dynamics seek to characterise a distribution of motions which is unknown, unknowable (with current methodology), and for which we do not currently have a good generalisable model. The method introduced in this Chapter seeks to investigate what information these relaxation rates can provide us regarding protein motions, in a manner which acknowledges and accepts this inherent imprecision. In doing so, it makes trade-offs with regards to the complexity of the model being used, with the hope that this will provide more accurate insight into these local motions.

It is hoped that future work will further build on such detector-based analyses of different facets of protein motions beyond amplitude and timescale of motion. For instance, the model of energetics utilised here is necessarily simplified relative to reality. Future work may enable this to be expanded to provide more clarity as to the energetics of these motions.

Chapter 7

Summary and Outlook

The development of techniques in the 20th century to study both the structure and dynamics of biomolecular systems has led to a revolution in our atomic-scale view of the natural world. This revolution has been enabled by the development of new techniques and methods: the discovery of X-ray radiation and later use of this in X-ray crystallography provided our first atom-scale view of molecular structure; the invention and rapid proliferation of computers enabled, among many other things, the development of molecular dynamics to allow for insight into local mobility; and the discovery of the Fourier Transform and later development of the Fast Fourier Transform algorithm permitted the use of FT-NMR and hence multidimensional NMR.

Despite these major gains in scientific understanding, we are still limited in many ways. Crystallographic techniques face limitations in their ability to study systems for which there is no long range order, such as in precipitates, biomembranes, and fibrils (though these issues are being at least partially alleviated by the CryoEM revolution). Molecular dynamics is a computational method, and therefore requires experimental verification. As such, further method development is necessary to allow deeper exploration of the physical underpinnings of the natural world.

Solid-state NMR could, in principle, be a very useful tool to answer many of these

outstanding challenges. Nuclear magnetic resonance is a phenomenon exquisitely sensitive to the local environment surrounding a nuclear spin, both in terms of its structural and dynamical properties. Therefore, solid-state NMR spectroscopy may provide great insight into both the local structure of systems inaccessible to other methods, and the local dynamics occurring within a whole range of systems. However, it faces significant limitations in terms of sensitivity, resolution, and long experimental times. As a result, to date, it has been a relatively under applied technique compared to other methods such as X-ray crystallography, with only 164 (0.080%) published solid-state NMR structures in the PDB as of writing (see Figure 7.1). Indeed, solution- and solid-state NMR combined make up only 6.8% of the PDB combined, a percentage which does not look to be massively increasing over time (see Figure 7.2).

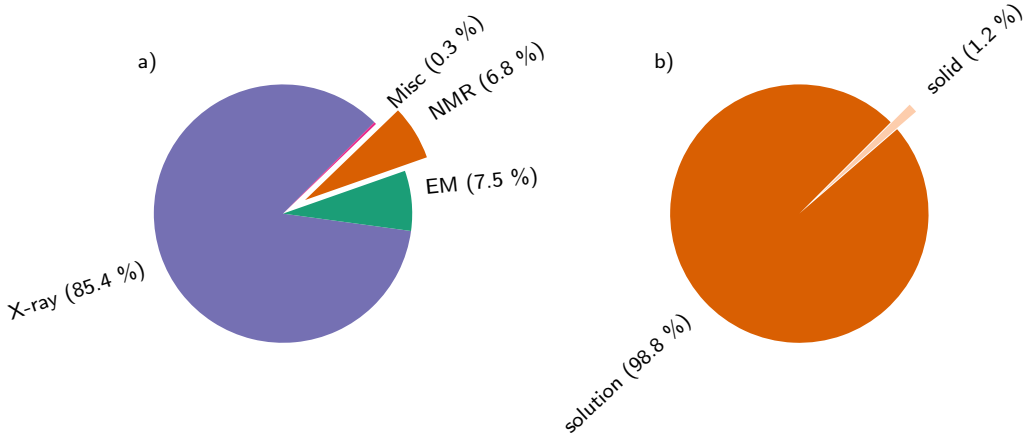

Figure 7.1: Pie chart showing the composition of the RCSB PDB[369,370] by experimental methodology. (a) The breakdown of all structures by experimental methodology. (b) Breakdown of structures determined by NMR methods into solid and solution state. It should be noted that many structures are composed of data from several techniques, in this figure these will be counted separately for each constituent technique. Values are correct as of 9th June 2023.

Recent advances and developments in solid-state NMR, however, may enable its broader appeal. The maximum attainable MAS frequency has been rising approxi-

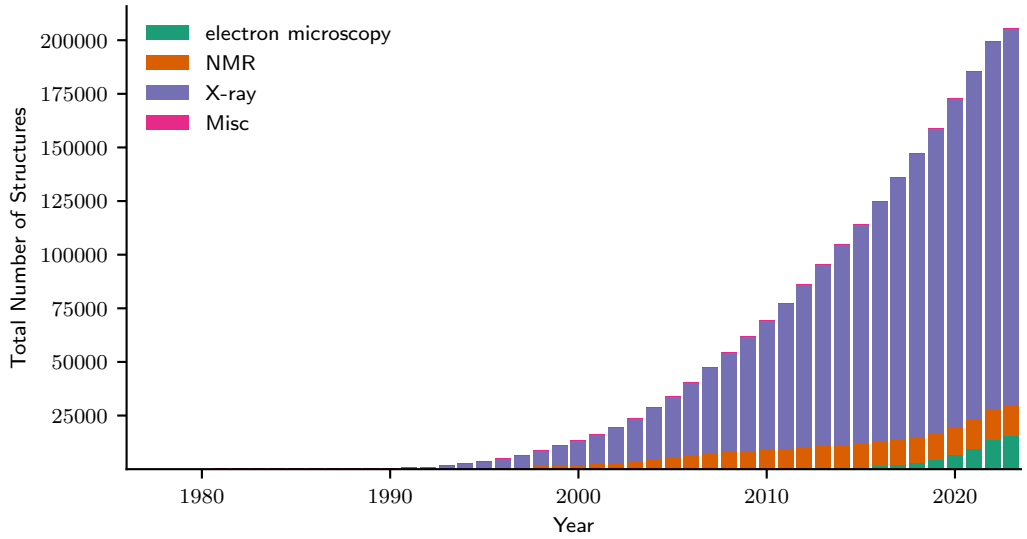

Figure 7.2: How the composition of the RCSB PDB[369,370] by experimental methodology has changed over time since its inception in 1971. Values are correct as of 9th June 2023.

mately exponentially (see Figure 7.3), with commensurate gains in sensitivity and resolution. The development of new optical spinning methods and spherical rotors[371–374] look set to keep this trend continuing into the future. The introduction of higher magnetic fields will also further enable greater applicability of the technique.[65,375]

The advent of these faster MAS probes and higher fields present both opportunities and challenges. This thesis has explored several different aspects of solid-state NMR. Chapter 4 focused on the impact that higher MAS frequencies and higher magnetic fields will have on spin diffusion. As an important tool for the characterisation of structure in solid-state NMR, understanding how spin diffusion is affected as we reach yet faster MAS frequencies will be important for the interpretation of experimental results. A new method of basis-set selection was introduced to enable the simulation of spin diffusion within larger spin systems at fast MAS frequencies. This was followed by an investigation of how such a model would predict spin diffusion to behave under these different experimental conditions, where it was found that, in moderate to high magnetic fields (14 T and above, corresponding

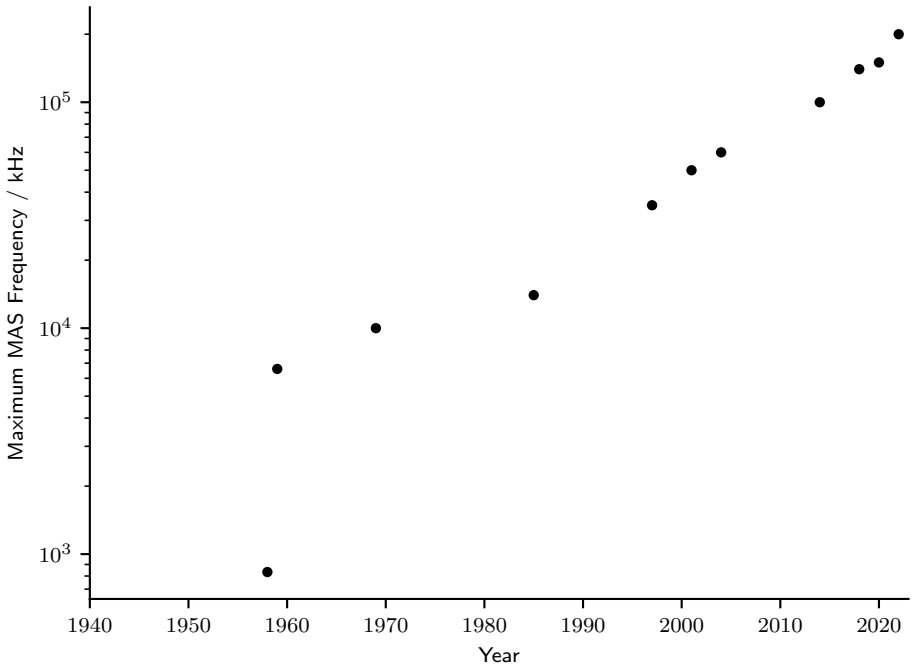

Figure 7.3: Maximum achieved MAS frequency over time as a log scale (for references, see Figure 1.4).

to ^{1}H Larmor frequencies in excess of 600 MHz), spinning frequencies ≥ 40 kHz MAS lead to significant resonance-offset truncation of spin diffusion. This effect was further investigated experimentally in Section 4.5. It was additionally found that, under these fast MAS conditions, incoherent cross-relaxation phenomena may come to dominate over the coherent spin dynamics; as a result, it may be the case that, at faster MAS frequencies, the truncation will be sufficient to enable solution-state-like nOe experiments to be performed on solids. This is likely to especially be the case in systems with significant μs dynamics, where the $J(0)$ spectral density term will come to dominate in the nuclear Overhauser effect (see equation 4.19).

In Chapters 5 and 6, different aspects relating to the use of solid-state NMR to study protein dynamics were discussed. The limited sensitivity of solid-state NMR leads to often very long experimental times. This is particularly the case for measuring relaxation rates, for which the slow relaxation of the nuclei of interest leads to a substantial increase in the time required to measure each coadded transient. While sensitivity and resolution may both be aided by technological and instrument devel-

opments, this limit of experimental time is unlikely to be as improved. Potentially a better way around this is to make use of either paramagnetic species[279,283] or selective excitation[196] to enhance the speed of experiments; however, such techniques necessarily affect the resulting measured quantities. The development of methods to enable analysis of the perturbed relaxation rates may therefore aid such experiments. In Chapter 5, the local dynamics occurring within a protein bound to an antibody (a >300 kDa protein complex, with $\approx$ 10% labelling) were studied in the presence of paramagnetic dopant. By combining analysis of the paramagnetic interaction with the dynamics, it was found to be possible to obtain a greater insight into the structure of the bound complex than would be possible by either individually. The advantages of this methodology could be extended to other systems and scenarios; for example, it might be possible to use well-placed paramagnetic tags and relaxation filters to enable spatial deconvolution of relaxation rates, thereby enabling yet faster experimental times and greater site resolution. Further, while the system used here was relatively well-suited (isotropic g-tensor, slow electron spin relaxation), it is possible that such a method could be extended to significantly more complex paramagnetic species to enable the dynamics within active sites of metalloproteins to be elucidated. The presence of anisotropic paramagnetic relaxation and interactions[376] may further enable this to be applied to gain insight into the asymmetry of motions.[377]

With recent advances in fast MAS probes, it has become possible to obtain site-specific $^{13}C'$ relaxation rates. These, in concert with ^{15}N relaxation and variable temperature measurements, were shown in Chapter 6 to enable the study of the local dynamics in a microcrystalline protein both in higher spatial and temporal resolution than previously possible, while additionally enabling the observation of anisotropic variation in the dynamics across the protein. While this technique requires a large amount of relaxation data, it is possible that the combination of this method with the separation of paramagnetic and dynamic contributions to relaxation introduced in Chapter 5 may enable this to be readily applied to a wide

range of systems of interest.

Overall, this thesis has investigated the utility of high MAS frequencies and high magnetic fields to enable the study of structure and dynamics of biological systems. Methods have been developed to investigate how spin diffusion is affected, and how these changes may affect experimental results. Some of the benefits of fast MAS for dynamical analysis have been studied in terms of how it can allow a wealth of dynamical information to be extracted from experimental data. Finally, methods to enhance the rate at which such dynamical analysis can be performed have been developed.

Bibliography

[1] W. H. Bragg and W. Bragg, "The reflection of X-rays by crystals" *P R Soc Lond A-conta*, vol. 88, pp. 428–438, 1913.

[2] W. L. Bragg, "The specular reflection of x-rays [3]" *Nature*, vol. 90, p. 410, 1912.

[3] W. L. Bragg, R. W. James, and C. H. Bosanquet, " I. The intensity of reflexion of X-rays by rock-salt .–Part II " *London*, vol. 42, pp. 1–17, 1921.

[4] W. L. Bragg, R. James, and C. Bosanquet, " XXIX. The intensity of reflexion of X-rays by rock-salt " *London*, vol. 41, pp. 309–337, 1921.

[5] W. L. Bragg, "The structure of some crystals as indicated by their diffraction of X-rays" *P R Soc Lond A-conta*, vol. 89, pp. 248–277, 1913.

[6] R. G. Dickinson and A. L. Raymond, "The Crystal Structure of Hexamethylene-Tetramine" *J. Am. Chem. Soc.*, vol. 45, pp. 22–29, 1923.

[7] W. H. Bragg, "IX. Bakerian Lecture.– X-rays and crystal structure" *Philos T R Soc Lond*, vol. 215, pp. 253–274, 1915.

[8] W. Bragg, "The determination of parameters in crystal structures by means of Fourier series" *P R Soc Lond A-conta*, vol. 123, pp. 537–559, 1929.

[9] F. L. Hünefeld, *Der Chemismus in der thierischen Organisation: physiologisch-chemische Untersuchungen der materiellen Veränderungen oder des Bildungslebens im thierischen Organismus, insbesondere des Blutbildungsprocesses, der Natur der Blutkörperchen und ihrer Kernchen;*. Brockhaus, 1840.

[10] R. Giegé, "A historical perspective on protein crystallization from 1840 to the present day" *FEBS J.*, vol. 280, pp. 6456–6497, 2013.

[11] J. D. Bernal and D. Crowfoot, "X-Ray Photographs of Crystalline Pepsin" *Nature*, vol. 133, pp. 794–795, 1934.

[12] J. C. Kendrew, G. Bodo, H. M. Dintzis, R. G. Parrish, H. Wyckoff, and D. C. Phillips, "A three-dimensional model of the myoglobin molecule obtained by x-ray analysis" *Nature*, vol. 181, pp. 662–666, 1958.

[13] J. D. Watson and F. H. Crick, "Molecular structure of nucleic acids: A structure for deoxyribose nucleic acid" *Nature*, vol. 171, pp. 737–738, 1953.

[14] M. H. Wilkins, A. R. Stokes, and H. R. Wilson, "Molecular structure of nucleic acids: Molecular structure of deoxypentose nucleic acids" *Nature*, vol. 171, pp. 738–740, 1953.

[15] R. E. Franklin and R. G. Gosling, "Molecular Configuration in Sodium Thymonucleate" *Nature*, vol. 171, pp. 740–741, 1953.

[16] D. C. Hodgkin, J. Kamper, M. MacKay, J. Pickworth, K. N. Trueblood, and J. G. White, "Structure of vitamin B_{12}" *Nature*, vol. 178, pp. 64–66, 1956.

[17] L. N. Becka and D. W. J. Cruickshank, "The crystal structure of hexamethylenetetramine I. X-ray studies at 298, 100 and 34 °K" *Proc. R Soc. Lon. Ser-a*, vol. 273, pp. 435–454, 1963.

[18] H. R. Drew, S. Samson, and R. E. Dickerson, "Structure of a B-DNA dodecamer at 16 K." *Proc. Natl. Acad. Sci.*, vol. 79, pp. 4040–4044, 1982.

[19] I. I. Rabi, J. R. Zacharias, S. Millman, and P. Kusch, "A New Method of Measuring Nuclear Magnetic Moment" *Phys. Rev.*, vol. 53, pp. 318–318, 1938.

[20] F. Bloch, W. W. Hansen, and M. Packard, "The nuclear induction experiment" *Phys. Rev.*, vol. 70, pp. 474–485, 1946.

[21] F. Bloch, "Nuclear Induction" *Phys. Rev.*, vol. 70, pp. 460–474, 1946.

[22] E. M. Purcell, H. C. Torrey, and R. V. Pound, "Resonance absorption by nuclear magnetic moments in a solid" *Phys. Rev.*, vol. 69, pp. 37–38, 1946.

[23] G. Demo, V. Papoušková, J. Komárek, P. Kadeřávek, O. Otrusinová, P. Srb, A. Rabatinová, L. Krásný, L. Žídek, V. Sklenář, and M. Wimmerová, "X-ray vs. NMR structure of N-terminal domain of δ-subunit of RNA polymerase" *J. Struct. Biol.*, vol. 187, pp. 174–186, 2014.

[24] E. Krissinel, "Macromolecular complexes in crystals and solutions" *Acta Crystallogr.*, vol. 67, pp. 376–385, 2011.

[25] R. R. Ernst and W. A. Anderson, "Application of Fourier Transform Spectroscopy to Magnetic Resonance" *Rev. Sci. Instrum.*, vol. 37, pp. 93–102, 1966.

[26] J. W. Cooley and J. W. Tukey, "An Algorithm for the Machine Calculation of Complex Fourier Series" *Math. Comput.*, vol. 19, p. 297, 1965.

[27] W. P. Aue, E. Bartholdi, and R. R. Ernst, "Two-dimensional spectroscopy. Application to nuclear magnetic resonance" *J. Chem. Phys.*, vol. 64, pp. 2229–2246, 1976.

[28] R. G. Shulman, S. Ogawa, K. Wüthrich, T. Yamane, J. Peisach, and W. E. Blumberg, "The absence of "heme-heme" interactions in hemoglobin" *Science*, vol. 165, pp. 251–257, 1969.

[29] K. Wuthrich, "Protein structure determination in solution by NMR spectroscopy" *J. Biol. Chem.*, vol. 265, pp. 22059–22062, 1990.

[30] M. P. Williamson, T. F. Havel, and K. Wüthrich, "Solution conformation of proteinase inhibitor IIA from bull seminal plasma by ^{1}H nuclear magnetic resonance and distance geometry" *J. Mol. Biol.*, vol. 182, pp. 295–315, 1985.

[31] M. F. Perutz, "Structure of hemoglobin." *Brookhaven Symp Biol*, vol. 13, pp. 165–183, 1960.

[32] I. Bertini, C. Luchinat, G. Parigi, and R. Pierattelli, "NMR Spectroscopy of Paramagnetic Metalloproteins" *ChemBioChem*, vol. 6, pp. 1536–1549, 2005.

[33] G. Wagner, "NMR investigations of protein structure" *Prog. Nucl. Magn. Reson. Spectrosc.*, vol. 22, pp. 101–139, 1990.

[34] L. Banci, I. Bertini, L. D. Eltis, I. C. Felli, D. H. Kastrau, C. Luchinat, M. Piccioli, R. Pierattelli, and M. Smith, "The three-dimensional structure in solution of the paramagnetic high-potential iron-sulfur protein I from Ectothiorhodospira halophila through nuclear magnetic resonance" *Eur J Biochem*, vol. 225, pp. 715–725, 1994.

[35] L. Pauling and C. D. Coryell, "The Magnetic Properties and Structure of Hemoglobin, Oxyhemoglobin and Carbonmonoxyhemoglobin" *Proc. Natl. Acad. Sci.*, vol. 22, pp. 210–216, 1936.

[36] M. F. Perutz, "Mechanisms of cooperativity and allosteric regulation in proteins" *Q Rev Biophys*, vol. 22, pp. 139–237, 1989.

[37] S. F. Jordan, I. Ioannou, H. Rammu, A. Halpern, L. K. Bogart, M. Ahn, R. Vasiliadou, J. Christodoulou, A. Maréchal, and N. Lane, "Spontaneous assembly of redox-active iron-sulfur clusters at low concentrations of cysteine" *Nat. Commun.*, vol. 12, 2021.

[38] W. Martin and M. J. Russell, "On the origin of biochemistry at an alkaline hydrothermal vent" *Philos T Roy Soc B*, vol. 362, pp. 1887–1925, 2007.

[39] V. Sojo, B. Herschy, A. Whicher, E. Camprubí, and N. Lane, "The Origin of Life in Alkaline Hydrothermal Vents" *Astrobiology*, vol. 16, pp. 181–197, 2016.

[40] N. Lane, J. F. Allen, and W. Martin, "How did LUCA make a living? Chemiosmosis in the origin of life" *Bioessays*, vol. 32, pp. 271–280, 2010.

[41] F. Castellani, B. Van Rossum, A. Diehl, M. Schubert, K. Rehbein, and H. Oschklnat, "Structure of a protein determined by solid-state magic-angle-spinning NMR spectroscopy" *Nature*, vol. 420, pp. 98–102, 2002.

[42] D. B. Good, S. Wang, M. E. Ward, J. Struppe, L. S. Brown, J. R. J. R. Lewandowski, and V. Ladizhansky, "Conformational Dynamics of a Seven Transmembrane Helical Protein Anabaena Sensory Rhodopsin Probed by Solid-State NMR" *J. Am. Chem. Soc.*, vol. 136, pp. 2833–2842, 2014.

[43] D. Good, C. Pham, J. Jagas, J. R. Lewandowski, and V. Ladizhansky, "Solid-State NMR Provides Evidence for Small-Amplitude Slow Domain Motions in a Multispanning Transmembrane α-Helical Protein" *J. Am. Chem. Soc.*, vol. 139, pp. 9246–9258, 2017.

[44] K. Xue, K. T. Movellan, X. C. Zhang, E. E. Najbauer, M. C. Forster, S. Becker, and L. B. Andreas, "Towards a native environment: Structure and function of membrane proteins in lipid bilayers by NMR" *Chem. Sci.*, vol. 12, pp. 14332–14342, 2021.

[45] R. Zhang, T. A. Cross, and R. Fu, "Detecting water-protein chemical exchange in membrane-bound proteins/peptides by solid-state NMR spectroscopy" *Magn. Reson. Lett.*, vol. 1, pp. 99–111, 2021.

[46] M. C. Forster, *Structure and function of the membrane protein Opa60 by solid-state NMR*. PhD thesis, Georg-August-Universität Göttingen, 2021.

[47] V. Ladizhansky, "Applications of solid-state NMR to membrane proteins" *Bba-proteins Proteom*, vol. 1865, pp. 1577–1586, 2017.

[48] E. Nimerovsky, K. T. Movellan, X. C. Zhang, M. C. Forster, E. Najbauer, K. Xue, R. Dervişoğlu, K. Giller, C. Griesinger, S. Becker, and L. B. Andreas, "Proton Detected Solid-State NMR of Membrane Proteins at 28 Tesla (1.2 GHz) and 100 kHz Magic-Angle Spinning" *Biomolecules*, vol. 11, p. 752, 2021.

[49] J. M. Lamley, D. Iuga, C. Öster, H. J. Sass, M. Rogowski, A. Oss, J. Past, A. Reinhold, S. Grzesiek, A. Samoson, and J. R. Lewandowski, "Solid-state NMR of a protein in a precipitated complex with a full-length antibody" *J. Am. Chem. Soc.*, vol. 136, pp. 16800–16806, 2014.

[50] C. Öster, S. Kosol, C. Hartlmüller, J. M. Lamley, D. Iuga, A. Oss, M.-L. Org, K. Vanatalu, A. Samoson, T. Madl, and J. R. Lewandowski, "Characterization of Protein–Protein Interfaces in Large Complexes by Solid-State NMR Solvent Paramagnetic Relaxation Enhancements" *J. Am. Chem. Soc.*, vol. 139, pp. 12165–12174, 2017.

[51] C. Öster, S. Kosol, and J. R. Lewandowski, "Quantifying Microsecond Exchange in Large Protein Complexes with Accelerated Relaxation Dispersion Experiments in the Solid State" *Sci. Rep.*, vol. 9, p. 11082, 2019.

[52] E. R. Andrew, A. Bradbury, and R. G. Eades, "Nuclear Magnetic Resonance Spectra from a Crystal rotated at High Speed" *Nature*, vol. 182, pp. 1659–1659, 1958.

[53] I. Lowe, "Free Induction Decays of Rotating Solids" *Phys. Rev. Lett.*, vol. 2, p. 285, 1959.

[54] K. M. Yip, N. Fischer, E. Paknia, A. Chari, and H. Stark, "Atomic-resolution protein structure determination by cryo-EM" *Nature*, vol. 587, pp. 157–161, 2020.

[55] T. Nakane, A. Kotecha, A. Sente, G. McMullan, S. Masiulis, P. M. G. E. Brown, I. T. Grigoras, L. Malinauskaite, T. Malinauskas, J. Miehling, T. Uchański, L. Yu, D. Karia, E. V. Pechnikova, E. de Jong, J. Keizer, M. Bischoff, J. McCormack, P. Tiemeijer, S. W. Hardwick, D. Y. Chirgadze, G. Murshudov, A. R. Aricescu, and S. H. W. Scheres, "Single-particle cryo-EM at atomic resolution" *Nature*, vol. 587, pp. 152–156, 2020.

[56] Y. Cheng, "Membrane protein structural biology in the era of single particle cryo-EM" *Curr Opin Struct Biol*, vol. 52, pp. 58–63, 2018.

[57] R. Y. R. Wang, M. Kudryashev, X. Li, E. H. Egelman, M. Basler, Y. Cheng, D. Baker, and F. Dimaio, "De novo protein structure determination from near-atomic-resolution cryo-EM maps" *Nat. Methods*, vol. 12, pp. 335–338, 2015.

[58] A. Bartesaghi, A. Merk, S. Banerjee, D. Matthies, X. Wu, J. L. Milne, and S. Subramaniam, "2.2 Å resolution cryo-EM structure of β-galactosidase in complex with a cell-permeant inhibitor" *Science*, vol. 348, pp. 1147–1151, 2015.

[59] S. C. Shoemaker and N. Ando, "X-rays in the Cryo-Electron Microscopy Era: Structural Biology's Dynamic Future" *Biochemistry (Mosc)*, vol. 57, pp. 277–285, 2018.

[60] J. Jumper, R. Evans, A. Pritzel, T. Green, M. Figurnov, R. Olaf, C. Meyer, S. A. A. Kohl, A. J. Ballard, A. Cowie, B. Romera-paredes, S. Nikolov, R. Jain, J. Adler, T. Back, S. Petersen, and D. Reiman, "Highly accurate protein structure prediction" *Nature*, vol. 596, pp. 583–589, 2021.

[61] M. Baek, F. DiMaio, I. Anishchenko, J. Dauparas, S. Ovchinnikov, G. R. Lee, J. Wang, Q. Cong, L. N. Kinch, R. Dustin Schaeffer, C. Millán, H. Park, C. Adams, C. R. Glassman, A. DeGiovanni, J. H. Pereira, A. V. Rodrigues, A. A. Van Dijk, A. C. Ebrecht, D. J. Opperman, T. Sagmeister, C. Buhlheller, T. Pavkov-Keller, M. K. Rathinaswamy, U. Dalwadi, C. K. Yip, J. E. Burke, K. Christopher Garcia, N. V. Grishin, P. D. Adams, R. J. Read, and D. Baker, "Accurate prediction of protein structures and interactions using a three-track neural network" *Science*, vol. 373, pp. 871–876, 2021.

[62] Callaway E, "The Entire Protein Universe: AI predicts shape of nearly every protein" *Nature*, vol. 608, pp. 15–16, 2022.

[63] M. Varadi, S. Anyango, M. Deshpande, S. Nair, C. Natassia, G. Yordanova, D. Yuan, O. Stroe, G. Wood, A. Laydon, A. Zídek, T. Green, K. Tunyasuvunakool, S. Petersen, J. Jumper, E. Clancy, R. Green, A. Vora, M. Lutfi, M. Figurnov, A. Cowie, N. Hobbs, P. Kohli, G. Kleywegt, E. Birney, D. Hassabis, and S. Velankar, "AlphaFold Protein Structure Database: Massively expanding the structural coverage of protein-sequence space with high-accuracy models" *Nucleic Acids Res*, vol. 50, pp. D439–D444, 2022.

[64] N. J. Fowler and M. P. Williamson, "The accuracy of protein structures in solution determined by AlphaFold and NMR" *Structure*, vol. 30, pp. 925–933.e2, 2022.

[65] H. Schwalbe, "Editorial: New 1.2 GHz NMR Spectrometers– New Horizons?" *Angew. Chem. - Int. Ed.*, vol. 56, pp. 10252–10253, 2017.

[66] E. Luchinat, L. Barbieri, M. Cremonini, and L. Banci, "Protein in-cell NMR spectroscopy at 1.2 GHz" *J. Biomol. NMR*, vol. 75, pp. 97–107, 2021.

[67] V. Agarwal, S. Penzel, K. Szekely, R. Cadalbert, E. Testori, A. Oss, J. Past, A. Samoson, M. Ernst, A. Böckmann, and B. H. Meier, "De Novo 3D Structure Determination from Sub-milligram Protein Samples by Solid-State 100 kHz MAS NMR Spectroscopy" *Angew. Chem. - Int. Ed.*, vol. 53, pp. 12253–12256, 2014.

[68] M. Schledorn, A. A. Malär, A. Torosyan, S. Penzel, D. Klose, A. Oss, M. L. Org, S. Wang, L. Lecoq, R. Cadalbert, A. Samoson, A. Böckmann, and B. H. Meier, "Protein NMR Spectroscopy at 150 kHz Magic-Angle Spinning Continues To Improve Resolution and Mass Sensitivity" *ChemBioChem*, vol. 21, pp. 2540–2548, 2020.

[69] A. Samoson, "H-MAS" *J. Magn. Reson.*, vol. 306, pp. 167–172, 2019.

[70] S. Penzel, A. Oss, M.-L. Org, A. Samoson, A. Böckmann, M. Ernst, and B. H. Meier, "Spinning faster: protein NMR at MAS frequencies up to 126 kHz" *J. Biomol. NMR*, vol. 73, pp. 19–29, 2019.

[71] B. Reif, B. J. Van Rossum, F. Castellani, K. Rehbein, A. Diehl, and H. Oschkinat, "Characterization of ^{1}H-^{1}H distances in a uniformly ^{2}H, ^{15}N-labeled SH3 domain by MAS solid-state NMR spectroscopy" *J. Am. Chem. Soc.*, vol. 125, pp. 1488–1489, 2003.

[72] B. Elena, G. Pintacuda, N. Mifsud, and L. Emsley, "Molecular Structure Determination in Powders by NMR Crystallography from Proton Spin Diffusion" vol. 128, pp. 9555–9560, 2006.

[73] E. Salager, R. S. Stein, C. J. Pickard, B. Elena, and L. Emsley, "Powder NMR crystallography of thymol" *Phys. Chem. Chem. Phys.*, vol. 11, pp. 2610–2621, 2009.

[74] B. Elena and L. Emsley, "Powder crystallography by proton solid-state NMR spectroscopy" *J. Am. Chem. Soc.*, vol. 127, pp. 9140–9146, 2005.

[75] D. Suter and R. R. Ernst, "Spin diffusion in resolved solid-state NMR spectra" *Phys. Rev. B*, vol. 32, pp. 5608–5627, 1985.

[76] A. Kubo and C. A. McDowell, "Spectral spin diffusion in polycrystalline solids under magic-angle spinning" *J. Chem. Soc.*, vol. 84, pp. 3713–3730, 1988.

[77] J. N. Dumez, M. C. Butler, and L. Emsley, "Numerical simulation of free evolution in solid-state nuclear magnetic resonance using low-order correlations in Liouville space" *J. Chem. Phys.*, vol. 133, p. 224501, 2010.

[78] J. N. Dumez, M. C. Butler, E. Salager, B. Elena-Herrmann, and L. Emsley, "Ab initio simulation of proton spin diffusion" *Phys. Chem. Chem. Phys.*, vol. 12, pp. 9172–9175, 2010.

[79] M. C. Butler, J. N. Dumez, and L. Emsley, "Dynamics of large nuclear-spin systems from low-order correlations in Liouville space" *Chem. Phys. Lett.*, vol. 477, pp. 377–381, 2009.

[80] T. Vosegaard, "Challenges in numerical simulations of solid-state NMR experiments: Spin exchange pulse sequences" *Solid State Nucl. Magn. Reson.*, vol. 38, pp. 77–83, 2010.

[81] M. Bak, J. T. Rasmussen, and N. C. Nielsen, "SIMPSON: A General Simulation Program for Solid-State NMR Spectroscopy" *J. Magn. Reson.*, vol. 147, pp. 296–330, 2000.

[82] I. Kuprov, "Large-scale NMR simulations in liquid state: A tutorial" *Magn. Reson. Chem.*, vol. 56, pp. 415–437, 2018.

[83] M. Veshtort and R. G. Griffin, "Proton-driven spin diffusion in rotating solids via reversible and irreversible quantum dynamics" *J. Chem. Phys.*, vol. 135, p. 134509, 2011.

[84] I. Kuprov, N. Wagner-Rundell, and P. J. Hore, "Polynomially scaling spin dynamics simulation algorithm based on adaptive state-space restriction" *J. Magn. Reson.*, vol. 189, pp. 241–250, 2007.

[85] F. A. Perras and M. Pruski, "Linear-scaling ab initio simulations of spin diffusion in rotating solids" *J. Chem. Phys.*, vol. 151, p. 034110, 2019.

[86] E. Andrew, L. Farnell, M. Firth, T. Gledhill, and I. Roberts, "High-speed rotors for nuclear magnetic resonance studies on solids" *J. Magn. Reson. (1969)*, vol. 1, pp. 27–34, 1969.

[87] I. Schnell, A. Lupulescu, S. Hafner, D. E. Demco, and H. W. Spiess, "Resolution Enhancement in Multiple-Quantum MAS NMR Spectroscopy" *J. Magn. Reson.*, vol. 133, pp. 61–69, 1998.

[88] A. Samoson, T. Tuherm, and J. Past, "Ramped-speed cross polarization MAS NMR" *J. Magn. Reson.*, vol. 149, pp. 264–267, 2001.

[89] M. Ernst, M. A. Meier, T. Tuherm, A. Samoson, and B. H. Meier, "Low-Power High-Resolution Solid-State NMR of Peptides and Proteins" *J. Am. Chem. Soc.*, vol. 126, pp. 4764–4765, 2004.

[90] Y. L. Lin, Y. S. Cheng, C. I. Ho, Z. H. Guo, S. J. Huang, M. L. Org, A. Oss, A. Samoson, and J. C. C. Chan, "Preparation of fibril nuclei of beta-amyloid peptides in reverse micelles" *Chem. Commun.*, vol. 54, pp. 10459–10462, 2018.

[91] N. Sinha and S. Smith-Gill, "Protein Structure to Function Via Dynamics" *Protein Pept. Lett.*, vol. 9, pp. 367–377, 2005.

[92] K. Henzler-Wildman and D. Kern, "Dynamic personalities of proteins" *Nature*, vol. 450, pp. 964–972, 2007.

[93] R. Elber and M. Karplus, "Multiple Conformational States of Myoglobin: A Molecular Dynamics Analysis" *Science*, vol. 235, pp. 15–19, 1987.

[94] J. Zhao, S. Benlekbir, and J. L. Rubinstein, "Electron cryomicroscopy observation of rotational states in a eukaryotic V-ATPase" *Nature*, vol. 521, pp. 241–245, 2015.

[95] D. Reichert, T. Zinkevich, K. Saalwächter, and A. Krushelnitsky, "The relation of the X-ray B-factor to protein dynamics: Insights from recent dynamic solid-state NMR data" *J. Biomol. Struct. Dyn.*, vol. 30, pp. 617–627, 2012.

[96] G. M. Clore and C. D. Schwieters, "Concordance of Residual Dipolar Couplings, Backbone Order Parameters and Crystallographic B-factors for a Small α/β Protein: A Unified Picture of High Probability, Fast Atomic Motions in Proteins" *J. Mol. Biol.*, vol. 355, pp. 879–886, 2006.

[97] A. Rahman, "Correlations in the motion of atoms in liquid argon" *Phys. Rev.*, vol. 136, pp. A405–A411, 1964.

[98] J. E. Lennard-Jones, "Cohesion" *Proc. Phys. Soc.*, vol. 43, pp. 461–482, 1931.

[99] M. Karplus, R. N. Porter, and R. D. Sharma, "Exchange Reactions with Activation Energy. I. Simple Barrier Potential for (H, H_2)" *J. Chem. Phys.*, vol. 43, pp. 3259–3287, 1965.

[100] B. R. Gelin, M. Karplus, and B. R. Gelin, "Side-Chain Torsional Potentials: Effect of Dipeptide, Protein, and Solvent Environment" *Biochemistry (Mosc)*, vol. 18, pp. 1256–1268, 1979.

[101] M. Levitt and S. Lifson, "Refinement of protein conformations using a macromolecular energy minimization procedure" *J. Mol. Biol.*, vol. 46, pp. 269–279, 1969.

[102] B. J. Alder and T. E. Wainwright, "Studies in Molecular Dynamics. I. General Method" *J. Chem. Phys.*, vol. 31, pp. 459–466, 1959.

[103] J. A. McCammon, B. R. Gelin, and M. Karplus, "Dynamics of folded proteins" *Nature*, vol. 267, pp. 585–590, 1977.

[104] B. R. Gelin, A. W. M. Lee, and M. Karplus, "Hemoglobin tertiary structural change on ligand binding its role in the co-operative mechanism" *J. Mol. Biol.*, vol. 171, pp. 489–559, 1983.

[105] M. Karplus and J. A. McCammon, "Dynamics of Proteins: Elements and Function" *Annu Rev Biochem*, vol. 52, pp. 263–300, 1983.

[106] J. A. McCammon and M. Karplus, "Dynamics of activated processes in globular proteins." *Proc Natl Acad Sci U S A*, vol. 76, pp. 3585–3589, 1979.

[107] R. A. Miron and K. A. Fichthorn, "Accelerated molecular dynamics with the bond-boost method" *J. Chem. Phys.*, vol. 119, pp. 6210–6216, 2003.

[108] D. Hamelberg, J. Mongan, and J. A. McCammon, "Accelerated molecular dynamics: A promising and efficient simulation method for biomolecules" *J. Chem. Phys.*, vol. 120, pp. 11919–11929, 2004.

[109] P. R. Markwick and J. A. McCammon, "Studying functional dynamics in bio-molecules using accelerated molecular dynamics" *Phys. Chem. Chem. Phys.*, vol. 13, pp. 20053–20065, 2011.

[110] P. R. Markwick, G. Bouvignies, and M. Blackledge, "Exploring multiple timescale motions in protein GB3 using accelerated molecular dynamics and NMR spectroscopy" *J. Am. Chem. Soc.*, vol. 129, pp. 4724–4730, 2007.

[111] L. C. Pierce, R. Salomon-Ferrer, C. Augusto F. De Oliveira, J. A. McCammon, and R. C. Walker, "Routine access to millisecond time scale events with accelerated molecular dynamics" *J. Chem. Theory Comput.*, vol. 8, pp. 2997–3002, 2012.

[112] D. E. Shaw, M. M. Deneroff, R. O. Dror, J. S. Kuskin, R. H. Larson, J. K. Salmon, C. Young, B. Batson, K. J. Bowers, J. C. Chao, M. P. Eastwood, J. Gagliardo, J. P. Grossman, C. R. Ho, D. J. Ierardi, I. Kolossváry, J. L. Klepeis, T. Layman, C. McLeavey, M. A. Moraes, R. Mueller, E. C. Priest, Y. Shan, J. Spengler, M. Theobald, B. Towles, and S. C. Wang, "Anton, a special-purpose machine for molecular dynamics simulation" *Commun. ACM*, vol. 51, pp. 91–97, 2008.

[113] A. Redfield, "The Theory of Relaxation Processes" in *Advances in Magnetic and Optical Resonance*, vol. 1, pp. 1–32, Academic Press Inc., 1965.

[114] Solomon I, "Relaxation Processes in a System of Two Spins" *Phys. Rev.*, vol. 953, pp. 559–565, 1955.

[115] G. Lipari and A. Szabo, "Model-Free Approach to the Interpretation of Nuclear Magnetic Resonance Relaxation in Macromolecules. 1. Theory and Range of Validity" *J. Am. Chem. Soc.*, vol. 104, pp. 4546–4559, 1982.

[116] G. Lipari and A. Szabo, "Model-Free Approach to the Interpretation of Nuclear Magnetic Resonance Relaxation in Macromolecules. 2. Analysis of Experimental Results" *J. Am. Chem. Soc.*, vol. 104, pp. 4559–4570, 1982.

[117] W. Peti, J. Meiler, R. Brüschweiler, and C. Griesinger, "Model-Free Analysis of Protein Backbone Motion from Residual Dipolar Couplings" *J. Am. Chem. Soc.*, vol. 124, pp. 5822–5833, 2002.

[118] G. Bouvignies, P. Bernadó, S. Meier, K. Cho, S. Grzesiek, R. Brüschweiler, and M. Blackledge, "Identification of slow correlated motions in proteins using residual dipolar and hydrogen-bond scalar couplings" *Proc Natl Acad Sci U S A*, vol. 102, pp. 13885–13890, 2005.

[119] Z. Zhang, Y. Shi, and H. Liu, "Molecular dynamics simulations of peptides and proteins with amplified collective motions" *Biophys J*, vol. 84, pp. 3583–3593, 2003.

[120] M. Khalili, A. Liwo, A. Jagielska, and H. A. Scheraga, "Molecular dynamics with the united-residue model of polypeptide chains. II. Langevin and Berendsen-bath dynamics and tests on model a-helical systems" *J. Phys. Chem. B*, vol. 109, pp. 13798–13810, 2005.

[121] A. Krushelnitsky, D. Gauto, D. C. R. Camargo, P. Schanda, and K. Saalwächter, "Microsecond motions probed by near-rotary-resonance $R_{1\rho}$ MAS NMR experiments: the model case of protein overall-rocking in crystals" *J. Biomol. NMR*, vol. 71, pp. 53–67, 2018.

[122] A. Krushelnitsky, T. Zinkevich, D. Reichert, V. Chevelkov, and B. Reif, "Microsecond time scale mobility in a solid protein as studied by the ^{15}N $R_{1\rho}$ site-specific NMR relaxation rates" *J. Am. Chem. Soc.*, vol. 132, pp. 11850–11853, 2010.

[123] J. R. Lewandowski, H. J. Sass, S. Grzesiek, M. Blackledge, and L. Emsley, "Site-Specific Measurement of Slow Motions in Proteins" *J. Am. Chem. Soc.*, vol. 133, pp. 16762–16765, 2011.

[124] R. A. Stevens, *The Development of Solid-Sate NMR Methodology to Study the Dynamics of Proteins and Ice*. PhD thesis, University of Warwick, 2018.

[125] T. Le Marchand, T. Schubeis, M. Bonaccorsi, P. Paluch, D. Lalli, A. J. Pell, L. B. Andreas, K. Jaudzems, J. Stanek, and G. Pintacuda, "^{1}H-Detected Biomolecular NMR under Fast Magic-Angle Spinning" *Chem. Rev.*, vol. 122, pp. 9943–10018, 2022.

[126] S. F. Lienin, T. Bremi, B. Brutscher, R. Brüschweiler, and R. R. Ernst, "Anisotropic Intramolecular Backbone Dynamics of Ubiquitin Characterized by NMR Relaxation and MD Computer Simulation" *J. Am. Chem. Soc.*, vol. 120, pp. 9870–9879, 1998.

[127] J. Engelke and H. Rüterjans, "Backbone dynamics of proteins derived from carbonyl carbon relaxation times at 500, 600 and 800 MHz: Application to ribonuclease T1" *J. Biomol. NMR*, vol. 9, pp. 63–78, 1997.

[128] A. A. Smith, A. Vogel, O. Engberg, P. W. Hildebrand, and D. Huster, "A method to construct the dynamic landscape of a bio-membrane with experiment and simulation" *Nat. Commun.*, vol. 13, pp. 1–13, 2022.

[129] A. A. Smith, M. Ernst, S. Riniker, and B. H. Meier, "Localized and Collective Motions in HET-s(218-289) Fibrils from Combined NMR Relaxation and MD Simulation" *International Edition*, vol. 131, pp. 9483–9488, 2019.

[130] A. A. Smith, "Interpreting NMR dynamic parameters via the separation of reorientational motion in MD simulation" *J. Magn. Reson. Open*, vol. 10-11, p. 100045, 2022.

[131] J. Keeler, *Understanding NMR Spectroscopy*. Chichester, U.K: John Wiley and Sons, second ed., 2010.

[132] A. Abragam, *The Principles of Nuclear Magnetism*. Comparative Pathobiology - Studies in the Postmodern Theory of Education, Clarendon Press, 1961.

[133] M. H. Levitt, *Spin Dynamics: Basics of Nuclear Magnetic Resonance*. Chichester: Wiley, second ed., 2008.

[134] G. Pileio, *Lectures on Spin Dynamics: The Theoretical Minimum*. Royal Society of Chemistry, 2022.

[135] N. J. Stone, "Table of recommended nuclear magnetic dipole moments" tech. rep., International Atomic Energy Agency (IAEA), 2019.

[136] U. Haeberlen and J. S. Waugh, "Coherent Averaging Effects in Magnetic Resonance" *Phys. Rev.*, vol. 175, pp. 453–467, 1968.

[137] J. H. Shirley, "Solution of the Schrödinger Equation with a Hamiltonian Periodic in Time" *Phys. Rev.*, vol. 138, pp. B979—-B987, 1963.

[138] A. Schmidt and S. Vega, "The Floquet theory of nuclear magnetic resonance spectroscopy of single spins and dipolar coupled spin pairs in rotating solids" *J. Chem. Phys.*, vol. 96, pp. 2655–2680, 1992.

[139] A. D. Bain and J. S. Martin, "FT NMR of nonequilibrium states of complex spin systems. I. A Lionville space description" *J. Magn. Reson. (1969)*, vol. 29, pp. 125–135, 1978.

[140] I. Kuprov, *Spin*. Southampton: Springer International Publishing, 1 ed., 2023.

[141] J. A. Gyamfi, "Fundamentals of quantum mechanics in Liouville space" *Eur. J. Phys.*, vol. 41, p. 063002, 2020.

[142] A. Brinkmann, "Introduction to average Hamiltonian theory. I. Basics" *Concepts Magn. Reson. Part A Bridg. Educ. Res*, vol. 45A, p. e21414, 2016.

[143] M. M. Maricq and J. S. Waugh, "NMR in rotating solids" *J. Chem. Phys.*, vol. 70, pp. 3300–3316, 1979.

[144] K. Xue, R. Sarkar, C. Motz, S. Asami, V. Decker, S. Wegner, Z. Tosner, and B. Reif, "Magic-Angle Spinning Frequencies beyond 300 kHz Are Necessary to Yield Maximum Sensitivity in Selectively Methyl Protonated Protein Samples in Solid-State NMR" *J. Phys. Chem. C*, vol. 122, pp. 16437–16442, 2018.

[145] M. W. F. Fischer, A. Majumdar, and E. R. P. Zuiderweg, "Protein NMR relaxation: theory, applications and outlook" *Prog. Nucl. Magn. Reson. Spectrosc.*, vol. 33, pp. 207–272, 1998.

[146] R. Kurbanov, T. Zinkevich, and A. Krushelnitsky, "The nuclear magnetic resonance relaxation data analysis in solids: General R_1 / $R_{1\rho}$ equations and the model-free approach" *J. Chem. Phys.*, vol. 135, p. 184104, 2011.

[147] I. Solomon, "Relaxation Processes in a System of Two Spins" *Phys. Rev.*, vol. 99, pp. 559–565, 1955.

[148] J. W. Peng and G. Wagner, "Mapping of spectral density functions using heteronuclear NMR relaxation measurements" *J. Magn. Reson. (1969)*, vol. 98, pp. 308–332, 1992.

[149] S. N. Khan, C. Charlier, R. Augustyniak, N. Salvi, V. Déjean, G. Bodenhausen, O. Lequin, P. Pelupessy, and F. Ferrage, "Distribution of Pico- and Nanosecond Motions in Disordered Proteins from Nuclear Spin Relaxation" *Biophys J*, vol. 109, pp. 988–999, 2015.

[150] A. A. Smith, M. Ernst, and B. H. Meier, "Because the Light is Better Here: Correlation-Time Analysis by NMR Spectroscopy" *Angew. Chem. - Int. Ed.*, vol. 56, pp. 13590–13595, 2017.

[151] R. Ishima, D. I. Freedberg, Y. X. Wang, J. M. Louis, and D. A. Torchia, "Flap opening and dimer-interface flexibility in the free and inhibitor- bound HIV protease, and their implications for function" *Structure*, vol. 7, pp. 1047–1055, 1999.

[152] J. W. Peng and G. Wagner, "Mapping of the Spectral Densities of N-H Bond Motions in Eglin C Using Heteronuclear Relaxation Experiments" *Biochemistry (Mosc)*, vol. 31, pp. 8571–8586, 1992.

[153] J. W. Peng and G. Wagner, "Frequency Spectrum of NH Bonds in Eglin c from Spectral Density Mapping at Multiple Fields" *Biochemistry (Mosc)*, vol. 34, pp. 16733–16752, 1995.

[154] J. M. L. Del Amo, V. Agarwal, R. Sarkar, J. Porter, S. Asami, M. Rübbelke, U. Fink, Y. Xue, O. F. Lange, and B. Reif, "Site-specific analysis of heteronuclear Overhauser effects in microcrystalline proteins" *J. Biomol. NMR*, vol. 59, pp. 241–249, 2014.

[155] D. M. Brink and G. R. Satchler, *Angular Momentum*. Oxford University Press, 1968.

[156] G. M. Clore, A. Szabo, A. Bax, L. E. Kay, P. C. Driscoll, and A. M. Gronenborn, "Deviations from the Simple Two-Parameter Model-Free Approach to the Interpretation of Nitrogen-15 Nuclear Magnetic Relaxation of Proteins" *J. Am. Chem. Soc.*, vol. 112, pp. 4989–4991, 1990.

[157] V. Chevelkov, U. Fink, and B. Reif, "Quantitative analysis of backbone motion in proteins using MAS solid-state NMR spectroscopy" *J. Biomol. NMR*, vol. 45, pp. 197–206, 2009.

[158] L. Mollica, M. Baias, J. R. Lewandowski, B. J. Wylie, L. J. Sperling, C. M. Rienstra, L. Emsley, and M. Blackledge, "Atomic-Resolution Structural Dynamics in Crystalline Proteins from NMR and Molecular Simulation" *J. Phys. Chem. Lett.*, vol. 3, pp. 3657–3662, 2012.

[159] K. Zumpfe and A. A. Smith, "Model-Free or Not?" *Front. Mol. Biosci.*, vol. 8, pp. 1–26, 2021.

[160] A. A. Smith, M. Ernst, and B. H. Meier, "Optimized "detectors" for dynamics analysis in solid-state NMR" *J. Chem. Phys.*, vol. 148, p. 045104, 2018.

[161] A. A. Smith, M. Ernst, B. H. Meier, and F. Ferrage, "Reducing bias in the analysis of solution-state NMR data with dynamics detectors" *J. Chem. Phys.*, vol. 151, p. 034102, 2019.

[162] P. Virtanen, R. Gommers, T. E. Oliphant, M. Haberland, T. Reddy, D. Cournapeau, E. Burovski, P. Peterson, W. Weckesser, J. Bright, S. J. van der Walt, M. Brett, J. Wilson, K. J. Millman, N. Mayorov, A. R. J. Nelson, E. Jones, R. Kern, E. Larson, C. J. Carey, I. Polat, Y. Feng, E. W. Moore, J. VanderPlas, D. Laxalde, J. Perktold, R. Cimrman, I. Henriksen, E. A. Quintero, C. R. Harris, A. M. Archibald, A. H. Ribeiro, F. Pedregosa, P. van Mulbregt, A. Vijaykumar, A. P. Bardelli, A. Rothberg, A. Hilboll, A. Kloeckner, A. Scopatz, A. Lee, A. Rokem, C. N. Woods, C. Fulton, C. Masson, C. Häggström, C. Fitzgerald, D. A. Nicholson, D. R. Hagen, D. V. Pasechnik, E. Olivetti, E. Martin, E. Wieser, F. Silva, F. Lenders, F. Wilhelm, G. Young, G. A. Price, G.-L. Ingold, G. E. Allen, G. R. Lee, H. Audren, I. Probst, J. P. Dietrich, J. Silterra, J. T. Webber, J. Slavič, J. Nothman, J. Buchner, J. Kulick, J. L. Schönberger, J. V. de Miranda Cardoso, J. Reimer, J. Harrington, J. L. C. Rodríguez, J. Nunez-Iglesias, J. Kuczynski, K. Tritz, M. Thoma, M. Newville, M. Kümmerer, M. Bolingbroke, M. Tartre, M. Pak, N. J. Smith, N. Nowaczyk, N. Shebanov, O. Pavlyk, P. A. Brodtkorb, P. Lee, R. T. McGibbon, R. Feldbauer, S. Lewis, S. Tygier, S. Sievert, S. Vigna, S. Peterson, S. More, T. Pudlik, T. Oshima, T. J. Pingel, T. P. Robitaille, T. Spura, T. R. Jones, T. Cera, T. Leslie, T. Zito, T. Krauss, U. Upadhyay, Y. O. Halchenko, and Y. Vázquez-Baeza, "SciPy 1.0: fundamental algorithms for scientific computing in Python" *Nat. Methods*, vol. 17, pp. 261–272, 2020.

[163] A. A. Malär, M. Callon, A. A. Smith, S. Wang, L. Lecoq, C. Pérez-Segura, J. A. Hadden-Perilla, A. Böckmann, and B. H. Meier, "Experimental Characterization of the Hepatitis B Virus Capsid Dynamics by Solid-State NMR" *Front. Mol. Biosci.*, vol. 8, pp. 1–15, 2022.

[164] S. R. Hartmann and E. L. Hahn, "Nuclear double resonance in the rotating frame" *Phys. Rev.*, vol. 128, pp. 2042–2053, 1962.

[165] A. Pines, M. G. Gibby, and J. S. Waugh, "Proton-enhanced nuclear induction spectroscopy. a method for high resolution NMR of dilute spins in solids" *J. Chem. Phys.*, vol. 56, pp. 1776–1777, 1972.

[166] D. Carnevale, X. Ji, and G. Bodenhausen, "Double cross polarization for the indirect detection of nitrogen-14 nuclei in magic angle spinning NMR spectroscopy" *J. Chem. Phys.*, vol. 147, p. 184201, 2017.

[167] I. Hung, P. Gor'kov, Z. Gan, P. Gor'kov, and Z. Gan, "Efficient and sideband-free ^{1}H-detected ^{14}N magic-angle spinning NMR" *J. Chem. Phys.*, vol. 151, pp. 1–9, 2019.

[168] G. Metz, X. Wu, and S. Smith, "Ramped-Amplitude Cross Polarization in Magic-Angle-Spinning NMR" *J. Magn. Reson. A*, vol. 110, pp. 219–227, 1994.

[169] D. H. Zhou and C. M. Rienstra, "High-performance solvent suppression for proton detected solid-state NMR" *J. Magn. Reson.*, vol. 192, pp. 167–172, 2008.

[170] D. Marion, M. Ikura, R. Tschudin, and A. Bax, "Rapid recording of 2D NMR spectra without phase cycling. Application to the study of hydrogen exchange in proteins" *J. Magn. Reson. (1969)*, vol. 85, pp. 393–399, 1989.

[171] D. States, R. Haberkorn, and D. Ruben, "A two-dimensional nuclear overhauser experiment with pure absorption phase in four quadrants" *J. Magn. Reson. (1969)*, vol. 48, pp. 286–292, 1982.

[172] D. Marion and K. Wüthrich, "Application of phase sensitive two-dimensional correlated spectroscopy (COSY) for measurements of ^{1}H-^{1}H spin-spin coupling constants in proteins" *Biochem Biophys Res Commun*, vol. 113, pp. 967–974, 1983.

[173] A. D. Bain, "Coherence levels and coherence pathways in NMR. A simple way to design phase cycling procedures" *J. Magn. Reson. (1969)*, vol. 56, pp. 418–427, 1984.

[174] G. Bodenhausen, H. Kogler, and R. Ernst, "Selection of coherence-transfer pathways in NMR pulse experiments" *J. Magn. Reson. (1969)*, vol. 58, pp. 370–388, 1984.

[175] C. Bauer, R. Freeman, T. Frenkiel, J. Keeler, and A. J. Shaka, "Gaussian pulses" *J. Magn. Reson. (1969)*, vol. 58, pp. 442–457, 1984.

[176] H. Kessler, H. Oschkinat, C. Griesinger, and W. Bermel, "Transformation of homonuclear two-dimensional NMR techniques into one-dimensional techniques using Gaussian pulses" *J. Magn. Reson. (1969)*, vol. 70, pp. 106–133, 1986.

[177] G. A. Morris and R. Freeman, "Enhancement of Nuclear Magnetic Resonance Signals by Polarization Transfer" *J. Am. Chem. Soc.*, vol. 101, pp. 760–762, 1979.

[178] J. R. Lewandowski, "Advances in solid-state relaxation methodology for probing site-specific protein dynamics" *Acc. Chem. Res.*, vol. 46, pp. 2018–2027, 2013.

[179] D. A. Torchia, "The measurement of proton-enhanced carbon-13 T_1 values by a method which suppresses artifacts" *J. Magn. Reson. (1969)*, vol. 33, p. 481, 1979.

[180] V. Kurauskas, S. A. Izmailov, O. N. Rogacheva, A. Hessel, I. Ayala, J. Woodhouse, A. Shilova, Y. Xue, T. Yuwen, N. Coquelle, J. P. Colletier, N. R. Skrynnikov, and P. Schanda, "Slow conformational exchange and overall rocking motion in ubiquitin protein crystals" *Nat. Commun.*, vol. 8, pp. 1–11, 2017.

[181] D. Marion, D. F. Gauto, I. Ayala, K. Giandoreggio-Barranco, and P. Schanda, "Microsecond Protein Dynamics from Combined Bloch-McConnell and Near-Rotary-Resonance $R_{1\rho}$ Relaxation-Dispersion MAS NMR" *ChemPhysChem*, vol. 20, pp. 276–284, 2019.

[182] J. Sein, N. Giraud, M. Blackledge, and L. Emsley, "The role of ^{15}N CSA and CSA/dipole cross-correlation in ^{15}N relaxation in solid proteins" *J. Magn. Reson.*, vol. 186, pp. 26–33, 2007.

[183] S. Asami, J. R. Porter, O. F. Lange, and B. Reif, "Access to Cα Backbone Dynamics of Biological Solids by ^{13}C T_1 Relaxation and Molecular Dynamics Simulation" *J. Am. Chem. Soc.*, vol. 137, pp. 1094–1100, 2015.

[184] E. A. Alharbi, A. Y. Alyamani, D. J. Kubicki, A. R. Uhl, B. J. Walder, A. Q. Alanazi, J. Luo, A. Burgos-Caminal, A. Albadri, H. Albrithen, M. H. Alotaibi, J.-E. Moser, S. M. Zakeeruddin, F. Giordano, L. Emsley, and M. Grätzel, "Atomic-level passivation mechanism of ammonium salts enabling highly efficient perovskite solar cells" *Nat. Commun.*, vol. 10, p. 3008, 2019.

[185] R. Cresswell, R. Dupree, S. P. Brown, C. S. Pereira, M. S. Skaf, M. Sorieul, P. Dupree, and S. Hill, "Importance of Water in Maintaining Softwood Secondary Cell Wall Nanostructure" *Biomacromolecules*, vol. 22, pp. 4669–4680, 2021.

[186] O. M. Terrett, J. J. Lyczakowski, L. Yu, D. Iuga, W. T. Franks, S. P. Brown, R. Dupree, and P. Dupree, "Molecular architecture of softwood revealed by solid-state NMR" *Nat. Commun.*, vol. 10, p. 4978, 2019.

[187] G. N. Reddy, A. Huqi, D. Iuga, S. Sakurai, A. Marsh, J. T. Davis, S. Masiero, and S. P. Brown, "Co-existence of Distinct Supramolecular Assemblies in Solution and in the Solid State" *Chem. Eur. J.*, vol. 23, pp. 2315–2322, 2017.

[188] S. Wang, R. A. Munro, L. Shi, I. Kawamura, T. Okitsu, A. Wada, S.-Y. Y. Kim, K.-H. H. Jung, L. S. Brown, and V. Ladizhansky, "Solid-state NMR spectroscopy structure determination of a lipid-embedded heptahelical membrane protein" *Nat. Methods*, vol. 10, pp. 1007–1012, 2013.

[189] Q. Stern, S. F. Cousin, F. Mentink-Vigier, A. C. Pinon, S. J. Elliott, O. Cala, and S. Jannin, "Direct observation of hyperpolarization breaking through the spin diffusion barrier" *Sci. Adv.*, vol. 7, pp. 1–14, 2021.

[190] F. A. Perras, M. Raju, S. L. Carnahan, D. Akbarian, A. C. Van Duin, A. J. Rossini, and M. Pruski, "Full-Scale Ab Initio Simulation of Magic-Angle-Spinning Dynamic Nuclear Polarization" *J. Phys. Chem. Lett.*, vol. 11, pp. 5655–5660, 2020.

[191] A. C. Pinon, J. Schlagnitweit, P. Berruyer, A. J. Rossini, M. Lelli, E. Socie, M. Tang, T. Pham, A. Lesage, S. Schantz, and L. Emsley, "Measuring Nano- to Microstructures from Relayed Dynamic Nuclear Polarization NMR" *J. Phys. Chem. C*, vol. 121, pp. 15993–16005, 2017.

[192] K. O. Tan, M. Mardini, C. Yang, J. H. Ardenkjær-Larsen, and R. G. Griffin, "Three-spin solid effect and the spin diffusion barrier in amorphous solids" *Sci. Adv.*, vol. 5, pp. 1–8, 2019.

[193] P. C. A. van der Wel, K.-N. Hu, J. Lewandowski, and R. G. Griffin, "Dynamic Nuclear Polarization of Amyloidogenic Peptide Nanocrystals: GNNQQNY, a Core Segment of the Yeast Prion Protein Sup35p" *J. Am. Chem. Soc.*, vol. 128, pp. 10840–10846, 2006.

[194] Ü. Akbey, W. T. Franks, A. Linden, S. Lange, R. G. Griffin, B. J. Van Rossum, and H. Oschkinat, "Dynamic nuclear polarization of deuterated proteins" *Angew. Chem. - Int. Ed.*, vol. 49, pp. 7803–7806, 2010.

[195] A. J. Robertson, M. K. Pandey, A. Marsh, Y. Nishiyama, and S. P. Brown, "The use of a selective saturation pulse to suppress t_1 noise in two-dimensional ^{1}H fast magic angle spinning solid-state NMR spectroscopy" *J. Magn. Reson.*, vol. 260, pp. 89–97, 2015.

[196] A. V. Wijesekara, A. Venkatesh, B. J. Lampkin, B. VanVeller, J. W. Lubach, K. Nagapudi, I. Hung, P. L. Gor'kov, Z. Gan, A. J. Rossini, P. L. Gor'kov, Z. Gan, and A. J. Rossini, "Fast Acquisition of Proton-Detected HETCOR Solid-State NMR Spectra of Quadrupolar Nuclei and Rapid Measurement of NH Bond Lengths by Frequency Selective HMQC and RESPDOR Pulse Sequences" *Chem. Eur. J.*, vol. 26, pp. 7881–7888, 2020.

[197] D. A. Hirsh, A. V. Wijesekara, S. L. Carnahan, I. Hung, J. W. Lubach, K. Nagapudi, and A. J. Rossini, "Rapid characterization of formulated pharmaceuticals using fast MAS ^{1}H solid-state NMR spectroscopy" *Mol. Pharmaceutics*, vol. 16, pp. 3121–3132, 2019.

[198] P. Rovó and R. Linser, "Microsecond Timescale Protein Dynamics: a Combined Solid-State NMR Approach" *ChemPhysChem*, vol. 19, pp. 34–39, 2018.

[199] J. J. Wittmann, V. Agarwal, J. Hellwagner, A. Lends, R. Cadalbert, B. H. Meier, and M. Ernst, "Accelerating proton spin diffusion in perdeuterated proteins at 100 kHz MAS" *J. Biomol. NMR*, vol. 66, pp. 233–242, 2016.

[200] V. Agarwal, "The Origin of Negative Cross-peaks in Proton-Spin Diffusion Spectrum of Fully Protonated Solids at Fast MAS: Coherent or Incoherent Effect?" *J. Magn. Reson.*, vol. 311, p. 106661, 2019.

[201] L.-S. Du, M. H. Levitt, and C. P. Grey, "High-Order Spin Diffusion Mechanisms in ^{19}F 2-D NMR of Oxyfluorides" *J. Magn. Reson.*, vol. 140, pp. 242–249, 1999.

[202] T. Vosegaard, "Fast simulations of multidimensional NMR spectra of proteins and peptides" *Magn. Reson. Chem.*, vol. 56, pp. 438–448, 2018.

[203] L. J. Edwards, D. V. Savostyanov, Z. T. Welderufael, D. Lee, and I. Kuprov, "Quantum mechanical NMR simulation algorithm for protein-size spin systems" *J. Magn. Reson.*, vol. 243, pp. 107–113, 2014.

[204] F. A. Perras, S. L. Carnahan, W.-s. Lo, C. J. Ward, J. Yu, W. Huang, and A. J. Rossini, "Hybrid quantum-classical simulations of magic angle spinning dynamic nuclear polarization in very large spin systems" *J. Chem. Phys.*, vol. 156, p. 124112, 2022.

[205] C. H. Görbitz, P. Strande, K. Undheim, R. W. Taft, and G. W. Fischer, "Crystal and Molecular Structures of the Isomeric Dipeptides alpha-L-Aspartyl-L-alanine and beta-L-Aspartyl-L-alanine." *Acta Chem Scand*, vol. 41b, pp. 679–685, 1987.

[206] M. C. Payne, M. P. Teter, D. C. Allan, T. A. Arias, and J. D. Joannopoulos, "Iterative minimization techniques for ab initio total-energy calculations: Molecular dynamics and conjugate gradients" *Rev. Mod. Phys.*, vol. 64, pp. 1045–1097, 1992.

[207] M. D. Segall, P. J. D. Lindan, M. J. Probert, C. J. Pickard, P. J. Hasnip, S. J. Clark, and M. C. Payne, "First-principles simulation: ideas, illustrations and the CASTEP code" *J. Phys.: Condens. Matter*, vol. 14, p. 2717, 2002.

[208] S. J. Clark, M. D. Segall, C. J. Pickard, P. J. Hasnip, M. I. Probert, K. Refson, and M. C. Payne, "First principles methods using CASTEP" *Kristallgeometrie*, vol. 220, pp. 567–570, 2005.

[209] J. P. Perdew, K. Burke, and M. Ernzerhof, "Generalized Gradient Approximation Made Simple" *Phys. Rev. Lett.*, vol. 77, pp. 3865–3868, 1996.

[210] C. J. Pickard and F. Mauri, "All-electron magnetic response with pseudopotentials: NMR chemical shifts" *Phys. Rev. B*, vol. 63, p. 245101, 2001.

[211] C. Gervais, R. Dupree, K. J. Pike, C. Bonhomme, M. Profeta, C. J. Pickard, and F. Mauri, "Combined First-Principles Computational and Experimental Multinuclear Solid-State NMR Investigation of Amino Acids" *J. Phys. Chem. A*, vol. 109, pp. 6960–6969, 2005.

[212] J. R. Yates, C. J. Pickard, and F. Mauri, "Calculation of NMR chemical shifts for extended systems using ultrasoft pseudopotentials" *Phys. Rev. B*, vol. 76, p. 24401, 2007.

[213] T. Charpentier, "The PAW/GIPAW approach for computing NMR parameters: A new dimension added to NMR study of solids" *Solid State Nucl. Magn. Reson.*, vol. 40, pp. 1–20, 2011.

[214] C. Bonhomme, C. Gervais, F. Babonneau, C. Coelho, F. Pourpoint, T. Azaïs, S. E. Ashbrook, J. M. Griffin, J. R. Yates, F. Mauri, and C. J. Pickard, "First-Principles Calculation of NMR Parameters Using the Gauge Including Projector Augmented Wave Method: A Chemist's Point of View" *Chem. Rev.*, vol. 112, pp. 5733–5779, 2012.

[215] S. Sturniolo, T. F. Green, R. M. Hanson, M. Zilka, K. Refson, P. Hodgkinson, S. P. Brown, and J. R. Yates, "Visualization and processing of computed solid-state NMR parameters: MagresView and MagresPython" *Solid State Nucl. Magn. Reson.*, vol. 78, pp. 64–70, 2016.

[216] U. Sternberg, R. Witter, I. Kuprov, J. M. Lamley, A. Oss, J. R. Lewandowski, and A. Samoson, "^{1}H Line Width Dependence on MAS Speed in Solid State NMR - Comparison of Experiment and Simulation" *J. Magn. Reson.*, vol. 291, pp. 32–39, 2018.

[217] M. Bak and N. C. Nielsen, "REPULSION, A Novel Approach to Efficient Powder Averaging in Solid-State NMR" *J. Magn. Reson.*, vol. 125, pp. 132–139, 1997.

[218] K. Stott, J. Keeler, Q. N. Van, and A. J. Shaka, "One-Dimensional NOE Experiments Using Pulsed Field Gradients" *J. Magn. Reson.*, vol. 125, pp. 302–324, 1997.

[219] K. K. Kumashiro, K. Schmidt-Rohr, O. J. Murphy, K. L. Ouellette, W. A. Cramer, and L. K. Thompson, "A Novel Tool for Probing Membrane Protein Structure: Solid-State NMR with Proton Spin Diffusion and X-Nucleus Detection" *J. Am. Chem. Soc.*, vol. 120, pp. 5043–5051, 1998.

[220] M. Mayer and B. Meyer, "Characterization of ligand binding by saturation transfer difference NMR spectroscopy" *Angew. Chem. - Int. Ed.*, vol. 38, pp. 1784–1788, 1999.

[221] K. R. Thurber and R. Tycko, "Measurement of sample temperatures under magic-angle spinning from the chemical shift and spin-lattice relaxation rate of ^{79}Br in KBr powder" *J. Magn. Reson.*, vol. 196, pp. 84–87, 2009.

[222] D. Cory and W. Ritchey, "Suppression of signals from the probe in bloch decay spectra" *J. Magn. Reson. (1969)*, vol. 80, pp. 128–132, 1988.

[223] J. J. Helmus and C. P. Jaroniec, "Nmrglue: An open source Python package for the analysis of multidimensional NMR data" *J. Biomol. NMR*, vol. 55, pp. 355–367, 2013.

[224] M. Newville, T. Stensitzki, D. B. Allen, M. Rawlik, A. Ingargiola, and A. Nelson, "Lmfit: Non-Linear Least-Square Minimization and Curve-Fitting for Python" p. ascl:1606.014, 2016.

[225] J. M. Lamley, M. J. Lougher, H. J. Sass, M. Rogowski, S. Grzesiek, and J. R. Lewandowski, "Unraveling the complexity of protein backbone dynamics with combined ^{13}C and ^{15}N solid-state NMR relaxation measurements" *Phys. Chem. Chem. Phys.*, vol. 17, pp. 21997–22008, 2015.

[226] D. S. Wishart, C. G. Bigam, J. Yao, F. Abildgaard, H. J. Dyson, E. Oldfield, J. L. Markley, and B. D. Sykes, "^{1}H, ^{13}C and ^{15}N chemical shift referencing in biomolecular NMR" *J. Biomol. NMR*, vol. 6, pp. 135–140, 1995.

[227] R. K. Harris, E. D. Becker, S. M. Cabral De Menezes, P. Granger, R. E. Hoffman, and K. W. Zilm, "Further conventions for NMR shielding and chemical shifts (IUPAC Recommendations 2008)" *Pure Appl. Chem.*, vol. 80, pp. 59–84, 2008.

[228] R. L. J. Keller, "The Computer Aided Resonance Assignment Tutorial." `http://www.cara.nmr-software.org/downloads/3-85600-112-3.pdf`, 2004.

[229] R. Brüschweiler and R. R. Ernst, "A Cog-Wheel Model for Nuclear-Spin Propagation in Solids" *J. Magn. Reson.*, vol. 124, pp. 122–126, 1997.

[230] M. E. Halse, J.-N. Dumez, and L. Emsley, "Quasi-equilibria in reduced Liouville spaces" *J. Chem. Phys.*, vol. 136, p. 224511, 2012.

[231] M. Suzuki, "Improved Trotter-like formula" *Phys. Lett. A*, vol. 180, pp. 232–234, 1993.

[232] M. Edén, "Computer simulations in solid-state NMR. I. Spin dynamics theory" *Concepts Magn Reso A*, vol. 17A, pp. 117–154, 2003.

[233] Z. Tošner, R. Andersen, B. Stevensson, M. Edén, N. C. Nielsen, and T. Vosegaard, "Computer-intensive simulation of solid-state NMR experiments using SIMPSON" *J. Magn. Reson.*, vol. 246, pp. 79–93, 2014.

[234] D. W. Juhl, Z. Tošner, and T. Vosegaard, "Versatile NMR simulations using SIMPSON" *Vol 72*, vol. 100, pp. 1–59, 2020.

[235] M. Veshtort and R. G. Griffin, "SPINEVOLUTION: A powerful tool for the simulation of solid and liquid state NMR experiments" *J. Magn. Reson.*, vol. 178, pp. 248–282, 2006.

[236] P. M. Henrichs, M. Linder, and J. M. Hewitt, "Dynamics of the ^{13}C spin-exchange process in solids: A theoretical and experimental study" *J. Chem. Phys.*, vol. 85, pp. 7077–7086, 1986.

[237] J.-N. Dumez and L. Emsley, "A master-equation approach to the description of proton -driven spin diffusion from crystal geometry using simulated zero-quantum lineshapes" *Phys. Chem. Chem. Phys.*, vol. 13, pp. 7363–7370, 2011.

[238] P. Ma, Y. Xue, N. Coquelle, J. D. Haller, T. Yuwen, I. Ayala, O. Mikhailovskii, D. Willbold, J.-P. Colletier, N. R. Skrynnikov, and P. Schanda, "Observing the overall rocking motion of a protein in a crystal" *Nat. Commun.*, vol. 6, p. 8361, 2015.

[239] J. M. Lamley and J. R. Lewandowski, "Relaxation-based magic-angle spinning NMR approaches for studying protein dynamics" vol. 5, pp. 1423–1434, 2016.

[240] J. Brus, H. Petříčková, and J. Dybal, "Influence of local molecular motions on the determination of ^{1}H-^{1}H internuclear distances measured by 2D ^{1}H spin-exchange experiments" *Solid State Nucl. Magn. Reson.*, vol. 23, pp. 183–197, 2003.

[241] D. C. Apperley, R. K. Harris, and P. Hodgkinson, *Solid-State NMR: Basic Principles and Practice*. EngineeringPro collection, Momentum Press, 2012.

[242] M. Dračínský and P. Hodgkinson, "A molecular dynamics study of the effects of fast molecular motions on solid-state NMR parameters" *CrystEngComm*, vol. 15, pp. 8705–8712, 2013.

[243] M. Dračínský, P. Bouř, and P. Hodgkinson, "Temperature Dependence of NMR Parameters Calculated from Path Integral Molecular Dynamics Simulations" *J. Chem. Theory Comput.*, vol. 12, pp. 968–973, 2016.

[244] P. M. J. Szell, S. P. Brown, L. P. Hughes, H. Blade, and S. O. N. Lill, "A curious case of dynamic disorder in pyrrolidine rings elucidated by NMR crystallography" *Chem. Commun.*, vol. 56, pp. 14039–14042, 2020.

[245] P. M. J. Szell, J. R. Lewandowski, H. Blade, L. P. Hughes, S. O. Nilsson Lill, and S. P. Brown, "Taming the dynamics in a pharmaceutical by cocrystallization: investigating the impact of the coformer by solid-state NMR" *CrystEngComm*, vol. 23, pp. 6859–6870, 2021.

[246] R. Ishima, A. P. Petkova, J. M. Louis, and D. A. Torchia, "Comparison of methyl rotation axis order parameters derived from model-free analyses of ^{2}H and ^{13}C longitudinal and transverse relaxation rates measured in the same protein sample" *J. Am. Chem. Soc.*, vol. 123, pp. 6164–6171, 2001.

[247] Y. Xue, M. S. Pavlova, Y. E. Ryabov, B. Reif, and N. R. Skrynnikov, "Methyl rotation barriers in proteins from ^{2}H relaxation data. Implications for protein structure" *J. Am. Chem. Soc.*, vol. 129, pp. 6827–6838, 2007.

[248] M. Mayer and B. Meyer, "Group Epitope Mapping by Saturation Transfer Difference NMR To Identify Segments of a Ligand in Direct Contact with a Protein Receptor" *J. Am. Chem. Soc.*, vol. 123, pp. 6108–6117, 2001.

[249] N. S. Barrow, *Homonuclear correlation in solid-state NMR: developing experiments for half-integer quadrupolar nuclei*. PhD thesis, University of Warwick, 2009.

[250] B. Busi, J. R. Yarava, A. Hofstetter, N. Salvi, D. Cala-De Paepe, J. R. Lewandowski, M. Blackledge, and L. Emsley, "Probing Protein Dynamics Using Multifield Variable Temperature NMR Relaxation and Molecular Dynamics Simulation" *J. Phys. Chem. B*, vol. 122, pp. 9697–9702, 2018.

[251] D. C. Chatfield and S. E. Wong, "Methyl motional parameters in crystalline L-alanine: Molecular dynamics simulation and NMR" *J. Phys. Chem. B*, vol. 104, pp. 11342–11348, 2000.

[252] S. E. Ashbrook, N. G. Dowell, I. Prokes, and S. Wimperis, "Nuclear overhauser effect (NOE) enhancement of ^{11}B NMR spectra of borane adducts in the solid state" *J. Am. Chem. Soc.*, vol. 128, pp. 6782–6783, 2006.

[253] J. S. Higgins, A. H. Hodgson, and R. V. Law, "Heteronuclear NOE in the solid state" *J. Mol. Struct.*, vol. 602-603, pp. 505–510, 2002.

[254] A. Lesage, L. Emsley, F. Penin, and A. Böckmann, "Investigation of dipolar-mediated water-protein interactions in microcrystalline Crh by solid-state NMR spectroscopy" *J. Am. Chem. Soc.*, vol. 128, pp. 8246–8255, 2006.

[255] J. Cui, J. Li, X. Peng, and R. Fu, "Transient NOE enhancement in solid-state MAS NMR of mobile systems" *J. Magn. Reson.*, vol. 284, pp. 73–79, 2017.

[256] E. Bartalucci, A. A. Malär, A. Mehnert, J. B. Kleine Büning, L. Günzel, M. Icker, M. Börner, C. Wiebeler, B. H. Meier, S. Grimme, B. Kersting, and T. Wiegand, "Probing a Hydrogen-π Interaction Involving a Trapped Water Molecule in the Solid State" *International Edition*, vol. 62, p. e202217725, 2023.

[257] K. H. Mroue, Y. Nishiyama, M. Kumar Pandey, B. Gong, E. McNerny, D. H. Kohn, M. D. Morris, and A. Ramamoorthy, "Proton-Detected Solid-State NMR Spectroscopy of Bone with Ultrafast Magic Angle Spinning" *Sci. Rep.*, vol. 5, p. 11991, 2015.

[258] J. M. Lamley, C. Öster, R. A. Stevens, and J. R. J. R. Lewandowski, "Intermolecular Interactions and Protein Dynamics by Solid-State NMR Spectroscopy" *Angew. Chem. - Int. Ed.*, vol. 54, pp. 15374–15378, 2015.

[259] M. Aluas, C. Tripon, J. M. Griffin, X. Filip, V. Ladizhansky, R. G. Griffin, S. P. Brown, and C. Filip, "CHHC and ^{1}H-^{1}H magnetization exchange: Analysis by experimental solid-state NMR and 11-spin density-matrix simulations" *J. Magn. Reson.*, vol. 199, pp. 173–187, 2009.

[260] D. P. Raleigh, M. H. Levitt, and R. G. Griffin, "Rotational resonance in solid state NMR" *Chem. Phys. Lett.*, vol. 146, pp. 71–76, 1988.

[261] Y. Nishiyama, M. Malon, Y. Ishii, and A. Ramamoorthy, "3D ^{15}N/^{15}N/^{1}H chemical shift correlation experiment utilizing an RFDR-based ^{1}H/^{1}H mixing period at 100kHz MAS" *J. Magn. Reson.*, vol. 244, pp. 1–5, 2014.

[262] M. K. Pandey, S. Vivekanandan, K. Yamamoto, S. Im, L. Waskell, and A. Ramamoorthy, "Proton-detected 2D radio frequency driven recoupling solid-state NMR studies on micelle-associated cytochrome-b5" *J. Magn. Reson.*, vol. 242, pp. 169–179, 2014.

[263] M. G. Jain, D. Lalli, J. Stanek, C. Gowda, S. Prakash, T. S. Schwarzer, T. Schubeis, K. Castiglione, L. B. Andreas, P. K. Madhu, G. Pintacuda, and V. Agarwal, "Selective ^{1}H-^{1}H Distance Restraints in Fully Protonated Proteins by Very Fast Magic-Angle Spinning Solid-State NMR" *J. Phys. Chem. Lett.*, vol. 8, pp. 2399–2405, 2017.

[264] N. T. Duong, S. Raran-Kurussi, Y. Nishiyama, and V. Agarwal, "Quantitative ^{1}H-^{1}H Distances in Protonated Solids by Frequency-Selective Recoupling at Fast Magic Angle Spinning NMR" *J. Phys. Chem. Lett.*, vol. 9, pp. 5948–5954, 2018.

[265] L. R. Potnuru, N. T. Duong, S. Ahlawat, S. Raran-Kurussi, M. Ernst, Y. Nishiyama, and V. Agarwal, "Accuracy of ^{1}H–^{1}H distances measured using frequency selective recoupling and fast magic-angle spinning" *J. Chem. Phys.*, vol. 153, p. 084202, 2020.

[266] N. T. Duong, S. Raran-Kurussi, Y. Nishiyama, and V. Agarwal, "Can proton-proton recoupling in fully protonated solids provide quantitative, selective and efficient polarization transfer?" *J. Magn. Reson.*, vol. 317, p. 106777, 2020.

[267] F. Ferrage, P. Pelupessy, D. Cowburn, and G. Bodenhausen, "Protein Backbone Dynamics through ^{13}C'-^{13}Cα Cross-Relaxation in NMR Spectroscopy" vol. 128, pp. 11072–11078, 2006.

[268] C. Charlier, S. F. Cousin, and F. Ferrage, "Protein dynamics from nuclear magnetic relaxation" *Chem. Soc. Rev.*, vol. 45, pp. 2410–2422, 2016.

[269] T. Zinkevich, V. Chevelkov, B. Reif, K. Saalwächter, and A. Krushelnitsky, "Internal protein dynamics on ps to μs timescales as studied by multi-frequency ^{15}N solid-state NMR relaxation" *J. Biomol. NMR*, vol. 57, pp. 219–235, 2013.

[270] Y. Gu, A. L. Hansen, Y. Peng, and R. Brüschweiler, "Rapid Determination of Fast Protein Dynamics from NMR Chemical Exchange Saturation Transfer Data" *International Edition*, vol. 128, pp. 3169–3171, 2016.

[271] A. A. Smith, E. Testori, R. Cadalbert, B. H. Meier, and M. Ernst, "Characterization of fibril dynamics on three timescales by solid-state NMR" *J. Biomol. NMR*, vol. 65, pp. 171–191, 2016.

[272] P. Schanda, "Relaxing with liquids and solids – A perspective on biomolecular dynamics" *J. Magn. Reson.*, vol. 306, pp. 180–186, 2019.

[273] M. R. Hansen, R. Graf, and H. W. Spiess, "Solid-state NMR in macromolecular systems: Insights on how molecular entities move" *Acc. Chem. Res.*, vol. 46, pp. 1996–2007, 2013.

[274] S. Asami, M. Rakwalska-Bange, T. Carlomagno, and B. Reif, "Protein-RNA interfaces probed by ^{1}H-detected MAS solid-state NMR spectroscopy" *Angew. Chem. - Int. Ed.*, vol. 52, pp. 2345–2349, 2013.

[275] Y. Liu, Y. Liu, M. B. Chan-Park, and Y. Mu, "Binding Modes of Teixobactin to Lipid II: Molecular Dynamics Study" *Sci. Rep.*, vol. 7, p. 17197, 2017.

[276] A. Parmar, S. H. Prior, A. Iyer, C. S. Vincent, D. Van Lysebetten, E. Breukink, A. Madder, E. J. Taylor, and I. Singh, "Defining the molecular structure of teixobactin analogues and understanding their role in antibacterial activities" vol. 53, pp. 2016–2019, 2017.

[277] R. Shukla, J. Medeiros-Silva, A. Parmar, B. J. Vermeulen, S. Das, A. L. Paioni, S. Jekhmane, J. Lorent, A. M. Bonvin, M. Baldus, M. Lelli, E. J. Veldhuizen, E. Breukink, I. Singh, and M. Weingarth, "Mode of action of teixobactins in cellular membranes" *Nat. Commun.*, vol. 11, pp. 1–10, 2020.

[278] C. Öster, G. P. Walkowiak, D. E. Hughes, A. L. Spoering, A. J. Peoples, A. C. Catherwood, J. A. Tod, A. J. Lloyd, T. Herrmann, K. Lewis, C. G. Dowson, and J. R. Lewandowski, "Structural studies suggest aggregation as one of the modes of action for teixobactin" *Chem. Sci.*, vol. 9, pp. 8850–8859, 2018.

[279] N. P. Wickramasinghe, S. Parthasarathy, C. R. Jones, C. Bhardwaj, F. Long, M. Kotecha, S. Mehboob, L. W.-M. Fung, J. Past, A. Samoson, and Y. Ishii, "Nanomole-scale Protein Solid-state NMR by Breaking Intrinsic ^{1}H-T_1 Boundaries" *Nat. Methods*, vol. 6, pp. 215–218, 2009.

[280] P. Schanda and B. Brutscher, "Very fast two-dimensional NMR spectroscopy for real-time investigation of dynamic events in proteins on the time scale of seconds" *J. Am. Chem. Soc.*, vol. 127, pp. 8014–8015, 2005.

[281] P. Schanda, E. Kupče, and B. Brutscher, "SOFAST-HMQC Experiments for Recording Two-dimensional Deteronuclear Correlation Spectra of Proteins within a Few Seconds" *J. Biomol. NMR*, vol. 33, pp. 199–211, 2005.

[282] P. Schanda, H. Van Melckebeke, and B. Brutscher, "Speeding up three-dimensional protein NMR experiments to a few minutes" *J. Am. Chem. Soc.*, vol. 128, pp. 9042–9043, 2006.

[283] R. Linser, V. Chevelkov, A. Diehl, and B. Reif, "Sensitivity enhancement using paramagnetic relaxation in MAS solid-state NMR of perdeuterated proteins" *J. Magn. Reson.*, vol. 189, pp. 209–216, 2007.

[284] G. Otting, "Protein NMR using paramagnetic ions" *Annu. Rev. Biophys.*, vol. 39, pp. 387–405, 2010.

[285] W. Hohlweg, S. Kosol, and K. Zangger, "Determining the Orientation and Localization of Membrane-Bound Peptides" *Curr Protein Pept Sci*, vol. 13, pp. 267–279, 2012.

[286] M. J. Knight, I. C. Felli, R. Pierattelli, L. Emsley, and G. Pintacuda, "Magic angle spinning NMR of paramagnetic proteins" *Acc. Chem. Res.*, vol. 46, pp. 2108–2116, 2013.

[287] S. J. Ullrich, S. Hölper, and C. Glaubitz, "Paramagnetic doping of a 7TM membrane protein in lipid bilayers by Gd^{3+}-complexes for solid-state NMR spectroscopy" *J. Biomol. NMR*, vol. 58, pp. 27–35, 2014.

[288] C. Liu, J. Liu, X. Xu, S. Q. Xiang, and S. Wang, "Gd^{3+}-chelated lipid accelerates solid-state NMR spectroscopy of seven-transmembrane proteins" *J. Biomol. NMR*, vol. 68, pp. 203–214, 2017.

[289] J. Zehnder, R. Cadalbert, M. Yulikov, G. Künze, and T. Wiegand, "Paramagnetic spin labeling of a bacterial DnaB helicase for solid-state NMR" *J. Magn. Reson.*, vol. 332, p. 107075, 2021.

[290] M. J. Knight, A. J. Pell, I. Bertini, I. C. Felli, L. Gonnelli, R. Pierattelli, T. Herrmann, L. Emsley, and G. Pintacuda, "Structure and backbone dynamics of a microcrystalline metalloprotein by solid-state NMR" *Proc Natl Acad Sci U S A*, vol. 109, pp. 11095–11100, 2012.

[291] Y. Okuno, A. Szabo, and G. M. Clore, "Quantitative Interpretation of Solvent Paramagnetic Relaxation for Probing Protein-Cosolute Interactions" *J. Am. Chem. Soc.*, vol. 142, pp. 8281–8290, 2020.

[292] P. M. Singer, A. Valiya Parambathu, T. J. Pinheiro dos Santos, Y. Liu, L. B. Alemany, G. J. Hirasaki, W. G. Chapman, and D. Asthagiri, "Predicting ^{1}H NMR relaxation in Gd^{3+} aqua using molecular dynamics simulations" *Phys. Chem. Chem. Phys.*, pp. 50–53, 2021.

[293] R. Linser, U. Fink, and B. Reif, "Probing surface accessibility of proteins using paramagnetic relaxation in solid-state NMR spectroscopy" *J. Am. Chem. Soc.*, vol. 131, pp. 13703–13708, 2009.

[294] B. Dangi, J. I. Blankman, C. J. Miller, B. F. Volkman, and R. D. Guiles, "Contribution of backbone dynamics to entropy changes occurring on oxidation of cytochrome b5. Can redox linked changes in hydrogen bond networks modulate reduction potentials?" *J. Phys. Chem. B*, vol. 102, pp. 8201–8208, 1998.

[295] L. Banci, I. Bertini, C. Cavazza, I. C. Felli, and D. Koulougliotis, "Probing the backbone dynamics of oxidized and reduced rat microsomal cytochrome b5 via ^{15}N rotating frame NMR relaxation measurements: Biological implications" *Biochemistry (Mosc)*, vol. 37, pp. 12320–12330, 1998.

[296] M. Assfalg, L. Banci, I. Bertini, S. Ciofi-Baffoni, and P. D. Barker, "^{15}N Backbone Dynamics of Ferricytochrome b_{562}: Comparison with the Reduced Protein and the R98C Variant" *Biochemistry (Mosc)*, vol. 40, pp. 12761–12771, 2001.

[297] J. P. Derrick and D. B. Wigley, "Crystal structure of a streptococcal protein G domain bound to an Fab fragment" *Nature*, vol. 359, pp. 752–754, 1992.

[298] J. P. Derrick and D. B. Wigley, "The Third IgG-Binding Domain from Streptococcal Protein G An Analysis by X-ray Crystallography of the Structure Alone and in a Complex with Fab" *J. Mol. Biol.*, vol. 243, pp. 906–918, 1994.

[299] A. Sauer-Eriksson, G. J. Kleywegt, M. Uhlén, and T. Jones, "Crystal structure of the C2 fragment of streptococcal protein G in complex with the Fc domain of human IgG" *Structure*, vol. 3, pp. 265–278, 1995.

[300] K. Kato, L.-Y. Lian, I. L. Barsukov, J. P. Derrick, H. Kim, R. Tanaka, A. Yoshino, M. Shiraishi, I. Shimada, Y. Arata, and G. C. Roberts, "Model for the complex between protein G and an antibody Fc fragment in solution" *Structure*, vol. 3, pp. 79–85, 1995.

[301] W. T. Franks, B. P. Tatman, J. Trenouth, and J. R. Lewandowski, "Dipolar Order Parameters in Large Systems With Fast Spinning" *Front. Mol. Biosci.*, vol. 8, p. 791026, 2021.

[302] J. Tognetti, W. Trent Franks, A. Gallo, and J. R. Lewandowski, "Accelerating ^{15}N and ^{13}C R_1 and $R_{1\rho}$ relaxation measurements by multiple pathway solid-state NMR experiments" *J. Magn. Reson.*, vol. 331, p. 107049, 2021.

[303] G. Pintacuda and G. Otting, "Identification of protein surfaces by NMR measurements with a paramagnetic Gd(III) chelate" *J. Am. Chem. Soc.*, vol. 124, pp. 372–373, 2002.

[304] Q. Miao, C. Nitsche, H. Orton, M. Overhand, G. Otting, and M. Ubbink, "Paramagnetic Chemical Probes for Studying Biological Macromolecules" *Chem. Rev.*, vol. 122, pp. 9571–9642, 2022.

[305] M. Benmelouka, A. Borel, L. Moriggi, L. Helm, and A. E. Merbach, "Design of Gd(III)-based magnetic resonance imaging contrast agents: Static and transient zero-field splitting contributions to the electronic relaxation and their impact on relaxivity" *J. Phys. Chem. B*, vol. 111, pp. 832–840, 2007.

[306] P. H. Fries, D. Imbert, and A. Melchior, "Determination of outer-sphere dipolar time correlation functions from high-field NMR measurements. Example of a Gd^{3+} complex in a viscous solvent" *J. Chem. Phys.*, vol. 132, 2010.

[307] P. H. Fries, "Computing Electronic Spin Relaxation for Gd^{3+} -Based Contrast Agents – Practical Implementation" *Eur. J. Inorg. Chem.*, vol. 2012, pp. 2156–2166, 2012.

[308] J. R. Lewandowski, J.-N. N. Dumez, Ü. Akbey, S. Lange, L. Emsley, and H. Oschkinat, "Enhanced resolution and coherence lifetimes in the solid-state NMR spectroscopy of perdeuterated proteins under ultrafast magic-angle spinning" *J. Phys. Chem. Lett.*, vol. 2, pp. 2205–2211, 2011.

[309] C. Hartlmüller, C. Göbl, and T. Madl, "Prediction of Protein Structure Using Surface Accessibility Data" *Angew. Chem. - Int. Ed.*, vol. 55, pp. 11970–11974, 2016.

[310] C. Hartlmüller, J. C. Günther, A. C. Wolter, J. Wöhnert, M. Sattler, and T. Madl, "RNA structure refinement using NMR solvent accessibility data" *Sci. Rep.*, vol. 7, pp. 1–10, 2017.

[311] G. Kervern, S. Steuernagel, F. Engelke, G. Pintacuda, and L. Emsley, "Absence of curie relaxation in paramagnetic solids yields long ^{1}H coherence lifetimes" *J. Am. Chem. Soc.*, vol. 129, pp. 14118–14119, 2007.

[312] C. P. Jaroniec, "Solid-state nuclear magnetic resonance structural studies of proteins using paramagnetic probes" *Solid State Nucl. Magn. Reson.*, vol. 43-44, pp. 1–13, 2012.

[313] D. A. Case, T. E. C. III, T. Darden, H. Gohlke, R. Luo, K. M. M. Jr., A. Onufriev, C. Simmerling, B. Wang, and R. J. Woods, "The Amber biomolecular simulation programs" *J. Comput. Chem.*, vol. 26, pp. 1668–1688, 2005.

[314] U. Doshi and D. Hamelberg, "Reoptimization of the AMBER force field parameters for peptide bond (Omega) torsions using accelerated molecular dynamics" *J. Phys. Chem. B*, vol. 113, pp. 16590–16595, 2009.

[315] W. T. Franks, B. J. Wylie, S. A. Stellfox, and C. M. Rienstra, "Backbone Conformational Constraints in a Microcrystalline U-^{15}N-Labeled Protein by 3D Dipolar-Shift Solid-State NMR Spectroscopy" *J. Am. Chem. Soc.*, vol. 128, pp. 3154–3155, 2006.

[316] M. R. Bennett, J. Dong, R. G. Bombardi, C. Soto, H. M. Parrington, R. S. Nargi, C. T. Schoeder, M. B. Nagel, K. L. Schey, J. Meiler, E. P. Skaar, and J. E. Crowe, "Human V H 1-69 Gene-Encoded Human Monoclonal Antibodies against Staphylococcus aureus IsdB Use at Least Three Distinct Modes of Binding To Inhibit Bacterial Growth and Pathogenesis" *Mbio*, vol. 10, pp. 1–14, 2019.

[317] T. D. Goddard, C. C. Huang, E. C. Meng, E. F. Pettersen, G. S. Couch, J. H. Morris, and T. E. Ferrin, "UCSF ChimeraX: Meeting modern challenges in visualization and analysis" *Protein Sci*, vol. 27, pp. 14–25, 2018.

[318] G. Martínez-Rosell, T. Giorgino, and G. De Fabritiis, "PlayMolecule ProteinPrepare: A Web Application for Protein Preparation for Molecular Dynamics Simulations" *J. Chem. Inf. Model.*, vol. 57, pp. 1511–1516, 2017.

[319] C. Tian, K. Kasavajhala, K. A. A. Belfon, L. Raguette, H. Huang, A. N. Migues, J. Bickel, Y. Wang, J. Pincay, Q. Wu, and C. Simmerling, "ff19SB: Amino-Acid-Specific Protein Backbone Parameters Trained against Quantum Mechanics Energy Surfaces in Solution" *J. Chem. Theory Comput.*, vol. 16, pp. 528–552, 2019.

[320] S. Izadi, R. Anandakrishnan, and A. V. Onufriev, "Building Water Models: A Different Approach" *J. Phys. Chem. Lett.*, vol. 5, pp. 3863–3871, 2014.

[321] J.-P. Ryckaert, G. Ciccotti, and H. J. C. Berendsen, "Numerical integration of the cartesian equations of motion of a system with constraints: molecular dynamics of n-alkanes" *J. Comput. Phys.*, vol. 23, pp. 327–341, 1977.

[322] D. R. Roe and T. E. Cheatham, "PTRAJ and CPPTRAJ: Software for processing and analysis of molecular dynamics trajectory data" *J. Chem. Theory Comput.*, vol. 9, pp. 3084–3095, 2013.

[323] M. F. Sanner, A. J. Olson, and J. C. Spehner, "Reduced surface: An efficient way to compute molecular surfaces" *Biopolymers*, vol. 38, pp. 305–320, 1996.

[324] M. A. Kaster, M. D. Levasseur, T. G. W. Edwardson, M. A. Caldwell, D. Hofmann, G. Licciardi, G. Parigi, C. Luchinat, D. Hilvert, and T. J. Meade, "Engineered Nonviral Protein Cages Modified for MR Imaging" *ACS Appl. Bio Mater.*, 2023.

[325] D. Lavalette, C. Tétreau, M. Tourbez, and Y. Blouquit, "Microscopic viscosity and rotational diffusion of proteins in a macromolecular environment" *Biophys J*, vol. 76, pp. 2744–2751, 1999.

[326] G. Nawrocki, A. Karaboga, Y. Sugita, and M. Feig, "Effect of protein–protein interactions and solvent viscosity on the rotational diffusion of proteins in crowded environments" *Phys. Chem. Chem. Phys.*, vol. 21, pp. 876–883, 2019.

[327] A. Aukrust, T. Engebretsen, L. K. Sydnes, L. J. Sæthre, and K. W. Törnroos, "Hydrates of gadolinium diethylenetriaminepentaacetic acid bis(methylamide) as studied by X-ray diffraction" *Org. Process Res. Dev.*, vol. 5, pp. 361–367, 2001.

[328] "ISO/TR Technical Report No. 3666" tech. rep., International Organization for Standardization, 1998.

[329] M. L. Huber, R. A. Perkins, A. Laesecke, D. G. Friend, J. V. Sengers, M. J. Assael, I. N. Metaxa, E. Vogel, R. Mareš, and K. Miyagawa, "New international formulation for the viscosity of H_2O" *J. Phys. Chem. Ref. Data*, vol. 38, pp. 101–125, 2009.

[330] D. Beece, L. Eisenstein, H. Frauenfelder, D. Good, M. C. Marden, L. Reinisch, A. H. Reynolds, L. B. Sorensen, and K. T. Yue, "Solvent viscosity and protein dynamics" *Biochemistry (Mosc)*, vol. 19, pp. 5147–5157, 1980.

[331] A. M. Petros, L. Mueller, and K. D. Kopple, "NMR identification of protein surfaces using paramagnetic probes" *Biochemistry (Mosc)*, vol. 29, pp. 10041–10048, 1990. PMID: 2176860.

[332] R. D. Shannon, "Revised effective ionic radii and systematic studies of interatomic distances in halides and chalcogenides" *Foundations of Crystallography*, vol. 32, pp. 751–767, 1976.

[333] D. H. Zhou, J. J. Shea, A. J. Nieuwkoop, W. T. Franks, B. J. Wylie, C. Mullen, D. Sandoz, and C. M. Rienstra, "Solid-State Protein-Structure Determination with Proton-Detected Triple-Resonance 3D Magic-Angle-Spinning NMR Spectroscopy" *Angew. Chem. - Int. Ed.*, vol. 46, pp. 8380–8383, 2007.

[334] D. C. Apperley, A. F. Markwell, I. Frantsuzov, A. J. Ilott, R. K. Harris, and P. Hodgkinson, "NMR characterisation of dynamics in solvates and desolvates of formoterol fumarate" *Phys. Chem. Chem. Phys.*, vol. 15, pp. 6422–6430, 2013.

[335] R. Kleinberg, W. Kenyon, and P. Mitra, "Mechanism of NMR Relaxation of Fluids in Rock" *J. Magn. Reson. A*, vol. 108, pp. 206–214, 1994.

[336] J.-P. Korb, "NMR and nuclear spin relaxation of cement and concrete materials" *Curr. Opin. Colloid Interface Sci.*, vol. 14, pp. 192–202, 2009.

[337] R. J. Messinger, T. Vu Huynh, R. Bouchet, V. Sarou-Kanian, and M. Deschamps, "Magic-angle-spinning-induced local ordering in polymer electrolytes and its effects on solid-state diffusion and relaxation NMR measurements" *Magn. Reson. Chem.*, vol. 58, pp. 1118–1129, 2020.

[338] D. J. Kubicki, S. D. Stranks, C. P. Grey, and L. Emsley, "NMR spectroscopy probes microstructure, dynamics and doping of metal halide perovskites" *Nat. Rev. Chem.*, vol. 5, pp. 624–645, 2021.

[339] Lamley, J. M., *Methods for the determination of the structures and dynamics of proteins by solid-state NMR spectroscopy*. PhD thesis, University of Warwick, 2015.

[340] J. McConnell, "Theory of nuclear magnetic relaxation by dipolar interaction" *Physica A*, vol. 135, pp. 38–62, 1986.

[341] J. McConnell, "Theory of nuclear magnetic relaxation by anisotropic chemical shift" *Physica A*, vol. 127, pp. 152–172, 1984.

[342] T. Wang, D. S. Weaver, S. Cai, and E. R. Zuiderweg, "Quantifying Lipari-Szabo modelfree parameters from ^{13}CO NMR relaxation experiments" *J. Biomol. NMR*, vol. 36, pp. 79–102, 2006.

[343] Y. Pang, M. Buck, and E. R. Zuiderweg, "Backbone dynamics of the ribonuclease binase active site area using multinuclear (^{15}N and ^{13}CO) NMR relaxation and computational molecular dynamics" *Biochemistry (Mosc)*, vol. 41, pp. 2655–2666, 2002.

[344] S. L. Chang and N. Tjandra, "Temperature dependence of protein backbone motion from carbonyl ^{13}C and amide ^{15}N NMR relaxation" *J. Magn. Reson.*, vol. 174, pp. 43–53, 2005.

[345] D. C. Chatfield, A. Szabo, and B. R. Brooks, "Molecular dynamics of staphylococcal nuclease: Comparison of simulation with ^{15}N and ^{13}C NMR relaxation data" *J. Am. Chem. Soc.*, vol. 120, pp. 5301–5311, 1998.

[346] K. H. Mayo, V. A. Daragan, D. Idiyatullin, and I. Nesmelova, "Peptide Internal Motions on Nanosecond Time Scale Derived from Direct Fitting of ^{13}C and ^{15}N NMR Spectral Density Functions" *J. Magn. Reson.*, vol. 146, pp. 188–195, 2000.

[347] Frank, S. F., *Anisotropic Dynamics in Molecular Systems*. PhD thesis, ETH Zurich, 1998.

[348] T. Bremi and R. Brüschweiler, "Locally anisotropic internal polypeptide backbone dynamics by NMR relaxation" *J. Am. Chem. Soc.*, vol. 119, pp. 6672–6673, 1997.

[349] T. Bremi, R. Brüschweiler, and R. R. Ernst, "A protocol for the interpretation of side-chain dynamics based on NMR relaxation: Application to phenylalanines in antamanide" *J. Am. Chem. Soc.*, vol. 119, pp. 4272–4284, 1997.

[350] T. S. Ulmer, B. E. Ramirez, F. Delaglio, and A. Bax, "Evaluation of backbone proton positions and dynamics in a small protein by liquid crystal NMR spectroscopy" *J. Am. Chem. Soc.*, vol. 125, pp. 9179–9191, 2003.

[351] M. W. MacArthur and J. M. Thornton, "Deviations from planarity of the peptide bond in peptides and proteins" *J. Mol. Biol.*, vol. 264, pp. 1180–1195, 1996.

[352] B. W. Matthews, "How planar are planar peptide bonds?" *Protein Sci*, vol. 25, pp. 776–777, 2016.

[353] B. J. Wylie, L. J. Sperling, A. J. Nieuwkoop, W. T. Franks, E. Oldfield, and C. M. Rienstra, "Ultrahigh resolution protein structures using NMR chemical shift tensors" *Proc. Natl. Acad. Sci.*, vol. 108, pp. 16974–16979, 2011.

[354] B. J. Wylie, L. J. Sperling, H. L. Frericks, G. J. Shah, W. T. Franks, and C. M. Rienstra, "Chemical-Shift Anisotropy Measurements of Amide and Carbonyl Resonances in a Microcrystalline Protein with Slow Magic-Angle Spinning NMR Spectroscopy" *J. Am. Chem. Soc.*, vol. 129, pp. 5318–5319, 2007.

[355] J. Wang, R. M. Wolf, J. W. Caldwell, P. A. Kollman, and D. A. Case, "Development and testing of a general Amber force field" *J. Comput. Chem.*, vol. 25, pp. 1157–1174, 2004.

[356] A. A. Smith, N. Bolik-Coulon, M. Ernst, B. H. Meier, and F. Ferrage, "How wide is the window opened by high-resolution relaxometry on the internal dynamics of proteins in solution?" *J. Biomol. NMR*, vol. 75, pp. 119–131, 2021.

[357] S. F. Cousin, C. Charlier, P. Kadeřávek, T. Marquardsen, J. M. Tyburn, P. A. Bovier, S. Ulzega, T. Speck, D. Wilhelm, F. Engelke, W. Maas, D. Sakellariou, G. Bodenhausen, P. Pelupessy, and F. Ferrage, "High-resolution two-field nuclear magnetic resonance spectroscopy" *Phys. Chem. Chem. Phys.*, vol. 18, pp. 33187–33194, 2016.

[358] P. Kadeřávek, N. Bolik-Coulon, S. F. Cousin, T. Marquardsen, J. M. Tyburn, J. N. Dumez, and F. Ferrage, "Protein Dynamics from Accurate Low-Field Site-Specific Longitudinal and Transverse Nuclear Spin Relaxation" *J. Phys. Chem. Lett.*, vol. 10, pp. 5917–5922, 2019.

[359] T. Wang, S. Cai, and E. R. Zuiderweg, "Temperature dependence of anisotropic protein backbone dynamics" *J. Am. Chem. Soc.*, vol. 125, pp. 8639–8643, 2003.

[360] E. Johnson, A. G. Palmer, and M. Rance, "Temperature dependence of the NMR generalized order parameter" *Proteins*, vol. 66, pp. 796–803, 2006.

[361] J. R. Lewandowski, M. E. Halse, M. Blackledge, and L. Emsley, "Direct observation of hierarchical protein dynamics" *Science*, vol. 348, pp. 578–581, 2015.

[362] B. Busi, J. R. Yarava, A. Bertarello, F. Freymond, W. Adamski, D. Maurin, M. Hiller, H. Oschkinat, M. Blackledge, and L. Emsley, "Similarities and differences among protein dynamics studied by variable temperature nuclear magnetic resonance relaxation" *J. Phys. Chem. B*, vol. 125, pp. 2212–2221, 2021.

[363] F. M. Paruzzo, A. Hofstetter, F. Musil, S. De, M. Ceriotti, and L. Emsley, "Chemical shifts in molecular solids by machine learning" *Nat. Commun.*, vol. 9, pp. 1–10, 2018.

[364] D. M. Jordan, K. M. Mills, I. Andricioaei, A. Bhattacharya, K. Palmo, and E. R. Zuiderweg, "Parameterization of peptide ^{13}C carbonyl chemical shielding anisotropy in molecular dynamics simulations" *ChemPhysChem*, vol. 8, pp. 1375–1385, 2007.

[365] S. Tang and D. A. Case, "Vibrational averaging of chemical shift anisotropies in model peptides" *J. Biomol. NMR*, vol. 38, pp. 255–266, 2007.

[366] D. Idiyatullin, V. A. Daragan, and K. H. Mayo, "^{15}NH Backbone Dynamics of Protein GB1: Comparison of Order Parameters and Correlation Times Derived Using Various "Model-Free" Approaches" *J. Phys. Chem. B*, vol. 107, pp. 2602–2609, 2003.

[367] D. Idiyatullin, I. Nesmelova, V. A. Daragan, and K. H. Mayo, "Comparison of $^{13}C_{\alpha}H$ and ^{15}NH backbone dynamics in protein GB1" *Protein Sci*, vol. 12, pp. 914–922, 2003.

[368] J. R. Lewandowski, J. Sein, M. Blackledge, and L. Emsley, "Anisotropic Collective Motion Contributes to Nuclear Spin Relaxation in Crystalline Proteins" *J. Am. Chem. Soc.*, vol. 132, pp. 1246–1248, 2010.

[369] RCSB Protein Data Bank, "RCSB PDB: Homepage — rcsb.org." `https://www.rcsb.org/`. [Accessed 9th-June-2023].

[370] "Crystallography: Protein Data Bank" *Nat New Biol*, vol. 233, pp. 223–223, 1971.

[371] P. H. Chen, B. J. Albert, C. Gao, N. Alaniva, L. E. Price, F. J. Scott, E. P. Saliba, E. L. Sesti, P. T. Judge, E. W. Fisher, and A. B. Barnes, "Magic angle spinning spheres" *Sci. Adv.*, vol. 4, pp. 1–8, 2018.

[372] P. H. Chen, C. Gao, and A. B. Barnes, "Perspectives on microwave coupling into cylindrical and spherical rotors with dielectric lenses for magic angle spinning dynamic nuclear polarization" *J. Magn. Reson.*, vol. 308, p. 106518, 2019.

[373] C. Gao, P. T. Judge, E. L. Sesti, L. E. Price, N. Alaniva, E. P. Saliba, B. J. Albert, N. J. Soper, P. H. Chen, and A. B. Barnes, "Four millimeter spherical rotors spinning at 28kHz with double-saddle coils for cross polarization NMR" *J. Magn. Reson.*, vol. 303, pp. 1–6, 2019.

[374] P.-H. Chen, C. Gao, L. E. Price, M. A. Urban, T. M. O. Popp, and A. B. Barnes, "Two millimeter diameter spherical rotors spinning at 68 kHz for MAS NMR" *J. Magn. Reson. Open*, vol. 8-9, p. 100015, 2021.

[375] P. Wikus, W. Frantz, R. Kümmerle, and P. Vonlanthen, "Commercial gigahertz-class NMR magnets" *Supercond. Sci. Technol.*, vol. 35, p. 033001, 2022.

[376] D. Parker, E. A. Suturina, I. Kuprov, and N. F. Chilton, "How the Ligand Field in Lanthanide Coordination Complexes Determines Magnetic Susceptibility Anisotropy, Paramagnetic NMR Shift, and Relaxation Behavior" *Acc. Chem. Res.*, vol. 53, pp. 1520–1534, 2020.

[377] E. A. Suturina, D. Häussinger, K. Zimmermann, L. Garbuio, M. Yulikov, G. Jeschke, and I. Kuprov, "Model-free extraction of spin label position distributions from pseudocontact shift data" *Chem. Sci.*, vol. 8, pp. 2751–2757, 2017.

Appendix A

Dynamical profiles arising from including 3 or 5 singular values for paramagnetic analysis.

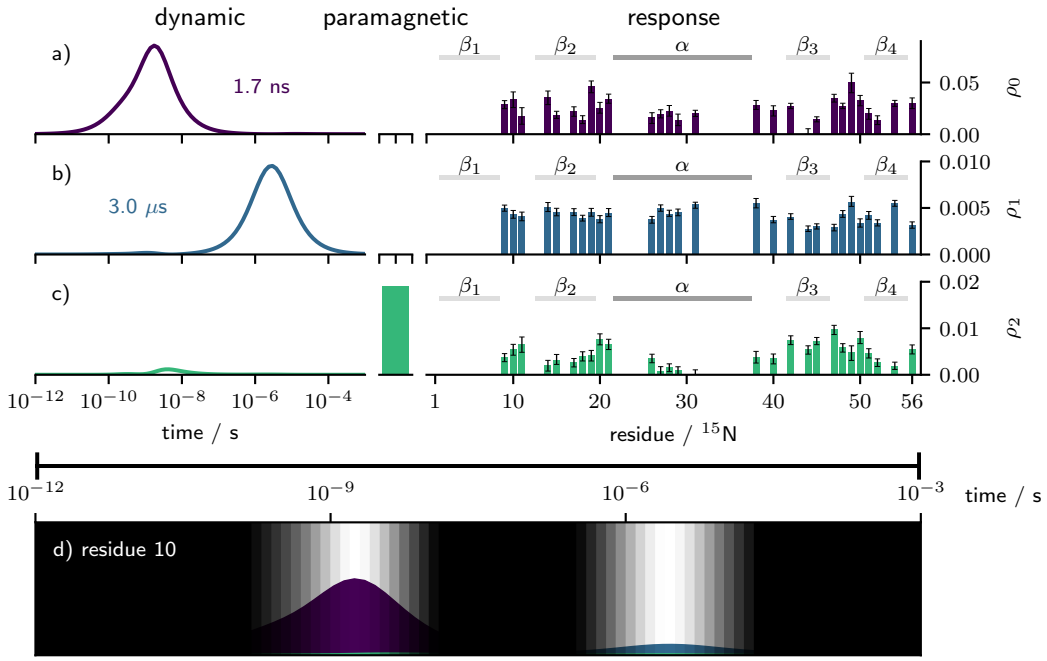

Figure A.1: Equivalent of Figure 5.5 using $k = 3$.

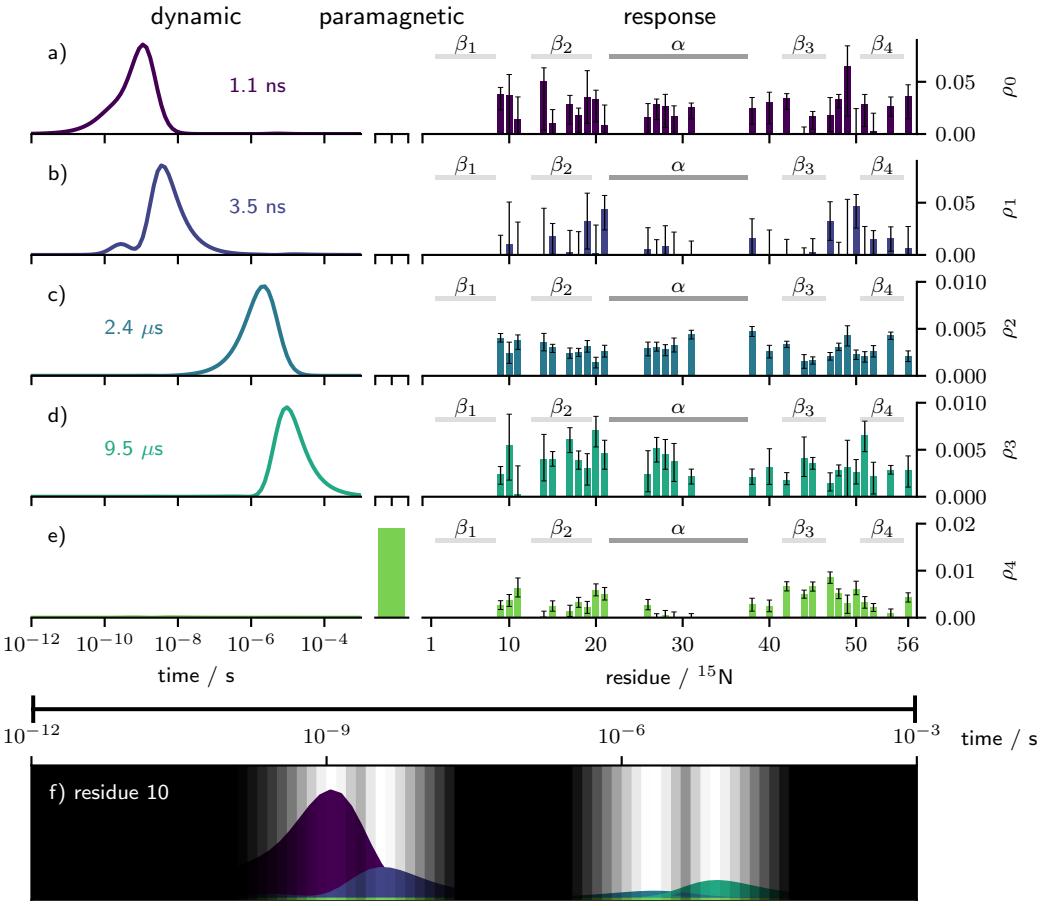

Figure A.2: Equivalent of Figure 5.5 using $k = 5$.

Appendix B

Effect of Activation Energy on Dynamical Profiles

B.1 Calculations assuming 30 kJ mol^{-1}

The analysis was performed as previously. The reduced $\hat{\chi}^2$ criterion selected $k = 5$ for ^{15}N and $k = 5$ for ^{13}C′. $k = 5$ was therefore used for the combined analysis.

Table B.1: (30 kJ mol^{-1} equivalent of Table 6.4) Summary model statistics for models with different values of k.

k	N^o ^{13}C′	N^o ^{15}N	$\frac{\chi^2}{n}$ ^{13}C′*	$\frac{\chi^2}{n}$ ^{15}N	$\hat{\chi}^2$ ^{13}C′†	$\hat{\chi}^2$ ^{15}N
2	2	2	10.66	56.94	12.16	36.96
3	3	3	10.00	34.26	11.64	27.89
4	4	4	9.62	31.36	11.23	26.03
5	5	5	7.90	24.00	9.05	17.08
6	6	7	7.99	22.78	9.94	19.48
7	7	7	7.55	23.45	10.03	19.30
8	8	9	8.15	22.93	11.71	20.59
9	9	10	8.04	23.76	12.72	21.90
10	11	9	8.40	24.04	16.33	21.82

*average χ^2 value, calculated over all data

†median reduced χ^2 value, calculated for each individual residue and then the median taken

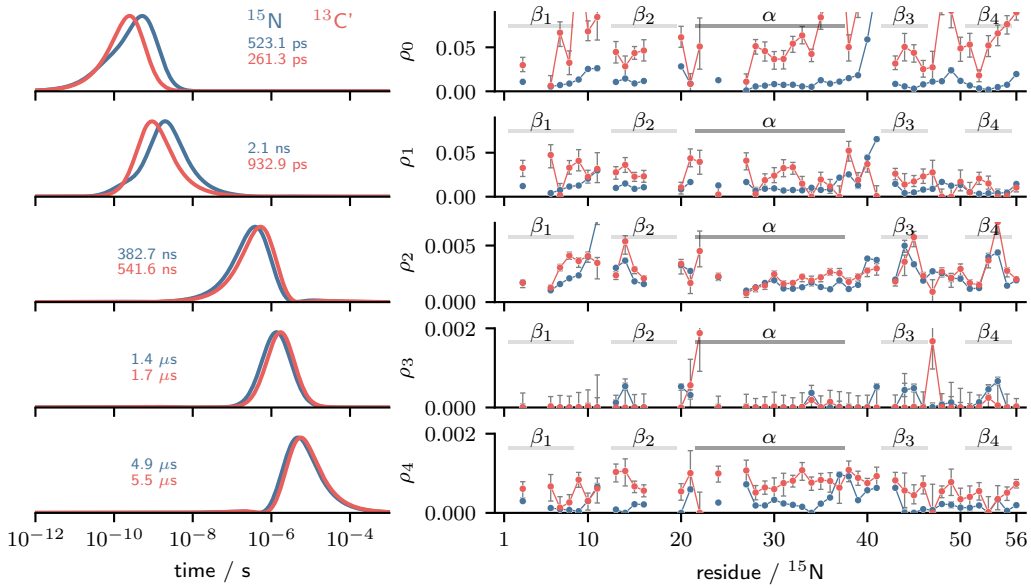

Figure B.1: (30 kJ mol^{-1} equivalent of Figure 6.9) Calculated detector responses for ^{15}N and ^{13}C′. Left: Paired detector sensitivities. Right: Paired detector responses.

Table B.2: (30 kJ mol^{-1} equivalent of Table 6.5) Scaling factors applied to carbonyl detector responses.

Detector	Scaling Factor
ρ_0	0.24
ρ_1	0.69
ρ_2	0.91
ρ_3	1.34
ρ_4	0.43

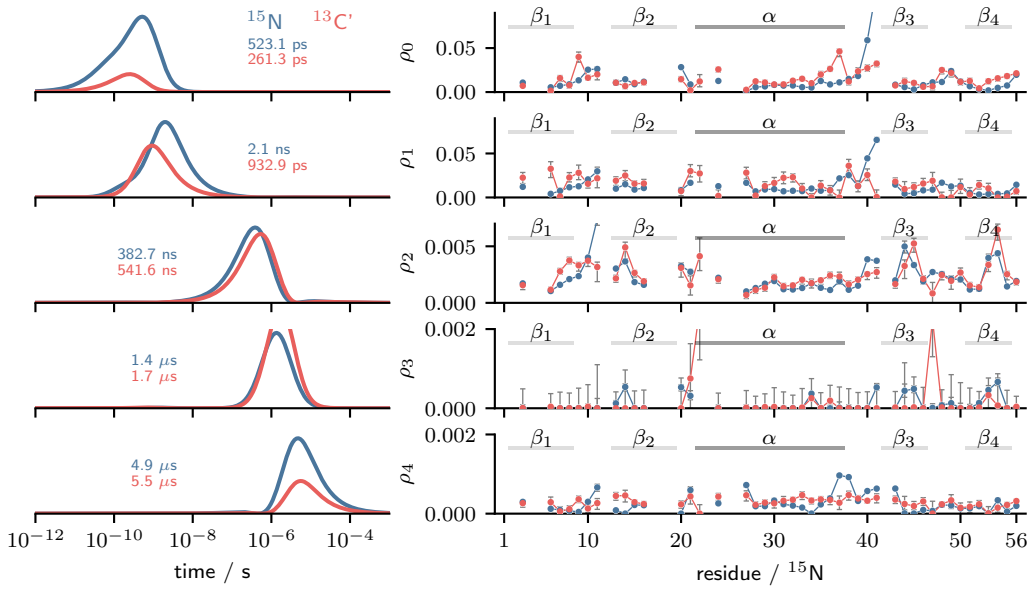

Figure B.2: (30 kJ mol^{-1} equivalent of Figure 6.11) Calculated (scaled) detector responses for ^{15}N and ^{13}C′. Left: Detector sensitivity profiles. Right: Detector responses.

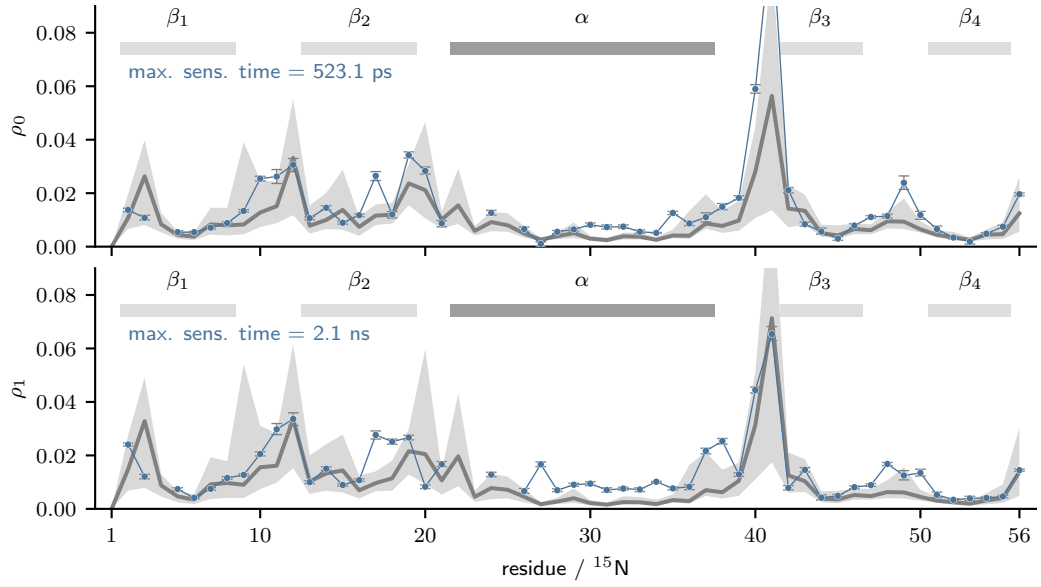

Figure B.3: (30 kJ mol^{-1} equivalent of Figure 6.12) Comparison of calculated detector responses for ^{15}N (left) and (scaled) ^{13}C′ (right) with molecular dynamics. Comparison is shown for detectors covering timescales for which the MD was sensitive to. MD response is shown as a grey band, with percentiles at 5%, 50%, 95%.

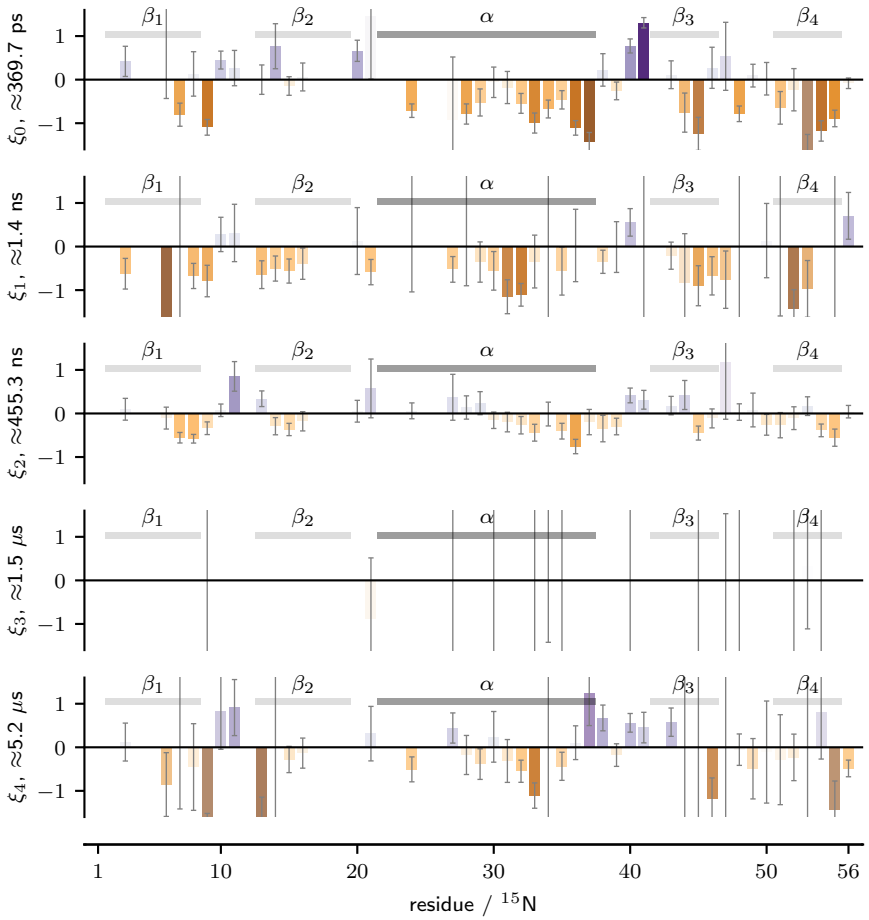

Figure B.4: (30 kJ mol^{-1} equivalent of Figure 6.13) Natural log of the ratio between the $^{13}C'$ response and the ^{15}N response for each pair of detectors. A negative (orange) value suggests dominant motion parallel to the $^{15}N-^{1}H$ bond axis, while a positive (purple) number indicates motion perpendicular to this. The transparency has been set according to the error, with an error of 0 being fully opaque and an error of 1.5 being fully transparent.

B.2 Calculations assuming 50 kJ mol^{-1}

The analysis was performed as previously. With 50 kJ mol^{-1} the reduced $\hat{\chi}^2$ criterion selected $k = 7$ for ^{15}N and $k = 7$ for ^{13}C′. $k = 7$ was therefore used for the combined analysis.

Table B.3: (50 kJ mol^{-1} equivalent of Table 6.4) Summary model statistics for models with different values of k.

k	N^o ^{13}C′	N^o ^{15}N	$\frac{\chi^2}{n}$ ^{13}C′‡	$\frac{\chi^2}{n}$ ^{15}N	$\hat{\chi}^2$ ^{13}C′§	$\hat{\chi}^2$ ^{15}N
2	2	2	10.38	71.77	11.09	30.39
3	3	3	9.35	29.38	10.62	19.84
4	4	4	9.00	26.58	10.72	17.19
5	5	5	7.30	22.74	8.55	16.13
6	7	8	6.31	20.75	8.51	18.92
7	7	7	6.35	19.80	8.32	15.45
8	8	9	6.33	19.19	8.79	17.39
9	9	9	6.26	19.06	9.39	17.20
10	10	12	6.68	19.27	11.63	22.36

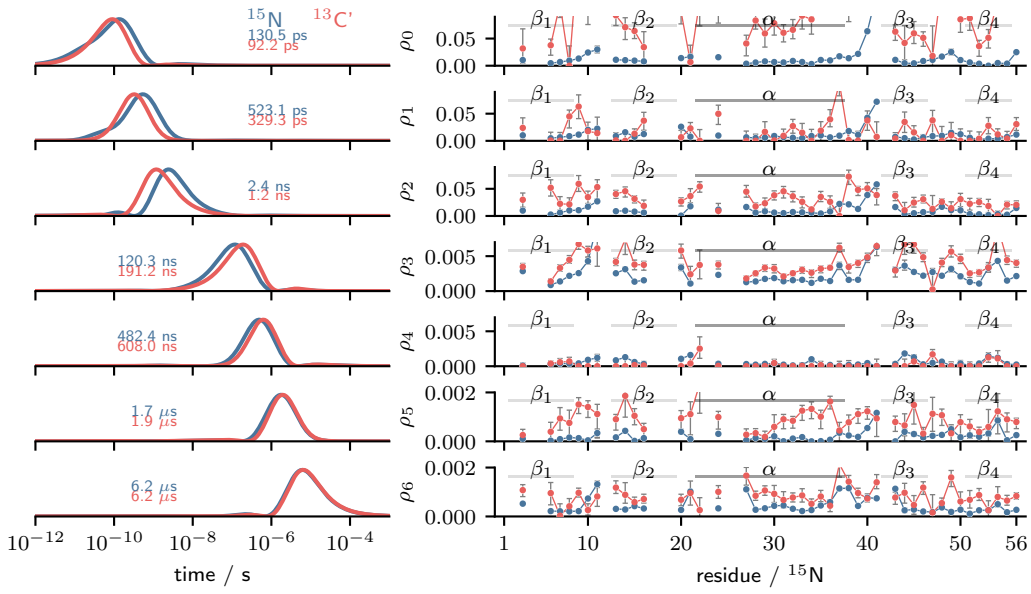

Figure B.5: (50 kJ mol^{-1} equivalent of Figure 6.9) Calculated detector responses for ^{15}N and ^{13}C′. Left: Paired detector sensitivities. Right: Paired detector responses.

‡average χ^2 value, calculated over all data
§median reduced χ^2 value, calculated for each individual residue and then the median taken

Table B.4: (50 kJ mol^{-1} equivalent of Table 6.5) Scaling factors applied to carbonyl detector responses.

Detector	Scaling Factor
ρ_0	0.16
ρ_1	0.73
ρ_2	0.39
ρ_3	0.65
ρ_4	2.32
ρ_5	0.30
ρ_6	0.56

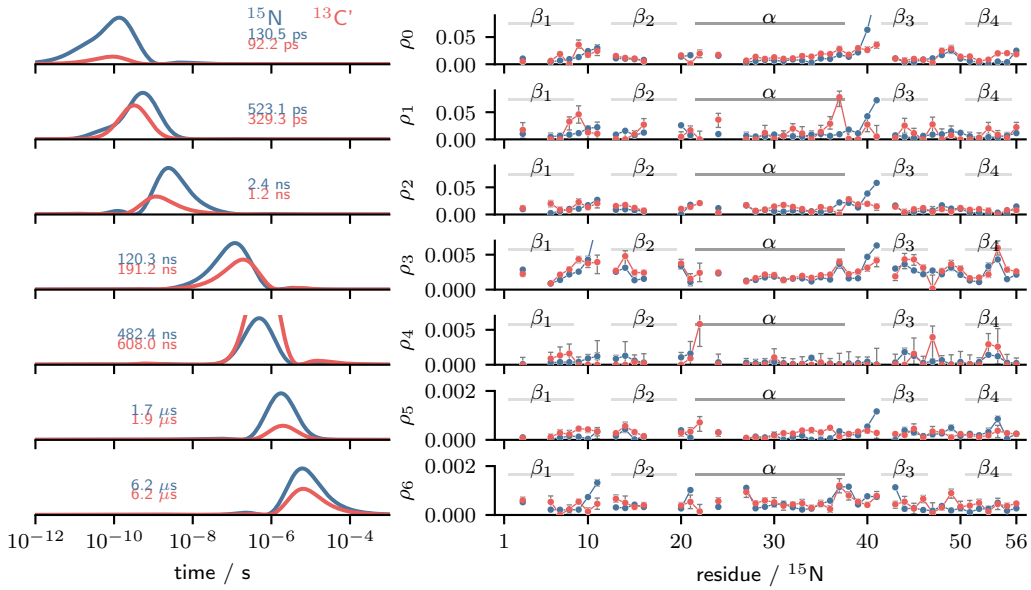

Figure B.6: (50 kJ mol^{-1} equivalent of Figure 6.11) Calculated (scaled) detector responses for ^{15}N and ^{13}C′. Left: Detector sensitivity profiles. Right: Detector responses.

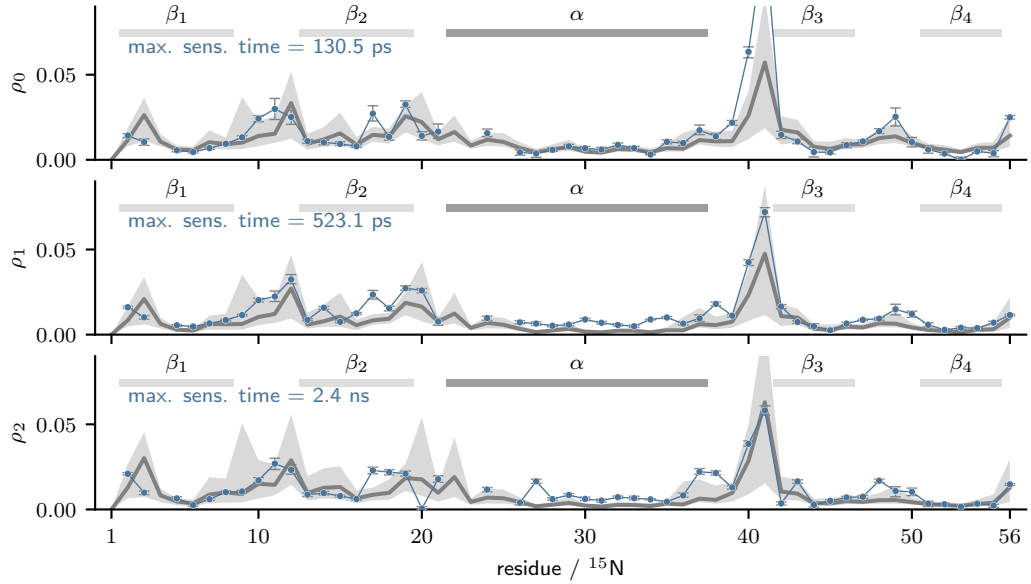

Figure B.7: (50 kJ mol^{-1} equivalent of Figure 6.12) Comparison of calculated detector responses for ^{15}N (left) and (scaled) ^{13}C′ (right) with molecular dynamics. Comparison is shown for detectors covering timescales for which the MD was sensitive to. MD response is shown as a grey band, with percentiles at 5%, 50%, 95%.

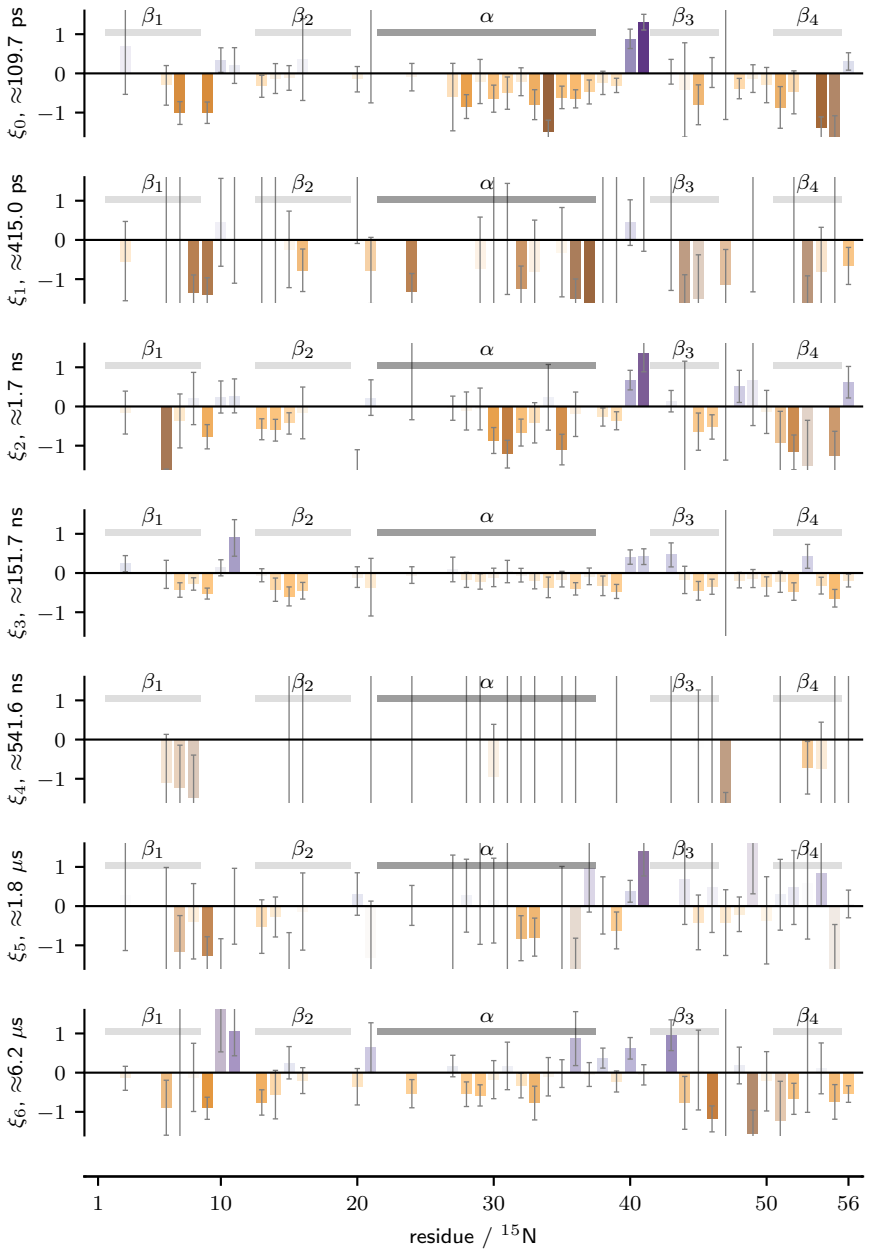

Figure B.8: (50 kJ mol^{-1} equivalent of Figure 6.13) Natural log of the ratio between the $^{13}C'$ response and the ^{15}N response for each pair of detectors. A negative (orange) value suggests dominant motion parallel to the $^{15}N-^{1}H$ bond axis, while a positive (purple) number indicates motion perpendicular to this. The transparency has been set according to the error, with an error of 0 being fully opaque and an error of 1.5 being fully transparent.

Appendix C

More Visualisations of Anisotropic Motion

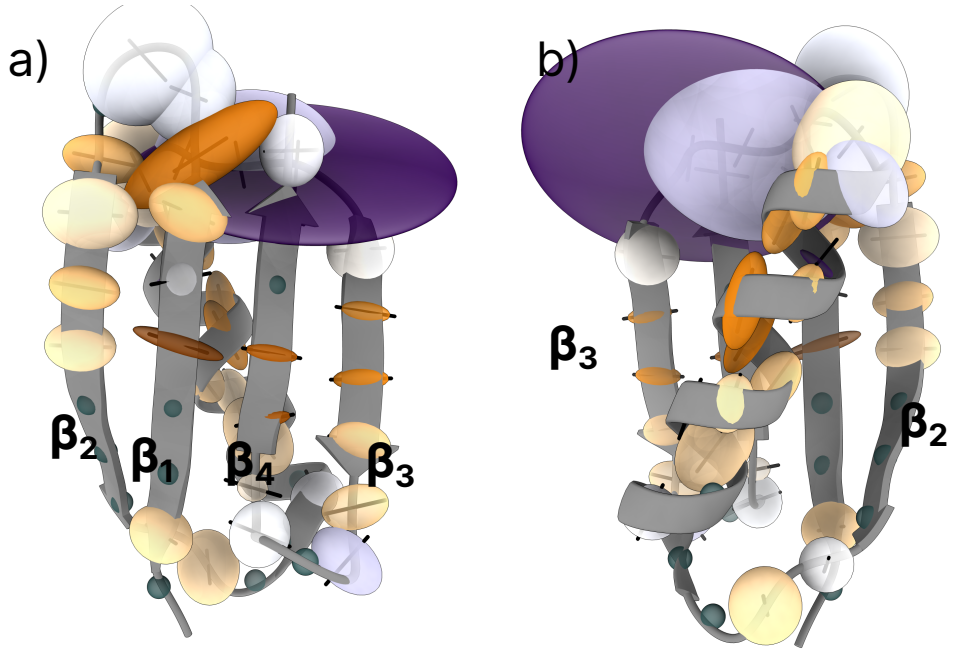

Figure C.1: Visualisation of the anisotropic motions of detector ρ_1 projected onto the structure of GB1. Motions are shown as ellipsoids as described in Figure 6.16, with the transparency set according to the error as in Figure 6.13. The backbone of the GB1 is shown as in grey, with black bars indicating the orientation of the N–H bond vector for each residue. (a) View of the β-sheet of GB1. (b) View of the α-helix of GB1.

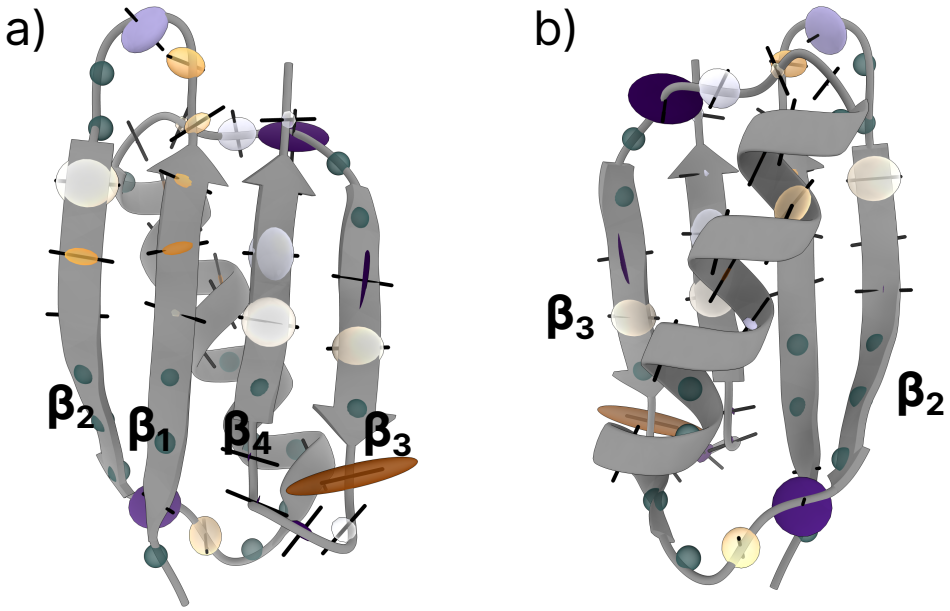

Figure C.2: Visualisation of the anisotropic motions of detector ρ_3 projected onto the structure of GB1. Motions are shown as ellipsoids as described in Figure 6.16, with the transparency set according to the error as in Figure 6.13. The backbone of the GB1 is shown as in grey, with black bars indicating the orientation of the N−H bond vector for each residue. (a) View of the β-sheet of GB1. (b) View of the α-helix of GB1. Note that for clarity, the responses have been scaled up $10\times$ relative to those shown in Figure 6.14.

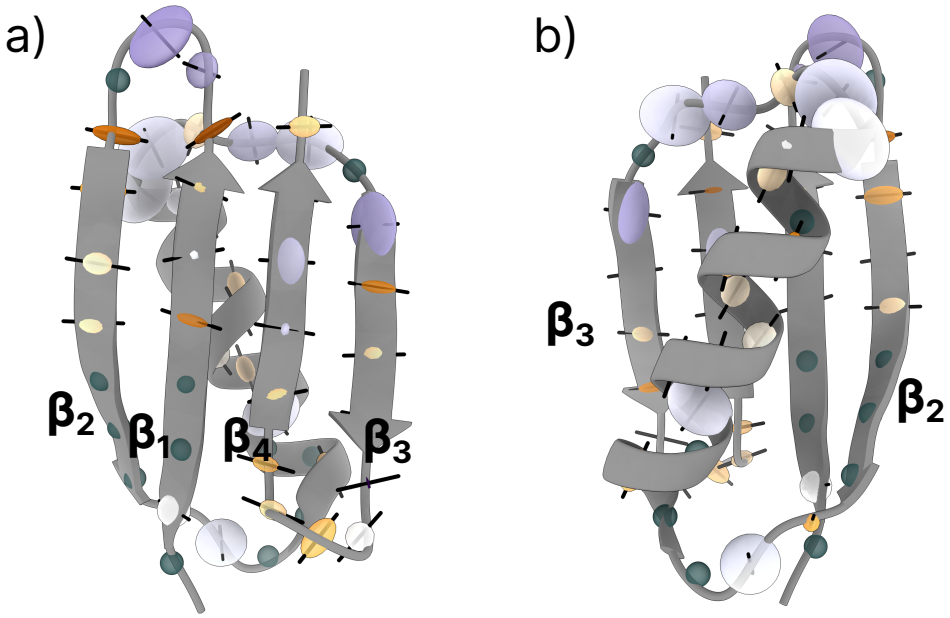

Figure C.3: Visualisation of the anisotropic motions of detector ρ_4 projected onto the structure of GB1. Motions are shown as ellipsoids as described in Figure 6.16, with the transparency set according to the error as in Figure 6.13. The backbone of the GB1 is shown as in grey, with black bars indicating the orientation of the N−H bond vector for each residue. (a) View of the β-sheet of GB1. (b) View of the α-helix of GB1. Note that for clarity, the responses have been scaled up $20\times$ relative to those shown in Figure 6.14.